

**UCSF**

**UC San Francisco Electronic Theses and Dissertations**

**Title**

X-ray crystal structures of the influenza A M2 proton channel

**Permalink**

<https://escholarship.org/uc/item/7jn6q27x>

**Author**

Thomaston, Jessica Leigh

**Publication Date**

2018

Peer reviewed|Thesis/dissertation

X-ray crystal structures of the influenza A M2 proton channel

by

Jessica Leigh Thomaston

DISSERTATION

Submitted in partial satisfaction of the requirements for the degree of

DOCTOR OF PHILOSOPHY

in

Chemistry and Chemical Biology

in the



Copyright 2018

by

Jessica Leigh Thomaston

*To my friends and family.*

## Acknowledgements

The work presented here would not have been possible without the support of many people. The scientific community at UCSF was particularly helpful throughout my time in graduate school. I would like to thank the members of my thesis committee, Bob Stroud, Dan Minor, and James Fraser, for productive discussions in our yearly meetings. I am also thankful to Natalia Jura for her words of encouragement while acting as a faculty coach for my yearly CCB talks. Early in my studies, UCSF postdocs Ryan Coleman and Magdalena Korczynska were of tremendous help, as was Chris Waddling in the X-ray Crystallography Facility. I also thank my fellow students in the CCB and iPQB programs for their advice and support.

The entire DeGrado lab has been a valuable resource over the years. Hyunil Jo was always available to discuss the finer points of peptide synthesis. Jun Wang's work on inhibitors of drug-resistant M2 paved the way for my structural studies of these mutants. Many other lab members over the years have been a source of discussion, advice, morale, and collaborations: Kathleen Molnar, Bruk Mensa, Yibing Wu, Gözde Ulas, Manasi Bhate, Nathan Schmidt, Marco Mravic, Nick Polizzi, and others.

The X-ray diffraction data presented here was collected at a number of beamlines. Many thanks are due to the staff scientists at all of these facilities for their help during data collection: George Meigs and James Holton at ALS 8.3.1, Rie Tanaka and Eriko Nango at SACLA, Surajit Banerjee and K. Rajashankar at the NECAT beamlines at APS, and Aina Cohen at SSRL 12-2.

Most of all I would like to thank my advisor Bill DeGrado, who has deeply impressed me with his enthusiasm for science, and his commitments to both doing good research and being a good person.

## Contributions

Many of the chapters presented here are edited versions of previously published work, or represent manuscripts currently in preparation. Author contributions for these works are as follows:

**Chapter 2:** Thomaston JL, Alfonso-Prieto M, Woldeyes R, Fraser JS, Klein ML, Fiorin G, DeGrado WF. "High resolution structures of the M2 proton channel from influenza A virus reveal dynamic pathways for proton stabilization and transduction." PNAS 112:14260-5. 2015.  
*Contributions:* J.L.T. and W.F.D. designed research; J.L.T. performed experimental work (synthesis and purification of M2 peptide, crystallization, diffraction) and data analysis (data processing, molecular replacement, refinement, model building). M.A.-P. performed molecular dynamics simulations. J.L.T., R.A.W., J.S.F., and W.F.D. M.A.-P., R.A.W., J.S.F., M.L.K., G.F., and W.F.D. analyzed data. J.L.T. and W.F.D. wrote the paper with input from all authors.

**Chapter 3:** Thomaston JL, Woldeyes RA, Nakane T, Yamashita A, Tanaka T, Koiwai K, Brewster AS, Barad BA, Chen Y, Lemmin T, Uervirojnangkoorn M, Arima T, Kobayashi J, Masuda T, Suzuki M, Sugahara M, Sauter NK, Tanaka R, Nureki O, Tono K, Joti Y, Nango E, Iwata S, Yumoto F, Fraser JS, DeGrado WF. "XFEL structures of the M2 proton channel of influenza A reveal pH-dependent water networks under room temperature conditions." PNAS vol. 114 no. 51 13357-13362. 2017.

*Contributions:* J.L.T, W.F.D, R.A.W., J.S.F., and F.Y. designed the research; J.L.T. synthesized, purified, and crystallized M2 samples for diffraction; J.L.T., A.Y., T.T., K.K., B.A.B., Y.C.,

T.A., J.K., T.M., M. Suzuki, M. Sugahara, R.T., and E.N. carried out SFX data collection; T.N., O.N., and R.A.W. did online data processing; K.T., Y.J., E.N. and S.I. developed the SFX system; S.I. supervised the SACLA-SFX project; R.A.W. processed the SFX data with support from A.S.B., M.U., T.N., and N.K.S.; J.L.T. phased and refined the structures; J.L.T., T.L., and W.F.D. analyzed the data; J.L.T and W.F.D. wrote the paper with input from all authors.

**Chapter 4:** Thomaston JL, Polizzi NF, Konstantinidi A, Wang J, Kolocouris A, DeGrado WF. "Inhibitors of the M2 proton channel engage and disrupt transmembrane networks of hydrogen-bonded waters" Submitted to JACS, 2018.

*Contributions:* J.L.T. carried out protein sample preparation (synthesis of WT M2 TM domain peptide, purification, crystallization), data collection, and data analysis (data processing, phasing, model building, refinement). J.W. designed and synthesized inhibitors. A. Konstantinidi and A. Kolocouris carried out and analyzed molecular dynamics simulations. N. Polizzi analyzed molecular dynamics simulations. J.L.T. and W.F.D. interpreted structural results and simulations and wrote the paper with input from all authors.

**Chapter 5:** Thomaston JL, DeGrado WF. "Crystal structure of the drug-resistant S31N influenza M2 proton channel." Protein Science 25:1551-4. 2016.

*Contributions:* J.L.T carried out all aspects of sample preparation (synthesis of S31N M2 TM domain peptide, purification, crystallization), data collection, and data analysis (data processing, phasing by molecular replacement, model building, refinement). J.L.T and W.F.D. interpreted the structural results and wrote the paper.

**Chapter 6:** "X-ray crystal structure of the S31N mutant of the influenza M2 proton channel in two conformational states: an open and shut case" Manuscript in preparation. J.L.T. carried out all aspects of sample preparation (peptide synthesis, purification, crystallization), data collection, data processing, phasing by molecular replacement, model building, and refinement. Lijun Li assisted with space group determination and analysis of crystal pathologies.

**Chapter 7:** Preliminary data. J.L.T. carried out sample preparation of the V27A TM peptide, crystallization, data collection, data processing, phasing, model building, and refinement. Jun Wang designed and synthesized inhibitors and also synthesized and purified peptide samples for the V27A and WT M2 TMC constructs.

# **X-ray crystal structures of the influenza A M2 proton channel**

Jessica Leigh Thomaston

The M2 proton channel is a drug target of the influenza A virus. It is also a model system for the study of the selective, unidirectional transport of protons across the membrane bilayer. The work presented here focuses on the structural study of the M2 proton channel using X-ray crystallography. High resolution (1.10 Å) X-ray crystal structures of the Inward<sub>open</sub> conformation of M2 reveal layers of ordered, carbonyl-associated waters in the M2 pore. These waters form hydrogen-bonded networks of "water wires" that potentially play a role in the transport of protons down to the channel's gating His37 residues. This crystal form was examined using three data collection techniques: cryogenic diffraction at a synchrotron source, room temperature diffraction at a synchrotron source, and room temperature diffraction at an XFEL source. The degree of solvent ordering observed within the M2 pore is dependent on pH, and is also sensitive to temperature and the effects of radiation damage. New structures of M2 bound to amantadine and rimantadine reveal that the adamantane drugs bind by forming hydrogen bonds with ordered waters in the M2 pore, interrupting the water wires that lead down to the His37 gate. These drugs take advantage of the channel's essential ability to stabilize hydronium; the drug ammonium group acts as a hydronium mimic, which positions the bulky adamantyl group to sterically block the diffusion of hydronium into the channel. Additionally, structural characterization of drug-resistant S31N and V27A mutants of M2 characterize the mechanisms through which mutation of pore-lining residues at the N-terminus of the channel disrupt the binding of the adamantane drugs. These structures provide information for the design of new drugs to target these adamantane-resistant M2 mutants that have become prevalent among currently circulating strains of influenza.

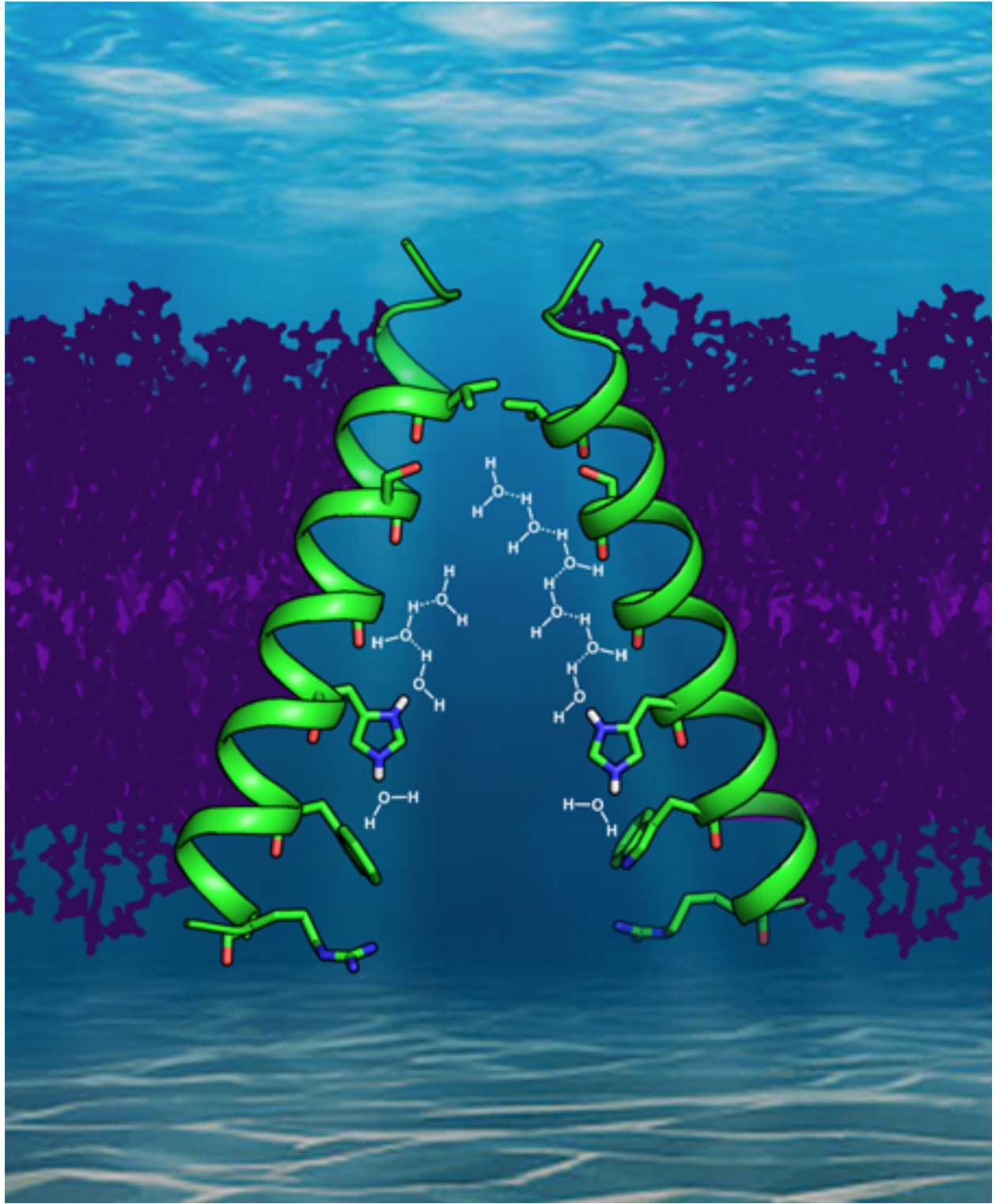




# Table of Contents

## **Chapter 1: Introduction: the M2 proton channel of the influenza A virus ..... 1-17**

|     |  |    |
|-----|--|----|
| 1.1 | Medical significance of influenza .....                                      | 1  |
| 1.2 | Life cycle of the influenza A virus .....                                    | 2  |
| 1.3 | The M2 protein .....   | 4  |
| 1.4 | Role of water in proton conduction in the M2 channel (Chapters 2 and 3)..... | 5  |
| 1.5 | Inhibition of wild type M2 by adamantane drugs (Chapter 4).....              | 8  |
| 1.6 | Drug-resistant mutants and ongoing research (Chapter 5-7) .....              | 12 |
| 1.7 | References .....   | 14 |

## **Chapter 2: High resolution structures of the M2 channel from influenza A virus reveal**

### **dynamic pathways for proton stabilization and transduction..... 18-83**

|       |  |    |
|-------|--|----|
| 2.1   | Abstract.....  | 18 |
| 2.2   | Significance .....   | 18 |
| 2.3   | Introduction.....  | 19 |
| 2.4   | Results and Discussion .....   | 20 |
| 2.4.1 | High resolution structures of M2TM .....   | 20 |
| 2.4.2 | A multitude of water wires lead to His37 .....                                     | 25 |
| 2.4.3 | Fluid water wires at room temperature .....  | 25 |
| 2.4.4 | An abundance of hydrogen bond donors relative to acceptors in the<br>channel ..... | 27 |
| 2.4.5 | Density of water by molecular dynamics simulations .....                           | 28 |
| 2.4.6 | Hydrogen bond network within the M2 pore.....                                      | 28 |

|        |  |    |
|--------|--|----|
| 2.4.7  | Hydrogen bond donor/acceptor water molecules along the M2 pore ..... | 31 |
| 2.5    | Conclusions.....   | 31 |
| 2.6    | Methods.....   | 33 |
| 2.6.1  | Experimental methods .....   | 33 |
| 2.6.2  | Molecular dynamics simulations .....                                 | 34 |
| 2.7    | Acknowledgements.....  | 36 |
| 2.8    | References.....  | 37 |
| 2.9    | Appendix A, Supplementary Figures and Tables .....                   | 42 |
| 2.10   | Appendix B, Detailed Methods.....                                    | 67 |
| 2.10.1 | Synthesis and purification of M2(22-46).....                         | 67 |
| 2.10.2 | Preparation of the lipid cubic phase and crystallization .....       | 68 |
| 2.10.3 | Data collection .....  | 69 |
| 2.10.4 | Data processing, phasing and refinement .....                        | 70 |
| 2.10.5 | Molecular dynamics simulation details .....                          | 70 |
| 2.10.6 | Appendix B References .....  | 81 |

**Chapter 3: XFEL structures of the influenza M2 proton channel: room temperature water networks and insights into proton conduction ..... 84-118**

|       |  |    |
|-------|--|----|
| 3.1   | Abstract .....   | 84 |
| 3.2   | Significance.....  | 85 |
| 3.3   | Introduction.....  | 85 |
| 3.4   | Results and Discussion .....   | 90 |
| 3.4.1 | Comparison of low pH XFEL structure to synchrotron structures .....  | 90 |
| 3.4.2 | Comparison of high pH XFEL structure to synchrotron structures ..... | 92 |

|       |  |     |
|-------|--|-----|
| 3.4.3 | XFEL datasets avoid artifacts from both cryocooling and radiation damage ..... | 93  |
| 3.4.4 | Continuous hydrogen bonding network at low pH .....                            | 94  |
| 3.4.5 | Intermediate pH XFEL structure compared to previous structures .....           | 99  |
| 3.4.6 | XFEL structures at low, intermediate, and high pH .....                        | 105 |
| 3.4.7 | Implications for proton conduction.....  | 100 |
| 3.5   | Materials and Methods.....   | 103 |
| 3.6   | Acknowledgements.....  | 106 |
| 3.7   | Detailed Methods .....   | 107 |
| 3.7.1 | Peptide synthesis, purification, and reconstitution into lipid .....           | 107 |
| 3.7.2 | Microcrystal optimization .....  | 107 |
| 3.7.3 | XFEL data collection .....   | 108 |
| 3.7.4 | Data processing .....  | 109 |
| 3.7.5 | Molecular replacement and refinement .....                                     | 110 |
| 3.7.6 | RMSDs to previous structures .....   | 110 |
| 3.7.7 | Analysis of hydrogen bonding networks in the low pH XFEL structure .....       | 111 |
| 3.8   | References.....  | 112 |

#### **Chapter 4: Inhibitors of the M2 proton channel engage and disrupt transmembrane**

#### **networks of hydrogen-bonded waters ..... 119-163**

|     |                              |     |
|-----|------------------------------|-----|
| 4.1 | Abstract.....                | 119 |
| 4.2 | Introduction.....            | 119 |
| 4.3 | Results and Discussion ..... | 123 |

|       |   |     |
|-------|---|-----|
| 4.3.1 | The adamantane groups of rimantadine and amantadine snip water-wires, while the ammonium group engages the remaining water networks in the Inward <sub>closed</sub> state ..... | 123 |
| 4.3.2 | The spiro-adamantyl amine inhibitor additionally displaces a second layer of water molecules in the Inward <sub>closed</sub> state .....  | 128 |
| 4.3.3 | Structure of rimantadine bound to M2 in the Inward <sub>open</sub> state.....   | 130 |
| 4.3.4 | Structural mechanism of drug binding and channel inhibition .....   | 133 |
| 4.3.5 | Explaining the effectiveness of adamantane as a substituent for drug design .....   | 134 |
| 4.3.6 | Molecular dynamics confirm the structural mechanism of drug binding .....   | 136 |
| 4.3.7 | Implications for design of drugs that target influenza A virus .....  | 139 |
| 4.4   | Methods .....   | 140 |
| 4.4.1 | Data availability .....   | 140 |
| 4.5   | Acknowledgements.....   | 141 |
| 4.6   | References.....   | 144 |
| 4.7   | Appendix C, Supplemental Information Figures and Tables.....  | 149 |
| 4.8   | Appendix D, Detailed Methods .....  | 154 |
| 4.8.1 | Experimental methods .....  | 154 |
| 4.8.2 | Molecular dynamics methods .....  | 157 |
| 4.8.3 | Appendix D references .....   | 161 |

## **Chapter 5: Crystal structure of the drug-resistant S31N influenza M2 proton channel in**

### **the Inward<sub>open</sub> conformation..... 164-180**

|   |     |
|---|-----|
| 5.1 Abstract .....  | 164 |
| 5.2 Introduction.....   | 164 |
| 5.3 Results and Discussion .....                                  | 166 |
| 5.3.1 Solvent network and partially occupied waters .....         | 166 |
| 5.3.2 Resistance to adamantane drugs and inhibitor binding.....   | 169 |
| 5.4 Methods .....   | 172 |
| 5.4.1 Synthesis, purification, and crystallization of S31N.....   | 172 |
| 5.4.2 Data collection and processing .....                        | 173 |
| 5.4.3 Ions and lipid molecules in the S31N crystal structure..... | 174 |
| 5.4.4 Accession numbers .....                                     | 174 |
| 5.5 Acknowledgements.....   | 175 |
| 5.6 Supplemental Figures and Tables .....                         | 176 |
| 5.7 References.....   | 179 |

## **Chapter 6: X-ray crystal structure of the S31N mutant of the influenza M2 proton channel**

### **in two conformational states: an open and shut case ..... 181-192**

|   |     |
|---|-----|
| 6.1 Introduction.....                                   | 181 |
| 6.2 Results and Discussion .....                        | 182 |
| 6.2.1 Conformation of the mutant Asn31 side chain ..... | 183 |
| 6.3 Methods.....  | 186 |

|   |   |                |
|---|---|----------------|
| 6.4                                       | Acknowledgements.....   | 189            |
| 6.5                                       | References.....   | 190            |
| <b>Chapter 7: Works in progress .....</b> |   | <b>193-202</b> |
| 7.1                                       | Motivation.....   | 193            |
| 7.2                                       | Structure of drug-resistant V27A mutant bound to a spiro-adamantyl<br>amine inhibitor ..... | 193            |
| 7.3                                       | Structures of longer M2 constructs .....  | 197            |
| 7.4                                       | Attempts to solve structure of S31N bound to inhibitors .....                               | 200            |
| 7.5                                       | References.....   | 202            |

## List of Figures

|                   |   |    |
|-------------------|---|----|
| <b>Figure 1.1</b> | The adamantane drugs: amantadine and rimantadine.....   | 2  |
| <b>Figure 1.2</b> | Life cycle of the influenza A virus .....   | 3  |
| <b>Figure 1.3</b> | Simultaneous equilibria between gating His tetrad charge state and the two<br>conformational states of M2 .....             | 5  |
| <b>Figure 1.4</b> | Grotthuss mechanism of proton transport .....   | 7  |
| <b>Figure 1.5</b> | Diffraction before destruction .....  | 8  |
| <b>Figure 1.6</b> | Density of bound amantadine from the previously solved 2008 drug-bound<br>crystal structure .....                           | 10 |
| <b>Figure 1.7</b> | Positive charges localize to specific regions of the M2 channel .....   | 11 |
| <b>Figure 1.8</b> | The ammonium group of the adamantane drugs acts as a hydronium mimic .....  | 11 |
| <b>Figure 2.1</b> | M2 is surrounded by monoolein molecules.....  | 22 |
| <b>Figure 2.2</b> | Crystal structure of M2TM at 1.10 Å at pH 8.0 (4QK7) under cryogenic<br>conditions .....                                    | 23 |
| <b>Figure 2.3</b> | Waters in the cryogenic crystal structures form ordered water wires while<br>room temperature waters are less ordered ..... | 26 |
| <b>Figure 2.4</b> | Electron density comparisons show differences and similarities between the<br>solvent density at high and low pH.....       | 27 |
| <b>Figure 2.5</b> | Hydrogen bond orientation calculated from MD simulations .....  | 30 |
| <b>Figure 2.6</b> | Further comparisons between density maps .....  | 42 |
| <b>Figure 2.7</b> | System setup used in the molecular dynamics simulations .....   | 43 |

|                    |   |    |
|--------------------|---|----|
| <b>Figure 2.8</b>  | Evolution of the root mean square deviation (RMSD) of the C $\alpha$ atoms of M2TM along the MD simulations .....                                 | 44 |
| <b>Figure 2.9</b>  | Evolution of the principal component, $p$ , along the MD simulations.....   | 45 |
| <b>Figure 2.10</b> | Two-dimensional profile of the hydrogen bond vectors at different charge states of the His37 tetrad.....  | 46 |
| <b>Figure 2.11</b> | Water wires calculated from the molecular dynamics simulations at different charge states of the His37 tetrad .....                               | 48 |
| <b>Figure 2.12</b> | Average hydrogen bond vectors along the M2 pore at different charge states of the His37 tetrad.....   | 49 |
| <b>Figure 2.13</b> | Difference between the number of water molecules acting as hydrogen bond donors and acceptors at different charge states of the His37 tetrad..... | 50 |
| <b>Figure 2.14</b> | Water wires calculated from the control simulations at different charge states of the His37 tetrad.....   | 51 |
| <b>Figure 2.15</b> | Evolution of the root mean square deviation (RMSD) of the C $\alpha$ atoms of M2TM along the MD simulations of the S31N mutant .....              | 52 |
| <b>Figure 2.16</b> | Evolution of the principal component, $p$ , along the MD simulations of the S31N M2TM mutant.....   | 53 |
| <b>Figure 2.17</b> | Two-dimensional profile of the hydrogen bond vectors at different charge states of the His37 tetrad for the S31N mutant .....                     | 54 |
| <b>Figure 2.18</b> | Water wires calculated from the molecular dynamics simulations at different charge states of the His37 tetrad for the S31N mutant .....           | 56 |
| <b>Figure 2.19</b> | Average hydrogen bond vectors along the M2 pore at different charge states of the His37 tetrad for the S31N mutant.....                           | 57 |



|                    |  |    |
|--------------------|--|----|
| <b>Figure 2.20</b> | Difference between the number of water molecules acting as hydrogen bond donors and acceptors at different charge states of the His37 tetrad for the S31N mutant ..... | 58 |
| <b>Figure 2.21</b> | Evolution of the root mean square deviation (RMSD) of the C $\alpha$ atoms of M2TM along the MD simulations of the D44N mutant. ....                                   | 59 |
| <b>Figure 2.22</b> | Evolution of the principal component, $p$ , along the MD simulations of the D44N M2TM mutant .....   | 60 |
| <b>Figure 2.23</b> | Two-dimensional profile of the hydrogen bond vectors at different charge states of the His37 tetrad for the D44N mutant .....  | 61 |
| <b>Figure 2.24</b> | Water wires calculated from the molecular dynamics simulations at different charge states of the His37 tetrad for the D44N mutant.....                                 | 63 |
| <b>Figure 2.25</b> | Average hydrogen bond vectors along the M2 pore at different charge states of the His37 tetrad for the D44N mutant .....   | 64 |
| <b>Figure 2.26</b> | Difference between the number of water molecules acting as hydrogen bond donors and acceptors at different charge states of the His37 tetrad for the D44N mutant.....  | 65 |
| <b>Figure 3.1</b>  | Protonation states of the M2 gating His37 tetrad .....   | 87 |
| <b>Figure 3.2</b>  | Low pH M2TM crystal structures .....   | 91 |
| <b>Figure 3.3</b>  | High pH M2TM crystal structures.....   | 94 |
| <b>Figure 3.4</b>  | Alternate occupancy water networks in the low pH (pH 5.5) room temperature XFEL structure (5JOO) .....   | 96 |
| <b>Figure 3.5</b>  | Possible water networks forming continuous hydrogen bonds to His37.....  | 97 |
| <b>Figure 3.6</b>  | Possible water networks not forming continuous hydrogen bonds to His37 .....   | 98 |

|                    |  |     |
|--------------------|--|-----|
| <b>Figure 3.7</b>  | Solvent layer above His37 expands in Inward <sub>open</sub> conformation.....  | 101 |
| <b>Figure 3.8</b>  | Room temperature XFEL structures of M2TM under all pH conditions .....   | 101 |
| <b>Figure 3.9</b>  | Distance of water from gating His37 residues in all XFEL structures .....  | 102 |
| <b>Figure 3.10</b> | High concentration solution of M2TM microcrystals .....  | 104 |
| <b>Figure 4.1</b>  | Structures and space-filling models of amantadine, rimantadine, and spiro-<br>adamantyl amine .....  | 121 |
| <b>Figure 4.2</b>  | X-ray crystal structures of the M2 proton channel bound to drugs and<br>inhibitors .....   | 125 |
| <b>Figure 4.3</b>  | Electron density in channel pore above the gating His37 residues .....   | 126 |
| <b>Figure 4.4</b>  | Water-mediated hydrogen bonds facilitate the binding of rimantadine<br>and amantadine to the M2 pore.....                                  | 128 |
| <b>Figure 4.5</b>  | Binding of spiro-adamantyl amine to the Inward <sub>closed</sub> state.....  | 130 |
| <b>Figure 4.6</b>  | Aligned rimantadine-bound Inward <sub>open</sub> (6BOC, pink) and amantadine-bound<br>Inward <sub>open</sub> (3C9J, gray) structures ..... | 132 |
| <b>Figure 4.7</b>  | Alignment of Inward <sub>open</sub> and Inward <sub>closed</sub> structures showing amantadine and<br>rimantadine binding .....            | 133 |
| <b>Figure 4.8</b>  | Molecular dynamics reproduces the positions of the crystallographic waters .....   | 138 |
| <b>Figure 4.9</b>  | Crystals of M2TM bound to drugs and inhibitors .....   | 141 |
| <b>Figure 4.10</b> | C $\alpha$ atoms RMSD .....  | 149 |
| <b>Figure 4.11</b> | Autocorrelation of amantadine rotation and displacement.....   | 149 |
| <b>Figure 4.12</b> | Amantadine tilt in MD simulation.....  | 150 |
| <b>Figure 4.13</b> | Molecular dynamics reproduces the positions of the crystallographic waters,<br>all snapshots .....   | 150 |

|   |     |
|---|-----|
| <b>Figure 4.14</b> Water RDF from MD simulation of amantadine bound to M2 in the<br>Inward <sub>closed</sub> state .....            | 151 |
| <b>Figure 4.15</b> Autocorrelation of spiro-adamantyl amine rotation and displacement .....   | 151 |
| <b>Figure 4.16</b> Water RDF from MD simulation of spiro-adamantyl amine bound to M2 in the<br>Inward <sub>closed</sub> state ..... | 152 |
| <b>Figure 4.17</b> KDE for amine displacement of amantadine and spiro-adamantyl amine .....   | 152 |
| <b>Figure 5.1</b> Crystals of M2TM S31N mutant .....  | 167 |
| <b>Figure 5.2</b> Contents of asymmetric unit of M2 S31N structure .....  | 168 |
| <b>Figure 5.3</b> Crystal structure of the S31N mutant of M2 in the Inward <sub>open</sub> conformation .....                       | 169 |
| <b>Figure 5.4</b> Drug resistance in the M2 S31N mutant .....   | 171 |
| <b>Figure 5.5</b> Arrangement of M2 tetramers within the crystal lattice .....  | 176 |
| <b>Figure 5.6</b> Tilt of M2 monomers relative to the channel's central axis .....  | 177 |
| <b>Figure 6.1</b> Two conformations of the M2 S31N mutant are observed in the asymmetric unit of a<br>new crystal form .....        | 182 |
| <b>Figure 6.2</b> Alignment of S31N Inward <sub>open</sub> conformation crystal structures .....                                    | 183 |
| <b>Figure 6.3</b> Top-down view of the M2 S31N crystal structure .....  | 184 |
| <b>Figure 6.4</b> Side view of Asn31 from the Inward <sub>closed</sub> conformation .....   | 184 |
| <b>Figure 6.5</b> Solvent-accessible surface area inside the M2 pore at the adamantane<br>binding site .....                        | 186 |
| <b>Figure 7.1</b> A spiro-adamantyl amine compound inhibits proton conduction in wild type,<br>V27A, and L26F M2 .....              | 194 |
| <b>Figure 7.2</b> Alignment of inhibitor-bound V27A M2 structure to amantadine-bound<br>WT M2 structure .....                       | 195 |

|  |     |
|--|-----|
| <b>Figure 7.3</b> Binding of spiro-adamantyl amine inhibitor to adamantane-resistant V27A mutant.....            | 197 |
| <b>Figure 7.4</b> Diffraction of V27A M2TMC plus spiro-adamantyl amine inhibitor to 3 Å resolution.....          | 199 |
| <b>Figure 7.5</b> The M2 channel's C-terminus is slightly more constricted with inclusion of the cyto helix..... | 200 |
| <b>Figure 7.6</b> Preliminary ~6 Å diffraction from crystals containing S31N TMC plus WJ352 inhibitor.....       | 201 |

## List of Tables

|                  |  |     |
|------------------|--|-----|
| <b>Table 2.1</b> | Crystallographic data tables .....   | 24  |
| <b>Table 2.2</b> | Average number of hydrogen bonds in the M2 pore at different charge states<br>of the His37 tetrad.....                         | 47  |
| <b>Table 2.3</b> | Average number of hydrogen bonds in the M2 pore at different charge states<br>of the His37 tetrad for the S31N M2 mutant ..... | 55  |
| <b>Table 2.4</b> | Average number of hydrogen bonds in the M2 pore at different charge states<br>of the His37 tetrad for the D44N M2 mutant.....  | 62  |
| <b>Table 2.5</b> | Comparison of the C $\alpha$ RMSD and <i>p</i> values along the MD simulations of wild-<br>type, S31N and D44N M2TM .....      | 66  |
| <b>Table 3.1</b> | Number of ordered waters in M2 pore .....  | 92  |
| <b>Table 3.2</b> | Data processing statistics for room temperature XFEL datasets .....  | 105 |
| <b>Table 3.3</b> | Twin fractions .....   | 105 |
| <b>Table 3.4</b> | Refinement statistics for room temperature XFEL structures.....  | 106 |
| <b>Table 4.1</b> | Data processing statistics .....   | 142 |
| <b>Table 4.2</b> | Refinement statistics .....  | 143 |
| <b>Table 4.3</b> | Structural and dynamic measures from 250 ns MD trajectories of M2TM-<br>ligand complexes in POPC bilayer at high pH. ....      | 153 |
| <b>Table 5.1</b> | Data processing and refinement statistics .....  | 178 |
| <b>Table 6.1</b> | Data processing and refinement statistics .....  | 188 |

# Chapter 1

## Introduction: the M2 proton channel of the influenza A virus

### 1.1 Medical significance of influenza

Influenza is a yearly, worldwide threat to human health. Each year, influenza infections are responsible for a total of 290,000 to 650,000 deaths worldwide.<sup>1</sup> In the United States, between 3,000 and 49,000 people per year<sup>2</sup> die from influenza infections, with the severity of each flu season depending on the subtypes circulating that year. The influenza virus has the potential to cause deadly pandemics; the most notable historical example of this is the 1918 Spanish Flu, which infected approximately one third of the human population and caused an estimated 50 million deaths.<sup>3</sup>

Currently, there are four FDA-approved anti-influenza medications: amantadine, rimantadine, zanamivir, and oseltamivir. Two of these, amantadine and rimantadine (**Fig. 1.1**), target the M2 proton channel. However, viral resistance to these drugs is an ongoing problem. Adamantane-resistant strains of influenza were first observed in the 1980s.<sup>4</sup> These mutants have become prevalent in recent years,<sup>5-7</sup> with 95% of influenza isolates worldwide being resistant to adamantane drugs.<sup>8</sup> The S31N mutant of M2 is found in 98% of adamantane-resistant viruses.<sup>5</sup> Because drug-resistant mutants are so widespread, amantadine and rimantadine are no longer clinically prescribed to treat influenza infections.<sup>9</sup>

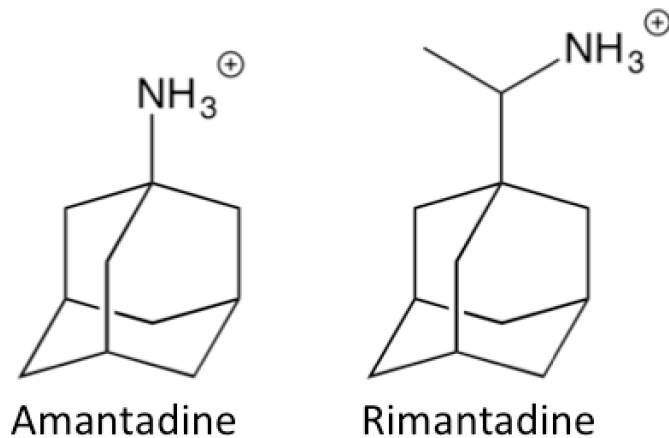


**Figure 1.1. The adamantane drugs: amantadine and rimantadine.**

## 1.2 Life cycle of the influenza A virus

The influenza A life cycle (**Fig. 1.2**) begins with the entry of the virus into the host cell. Sialic acid bound to the hemagglutinin (HA) protein interacts with sialic acid receptors on the surface of the host cell.<sup>10</sup> After being recognized by these receptors, the influenza virus particle enters the cell through endocytosis. In the low pH environment of the endosome, the M2 proton channel transports protons into the viral interior.<sup>11-13</sup> This lowering of the intraviral pH allows for RNA within the virus to uncoat from RNPs.<sup>14,15</sup> There is then a pH-activated membrane fusion step involving HA,<sup>16</sup> which releases this newly uncoated RNA into the host cell. The viral RNA is replicated in the nucleus, viral proteins are produced, then the viral RNA and proteins are transported to the cell membrane. M2 plays a secondary role in equilibrating the pH within the Golgi apparatus as proteins are being transported through it. If the trans-Golgi pH becomes too

low, then the acid-sensitive HA protein will prematurely undergo the conformational change associated with membrane fusion.<sup>17,18</sup> After the transport of viral RNA and proteins to the host cell membrane, new viruses bud off from the host cell, then the viral life cycle begins anew.

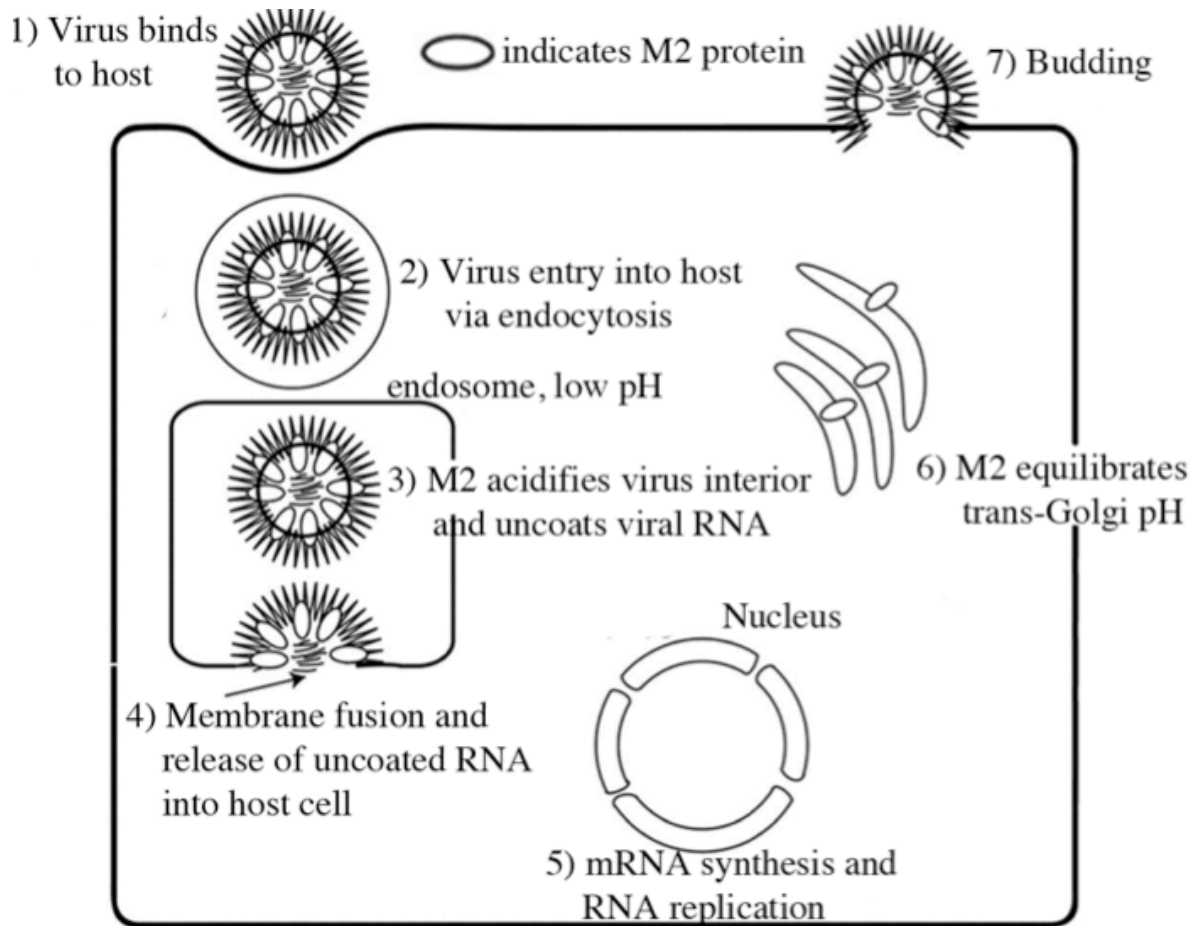


**Figure 1.2. Life cycle of the influenza A virus.** The M2 protein acidifies the viral interior (step 3), which then allows viral RNA to uncoat. M2 plays a secondary role in the de-acidification of the Golgi lumen (step 6), and the C-terminal tail of M2 also plays a role in budding (step 7). Figure from Pinto and Lamb 2006.<sup>19</sup>

The proton channel function of M2 is necessary for viral replication. If the pH within the viral interior is not lowered after endocytosis of the virus particle, then the viral RNA remains packed against viral RNPs and is incapable of utilizing host cellular machinery to produce new



viral components after release from the endosome. The proton channel function of M2 and its inhibition by the adamantane drugs are the main focus of the body of work presented in this dissertation.

### 1.3 The M2 protein

Like many viral proteins, M2 is multifunctional, playing different roles during different steps of the viral replication cycle. M2 is a homotetrameric channel whose monomer consists of 97 amino acids. The N-terminus of the channel is involved in the incorporation of M2 into the virion.<sup>20</sup> The transmembrane (TM) domain is made up of residues 22-46 and is the minimum construct needed for the selective and unidirectional transport of protons.<sup>11,21-23</sup> The cytosolic helix consists of residues 45-62; this amphipathic domain plays a role in budding and membrane scission.<sup>24-26</sup> The disordered C-terminal tail (62-97) interacts with the M1 protein and is involved in the packing of viral RNA.<sup>14,27</sup> Deletion of the cytosolic helix and C-terminal tail results in the formation of virus particles that are filamentous instead of spherical.<sup>28</sup>

Four His37 and four Trp41 residues make up the channel's pH sensitive, proton selective gate.<sup>29,30</sup> The gating His tetrad can have a charge state ranging from neutral to +4. The pKa values for successive protonation of these four His residues have been experimentally determined.<sup>31-33</sup> Interestingly, the first two protonation events occur with pKa > 6, so the channel gate is expected to have a +2 charge near neutral pH. Maximum conductance of protons through the M2 channel occurs near pH 5.5 within physiologically relevant pH ranges;<sup>11,30,34,35</sup> at this pH, the gating His tetrad is expected to have a charge state of +2 to +3.

Two conformational states of the M2 channel have been observed using X-ray crystallography. In the Inward<sub>closed</sub> state,<sup>36</sup> the C-terminus of the channel is tightly packed and the

monomer helices are kinked at residue Gly34. In the  $\text{Inward}_{\text{open}}$  state, the channel's C-terminus is splayed open and the monomer helices are straightened.<sup>35</sup> The  $\text{Inward}_{\text{closed}}$  state is predominantly observed in higher pH ranges, and has been characterized using a number of experimental techniques: X-ray crystallography,<sup>36</sup> solution NMR,<sup>37,38</sup> and solid state NMR.<sup>39,40</sup> In low pH ranges, the  $\text{Inward}_{\text{closed}}$  state is predicted to exist in conformational equilibrium<sup>41-43</sup> with the  $\text{Inward}_{\text{open}}$  state, resulting in peak broadening in NMR experiments at these pH ranges.<sup>39,44,45</sup> Simultaneous equilibria exist between these two conformational states and the five possible protonation states of the gating His37 tetrad (**Fig. 1.3**).

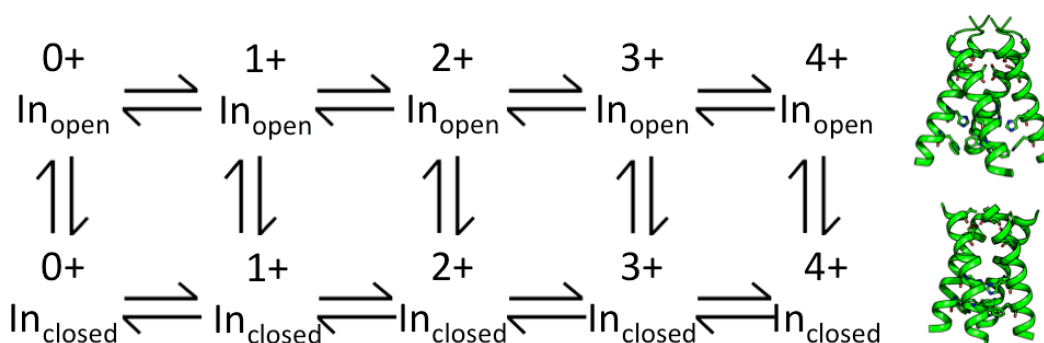


**Figure 1.3. Simultaneous equilibria between gating His tetrad charge state and the two conformational states of M2.** The gating His37 tetrad of M2 can exist in a number of possible charge states, ranging from neutral to +4. These charge states are in equilibrium with the two possible conformational states,  $\text{Inward}_{\text{open}}$  and  $\text{Inward}_{\text{closed}}$ .

#### 1.4 Role of water in proton conduction in the M2 channel (Chapters 2 and 3)

Chapters 2 and 3 discuss the presence of ordered water molecules in X-ray crystal structures of the wild type M2 channel in its  $\text{Inward}_{\text{open}}$  conformation, and the potential role of water in the transport of protons through the channel. The M2 pore is lined with mostly hydrophobic residues, which is perhaps surprising considering that the channel must stabilize

positive charges inside its tightly constricted transmembrane pore. Moreover, the gating His37 tetrad occupies a charge state of +2 to +3 in the pH ranges of maximal conductance--so the M2 pore draws protons into and through this narrow hydrophobic pore that *already* contains multiple positive charges. We observe that the pore leading down to the His37 gate is filled with layers of ordered waters. The only hydrophilic moieties available for these waters to bind to are pore-facing carbonyls within the main chain of the protein, which can only act as hydrogen bond acceptors. This creates a proton deficient environment within the pore, and could play a role in drawing protons into the channel.

These ordered waters form hydrogen-bonded networks of "water wires" that connect the top of the channel to the gating His37 residues. These waters could take part in the concerted transport of a proton from the top of the pore, through the ordered waters, and down to the gating His37 residues via the Grotthuss mechanism (**Fig. 1.4**). Chapter 3 is a further discussion of the role of pH (and, subsequently, the protonation state of the gating His37 tetrad) on the degree of solvent ordering in the M2 pore. Continuous water wires are observed in the channel at the pH of maximum proton conductance (pH 5.5), but at intermediate pH (6.5) fewer H-bonds are formed within the water network, with the smallest number of hydrogen bonds observed between the layers waters at high pH (8.0). This suggests that an increasing number of hydrogen bonds are formed by the waters within the M2 channel as the total charge state of the gating His37 tetrad increases to +3/+4 at low pH ranges, and that ordered waters are positioned to transport protons via the Grotthuss mechanism at low pH but not at higher pH ranges.

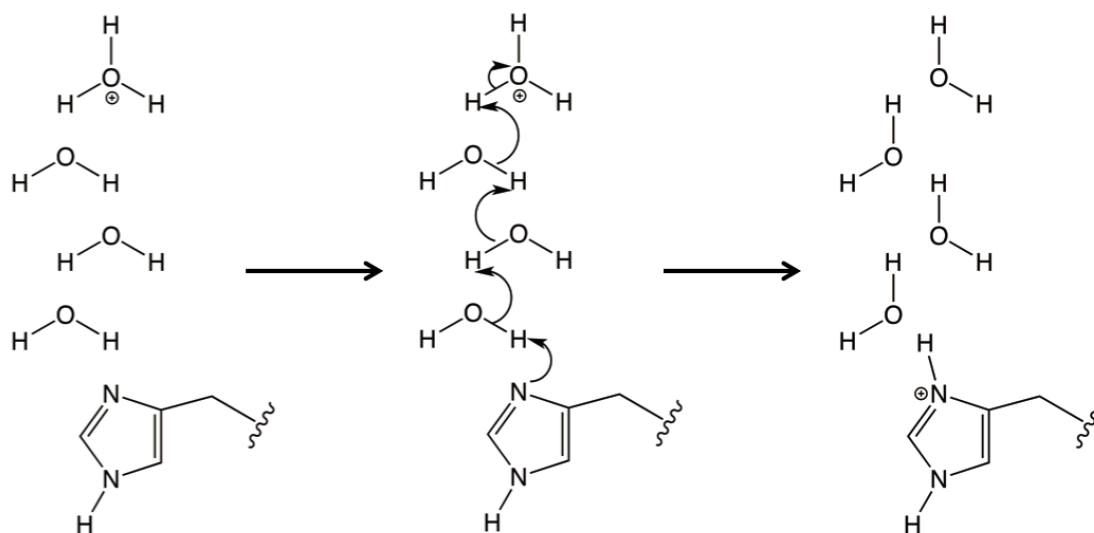


**Figure 1.4. Grotthuss mechanism of proton transport.** Left: A hydronium ion diffuses down to a hydrogen bonded network of waters. Middle: Concerted transport of a proton from the hydronium down to the His residue via the Grotthuss mechanism. Right: The proton has been transferred to the His and the dipoles of the waters have changed their directionality.

Chapters 2 and 3 also compare multiple data collection techniques in the field of X-ray crystallography. In Chapter 2, single crystals containing the  $\text{Inward}_{\text{open}}$  conformation of M2 are diffracted at a synchrotron source under cryogenic conditions and also under room temperature conditions. In Chapter 3, this same crystal form is examined using serial diffraction at an XFEL source. Because the timescale of diffraction is faster than the rate at which radiation damage propagates through the sample (**Fig. 1.5**), XFEL data collection minimizes the impact of radiation damage on datasets collected at room temperature. The use of XFEL sources is relatively new in the field of crystallography. At the time of data collection, there were only two functioning XFEL light sources in the world: LCLS and SACLA. Compared to the XFEL datasets, the M2 crystals diffracted at a synchrotron source under cryogenic conditions are

observed to have an artificially large degree of solvent ordering within the pore, while crystals diffracted at a synchrotron source under room temperature data collection conditions have a reduced amount of solvent in the pore density, likely from some combination of radiation damage and possible dehydration. Serial data collection at an XFEL source side-steps these potential experimental artifacts and provides a room-temperature dataset while minimizing the effects of radiation damage.

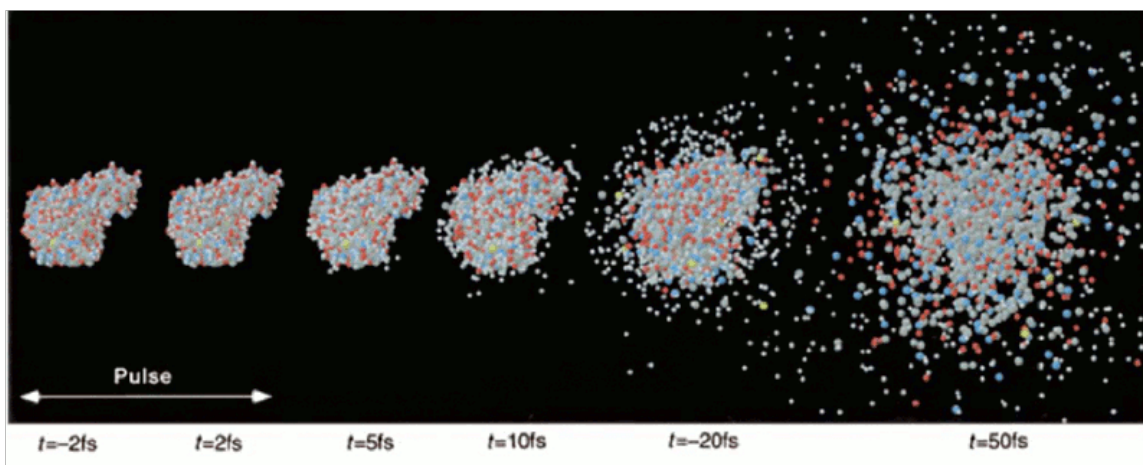


**Figure 1.5. Diffraction before destruction.** In XFEL data collection experiments, the time scale of the X-ray pulse is shorter than the time scale at which radiation damage propagates through and then destroys the sample. Figure from Neutze et al. 2000.<sup>46</sup>

### 1.5 Inhibition of wild type M2 by adamantane drugs (Chapter 4)

Chapter 4 describes the binding of drugs and inhibitors to the wild type M2 channel in multiple conformational states as observed by X-ray crystallography. Prior to this work, only one crystal structure of drug-bound M2 existed in the literature. This 2008 structure<sup>35</sup> of amantadine bound to the Inward<sub>open</sub> conformation of M2 was limited to 3.5 Å resolution (**Fig. 1.6**), which is

the minimum resolution needed to place alpha helices into electron density. The orientation of the bound drug at the center of the channel was ambiguous based on the electron density alone. The new structures presented in this work are of rimantadine bound to the Inward<sub>closed</sub> state (2.00 Å, 6BKL), amantadine bound to the Inward<sub>closed</sub> state (2.00 Å, 6BKK), a spiro-adamantyl amine inhibitor bound to the Inward<sub>closed</sub> state (2.63 Å, 6BMZ), and rimantadine bound to the Inward<sub>open</sub> state (2.25 Å, 6BOC).

These new structures provide a number of insights into drug binding and inhibition of the M2 channel. The orientation of the bound drugs and inhibitors is unambiguous because of the resolution of the electron density maps, and the compounds are observed to bind with their ammonium groups pointing down toward the gating His37 residues. The ammonium groups of drugs and inhibitors localize to positions within the pore where positive charges are predicted to be stable in molecular dynamics simulations (**Fig. 1.7**). Layers of ordered waters are observed in the channel pore between the bound compounds and the gating His37 tetrad. These waters form hydrogen bonds to pore-facing carbonyls, and also interact with other waters to form hydrogen bonded water wires leading down to the His37 gate. These hydrogen-bonded networks of waters could shuttle protons down to the gating His37 residues in the absence of drugs. The ammonium groups of drugs and inhibitors act as hydronium mimics, associating with these water wires in positions where a hydronium would be stabilized (**Fig. 1.8**). These hydrogen bonding interactions position the drugs to plug up the channel pore with their hydrophobic adamantyl groups. Interestingly, the pore-facing carbonyls can act either to stabilize these H-bonded waters or to stabilize bound drugs and inhibitors through hydrophobic interactions. The binding of the spiro-adamantyl amine compound displaces the layer of waters associated with the Ala30 carbonyls in the adamantane-bound structures. Amantadine and rimantadine are observed to bind

to both conformational states of the channel, which is consistent with the experimental observation that inhibition of the channel is not pH-dependent. Even though the M2 channel is in conformational equilibrium under low pH conditions, the adamantane drugs are capable of binding to both of these states.

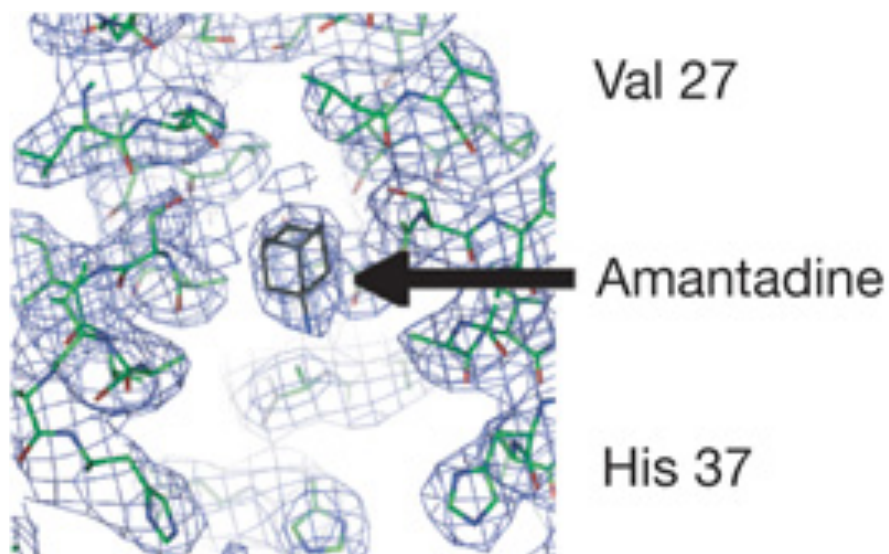


**Figure 1.6. Density of bound amantadine from the previously solved 2008 drug-bound crystal structure.** The 2008 crystal structure was limited to 3.5 Å resolution. The density corresponding to the bound amantadine is spherical in this resolution range, so the orientation of the bound drug is ambiguous. Figure from Stouffer et al. 2008.<sup>35</sup>

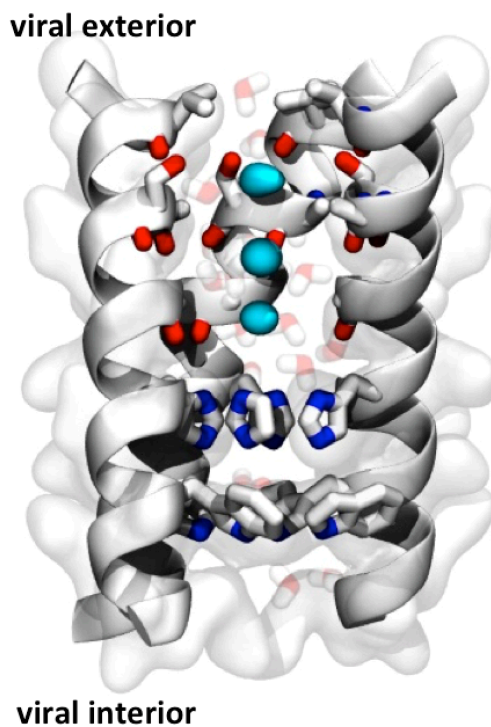


**Figure 1.7. Positive charges localize to specific regions of the M2 channel.** Results of a molecular dynamics simulation using methylammonium as a probe show that positive charges within the M2 pore preferentially localize to specific sites. Figure from Carnevale et al. 2010.<sup>47</sup>

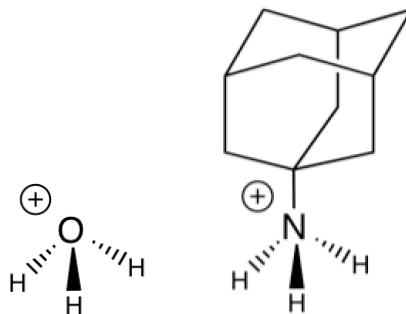


**Figure 1.8. The ammonium group of the adamantane drugs acts as a hydronium mimic.** Similarity between a hydronium ion (left) and the ammonium group of the drug amantadine (right).



## 1.6 Drug-resistant mutants and ongoing research (Chapters 5-7)

Chapter 5 presents the first X-ray crystal structure of the drug-resistant S31N mutant M2 channel in the  $\text{Inward}_{\text{open}}$  conformation to a resolution of 1.59 Å (5C02). The mutant Asn31 side chain faces the center of the channel pore, forming hydrogen bonds with the neighboring Asn31 side chains repeated across the 4-fold symmetry axis at the center of the homotetrameric channel. Based on this structure, the hypothesized mechanism of drug resistance in the S31N mutant channel was assumed to be a steric block of the binding site as a result of replacing the Ser31 hydroxyl with the larger and more hydrophilic Asn31 carboxamide. Additionally, networks of ordered waters similar to those described in Chapters 2 and 3 are observed to form continuous hydrogen-bonded "water wires" leading down to the His37 gate.

In Chapter 6, a new structure of the S31N mutant M2 channel is presented in a crystal form that contains both the  $\text{Inward}_{\text{open}}$  and  $\text{Inward}_{\text{closed}}$  conformational states in the same asymmetric unit. Here, we are able to observe a high-resolution structure of the  $\text{Inward}_{\text{closed}}$  conformation for the first time. The M2 tetramer in the  $\text{Inward}_{\text{open}}$  conformation is comparable to the previously solved crystal structure, with RMSD = 0.509 Å. As before, the side chain of the mutant Asn31 residue in the  $\text{Inward}_{\text{open}}$  state faces the center of the channel pore and forms hydrogen bonds with neighboring Asn31 side chains. However, in the  $\text{Inward}_{\text{closed}}$  conformation, this Asn31 side chain faces away from the channel pore, instead forming hydrogen bonds at the channel's monomer-monomer interface. This twists the monomer helices, causing Ala30 to face the aqueous pore and resulting in a narrowing and elongation the channel at its N-terminus. This new structure is an intriguing case in which two different conformational states have been isolated within the same crystal lattice, and provides new information about the mechanism of drug resistance in the S31N mutant M2 channel.

Chapter 7 discusses ongoing research. Having examined the binding of drugs and inhibitors to the wild type channel and having characterized both conformations of the S31N mutant channel in the absence of inhibitors, we now aim to characterize these drug-resistant mutants bound to inhibitors, and to explore the structural features of longer M2 constructs. A structure of the spiro-adamantyl amine inhibitor bound to the V27A mutant is presented; this compound is a dual inhibitor of both the V27A mutant and the wild type M2 channel, and a comparison with the previously solved structure of this inhibitor bound to WT M2 shows that the inhibitor shifts its binding position depending on which residue is at position 27. Additionally, a preliminary structure of this same spiro-adamantyl amine inhibitor bound to a longer construct of the V27A mutant is presented. This construct includes the cytosolic helix (residues 45-60); the presence of these residues influences the conformation of the C-terminal half of the channel below the His37 and Trp41 gate. Ongoing crystallization trials to study the structure of the S31N mutant bound to inhibitors are also discussed.

## 1.7 References

- 1 CDC. Influenza Fact Sheet. (2018).
- 2 Thompson, W. W. *et al.* Mortality Associated With Influenza and Respiratory Syncytial Virus in the United States. *JAMA: The Journal of the American Medical Association* **289**, 179-186, doi:10.1001/jama.289.2.179 (2003).
- 3 Taubenberger, J. K. & Morens, D. M. 1918 influenza: the mother of all pandemics. *Emerging Infectious Diseases* **12**, 15-22 (2006).
- 4 Heider, H. A., B; Presber, HW; Schroeder, C; Feldblum, R; Indulen, MK. Occurrence of amantadine- and rimantadine-resistant influenza A virus strains during the 1980 epidemic. *Acta Virologica* **25**, 395-400 (1981).
- 5 Bright, R. A. *et al.* Incidence of adamantane resistance among influenza A (H3N2) viruses isolated worldwide from 1994 to 2005: a cause for concern. *Lancet* **366**, 1175-1181, doi:10.1016/s0140-6736(05)67338-2 (2005).
- 6 Deyde, V. M. *et al.* Surveillance of resistance to adamantanes among influenza A(H3N2) and A(H1N1) viruses isolated worldwide. *Journal of Infectious Diseases* **196**, 249-257, doi:10.1086/518936 (2007).
- 7 Hussain, M. G., HD; Haw, TY; Nutsford, AN; Husain M. Drug resistance in influenza A virus: the epidemiology and management. *Infect Drug Resist.* **10**, 121–134, doi:10.2147/IDR.S105473 (2017).
- 8 Dong, G. *et al.* Adamantane-resistant influenza A viruses in the world (1902-2013): frequency and distribution of M2 gene mutations. *Plos One* **10**, e0119115, doi:10.1371/journal.pone.0119115 (2015).
- 9 CDC. CDC Recommends against the Use of Amantadine and Rimantadine for the Treatment or Prophylaxis of Influenza in the United States during the 2005–06 Influenza Season. (2006).
- 10 Skehel, J. J. & Wiley, D. C. Receptor binding and membrane fusion in virus entry: the influenza hemagglutinin. *Annual Review of Biochemistry* **69**, 531-569, doi:10.1146/annurev.biochem.69.1.531 (2000).
- 11 Chizhnikov, I. V. *et al.* Selective proton permeability and pH regulation of the influenza virus M2 channel expressed in mouse erythroleukaemia cells. *Journal of Physiology-London* **494**, 329-336 (1996).
- 12 Pinto, L. H., Holsinger, L. J. & Lamb, R. A. Influenza virus M2 protein has ion channel activity. *Cell* **69**, 517-528, doi:[http://dx.doi.org/10.1016/0092-8674\(92\)90452-I](http://dx.doi.org/10.1016/0092-8674(92)90452-I) (1992).

- 13 Wang, C., Takeuchi, K., Pinto, L. H. & Lamb, R. A. Ion-channel activity of influenza-A virus M(2) protein - characterization of the amantadine block. *Journal of Virology* **67**, 5585-5594 (1993).
- 14 Martin, K. & Helenius, A. Nuclear transport of influenza virus ribonucleoproteins: The viral matrix protein (M1) promotes export and inhibits import. *Cell* **67**, 117-130, doi:[http://dx.doi.org/10.1016/0092-8674\(91\)90576-K](http://dx.doi.org/10.1016/0092-8674(91)90576-K) (1991).
- 15 GK., B. A. V. N. K. G. N. R. V. Influenza virus uncoating in infected cells and effect of rimantadine. *J Gen Virol.* **60**, 49-59 (1982).
- 16 Wiley, D. C. & Skehel, J. J. The Structure and Function of the Hemagglutinin Membrane Glycoprotein of Influenza Virus. *Annual Review of Biochemistry* **56**, 365-394, doi:10.1146/annurev.bi.56.070187.002053 (1987).
- 17 Grambas, S. & Hay, A. J. Maturation of influenza-A virus hemagglutinin - estimates of the pH encountered during transport and its regulation by the M2 protein. *Virology* **190**, 11-18, doi:10.1016/0042-6822(92)91187-y (1992).
- 18 Sakaguchi T, L. G., Lamb RA. The ion channel activity of the influenza virus M2 protein affects transport through the Golgi apparatus. *The Journal of Cell Biology* **133**, 733-747 (1996).
- 19 Pinto, L. H. & Lamb, R. A. The M2 proton channels of influenza A and B viruses. *Journal of Biological Chemistry* **281**, 8997-9000, doi:10.1074/jbc.R500020200 (2006).
- 20 Park, E. K., Castrucci, M. R., Portner, A. & Kawaoka, Y. The M2 ectodomain is important for its incorporation into influenza A virions. *Journal of Virology* **72**, 2449-2455 (1998).
- 21 Lin, T. I. & Schroeder, C. Definitive assignment of proton selectivity and attoampere unitary current to the M2 ion channel protein of influenza A virus. *Journal of Virology* **75**, 3647-3656, doi:10.1128/jvi.75.8.3647-3656.2001 (2001).
- 22 Mould, J. A. *et al.* Permeation and activation of the M-2 ion channel of influenza A virus. *Journal of Biological Chemistry* **275**, 31038-31050, doi:10.1074/jbc.M003663200 (2000).
- 23 Shimbo, K., Brassard, D. L., Lamb, R. A. & Pinto, L. H. Ion selectivity and activation of the M2 ion channel of influenza virus. *Biophysical Journal* **70**, 1335-1346 (1996).
- 24 Roberts, K. L., Leser, G. P., Ma, C. & Lamb, R. A. The amphipathic helix of influenza A virus M2 protein is required for filamentous bud formation and scission of filamentous and spherical particles. *Journal of Virology* **87**, 9973-9982, doi:10.1128/JVI.01363-13 (2013).

- 25 Rossman, J. S., Jing, X., Leser, G. P. & Lamb, R. A. Influenza virus M2 protein mediates ESCRT-independent membrane scission. *Cell* **142**, 902-913, doi:10.1016/j.cell.2010.08.029 (2010).
- 26 Schmidt, N. W., Mishra, A., Wang, J., DeGrado, W. F. & Wong, G. C. L. Influenza virus A M2 protein generates negative gaussian membrane curvature necessary for budding and scission. *Journal of the American Chemical Society* **135**, 13710-13719, doi:10.1021/ja400146z (2013).
- 27 McCown, M. F. & Pekosz, A. Distinct domains of the influenza A virus M2 protein cytoplasmic tail mediate binding to the M1 protein and facilitate infectious virus production. *Journal of Virology* **80**, 8178-8189 (2006).
- 28 Iwatsuki-Horimoto, K. *et al.* The cytoplasmic tail of the influenza A virus M2 protein plays a role in viral assembly. *Journal of Virology* **80**, 5233-5240 (2006).
- 29 Tang, Y. J., Zaitseva, F., Lamb, R. A. & Pinto, L. H. The gate of the influenza virus M-2 proton channel is formed by a single tryptophan residue. *Journal of Biological Chemistry* **277**, 39880-39886, doi:10.1074/jbc.M206582200 (2002).
- 30 Wang, C., Lamb, R. A. & Pinto, L. H. Activation of the M2 ion channel of influenza virus: a role for the transmembrane domain histidine residue. *Biophysical Journal* **69**, 1363-1371 (1995).
- 31 Hu, F. H., Schmidt-Rohr, K. & Hong, M. NMR detection of pH-dependent histidine-water proton exchange reveals the conduction mechanism of a transmembrane proton channel. *Journal of the American Chemical Society* **134**, 3703-3713, doi:10.1021/ja2081185 (2012).
- 32 Hu, J. *et al.* Histidines, heart of the hydrogen ion channel from influenza A virus: Toward an understanding of conductance and proton selectivity. *Proceedings of the National Academy of Sciences of the United States of America* **103**, 6865-6870, doi:10.1073/pnas.0601944103 (2006).
- 33 Liao, S. Y., Yang, Y., Tietze, D. & Hong, M. The influenza M2 cytoplasmic tail changes the proton-exchange equilibria and the backbone conformation of the transmembrane histidine residue to facilitate proton conduction. *Journal of the American Chemical Society* **137**, 6067-6077, doi:10.1021/jacs.5b02510 (2015).
- 34 Pielak, R. M. & Chou, J. J. Kinetic Analysis of the M2 Proton Conduction of the Influenza Virus. *Journal of the American Chemical Society* **132**, 17695-17697, doi:10.1021/ja108458u (2010).
- 35 Stouffer, A. L. *et al.* Structural basis for the function and inhibition of an influenza virus proton channel. *Nature* **451**, 596-U513, doi:10.1038/nature06528 (2008).

- 36 Acharya, R. *et al.* Structure and mechanism of proton transport through the transmembrane tetrameric M2 protein bundle of the influenza A virus. *Proceedings of the National Academy of Sciences* **107**, 15075-15080, doi:10.1073/pnas.1007071107 (2010).
- 37 Schnell, J. R. & Chou, J. J. Structure and mechanism of the M2 proton channel of influenza A virus. *Nature* **451**, 591-U512, doi:10.1038/nature06531 (2008).
- 38 Wang, J. *et al.* Structure and inhibition of the drug-resistant S31N mutant of the M2 ion channel of influenza A virus. *Proc Natl Acad Sci U S A* **110**, 1315-1320, doi:10.1073/pnas.1216526110 (2013).
- 39 Cady, S. D. *et al.* Structure of the amantadine binding site of influenza M2 proton channels in lipid bilayers. *Nature* **463**, 689-U127, doi:10.1038/nature08722 (2010).
- 40 Sharma, M. *et al.* Insight into the mechanism of the influenza a proton channel from a structure in a lipid bilayer. *Science* **330**, 509-512, doi:10.1126/science.1191750 (2010).
- 41 Khurana, E. *et al.* Molecular dynamics calculations suggest a conduction mechanism for the M2 proton channel from influenza A virus. *Proc Natl Acad Sci U S A* **106**, 1069-1074, doi:10.1073/pnas.0811720106 (2009).
- 42 Liang, R., Li, H., Swanson, J. M. & Voth, G. A. Multiscale simulation reveals a multifaceted mechanism of proton permeation through the influenza A M2 proton channel. *Proc Natl Acad Sci U S A* **111**, 9396-9401, doi:10.1073/pnas.1401997111 (2014).
- 43 Liang, R. *et al.* Acid activation mechanism of the influenza A M2 proton channel. *Proceedings of the National Academy of Sciences* **113**, E6955 (2016).
- 44 Hu, F. H., Luo, W. B., Cady, S. D. & Hong, M. Conformational plasticity of the influenza A M2 transmembrane helix in lipid bilayers under varying pH, drug binding, and membrane thickness. *Biochimica Et Biophysica Acta-Biomembranes* **1808**, 415-423, doi:10.1016/j.bbamem.2010.09.014 (2011).
- 45 Li, C., Qin, H., Gao, F. P. & Cross, T. A. Solid-state NMR characterization of conformational plasticity within the transmembrane domain of the influenza A M2 proton channel. *Biochim Biophys Acta* **1768**, 3162-3170 (2007).
- 46 Neutze, R., Wouts, R., van der Spoel, D., Weckert, E. & Hajdu, J. Potential for biomolecular imaging with femtosecond X-ray pulses. *Nature* **406**, 752-757 (2000).
- 47 Carnevale, V., Fiorin, G., Levine, B. G., DeGrado, W. F. & Klein, M. L. Multiple proton confinement in the M2 channel from the influenza A virus. *Journal of Physical Chemistry C* **114**, 20856-20863, doi:Doi 10.1021/Jp107431g (2010).

## Chapter 2

### **High resolution structures of the M2 channel from influenza A virus reveal dynamic pathways for proton stabilization and transduction.**

#### **2.1 Abstract**

The M2 protein from influenza A virus is a proton channel that uses His37 as a selectivity filter. Here we report high-resolution (1.10 Å) cryogenic crystallographic structures of its transmembrane domain at low and high pH. These structures reveal that waters within the pore form hydrogen-bonded networks or “water-wires” spanning 17 Å from the channel entrance to His37. Pore-lining carbonyl groups are well situated to stabilize hydronium via second-shell interactions involving bridging water molecules. In addition, room temperature crystallographic structures indicate that water becomes increasingly fluid with increasing temperature and decreasing pH, despite the higher electrostatic field. Complementary molecular dynamics simulations reveal a collective switch of hydrogen bond orientations that can contribute to the directionality of proton flux as His37 is dynamically protonated and deprotonated in the conduction cycle.

#### **2.2 Significance**

The conduction of protons through the highly restricted paths of transmembrane proteins is an essential process of living systems and an intriguing problem in modern physical chemistry. The small size of the influenza M2 proton channel makes it an ideal system for the study of proton transport across a membrane. Additionally, the M2 channel has medical relevance as an anti-flu drug target. These high-resolution structures of the channel were obtained by

crystallizing the protein in a membrane-like environment; they reveal networks of hydrogen-bonded waters that change with temperature and pH. The locations of these waters, in conjunction with molecular dynamics simulations that predict their hydrogen bond orientations, provide insight into the mechanism of proton stabilization and transduction within the channel.

## 2.3 Introduction

Proton transport and conduction is essential to life. Proteins conduct protons over long distances through membranes to facilitate proton-coupled electron transfer and also the formation and utilization of proton gradients. The M2 proton channel from the influenza A virus<sup>1</sup> is not only a medically important protein but also a simple, well-defined system for studying proton transport through confined spaces.<sup>2-4</sup> This channel is the target of the anti-flu drug amantadine. M2 is activated at low pH by protonation of His37, which also participates in proton conduction by shuttling protons into the interior of the virus.<sup>5-7</sup> His37 lies near the center of the bilayer, where it is connected to the viral exterior by a water-filled pore through which protons must pass to gain access to the viral interior.<sup>8-13</sup>

Visualizing the flow of protons within protein channels such as M2 is one of the long-standing challenges in molecular biophysics. It has been suggested based on computational studies<sup>9,14-19</sup> that protons reach His37 through “water wires” via the Grotthuss mechanism, but there is little high-resolution information concerning the path by which protons are conducted. A previously solved 1.65 Å crystal structure<sup>9</sup> showed six ordered waters immediately above the His37 tetrad, but ordered waters spanning the entire aqueous pore of M2 have not been observed until now. Previous MD simulations suggested a pore with mobile waters,<sup>12,15</sup> while the results of NMR and IR experiments are more consistent with an environment that is more similar to bulk



water at low pH.<sup>13,19,20</sup> However, it is difficult to deconvolute the changes in the water structure and dynamics when the protonation of His37 is raised from those induced indirectly via the conformation of the protein's main chain.

The M2 channel is known to have at least two conformational states that are populated to differing extents at low *versus* high pH.<sup>1,10,12</sup> One, seen primarily at high pH, has been characterized extensively by solution NMR,<sup>21,22</sup> solid state NMR (SSNMR),<sup>10,12</sup> and X-ray crystallography.<sup>9</sup> A second form is observed in equilibrium at lower pH,<sup>21-23</sup> as evidenced by a broadening of magnetic resonances that has made thus far impractical to determine a high-resolution structure of the protein in this state by SSNMR or solution NMR. X-ray crystallographic studies, however, have provided structures of both states,<sup>8,9</sup> which differ primarily in the conformation of the C-terminus where protons exit the channel. Here we have obtained crystals that diffract to high resolution (1.10 Å) at both low and high pH, allowing visualization of water wires leading to His37 as a function of pH. The conformations of the backbone at the two pH values are essentially identical, permitting us to isolate changes in the organization of the water without any confounding factors.

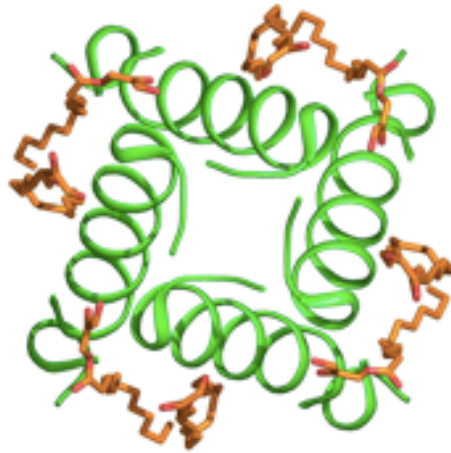
## 2.4 Results and Discussion

**2.4.1 High resolution structures of M2TM.** In this work, we use a minimal construct, M2TM, which is fully active as a proton channel.<sup>24</sup> M2TM was crystallized using lipid cubic phase (LCP) techniques, which provide a continuous lipid bilayer in which crystallization can occur.<sup>25</sup> Indeed, the channel is surrounded by a layer of monoolein molecules and very few protein-protein interactions are present in the crystal lattice (**Fig. 2.1**). The conformation of the protein lies between the C-terminally closed conformation previously seen in several crystal and NMR structures<sup>9,10,12,21,22</sup> and a conformation with a dilation of the C-terminal end of the pore

seen in some crystal structures.<sup>8</sup> The primary focus of the current study is on the water-filled pore leading to His37, whose backbone structure is very similar in all previously solved structures of M2, including a structure of a longer construct determined by SSNMR in phospholipid bilayers<sup>12</sup> (**Fig. 2.2a**). However, the current structures are novel with respect to the number of water molecules seen in the pore as well as the exceptional resolution (1.10 Å). At the time of this publication (2015), fewer than 10 structures of membrane proteins had been defined to less than 1.2 Å resolution. The structures presented here are also among the first high-resolution structures of a membrane protein near room temperature. Because of their high resolution, these structures provide novel insights into the water molecules that work in concert with the protein macromolecule to affect biological proton transport.

Crystals were grown at pH 8.0 ("high pH") and 5.5 ("low pH") and crystallographic data were collected at cryogenic and room temperatures (**Table 2.1**). Although the conformations of the backbone and even most sidechains are essentially identical between the structures, there are marked differences in the distribution and occupancy of solvent molecules as a function of pH and temperature throughout the channel in the N-terminal pore leading to His37. The cryo-cooled structures were solved to 1.10 Å resolution and show electron density maps typical of high-resolution structures, including features from the hydrogen atoms of CH bonds (**Fig. 2.2b-e**). As in a previous crystallographic structure<sup>9</sup> and consistent with SSNMR,<sup>10,11</sup> water molecules bind to both the delta and epsilon nitrogens of His37. The N-terminal part of the pore is occluded by four Val27 residues, but it is possible for protons entering from the outside of the virus to gain access to water in the pore via low-energy fluctuations of the Val27 residues.<sup>19,26</sup>

Top-down view of the M2TM cryo high pH structure:



Side view of three M2TM tetramers within the crystal lattice:

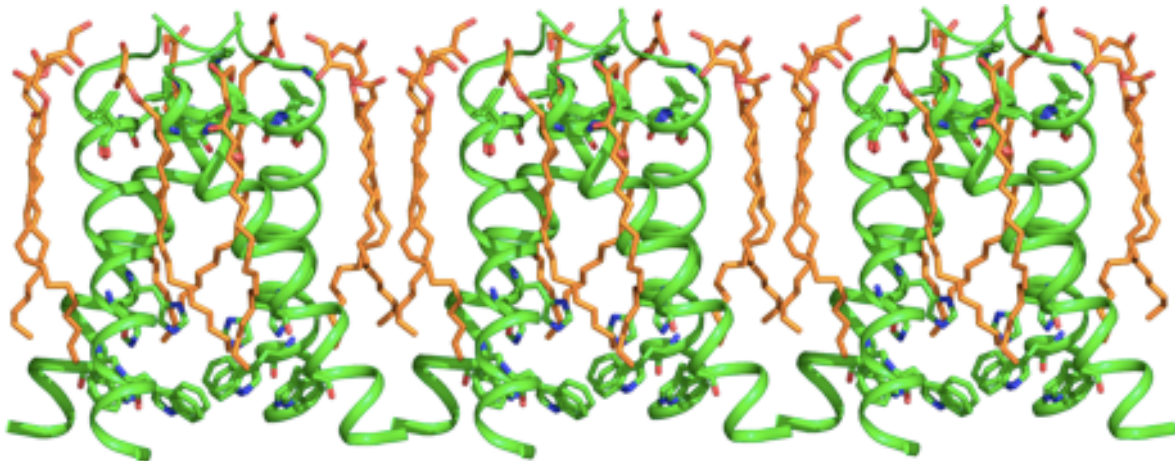


**Figure 2.1. M2 is surrounded by monoolein molecules.** The structure of the M2TM tetramer solved here using lipid cubic phase methods is completely surrounded with monoolein molecules (orange) (see top image) at its N-terminus and shows few protein-protein contacts within the crystal lattice (see bottom image). The few protein-protein interactions that are observed take place at the C-terminus of the protein.

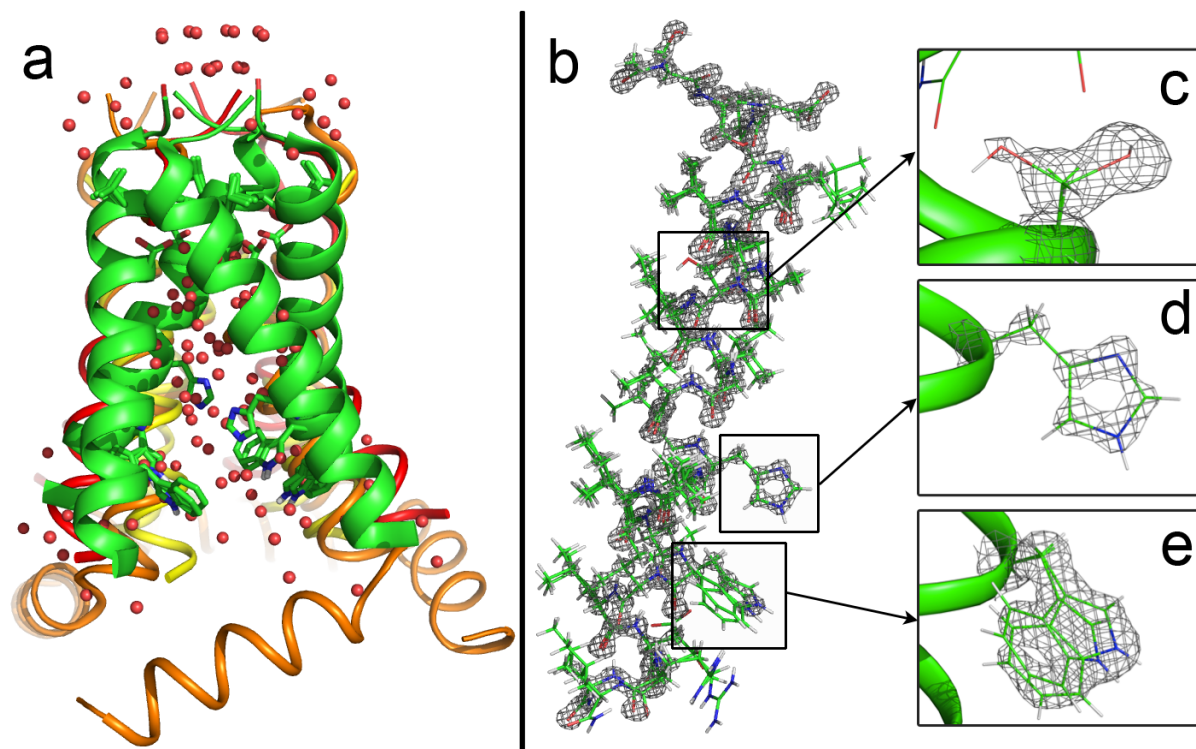


**Figure 2.2. Crystal structure of M2TM at 1.10 Å at pH 8.0 (4QK7) under cryogenic conditions.** **a.** Superposition of this structure (green) with previously solved structures of M2 2LOJ<sup>12</sup> (orange), 3LBW<sup>9</sup> (yellow) and 3BKD<sup>8</sup> (red) shows that the conformation of the N-terminal half of the channel is relatively conserved while the conformation of the C-terminus varies. Waters from the high pH cryogenic structure (red spheres) are overlaid with waters from the low pH cryogenic structure (pink spheres). **b.** Density of backbone and side chains of a monomer of M2TM at a contour of 3.0  $\sigma$  shows features typical of high resolution structures. **c.** Ser31 side chain (conformer A and B) at a contour of 1.0  $\sigma$ ; **d.** His37 side chain at a contour of 3.0  $\sigma$ ; **e.** Trp41 side chain (conformer A and B) at a contour of 1.5  $\sigma$ .

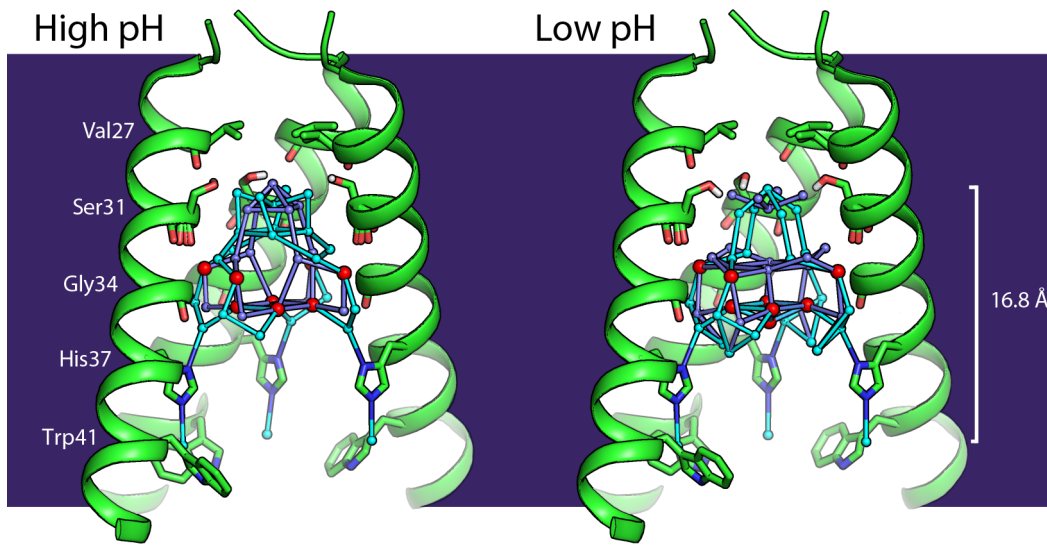
**Table 2.1. Crystallographic data tables.** Data processing and refinement statistics for all of the M2TM structures in the main text.

| <b>Data processing</b>                   | <b>cryo pH 8.0<br/>(4QK7)</b> | <b>cryo pH 5.5<br/>(4QKC)</b> | <b>RT pH 8.0<br/>(4QKL)</b>     | <b>RT pH 5.5<br/>(4QKM)</b>   |
|--|-------------------------------|-------------------------------|---------------------------------|-------------------------------|
| <b>Resolution range<br/>(Å)</b>          | 13.05 - 1.1<br>(1.12 - 1.1)   | 13.06 - 1.1<br>(1.11 - 1.1)   | 20.93 - 1.711<br>(1.77 - 1.711) | 18 - 1.44<br>(1.491 - 1.44)   |
| <b>Space group</b>                       | I <sub>4</sub>                | I <sub>4</sub>                | I <sub>4</sub>                  | I <sub>4</sub>                |
| <b>Unit cell</b>                         | 29.54 29.54 66.85<br>90 90 90 | 29.31 29.3 67.31<br>90 90 90  | 29.6 29.6 68.14<br>90 90 90     | 30.09 30.09 67.39<br>90 90 90 |
| <b>Total reflections</b>                 | 81496(3943)                   | 77823(3516)                   | 5854 (622)                      | 9117 (920)                    |
| <b>Unique reflections</b>                | 11581(575)                    | 11596 (561)                   | 3126 (318)                      | 5252 (523)                    |
| <b>Multiplicity</b>                      | 7.0(6.9)                      | 6.7(6.3)                      | 1.9 (2.0)                       | 1.7 (1.8)                     |
| <b>Completeness (%)</b>                  | 99.60 (100.00)                | 99.5 (66.1)                   | 97.44 (100.00)                  | 96.38 (97.39)                 |
| <b>Mean I/sigma(I)</b>                   | 13.37 (2.8)                   | 17.3 (3.0)                    | 3.64 (1.65)                     | 11.45 (1.61)                  |
| <b>Wilson B-factor</b>                   | 9.19                          | 9.19                          | 18.65                           | 15                            |
| <b>R-merge</b>                           | 0.072(0.863)                  | 0.050(0.544)                  | 0.1082 (0.3675)                 | 0.03625 (0.4499)              |
| <b>R-meas</b>                            | 0.078(0.935)                  | 0.054(0.593)                  | 0.153                           | 0.05127                       |
| <b>CC1/2</b>                             | 0.999(0.919)                  | 0.999(0.934)                  | 0.97 (0.741)                    | 0.999 (0.798)                 |
| <b>CC*</b>                               |                               |                               | 0.992 (0.922)                   | 1 (0.942)                     |
| <b>Refinement</b>                        | <b>cryo pH 8.0<br/>(4QK7)</b> | <b>cryo pH 5.5<br/>(4QKC)</b> | <b>RT pH 8.0<br/>(4QKL)</b>     | <b>RT pH 5.5<br/>(4QKM)</b>   |
| <b>Resolution range<br/>(Å)</b>          | 13.05 - 1.1<br>(1.139 - 1.1)  | 13.06 - 1.1<br>(1.139 - 1.1)  | 20.93 - 1.711<br>(1.77 - 1.711) | 18 - 1.44 (1.491 -<br>1.44)   |
| <b>R-work</b>                            | 0.1070 (0.1879)               | 0.1067 (0.1551)               | 0.1658 (0.2374)                 | 0.1350 (0.1993)               |
| <b>R-free</b>                            | 0.1263 (0.1859)               | 0.1235 (0.1981)               | 0.1976 (0.2845)                 | 0.1715 (0.2876)               |
| <b>Number of non-<br/>hydrogen atoms</b> | 454                           | 458                           | 282                             | 323                           |
| <b>macromolecules</b>                    | 356                           | 349                           | 244                             | 268                           |
| <b>ligands</b>                           | 62                            | 62                            | 11                              | 36                            |
| <b>water</b>                             | 32                            | 42                            | 26                              | 18                            |
| <b>Protein residues</b>                  | 27                            | 27                            | 27                              | 27                            |
| <b>RMS(bonds)</b>                        | 0.015                         | 0.014                         | 0.004                           | 0.016                         |
| <b>RMS(angles)</b>                       | 2.27                          | 1.87                          | 0.62                            | 1.6                           |
| <b>Ramachandran<br/>favored (%)</b>      | 100                           | 100                           | 100                             | 100                           |
| <b>Clashscore</b>                        | 14.1                          | 9.9                           | 0                               | 0                             |
| <b>Average B-factor</b>                  | 21.3                          | 20.7                          | 23                              | 28.1                          |
| <b>macromolecules</b>                    | 14.6                          | 12.5                          | 21                              | 19.6                          |
| <b>ligands</b>                           | 47.7                          | 48.9                          | 29.4                            | 80                            |
| <b>solvent</b>                           | 42.1                          | 44.3                          | 38.2                            | 50.6                          |

2.4.2 *A multitude of water wires lead to His37.* The cryo structures determined at high pH (4QK7) and low pH (4QKC) show multiple continuous paths of water molecules stretching approximately 17 Å from Val27 to His37 (**Fig. 2.3**). Some water molecules are found at full occupancy, while others are found at one of two closely adjoining sites that together add up to full occupancy. The water wires have multiple branching points that create multiple hydrogen bond pathways by which a proton can pass through the pore *en route* to one of the four His37 residues. Thus, the low temperature structures (app. 100 K) identify a highly degenerate path of enthalpically stable<sup>27</sup> water wires.

2.4.3 *Fluid water wires at room temperature.* To determine whether additional paths would be present near room temperature, two additional structures were determined at 273 K, at high pH (4QKL) and low pH (4QKM) to 1.71 Å and 1.44 Å resolution, respectively. The electron density maps for the RT *versus* the cryo temperatures, calculated to a common resolution, show a number of striking similarities and also differences in electron density originating from water in the pore (**Fig. 2.4a-b**, also **SI Fig. 2.6**). Water molecules remain bound to the highly conserved His37 residue, but higher variability is seen across the other pore-lining water molecules. At pH 8, a clathrate-like structure is observed below Val27 and is anchored by hydrogen bonds to the main chain carbonyls facing the pore, but the water layer connecting to the hydrated His37 residues has become too diffuse to be seen clearly in the electron density. At pH 5.5 the water density in most of the pore is diffuse and a fully connected hydrogen bond network can not be observed. The water in this region is disordered, indicating that the wires seen at low temperature represent snapshots of the energetically most favorable pathways among a larger ensemble of dynamically exchanging sites populated at room temperature.

## Cryogenic temperature



## Room temperature

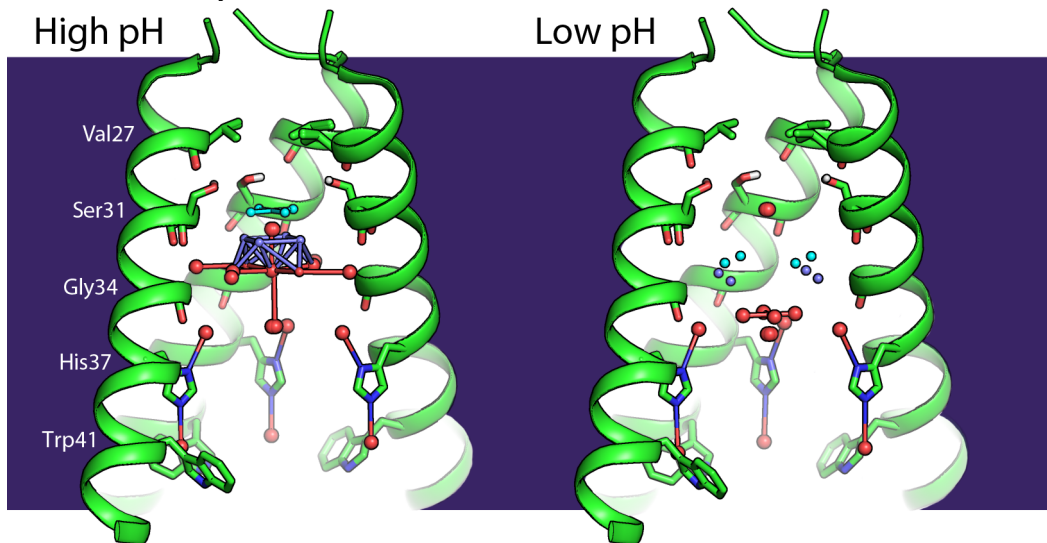


**Figure 2.3. Waters in the cryogenic crystal structures form ordered water wires while room temperature waters are less ordered.** The front helix of each tetramer has been removed. *Top:* Water wires inferred from crystallographic water positions from the 1.10 Å resolution cryo crystal structures at pH 8.0 (left, PDB code 4QK7) and pH 5.5 (right, PDB code 4QKC) form a continuous network of water wires within the N-terminal half of the pore leading to the gating His37 residue, with some positional changes in the waters between the two pH conditions. Alternate occupancy water wire networks A (light blue) and B (dark blue) intersect at full occupancy waters (red). Continuous water wires span 16.8 Å of the channel pore. *Bottom:* Water networks observed under room temperature conditions at pH 8.0 at 1.71 Å resolution (left, PDB code 4QKL) and pH 5.5 at 1.44 Å resolution (right, PDB code 4QKM) have fewer ordered waters and no longer form a continuous path leading to His37; in the low pH structure the waters do not form ordered networks at all and instead appear fluid-like.

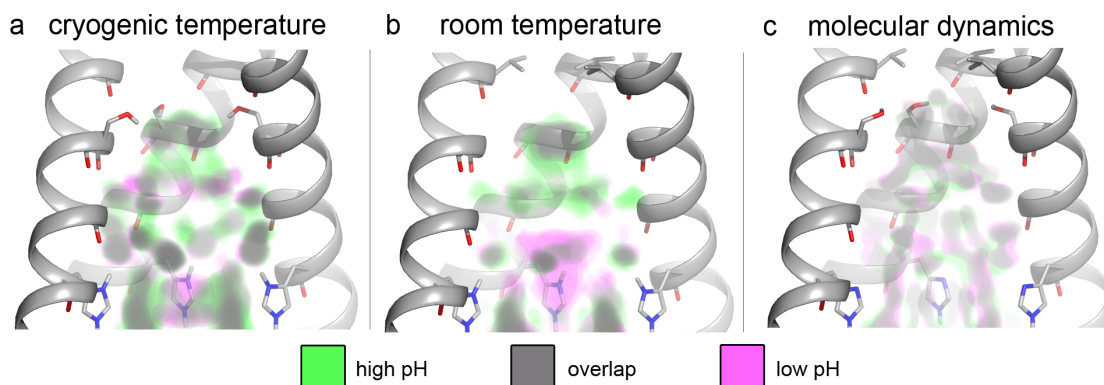


**Figure 2.4. Electron density comparisons show differences and similarities between the solvent density at high and low pH.** The front helices have been removed. Electron density at a contour of 0.5 sigma under **a.** cryogenic conditions, **b.** room temperature conditions, and **c.** calculated electron density from molecular dynamics simulations is shown for both high (green) and low (magenta) pH experiments/simulations (high pH corresponds to a neutral His37 cluster, and low pH to a 4<sup>+</sup> charge state). Areas where low and high pH densities overlap are shown in gray. Electron density from water binding to carbonyl groups and histidines is relatively conserved in all conditions while variations in density are seen elsewhere.

*2.4.4 An abundance of hydrogen bond donors relative to acceptors in the channel.* The pore of the protein is overall richer in hydrogen bond acceptors than donors. This presents an environment that should intrinsically stabilize a hydronium ion, which has three hydrogen bond donors and only one relatively weak acceptor. The water molecules in the channel form hydrogen bonds with the accepting carbonyl groups of Gly34, Ala30, and Val27. The hydroxyl group of Ser31 donates an intramolecular hydrogen bond to a carbonyl in the helix, leaving its two electron lone pairs free to accept hydrogen bonds from water molecules in the pore. At high pH, the delta nitrogen of His37 also presents a hydrogen bond acceptor,<sup>7,11</sup> though this residue switches to being a donor with protonation at low pH. Thus, the channel would appear to be intrinsically suited to stabilize hydronium in the pore, particularly when His37 residues are in the neutral state. This environment is consistent with the idea that M2-blocking drugs, such as amantadine and rimantadine, act as substrate analogues of the hydronium ion due to their positively charged ammonium groups and lack of hydrogen bond acceptors.<sup>28</sup>



*2.4.5 Density of water by molecular dynamics simulations.* To gain further insight into the water network inside the M2 pore and its response to pH changes (*i.e.* the protonation state of His37), we performed force field-based molecular dynamics (MD) simulations of the hydrated protein crystals (**SI Figs. 2.7-2.9**) at a temperature of 310 K as in other simulations of M2TM.<sup>9</sup> Computational studies of different proteins have shown that MD simulations in a crystal environment yield water densities in good agreement with experimentally determined electron densities.<sup>29-32</sup> Additionally, MD simulations can complement the X-ray data by providing an atomic picture of the water hydrogens and their H-bonding connectivity and dynamics, as recently shown for aquaporin.<sup>4</sup> The highest calculated density of water is near His37 and the pore-facing carbonyls of residue 34 (**Fig. 2.4**), similarly to what is indicated by the present structures and by the previous X-ray structure of M2TM.<sup>9</sup> In addition to these, simulations also predict the presence of water molecules at other positions (**SI Fig. 2.6**), including molecules that are not in direct contact with the protein's side chains. Although the measured and calculated densities bear many similarities, it is possible that the mismatches between the two may affect the calculation of the hydrogens' positions. To assess this potential issue, we also performed control simulations with all water molecules restrained at their crystallographic positions: these yield nearly identical distributions of donors and acceptors of H-bonds as when water molecules are left free to diffuse in the pore (**SI Fig. 2.14**).

*2.4.6 Hydrogen bond network within the M2 pore.* The M2 proton channel has the interesting property of being an asymmetric conductor: it conducts protons from the outside to the inside of the virus when the outside pH is low (as in an acidifying endosome), but does not conduct protons outward as easily when the pH gradient is reversed. The current crystallographic

structures and MD simulations provide a detailed molecular description for this behavior. As the protonation state of the His37 tetrad changes, the polarity of the H-bonds between water molecules becomes increasingly aligned with the axis of the channel (**SI Fig. 2.10** and **SI Table 2.2**). The total number of H-bonds is higher in the charge states of the histidine tetrad accessible at high pH (0 and 1<sup>+</sup>), than in the higher charge states populated at low pH (3<sup>+</sup> and 4<sup>+</sup>). Nevertheless, the H-bonds in the high pH states do not adopt a preferred orientation, whereas in the low pH states all H-bonds are highly directional. In the 3<sup>+</sup> and 4<sup>+</sup> charge states (**Fig. 2.5c** and **SI Fig. 2.11h**), the H-bonds are oriented outwards in the extraviral half of the pore, and are oriented inwards in the intraviral half. The change of polarity occurs at His37 (**SI Fig. 2.12**). The protonated His can donate two H-bonds, one upwards to the water molecules in the extraviral side of the pore and one downwards to the water molecules in the intraviral side. By contrast, in the 0 and 1<sup>+</sup> states (**Fig. 2.5b** and **SI Fig. 2.11e**), the water molecules can form both outward- and inward-oriented H-bonds with their neighbors regardless of their position along the pore, and the flipping between the two orientations occurs in the sub-nanosecond time scale. Except for the two H-bonds the neutral His37 forms with the two immediately adjacent water molecules (accepting one from the water molecule above and donating one to the water below), in the high pH states the H-bonds outwards and inwards cancel out (**SI Fig. 2.10**). Hence, the H-bond network inside the M2 pore can be described as an assembly of “loopback circuits” at high pH, and as a single “parallel circuit” at low pH. The switch between the two configurations takes place at the 2<sup>+</sup> charge state (**SI Fig. 2.11f-g**), which is most populated at neutral pH.<sup>7,24</sup>

We compared this behavior with analogous simulations of the two most prevalent M2 mutants, S31N-M2TM and D44N-M2TM(34), in the same unit cell (S31N-M2TM crystallizes in the LCP with unit cell parameters within 1 Å from those shown here, and the backbone of

D44N-M2TM modeled by MD and NMR<sup>33</sup> is at less than 2 Å RMSD from the current structures). S31N-M2TM also exhibits “loopback circuits” at high pH (SI Figs. 2.17-2.19), but D44N-M2TM features a “parallel circuit” configuration at all pH levels (SI Figs. 2.23-2.25). Electrophysiology experiments showed that WT-M2 and S31N-M2 have similar pH/current profiles,<sup>34</sup> but the proton conductance of D44N-M2 saturates below pH 5.<sup>33</sup> Thus, the “loopback circuits” appear to correlate with the ability to promote the addition of protons onto a charged His37 cluster. A similar H-bond network structure was also seen for the water molecules adjacent to His37 in the previous 1.65 Å crystal structure of M2TM.<sup>9</sup>

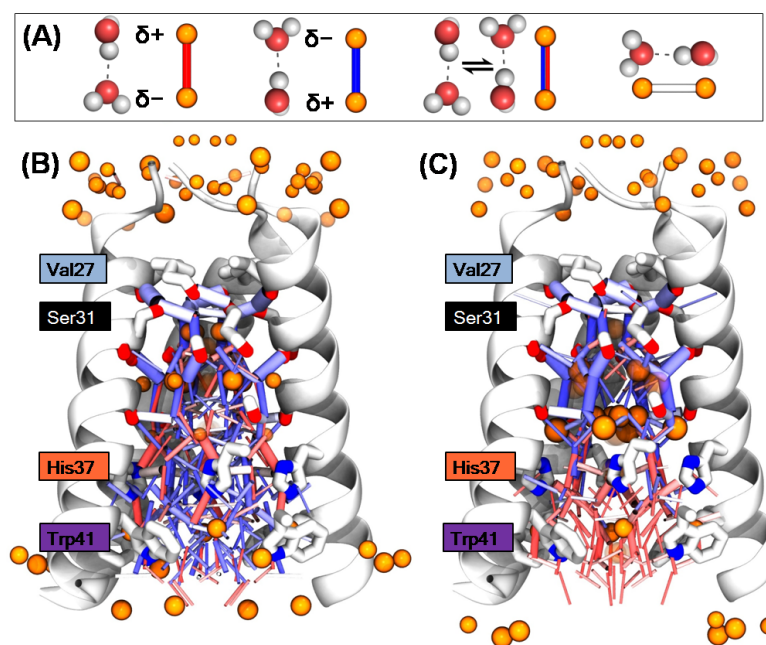


**Figure 2.5. Hydrogen bond orientation calculated from MD simulations.** **a**, Schematic representation of the water wires and the hydrogen bond orientation. The oxygens of water molecules observed in the room temperature X-ray structures are shown as van der Waals spheres (orange color), with diameter proportional to the crystallographic B-factors and transparency reflecting the partial occupancy. Hydrogen bonds are displayed as sticks, with a color scale denoting their orientation, and the thickness proportional to their population. **b**, Water wires for a neutral channel. **c**, Water wires at the 4<sup>+</sup> charge state.

*2.4.7 Hydrogen bond donor/acceptor water molecules along the M2 pore.* As posited above, the M2 pore-lining residues are expected to act preferentially as H-bond acceptors, thus providing the ideal environment to stabilize a hydronium ion. Our MD simulations show that, in response, the water molecules behave preferentially as H-bond donors along the 17 Å stretch between Val27 and His37 (**SI Fig. 2.13**). There is a larger net number of water molecules acting as H-bond donors in the extraviral side of the M2 pore, irrespective of the charge state of the histidine tetrad. By contrast, the H-bonding population in the C-terminal part of the pore (between Trp41 and Leu46) is highly sensitive to pH. In the neutral state, there is only a marginal preference for the water molecules to act as donors in the direction of proton influx. As the charge on the His37 tetrad increases, the water molecules switch into H-bond acceptors so that they can establish H-bonds with the protonated His37, which can donate two H-bonds (**Fig. 2.5** and **SI Table 2.2**). These interactions are also seen in the S31N- and D44N-M2TM simulations (**SI Tables 2.3-2.4** and **SI Figs. 2.20, 2.26**), indicating that no significant changes in the H-bonds between protein and water are brought about by naturally occurring mutations.

## **2.5 Conclusions**

It is interesting to compare the present studies of the M2 channel with previous studies of the water channel<sup>4</sup> and ammonia channel,<sup>3</sup> both structures that have been solved at moderate to high resolution and are responsible for diffusion of solvent molecules. In the case of the ammonia and water channels, the conduction pore allows for diffusion of single molecules of neutral H<sub>2</sub>O or NH<sub>3</sub> while excluding ammonium or hydronium ions. By contrast, the selectivity filter of the M2 channel is formed by a general acid/base, His37, which shuttles protons through the channel. The conduction path leading to this selectivity filter in M2 is markedly different

from the ammonia and water channels in that it is broader and able to conduct protons through partially occupied water wires. Although there are only approximately 16 water molecules at a given time in the path leading to His37, they are at partial occupancy at low temperature, giving rise to hundreds of potential paths conducive to proton conduction. The apparent fluid nature of the pore becomes even more apparent near room temperature, where the density suggests greater disorder, particularly at low pH. Moreover, examination of the structures and the predominant protonation state of His37 suggests that the overall collection of individual water molecules, although likely mobile, are on average highly polarized to favor hydrogen bond orientations that encourage entry of protons when the His37 residues are deprotonated; similarly, as His37 becomes more protonated, diffusion of protons into the channel might be encouraged. This dipolar switching might work in concert with rotameric switching to create the asymmetric proton conductance of the channel. Finally, the water molecules in the channel are surrounded by hydrogen bond donating carbonyl groups, which should serve to stabilize hydronium through second-shell effects via bridging water molecules. It is encouraging that the present MD simulations in a crystal environment are consistent with experimental observations and add quantitative detail to these qualitative conclusions. Moreover, given the small size and biological relevance of the M2 channel, these structures should be ideally suited for more detailed simulations based on valence bond,<sup>15,35</sup> quantum, and quantum mechanics/molecular mechanics simulations<sup>14,36</sup> in which the formation and cleavage of covalent bonds associated with proton transfer can be examined in atomic detail.

## 2.6 Methods

*2.6.1 Experimental methods.* The peptide construct used in this study is M2(22-46) from influenza A/Udorn/307/1972. The sequence, whose molecular weight is 2682.268 Da (av.), is as follows: Ac-SSDPLVVAASIIGILHLILWILDRL-NH<sub>3</sub>. The peptide was synthesized manually at high temperature using Fmoc chemistry, cleaved from the resin then purified using reverse-phase HPLC. The molecular weight of the desired product was confirmed using mass spectrometry and the purity of the product was tested using analytical HPLC. The purified peptide was dissolved in ethanol and stored at -80°C. The lipid cubic phase was prepared with some modifications to the protocol described by Caffrey and Cherezov,<sup>37</sup> then crystallization conditions were screened in 96-well plastic sandwich plates. Square-shaped crystals belonging to space group I<sub>4</sub> formed after 2-4 weeks of incubation at 10°C. These conditions were optimized to grow 20-120 μm sized crystals. The crystals used for data collection at cryogenic conditions were grown in 96-well plates at 10°C then harvested into liquid nitrogen. The crystals used for room temperature data were grown in 96-well plates at 20°C then were transported to the beam line at ambient temperature for harvesting and data collection.

All crystallographic data was collected at the Advanced Light Source on beam 8.3.1. The beam size was 100 μm for all data sets; the detector used was a 3 x 3 CCD array (ADSC Q315r). Data from the two cryo condition crystals that diffracted to 1.1 Å were collected at a temperature of < 100K with a 13.0 keV beam and a detector-to-sample distance of 125 mm. The high pH cryo condition crystal (PDB entry 4QK7) was exposed to the beam for 6 seconds per frame and the low pH cryo condition crystal (PDB entry 4QKC) was exposed for 4 seconds per frame; both crystals were oscillated 1 degree during data collection. The room temperature data was collected at 273 K using room temperature data collection techniques<sup>37</sup> with a 11.111 keV beam and an

aluminum foil attenuator for both data sets. The crystals accumulated radiation damage faster under room temperature diffraction conditions, so larger crystals (50-120  $\mu\text{m}$ ) were used to obtain complete data sets. The low pH room temperature condition crystal (PDB entry 4QKM) was exposed to the beam for 3 seconds per frame with a detector-to-sample distance of 125 mm; the high pH room temperature condition crystal (PDB entry 4QKL) was exposed to the beam for one second per frame with a detector-to-sample distance of 150 mm; both crystals were oscillated 1 degree during data collection.

Data processing was done in iMosflm.<sup>38</sup> Phasing was done by molecular replacement in the Phenix suite using Phaser MR<sup>39</sup> with chain A from PDB entry 3C9J<sup>8</sup> as a search model, then refinement was carried out in Phenix Refine.<sup>17</sup> Protein model manipulation and addition of water and ions were done in Coot,<sup>40</sup> and monoolein molecules were manually fit into Fo-Fc density using both Coot and PyMol.<sup>41</sup> Alternate conformers were predicted using the qFit web server<sup>25</sup> and Ringer,<sup>42</sup> and were also manually added where positive Fo-Fc density indicated they were present. See **Table 2.1** for data processing and refinement statistics. Anisotropic B-factors were used for both cryo conditions (PDB entries 4QK7 and 4QKC) and the low pH room temperature condition (PDB entry 4QKM), but not the high pH room temperature condition (PDB entry 4QKL).

*2.6.2 Molecular dynamics simulations.* Classical molecular dynamics (MD) simulations of the hydrated protein crystal were performed to study the network of water molecules inside the M2 pore and its response to pH changes (i.e. the protonation state of His37). The initial configurations were built using the two cryo X-ray structures of the transmembrane region of the M2 bundle solved either at low pH (PDB entry 4QKC) or high pH (PDB entry 4QK7). In order

to model the  $I_4$  symmetry of the crystal, two staggered tetramers were included in the simulation box (**SI Fig. 2.7**), along with the crystallographically resolved water molecules. Simulations were performed starting from either of the solved structures for each of the five possible protonation states of the His37 tetrad (0, +1, +2, +3, and +4). The neutral histidine residues were set in the  $\epsilon$ -tautomeric state and the histidine charge was increased by protonating one, two (non-adjacent), three, or all four histidines, respectively, for each of the two tetramers. Each of the ten resulting systems consists of  $\sim 7,000$  atoms. The simulations were performed in the NVT ensemble at 310K and using the measured crystal lattice dimensions ( $29.310 \text{ \AA} \times 29.310 \text{ \AA} \times 67.310 \text{ \AA}$  for the low pH structure and  $29.536 \text{ \AA} \times 29.536 \text{ \AA} \times 66.853 \text{ \AA}$  for the high pH); periodic boundary conditions were applied to mimic the crystal environment. The protein was modeled using the CHARMM force field<sup>29,30</sup> with CMAP corrections<sup>32</sup> and the water molecules were described using the TIP3P model.<sup>43</sup> All MD simulations were carried out with NAMD<sup>44</sup> and a production trajectory of  $\sim 350$  ns was sampled for each system.

Analysis of the MD trajectories was performed over the last  $\sim 250$  ns of the MD trajectories and enforcing four-fold rotational symmetry. Water densities (**Fig. 2.4**) were obtained from the MD simulations using the Volmap plugin<sup>45</sup> in VMD.<sup>46</sup> Populations of hydrogen bonded water molecules (**Fig. 2.5** and **SI Fig. 2.11**) were calculated using the following clustering protocol. A hydrogen-bond vector was defined between a donor and an acceptor when the two oxygen atoms are at a distance less than  $3.5 \text{ \AA}$  and the donor-hydrogen-acceptor angle is between  $150^\circ$ - $180^\circ$ . The clusters of these vectors were calculated using g\_cluster<sup>47</sup> with a  $1.5 \text{ \AA}$  cutoff. The occupancy of a hydrogen bond represented by the centroid of one cluster was obtained by dividing the population of the cluster by the total



number of MD frames and by 4 (to normalize upon symmetrization), such that the occupancy of a given hydrogen bond is at most 1. A similar protocol was used in Gianti et al. 2015.<sup>48</sup>

## **2.7 Acknowledgements**

Experimental work was funded by NIH grant R01-GM056423. Use of the LCP crystallization robot was made possible by NCCR grant 1S10RR027234-01. All experimental data was collected at the Advanced Light Source on beam 8.3.1: UC Office of the President, Multicampus Research Programs and Initiatives grant MR-15-328599, and Program for Breakthrough Biomedical Research, which is partially funded by the Sandler Foundation. Molecular dynamics simulations were performed using the Temple University High-Performance Computing System Owl's Nest (purchased in part with NSF Grant MRI-R2 0958854). J.S.F. is a Searle Scholar and a Pew Scholar, and is supported by NIH OD009180, GM110580, and NSF STC-1231306. R.A.W is supported by NSF GRFP. We also acknowledge partial support from the NSF through grants DMR-1120901 (M.A.-P.) and CHE-1212416 (G.F.).

## 2.8 References

- 1 Hong, M. & DeGrado, W. F. Structural basis for proton conduction and inhibition by the influenza M2 protein. *Protein science : a publication of the Protein Society* **21**, 1620-1633, doi:10.1002/pro.2158 (2012).
- 2 Hummer, G., Rasaiah, J. C. & Noworyta, J. P. Water conduction through the hydrophobic channel of a carbon nanotube. *Nature* **414**, 188-190, doi:10.1038/35102535 (2001).
- 3 Khademi, S. *et al.* Mechanism of ammonia transport by Amt/MEP/Rh: structure of AmtB at 1.35 Å. *Science* **305**, 1587-1594, doi:10.1126/science.1101952 (2004).
- 4 Kosinska Eriksson, U. *et al.* Subangstrom resolution X-ray structure details aquaporin-water interactions. *Science* **340**, 1346-1349, doi:10.1126/science.1234306 (2013).
- 5 Wang, C., Lamb, R. A. & Pinto, L. H. Activation of the M2 ion channel of influenza virus: a role for the transmembrane domain histidine residue. *Biophys J* **69**, 1363-1371 (1995).
- 6 Chizhnikov, I. V. *et al.* Selective proton permeability and pH regulation of the influenza virus M2 channel expressed in mouse erythrocyte cells. *J. Physiol. (Lond.)* **494**, 329-336 (1996).
- 7 Hu, J. *et al.* Histidines, heart of the hydrogen ion channel from influenza A virus: Toward an understanding of conductance and proton selectivity. *Proc. Natl. Acad. Sci. U. S. A.* **103**, 6865-6870, doi:10.1073/pnas.0601944103 (2006).
- 8 Stouffer, A. L. *et al.* Structural basis for the function and inhibition of an influenza virus proton channel. *Nature* **451**, 596-U513, doi:10.1038/nature06528 (2008).
- 9 Acharya, R. *et al.* Structure and mechanism of proton transport through the transmembrane tetrameric M2 protein bundle of the influenza A virus. *Proc Natl Acad Sci U S A* **107**, 15075-15080, doi:10.1073/pnas.1007071107 (2010).
- 10 Hu, F., Schmidt-Rohr, K. & Hong, M. NMR Detection of pH-Dependent Histidine-Water Proton Exchange Reveals the Conduction Mechanism of a Transmembrane Proton Channel. *J Am Chem Soc* **134**, 3703-3713, doi:10.1021/ja2081185 (2012).
- 11 Hu, F. H., Luo, W. B. & Hong, M. Mechanisms of proton conduction and gating in influenza M2 proton channels from solid-state NMR. *Science* **330**, 505-508, doi:DOI 10.1126/science.1191714 (2010).
- 12 Sharma, M. *et al.* Insight into the mechanism of the influenza a proton channel from a structure in a lipid bilayer. *Science* **330**, 509-512, doi:10.1126/science.1191750 (2010).

- 13 Luo, W. & Hong, M. Conformational changes of an ion channel detected through water-protein interactions using solid-state NMR spectroscopy. *J Am Chem Soc* **132**, 2378-2384, doi:10.1021/ja9096219 (2010).
- 14 Carnevale, V., Fiorin, G., Levine, B. G., DeGrado, W. F. & Klein, M. L. Multiple proton confinement in the M2 channel from the influenza A virus. *J Phys Chem C* **114**, 20856-20863, doi:Doi 10.1021/Jp107431g (2010).
- 15 Chen, H., Wu, Y. & Voth, G. A. Proton transport behavior through the influenza A M2 channel: insights from molecular simulation. *Biophys. J.* **93**, 3470-3479, doi:10.1529/biophysj.107.105742 (2007).
- 16 Otwinowski, Z. & Minor, W. Processing of X-ray diffraction data collected in oscillation mode. *Methods Enzymol.* **276**, 307-326, doi:10.1016/s0076-6879(97)76066-x (1997).
- 17 Adams, P. D. *et al.* PHENIX: a comprehensive Python-based system for macromolecular structure solution. *Acta Crystallogr. Sect. D-Biol. Crystallogr.* **66**, 213-221, doi:10.1107/s0907444909052925 (2010).
- 18 Wei, C. & Pohorille, A. Activation and proton transport mechanism in influenza A M2 channel. *Biophys J* **105**, 2036-2045, doi:10.1016/j.bpj.2013.08.030 (2013).
- 19 Yi, M., Cross, T. A. & Zhou, H. X. A secondary gate as a mechanism for inhibition of the M2 proton channel by amantadine. *J Phys Chem B* **112**, 7977-7979, doi:10.1021/jp800171m (2008).
- 20 Ghosh, A., Qiu, J., DeGrado, W. F. & Hochstrasser, R. M. Tidal surge in the M2 proton channel, sensed by 2D IR spectroscopy. *Proc Natl Acad Sci U S A* **108**, 6115-6120, doi:10.1073/pnas.1103027108 (2011).
- 21 Schnell, J. R. & Chou, J. J. Structure and mechanism of the M2 proton channel of influenza A virus. *Nature* **451**, 591-U512, doi:10.1038/nature06531 (2008).
- 22 Wang, J. *et al.* Structure and inhibition of the drug-resistant S31N mutant of the M2 ion channel of influenza A virus. *Proc Natl Acad Sci U S A* **110**, 1315-1320, doi:10.1073/pnas.1216526110 (2013).
- 23 Li, C., Qin, H., Gao, F. P. & Cross, T. A. Solid-state NMR characterization of conformational plasticity within the transmembrane domain of the influenza A M2 proton channel. *Biochim Biophys Acta* **1768**, 3162-3170 (2007).
- 24 Ma, C. L. *et al.* Identification of the functional core of the influenza A virus A/M2 proton-selective ion channel. *Proc. Natl. Acad. Sci. U. S. A.* **106**, 12283-12288, doi:10.1073/pnas.0905726106 (2009).

- 25 Landau, E. M. & Rosenbusch, J. P. Lipidic cubic phases: A novel concept for the crystallization of membrane proteins. *Proc. Natl. Acad. Sci. U. S. A.* **93**, 14532-14535, doi:10.1073/pnas.93.25.14532 (1996).
- 26 Khurana, E. *et al.* Molecular dynamics calculations suggest a conduction mechanism for the M2 proton channel from influenza A virus. *Proc Natl Acad Sci U S A* **106**, 1069-1074, doi:10.1073/pnas.0811720106 (2009).
- 27 Halle, B. Biomolecular cryocrystallography: structural changes during flash-cooling. *Proc Natl Acad Sci U S A* **101**, 4793-4798, doi:10.1073/pnas.0308315101 (2004).
- 28 Wang, J. *et al.* Molecular dynamics simulation directed rational design of inhibitors targeting drug-resistant mutants of influenza A virus M2. *J. Am. Chem. Soc.* **133**, 12834-12841, doi:Doi 10.1021/Ja204969m (2011).
- 29 Vangunsteren, W. F., Berendsen, H. J. C., Hermans, J., Hol, W. G. J. & Postma, J. P. M. Computer-simulation of the dynamics of hydrated protein crystals and its comparison with X-ray data. *Proceedings of the National Academy of Sciences of the United States of America-Biological Sciences* **80**, 4315-4319 (1983).
- 30 Liu, P., Huang, X. H., Zhou, R. H. & Berne, B. J. Observation of a dewetting transition in the collapse of the melittin tetramer. *Nature* **437**, 159-162, doi:10.1038/nature03926 (2005).
- 31 Cerutti, D. S., Le Trong, I., Stenkamp, R. E. & Lybrand, T. P. Simulations of a protein crystal: explicit treatment of crystallization conditions links theory and experiment in the streptavidin-biotin complex. *Biochemistry* **47**, 12065-12077, doi:10.1021/bi800894u (2008).
- 32 Hu, Z. Q. & Jiang, J. W. Molecular dynamics simulations for water and ions in protein crystals. *Langmuir* **24**, 4215-4223, doi:10.1021/la703591e (2008).
- 33 Ma, C. *et al.* Asp44 stabilizes the Trp41 gate of the M2 proton channel of influenza A virus. *Structure* **21**, 2033-2041, doi:10.1016/j.str.2013.08.029 (2013).
- 34 Balannik, V. *et al.* Functional Studies and Modeling of Pore-Lining Residue Mutants of the Influenza A Virus M2 Ion Channel. *Biochemistry* **49**, 696-708, doi:10.1021/bi901799k (2010).
- 35 Liang, R., Li, H., Swanson, J. M. & Voth, G. A. Multiscale simulation reveals a multifaceted mechanism of proton permeation through the influenza A M2 proton channel. *Proc Natl Acad Sci U S A* **111**, 9396-9401, doi:10.1073/pnas.1401997111 (2014).

- 36 Dong, H., Fiorin, G., DeGrado, W. F. & Klein, M. L. Exploring histidine conformations in the M2 channel lumen of the influenza A virus at neutral pH via molecular simulations. *J Phys Chem Lett* **4**, 3067-3071, doi:Doi 10.1021/Jz401672h (2013).
- 37 Fraser, J. S. *et al.* Accessing protein conformational ensembles using room-temperature X-ray crystallography. *Proc. Natl. Acad. Sci. U. S. A.* **108**, 16247-16252, doi:10.1073/pnas.1111325108 (2011).
- 38 Tang, Y. J., Zaitseva, F., Lamb, R. A. & Pinto, L. H. The gate of the influenza virus M-2 proton channel is formed by a single tryptophan residue. *J. Biol. Chem.* **277**, 39880-39886, doi:10.1074/jbc.M206582200 (2002).
- 39 Lang, P. T. *et al.* Automated electron-density sampling reveals widespread conformational polymorphism in proteins. *Protein Sci.* **19**, 1420-1431, doi:10.1002/pro.423 (2010).
- 40 Ghosh, A., Qiu, J., DeGrado, W. F. & Hochstrasser, R. M. Tidal surge in the M2 proton channel, sensed by 2D IR spectroscopy. *Proc. Natl. Acad. Sci. U. S. A.* **108**, 6115-6120, doi:10.1073/pnas.1103027108 (2011).
- 41 Schrodinger, LLC. *The PyMOL Molecular Graphics System, Version 1.3r1* (2010).
- 42 van den Bedem, H., Dhanik, A., Latombe, J. C. & Deacon, A. M. Modeling discrete heterogeneity in X-ray diffraction data by fitting multi-conformers. *Acta Crystallogr. Sect. D-Biol. Crystallogr.* **65**, 1107-1117, doi:10.1107/s0907444909030613 (2009).
- 43 Jorgensen, W. L., Chandrasekhar, J., Madura, J. D., Impey, R. W. & Klein, M. L. Comparison of simple potential functions for simulating liquid water. *J. Chem. Phys.* **79**, 926-935, doi:10.1063/1.445869 (1983).
- 44 Phillips, J. C. *et al.* Scalable molecular dynamics with NAMD. *J. Comput. Chem.* **26**, 1781-1802, doi:10.1002/jcc.20289 (2005).
- 45 MacKerell, A. D. *et al.* All-atom empirical potential for molecular modeling and dynamics studies of proteins. *J. Phys. Chem. B* **102**, 3586-3616 (1998).
- 46 Humphrey, W., Dalke, A. & Schulten, K. VMD: Visual molecular dynamics. *J. Mol. Graph.* **14**, 33-38, doi:10.1016/0263-7855(96)00018-5 (1996).
- 47 Best, R. B. *et al.* Optimization of the additive CHARMM all-atom protein force field targeting improved sampling of the backbone phi, psi and side-chain chi(1) and chi(2) dihedral angles. *J. Chem. Theory Comput.* **8**, 3257-3273, doi:10.1021/ct3004000x (2012).
- 48 Gianti, E., Carnevale, V., DeGrado, W. F., Klein, M. L. & Fiorin, G. Hydrogen-Bonded Water Molecules in the M2 Channel of the Influenza A Virus Guide the Binding Preferences of Ammonium-Based Inhibitors. *The Journal of Physical Chemistry B* **119**, 1173-1183, doi:10.1021/jp506807y (2015).

- 49 Caffrey, M. & Cherezov, V. Crystallizing membrane proteins using lipidic mesophases. *Nat. Protoc.* **4**, 706-731, doi:10.1038/nprot.2009.31 (2009).
- 50 Battye, T. G. G., Kontogiannis, L., Johnson, O., Powell, H. R. & Leslie, A. G. W. iMOSFLM: a new graphical interface for diffraction-image processing with MOSFLM. *Acta Crystallogr. Sect. D-Biol. Crystallogr.* **67**, 271-281, doi:10.1107/s0907444910048675 (2011).
- 51 McCoy, A. J. *et al.* Phaser crystallographic software. *J. Appl. Crystallogr.* **40**, 658-674, doi:10.1107/s0021889807021206 (2007).
- 52 Emsley, P., Lohkamp, B., Scott, W. G. & Cowtan, K. Features and development of Coot. *Acta Crystallogr. Sect. D-Biol. Crystallogr.* **66**, 486-501, doi:10.1107/s0907444910007493 (2010).

## 2.9 Appendix A, Supplementary Figures and Tables

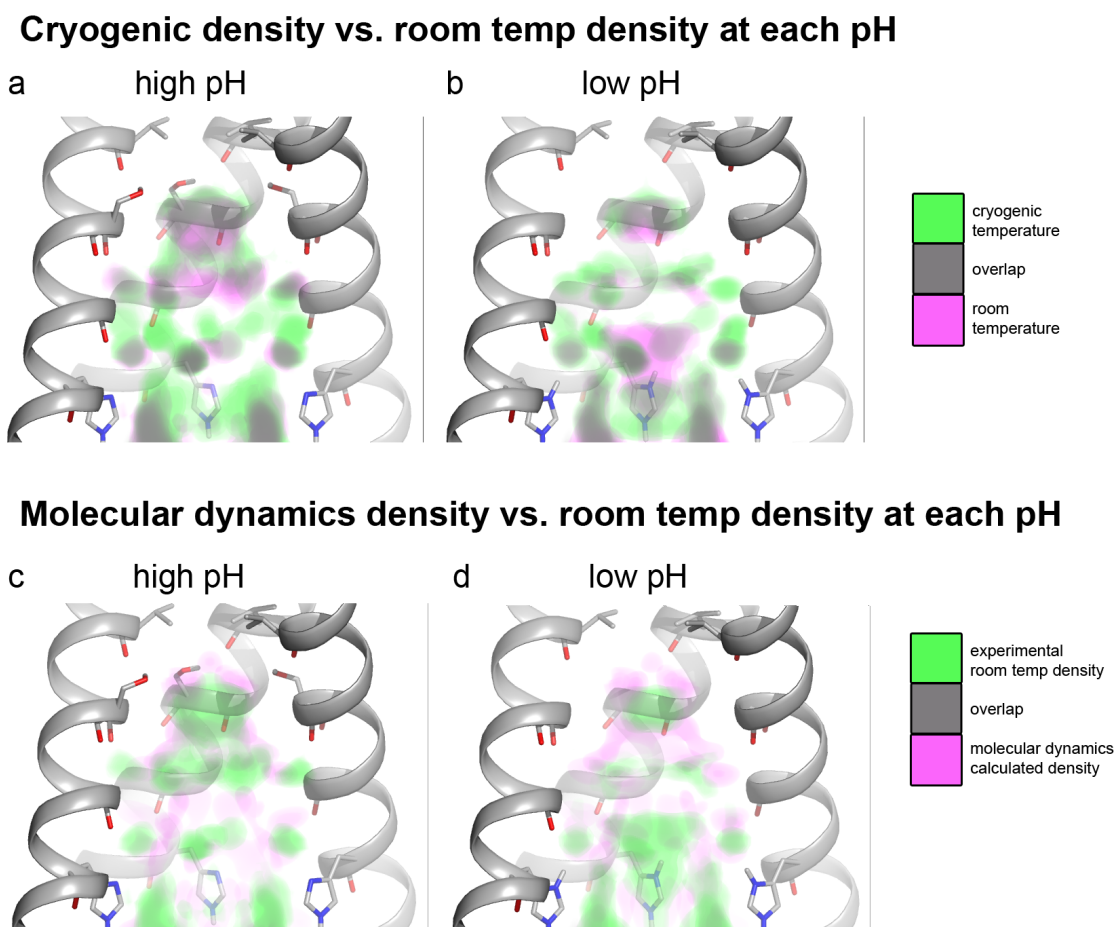


**Figure 2.6. Further comparisons between density maps.** *Top, a-b:* Comparison of experimentally observed density for the cryogenic and room temperature experimental conditions at high and low pH. *Bottom, c-d:* comparison between calculated electron density from molecular dynamics simulations and experimental density from room temperature conditions at high and low pH. The overlap between densities, shown in gray, is largest in all conditions where the waters bind to the carbonyls of the channel and also where they bind to His37.

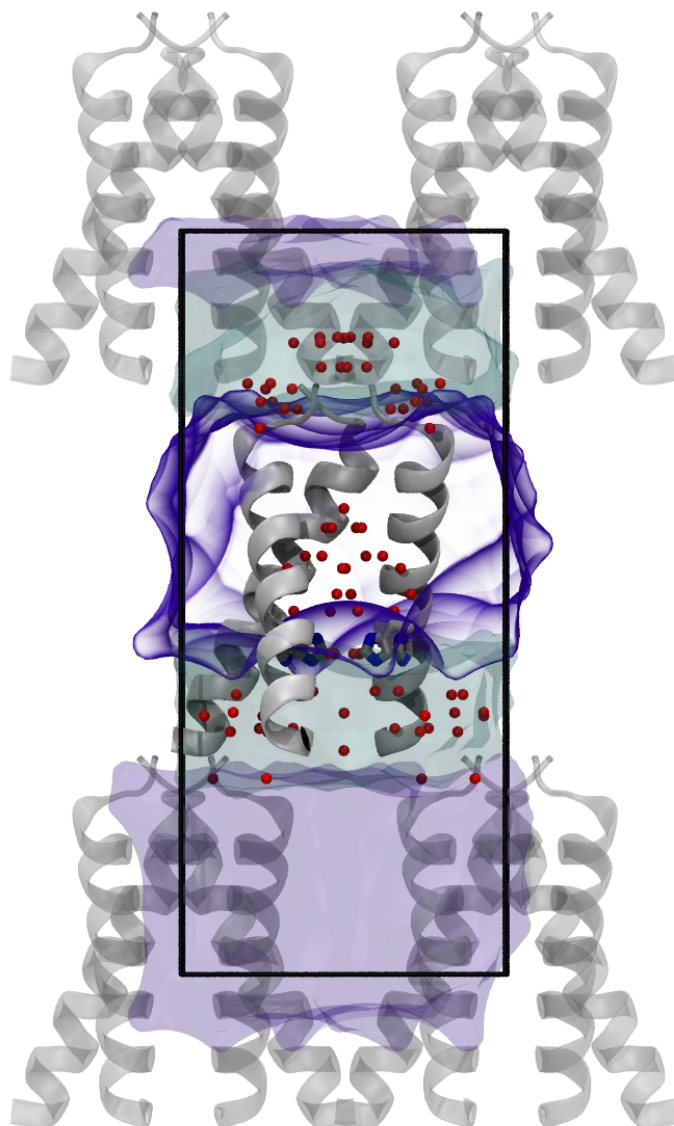


**Figure 2.7. System setup used in the molecular dynamics simulations.** The central tetramer is displayed as a grey cartoon, removing one of the helices of the tetramer in order to show the crystallographic water molecules and the His37 tetrad. The rest of the water is shown in cyan and the lipid phase in purple. The simulation box is indicated with black lines, and contains an additional staggered tetramer in order to model the  $I_4$  crystallographic symmetry.



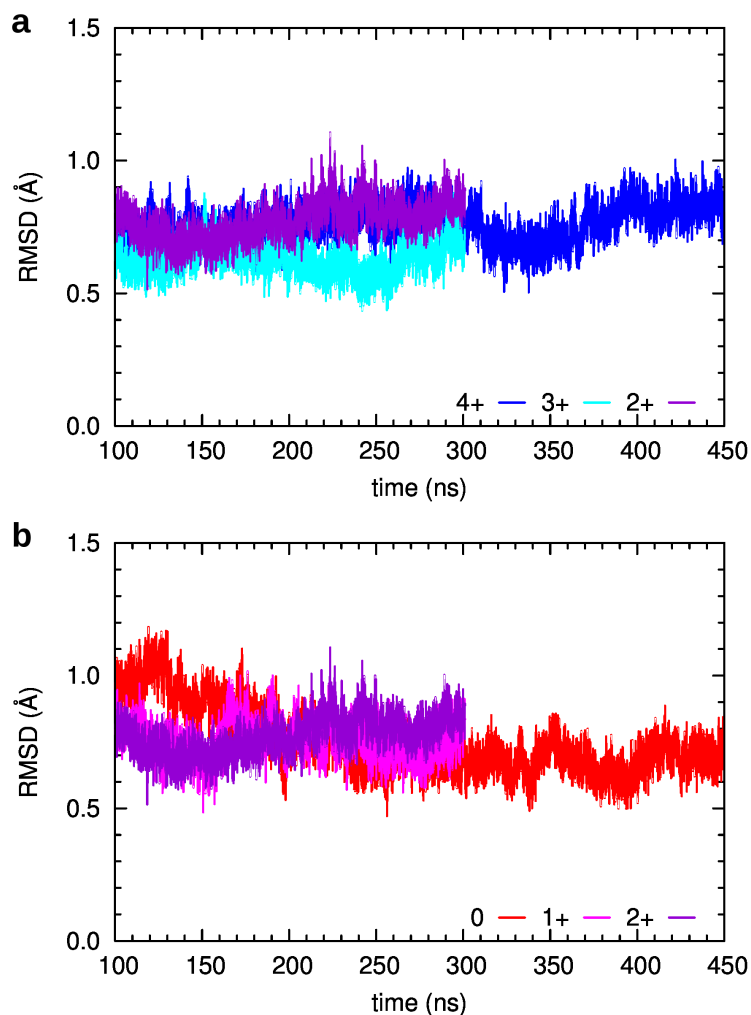


**Figure 2.8. Evolution of the root mean square deviation (RMSD) of the C $\alpha$  atoms of M2TM along the MD simulations.** RMSD is calculated with respect to the cryogenic crystal structures. **a**, RMSD for the 4+ (blue), 3+ (cyan) and 2+ (purple) states with respect to the low pH structure (PDB entry 4QKC). **b**, RMSD for neutral (red), 1+ (magenta) and 2+ (purple) states with respect to the high pH structure (PDB entry 4QK7).

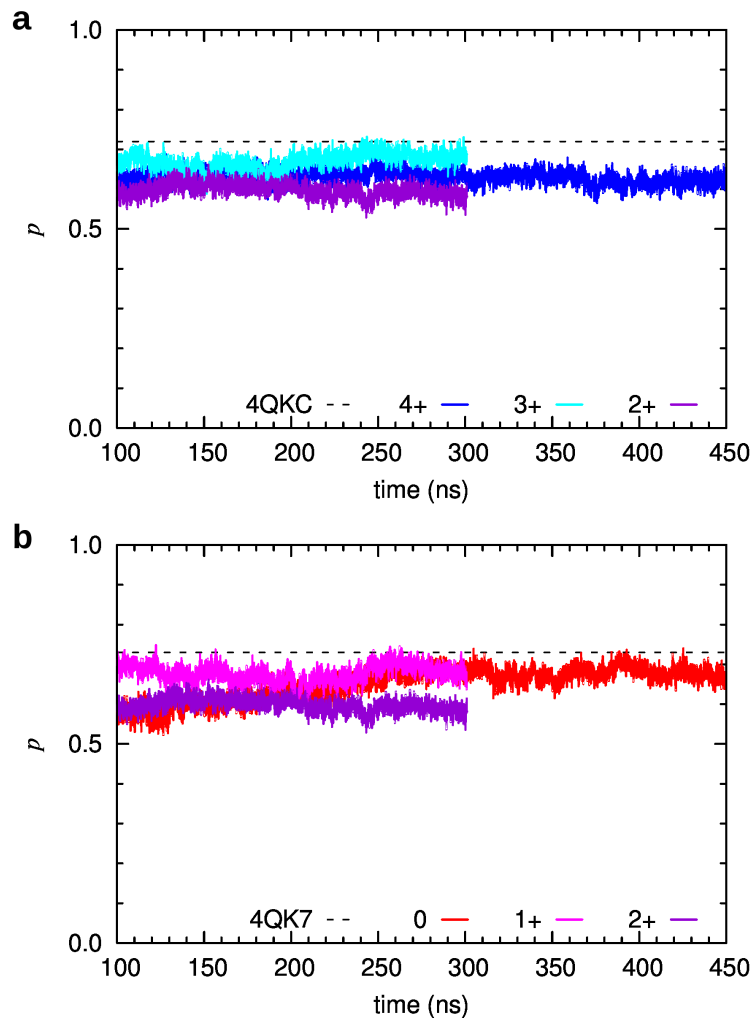


**Figure 2.9. Evolution of the principal component,  $p$ , along the MD simulations.**  $p$  describes the fraction of C-terminally closed *versus* dilated protein conformation. **a**, Principal component for the 4+ (blue), 3+ (cyan) and 2+ (purple) states; the principal component of the cryogenic crystal structure at low pH (PDB entry 4QKC) is shown as a black dashed line. **b**, Principal component for the neutral (red), 1+ (magenta) and 2+ (purple) states; the principal component of the cryogenic crystal structure at high pH (PDB entry 4QK7) is shown as a black dashed line.

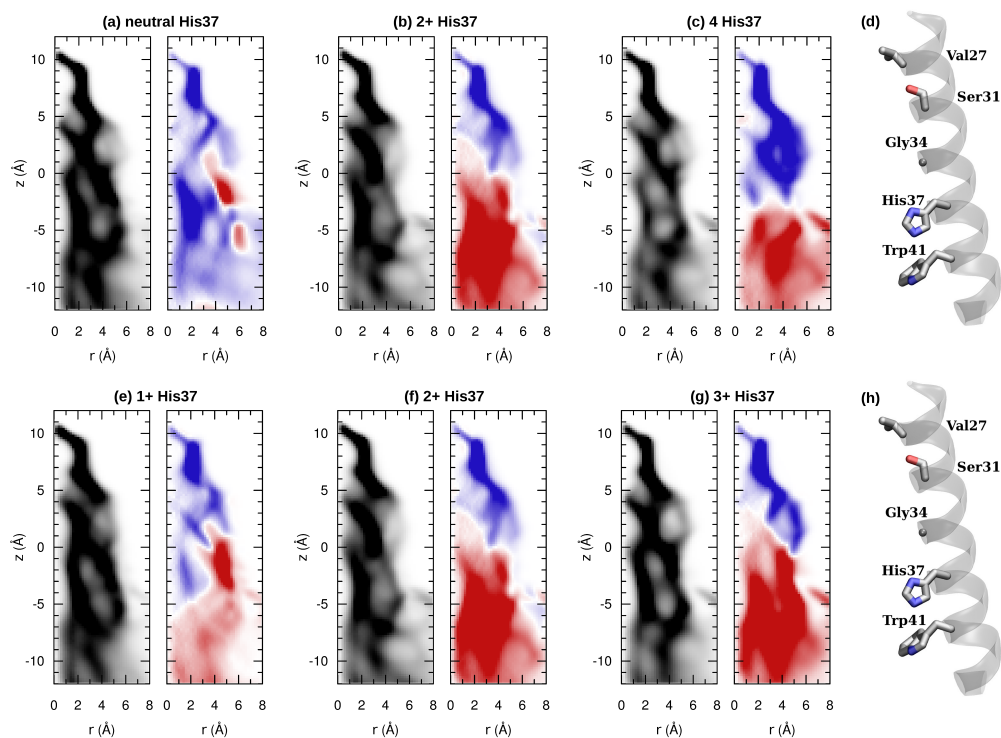


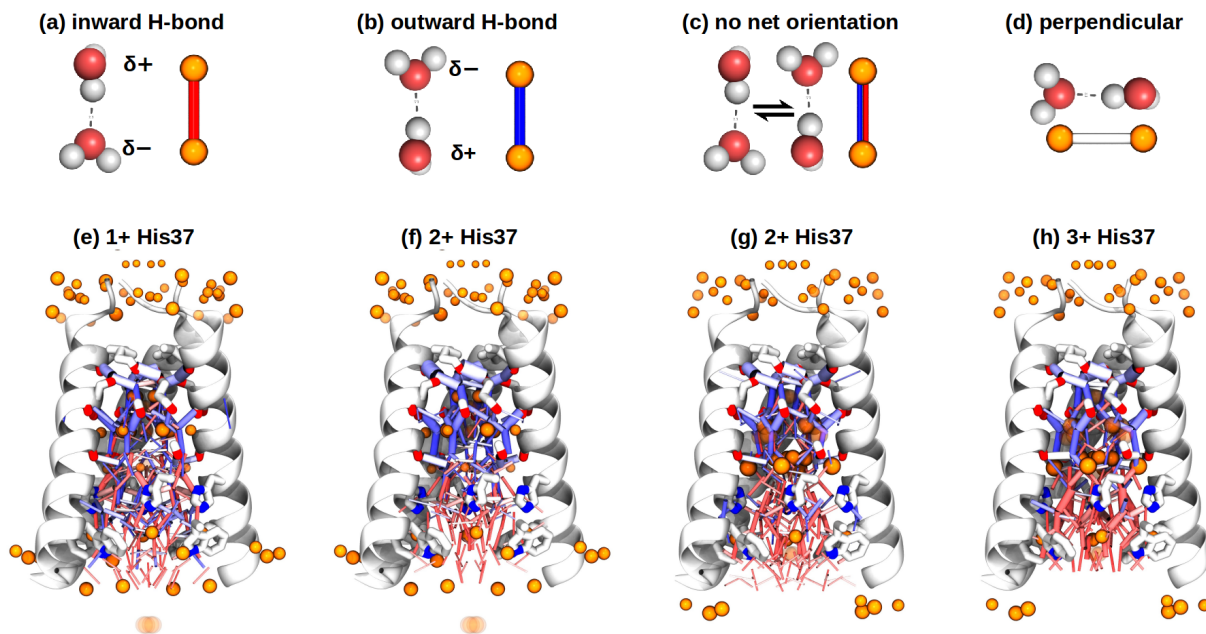
**Figure 2.10. Two-dimensional profile of the hydrogen bond vectors at different charge states of the His37 tetrad.** Shown are the density (black,  $\text{\AA}^{-3}$  units) and average orientation (red and blue,  $\text{\AA}^{-2}$  units) of hydrogen bond vectors as a function of the distance from the pore axis,  $r$ , and the displacement along the axis,  $z$ . Blue areas indicate regions populated by outward-oriented H-bonds, red denote inward-oriented H-bonds. *Top: a-c*, Density and average orientation of hydrogen bond vectors for a neutral channel, at the 2+ charge state and at the 4+ charge state, respectively. *d*, M2TM monomer, indicating the position of the pore-lining residues (Val27, Ser31, His37 and Trp41). *Bottom: e-g*, Density and average orientation of hydrogen bond vectors at the 1+, 2+ and the 3+ charge states, respectively; the 2+ charge state is the same as in (b). *h*, M2TM monomer, indicating the position of the pore-lining residues (Val27, Ser31, His37 and Trp41).

**Table 2.2. Average number of hydrogen bonds in the M2 pore at different charge states of the His37 tetrad.** The hydrogen bonds are classified as extraviral or intraviral depending on their position (either above or below) with respect to the His37 tetrad. The total number of hydrogen bonds is decomposed in outwards (in blue) or inwards (in red) depending on the hydrogen bond orientation (either towards the viral exterior or interior, respectively).

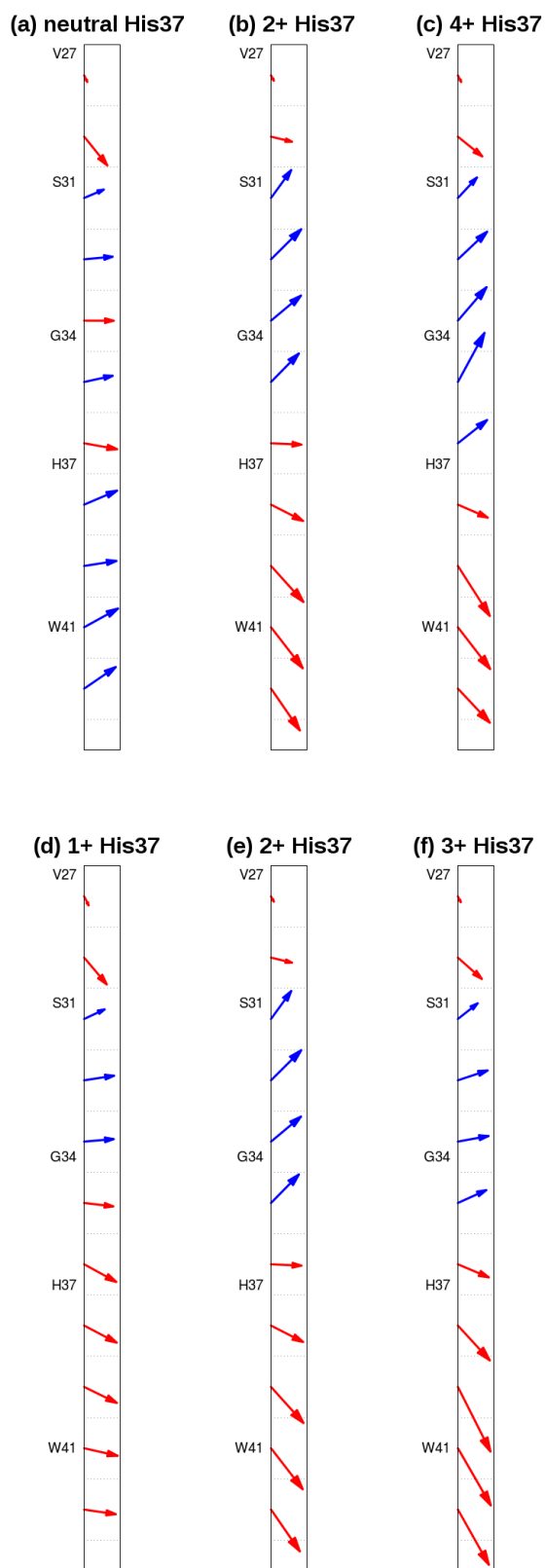
|                                     |          | <b>neutral His37</b> | <b>2+ His37</b> | <b>4+ His37</b> |
|-------------------------------------|----------|----------------------|-----------------|-----------------|
| <b>extraviral<br/>(above His37)</b> | total    | 41.8 ± 4.8           | 37.7 ± 4.3      | 33.3 ± 4.2      |
|                                     | outwards | 22.4 ± 3.7           | 22.1 ± 3.6      | 20.7 ± 4.0      |
|                                     | inwards  | 19.5 ± 3.6           | 15.6 ± 3.4      | 12.6 ± 3.8      |
| <b>intraviral<br/>(below His37)</b> | total    | 53.8 ± 6.2           | 38.0 ± 5.8      | 46.3 ± 6.2      |
|                                     | outwards | 29.8 ± 5.0           | 13.8 ± 3.9      | 16.9 ± 4.9      |
|                                     | inwards  | 24.0 ± 4.7           | 24.2 ± 4.9      | 29.4 ± 5.6      |

|                                     |          | <b>1+ His37</b> | <b>2+ His37</b> | <b>3+ His37</b> |
|-------------------------------------|----------|-----------------|-----------------|-----------------|
| <b>extraviral<br/>(above His37)</b> | total    | 41.2 ± 4.7      | 37.7 ± 4.3      | 40.5 ± 4.4      |
|                                     | outwards | 20.5 ± 3.6      | 22.1 ± 3.6      | 20.1 ± 3.5      |
|                                     | inwards  | 20.8 ± 3.6      | 15.6 ± 3.4      | 20.4 ± 3.5      |
| <b>intraviral<br/>(below His37)</b> | total    | 49.7 ± 5.8      | 38.0 ± 5.8      | 48.9 ± 6.6      |
|                                     | outwards | 22.5 ± 4.3      | 13.8 ± 3.9      | 13.4 ± 4.0      |
|                                     | inwards  | 27.2 ± 4.9      | 24.2 ± 4.9      | 35.5 ± 5.8      |



**Figure 2.11. Water wires calculated from the molecular dynamics simulations at different charge states of the His37 tetrad.** *Top*, Schematic representation of the four possible hydrogen bond patterns between water molecules inside the M2 pore. **a-b**, Directional hydrogen bonds oriented towards either the viral interior (a) or the channel exterior (b), respectively. **c**, Hydrogen bonds without a preferred directionality (*i.e.* flips back and forth between the two orientations). **d**, Hydrogen bonds perpendicular to the pore axis. For each possible hydrogen bond pattern, the atomistic representation of the corresponding water dimer is shown on the left and the water wire counterpart on the right, with the water oxygen atoms as orange spheres and the hydrogen bonds as sticks; the color scale denotes the hydrogen bond orientation, either inwards (in red), outwards (in blue) or perpendicular to the pore axis (in white). *Bottom*, Water wires calculated from the MD simulations. The oxygen atoms of the water molecules observed in the room temperature X-ray structures are shown as van der Waals spheres (orange color), with the diameter proportional to the crystallographic B-factors and transparency reflecting partial occupancy. Hydrogen bonds are represented as sticks, with a color scale denoting their orientation (see panels a-d), and thickness proportional to their population. **e-f**, Water wires for the 1+ and 2+ charge states, respectively, for the production simulations starting from the cryogenic high pH crystal structure (PDB entry 4QK7). **g-h**, Water wires at the 2+ and 3+ charge states, respectively, for the production simulations starting from the cryogenic low pH crystal structure (PDB entry 4QKC).



**Figure 2.12. Average hydrogen bond vectors along the M2 pore at different charge states of the His37 tetrad.** The vector direction reflects the net orientation with respect to the pore axis, with the H-bonds pointing to the exterior of the channel (outwards) colored in blue and the ones pointing to the viral interior (inwards) in red. The vector length is proportional to the magnitude of the net hydrogen bond (i.e. the longer, the larger the preference to be oriented in that direction). The hydrogen bonds are averaged over 2 Å bins along the pore axis (delimited by dashed black lines). **a-c**, Average hydrogen bond vectors for a neutral channel, at the 2+ charge state and at the 4+ charge state, respectively. **d-f**, Average hydrogen bond vectors at the 1+, 2+ and 3+ charge states, respectively.

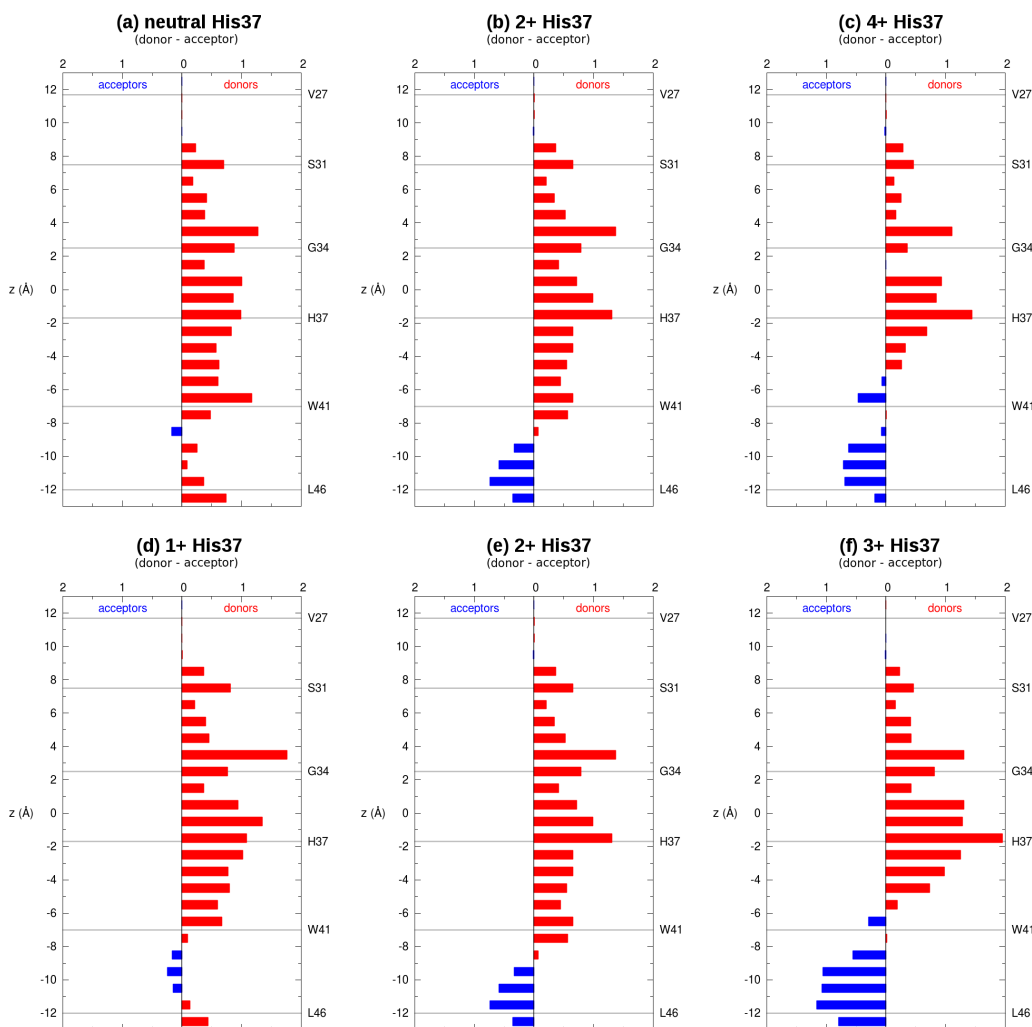


**Figure 2.13. Difference between the number of water molecules acting as hydrogen bond donors and acceptors at different charge states of the His37 tetrad.** The (*donor-acceptor*) difference along the M2 pore axis ( $z$ , in Å) is shown. Red bars represent a net number of donors at that pore position and blue bars a net number of acceptors. The position of the pore-lining M2 residues ( $C_{\alpha}$  atom of Val27, Ser31, Gly34, His37, Trp41 and Leu46) is indicated by horizontal grey lines. **a-c**, Difference (*donor-acceptor*) for a neutral channel, at the 2+ charge state and at the 4+ charge state, respectively. **d-f**, Difference (*donor-acceptor*) at the 1+, 2+ and 3+ charge states; the 2+ state is the same as in **b**.

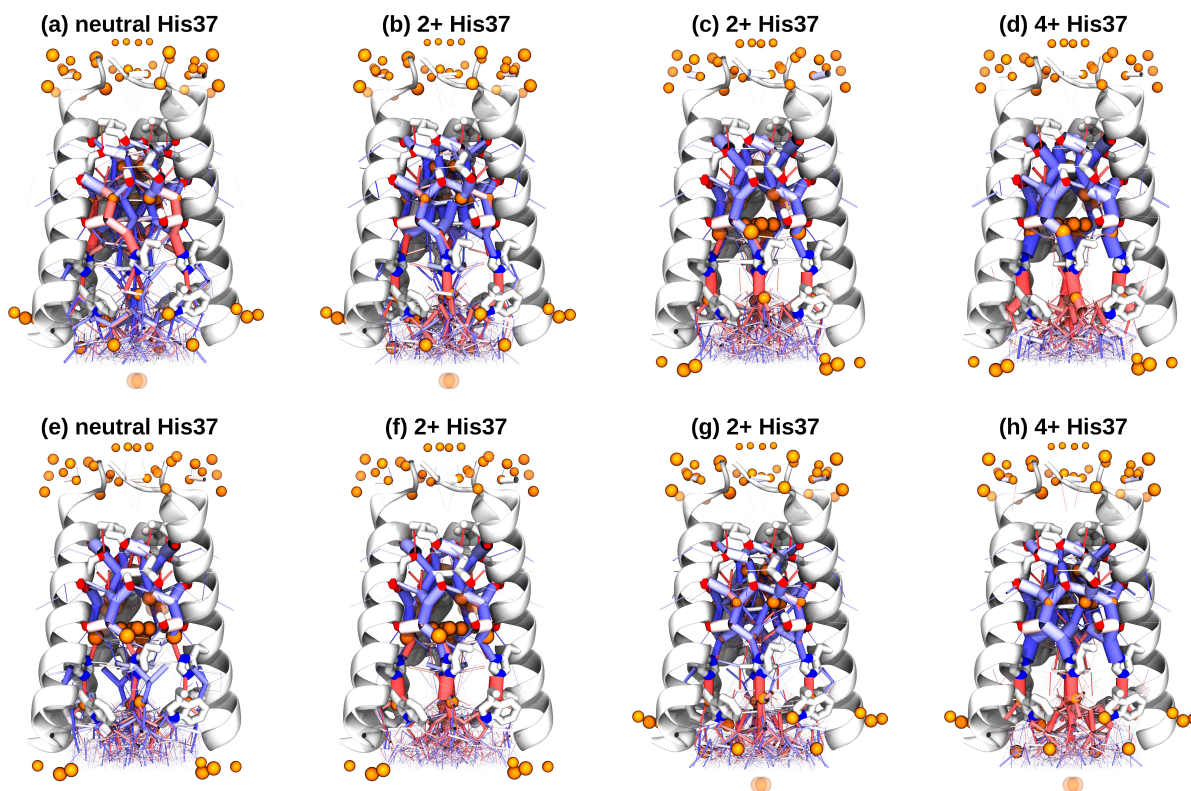


**Figure 2.14. Water wires calculated from the control simulations at different charge states of the His37 tetrad.** The oxygen atoms of the water molecules observed in the room temperature X-ray structures are shown as van der Waals spheres (orange color), with the diameter proportional to the crystallographic B-factors and transparency reflecting partial occupancy. Hydrogen bonds are represented as sticks, with a color scale denoting their orientation (see **SI Fig. 2.11**), and thickness proportional to their population. *Top*, Restrained MD simulations. **a-b**, Water wires for the neutral charge state and at the 2+ charge state, respectively, for the restrained simulations starting from the high pH crystal structure (PDB entry 4QK7). **c-d**, Water wires at the 2+ and 4+ charge states, respectively, for the restrained simulations starting from the low pH crystal structure (PDB entry 4QKC). *Bottom*, Swapped MD simulations. **e-h**, Water wires calculated from the swapped control simulations at different charge states of the His37 tetrad. **e-f**, Water wires for the neutral charge state and at the 2+ charge state, respectively, for the swapped simulations with the high pH protein structure and low pH water sites. **g-h**, Water wires at the 2+ and 4+ charge states, respectively, for the swapped simulations with the low pH protein structure and high pH water sites.



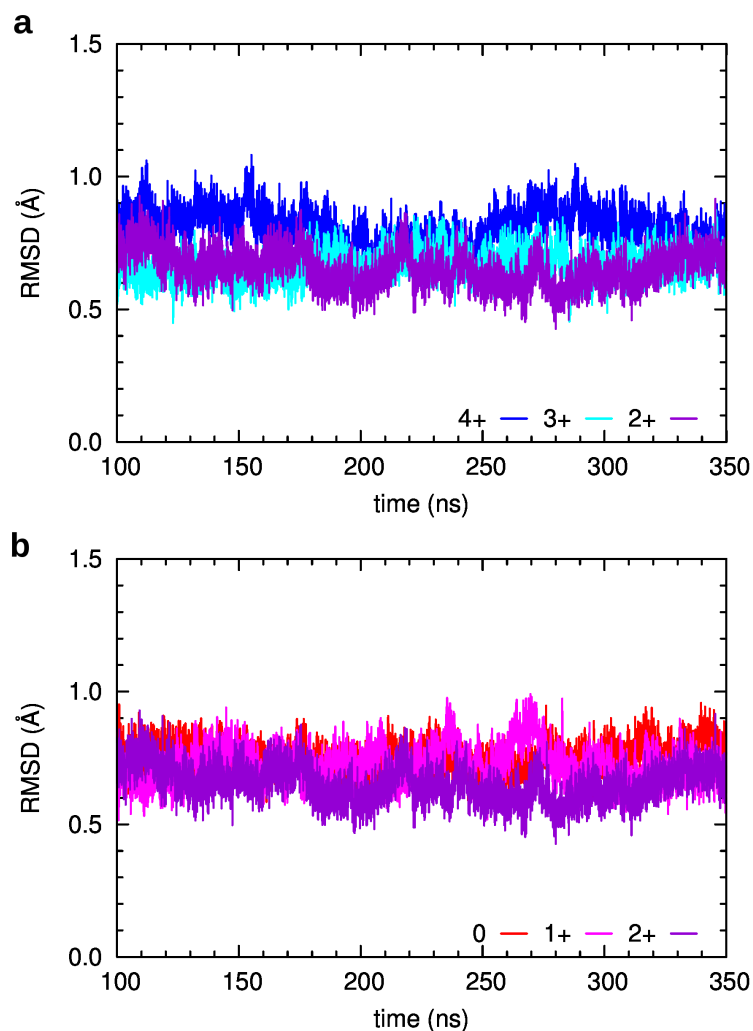


**Figure 2.15. Evolution of the root mean square deviation (RMSD) of the C $\alpha$  atoms of M2TM along the MD simulations of the S31N mutant.** RMSD is calculated with respect to the cryogenic crystal structures. **a**, RMSD for the 4+ (blue), 3+ (cyan) and 2+ (purple) states with respect to the low pH structure (PDB entry 4QKC). **b**, RMSD for neutral (red), 1+ (magenta) and 2+ (purple) states with respect to the high pH structure (PDB entry 4QK7).

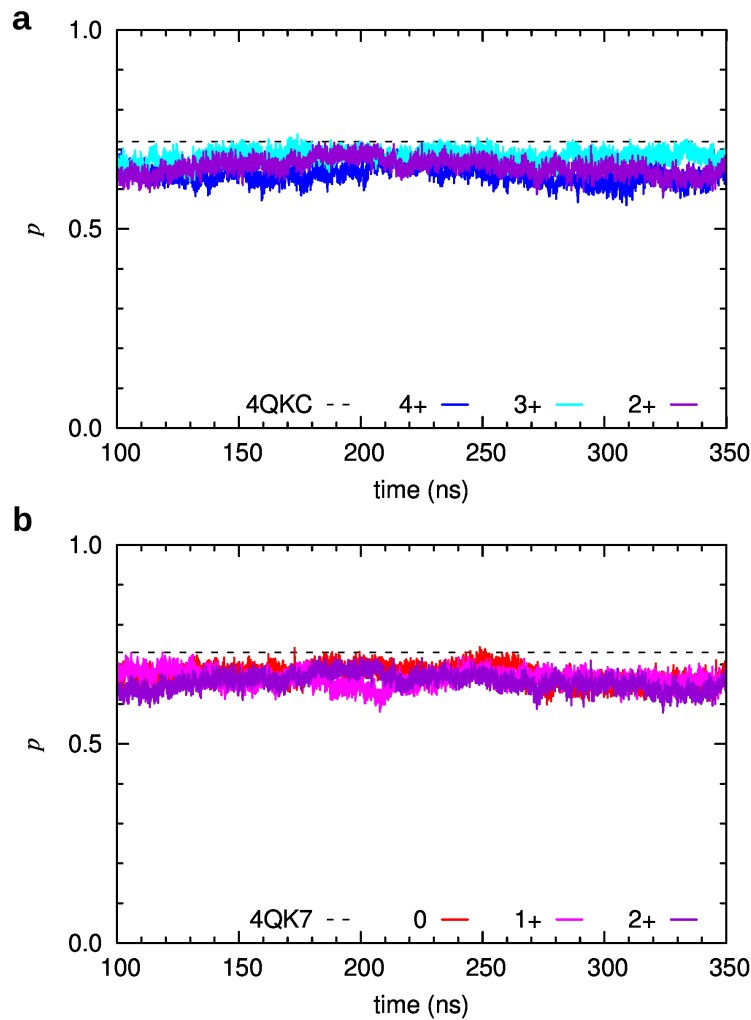


**Figure 2.16. Evolution of the principal component,  $p$ , along the MD simulations of the S31N M2TM mutant.**  $p$  describes the fraction of C-terminally closed *versus* dilated protein conformation. **a**, Principal component for the 4+ (blue), 3+ (cyan) and 2+ (purple) states; the principal component of the cryogenic crystal structure at low pH (PDB entry 4QKC) is shown as a black dashed line. **b**, Principal component for the neutral (red), 1+ (magenta) and 2+ (purple) states; the principal component of the cryogenic crystal structure at high pH (PDB entry 4QK7) is shown as a black dashed line.

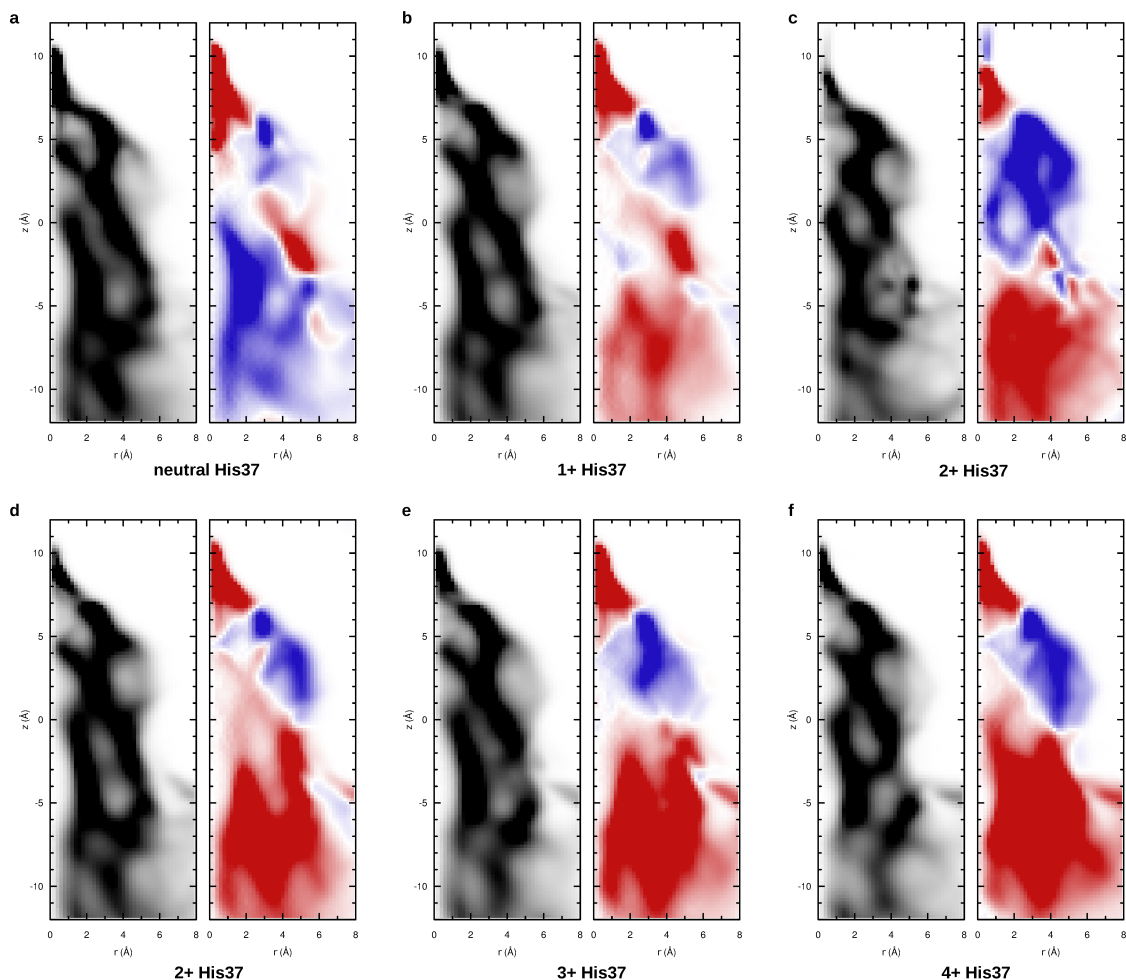


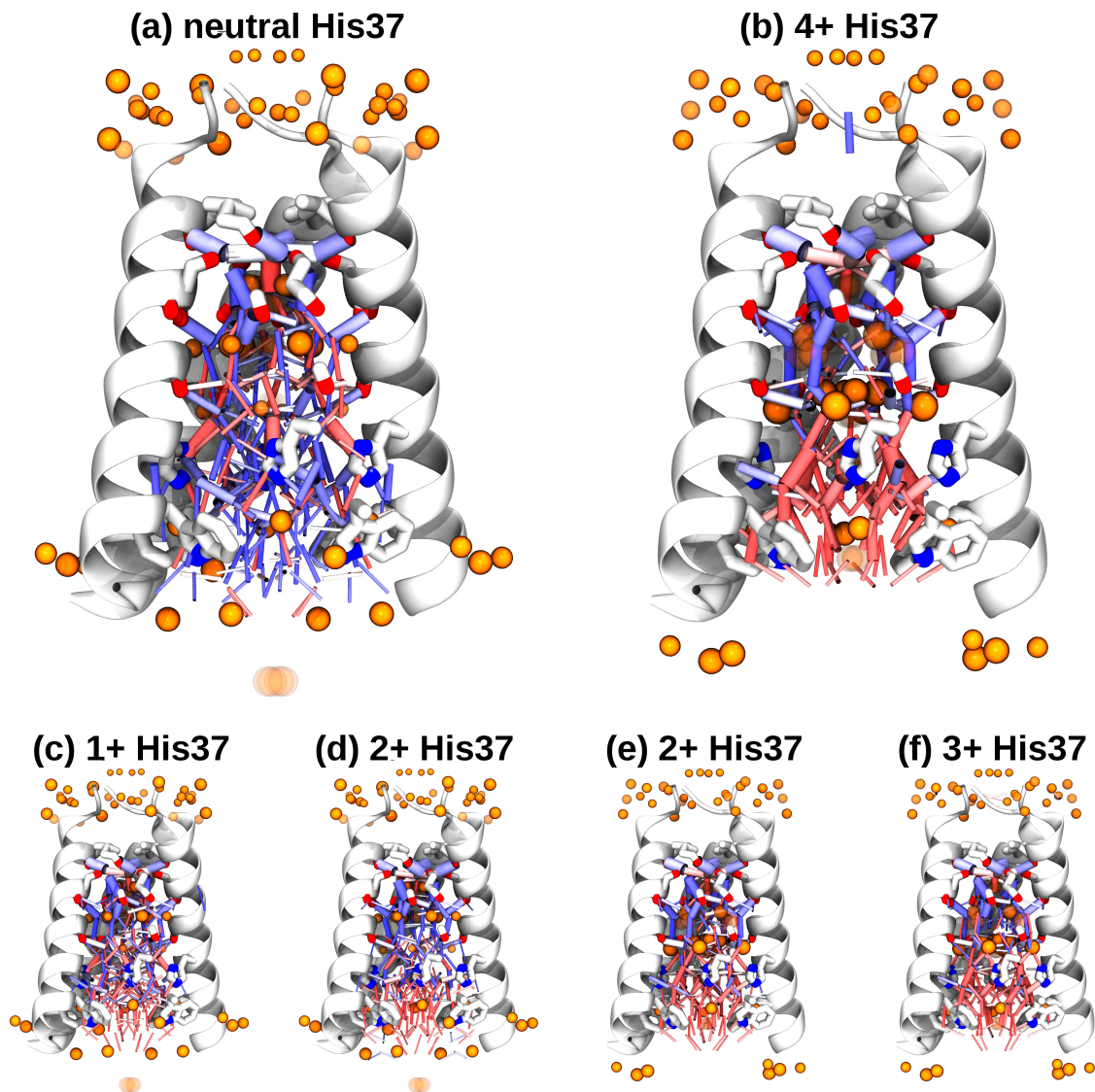
**Figure 2.17. Two-dimensional profile of the hydrogen bond vectors at different charge states of the His37 tetrad for the S31N mutant.** Shown are the density (black,  $\text{\AA}^{-3}$  units) and average orientation (red and blue,  $\text{\AA}^{-2}$  units) of hydrogen bond vectors as a function of the distance from the pore axis,  $r$ , and the displacement along the axis,  $z$ . Blue areas indicate regions populated by outward-oriented H-bonds, red denote inward-oriented H-bonds. *Top: a-c*, Density and average orientation of hydrogen bond vectors at the 0, 1+, 2+ charge states, respectively, started from the high pH cryo structure. *Bottom: d-f*, Density and average orientation of hydrogen bond vectors for at the 2+, 3+ and 4+ charge states, respectively, started from the low pH cryo structure.

**Table 2.3. Average number of hydrogen bonds in the M2 pore at different charge states of the His37 tetrad for the S31N M2 mutant.** The hydrogen bonds are classified as extraviral or intraviral depending on their position (either above or below) with respect to the His37 tetrad. The total number of hydrogen bonds is decomposed in outwards (in blue) or inwards (in red) depending on the hydrogen bond orientation (either towards the viral exterior or interior, respectively). The 4QK7-based simulations were started from the low pH cryogenic X-ray structure and the 4QKC-based from the high pH cryogenic X-ray structure.

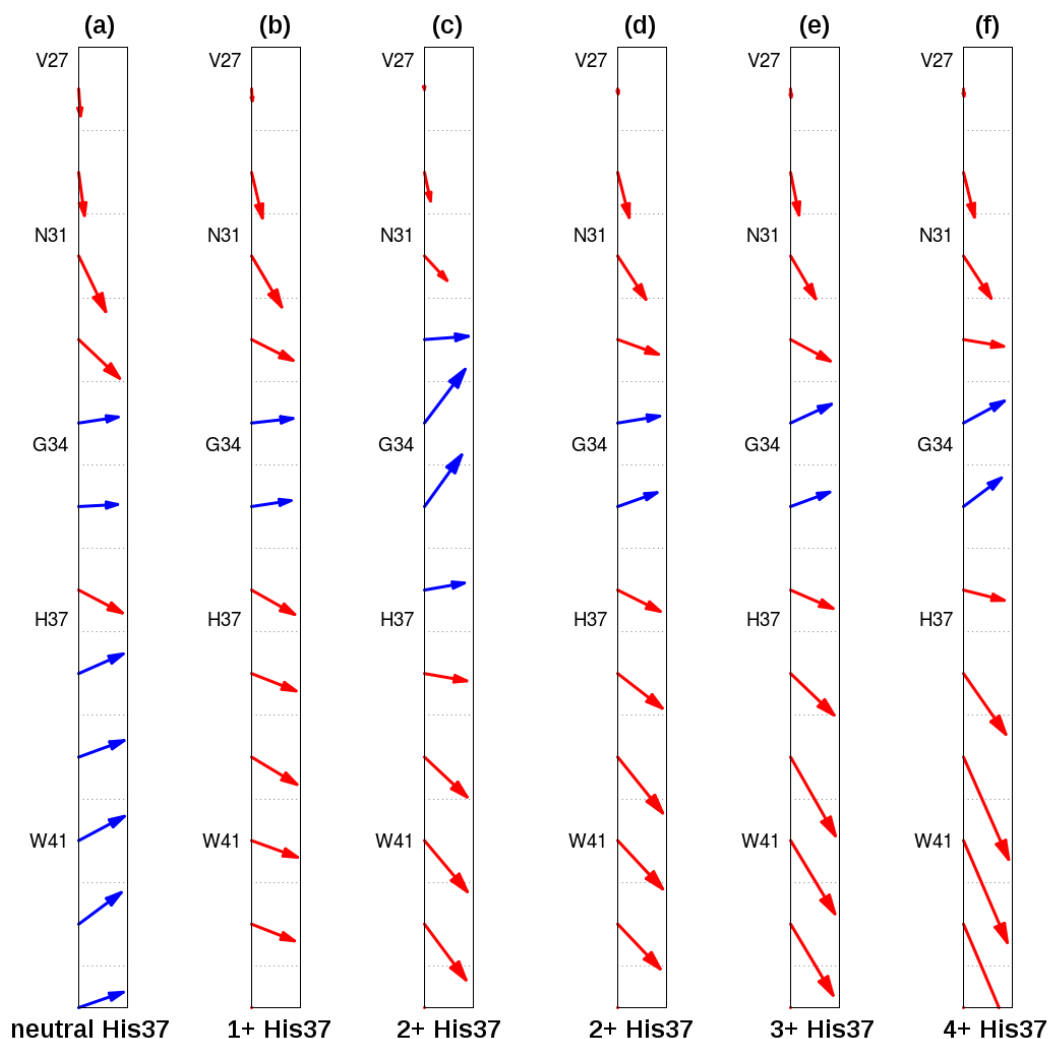
| <b>4QK7-based simulations</b>       |          | <b>neutral His37</b> | <b>1+ His37</b> | <b>2+ His37</b> |
|-------------------------------------|----------|----------------------|-----------------|-----------------|
| <b>extraviral<br/>(above His37)</b> | total    | 38.1 ± 4.8           | 39.9 ± 5.0      | 31.1 ± 4.1      |
|                                     | outwards | 18.9 ± 3.6           | 18.9 ± 3.5      | 18.4 ± 3.3      |
|                                     | inwards  | 19.4 ± 3.5           | 21.0 ± 3.9      | 12.7 ± 3.0      |
| <b>intraviral<br/>(below His37)</b> | total    | 52.5 ± 6.2           | 52.0 ± 6.5      | 46.5 ± 5.9      |
|                                     | outwards | 30.1 ± 5.1           | 22.8 ± 4.7      | 17.9 ± 4.2      |
|                                     | inwards  | 22.4 ± 4.5           | 29.2 ± 5.3      | 28.6 ± 5.1      |

| <b>4QKC-based simulations</b>       |          | <b>2+ His37</b> | <b>3+ His37</b> | <b>4+ His37</b> |
|-------------------------------------|----------|-----------------|-----------------|-----------------|
| <b>extraviral<br/>(above His37)</b> | total    | 39.5 ± 4.5      | 38.3 ± 4.4      | 35.7 ± 4.2      |
|                                     | outwards | 18.8 ± 3.4      | 18.1 ± 3.3      | 17.3 ± 3.1      |
|                                     | inwards  | 20.7 ± 3.5      | 20.2 ± 3.5      | 18.4 ± 3.4      |
| <b>intraviral<br/>(below His37)</b> | total    | 53.2 ± 6.6      | 48.6 ± 5.6      | 45.7 ± 5.7      |
|                                     | outwards | 18.9 ± 4.4      | 14.1 ± 3.8      | 10.1 ± 3.4      |
|                                     | inwards  | 34.2 ± 5.6      | 34.5 ± 5.3      | 35.6 ± 5.4      |



**Figure 2.18. Water wires calculated from the molecular dynamics simulations at different charge states of the His37 tetrad for the S31N mutant.** The oxygen atoms of the water molecules observed in the room temperature X-ray structures are shown as orange van der Waals spheres (orange color), with the diameter proportional to the crystallographic B-factors and transparency reflecting partial occupancy. Hydrogen bonds are represented as sticks, with a color scale denoting their orientation (see panels a-d), and thickness proportional to their population. **a** and **c-d**, Water wires for the 0, 1+ and 2+ charge states, respectively, for the production simulations starting from the cryogenic high pH crystal structure (PDB entry 4QK7). **b** and **d-e**, Water wires at the 4+, 2+ and 3+ charge states, respectively, for the production simulations starting from the cryogenic low pH crystal structure (PDB entry 4QKC). N.B.: the water wires of the S31N simulation are shown over the room temperature structure of wild-type M2TM, thus the residue displayed at position 31 is a serine instead of the asparagine used in the simulation.



**Figure 2.19. Average hydrogen bond vectors along the M2 pore at different charge states of the His37 tetrad for the S31N mutant.** The vector direction reflects the net orientation with respect to the pore axis, with the H-bonds pointing to the exterior of the channel (outwards) colored in blue and the ones pointing to the viral interior (inwards) in red. The vector length is proportional to the magnitude of the net hydrogen bond (i.e. the longer, the larger the preference to be oriented in that direction). The hydrogen bonds are averaged over 2 Å bins along the pore axis (delimited by dashed black lines). **a-c**, Average hydrogen bond vectors at the 0, 1+, 2+ charge states, respectively, for the production simulations starting from the high pH cryogenic crystal structure (PDB entry 4QK7). **d-f**, Average hydrogen bond vectors at the 2+, 3+, 4+ charge states, respectively, for the production simulations starting from the low pH cryogenic crystal structure (PDB entry 4QKC).

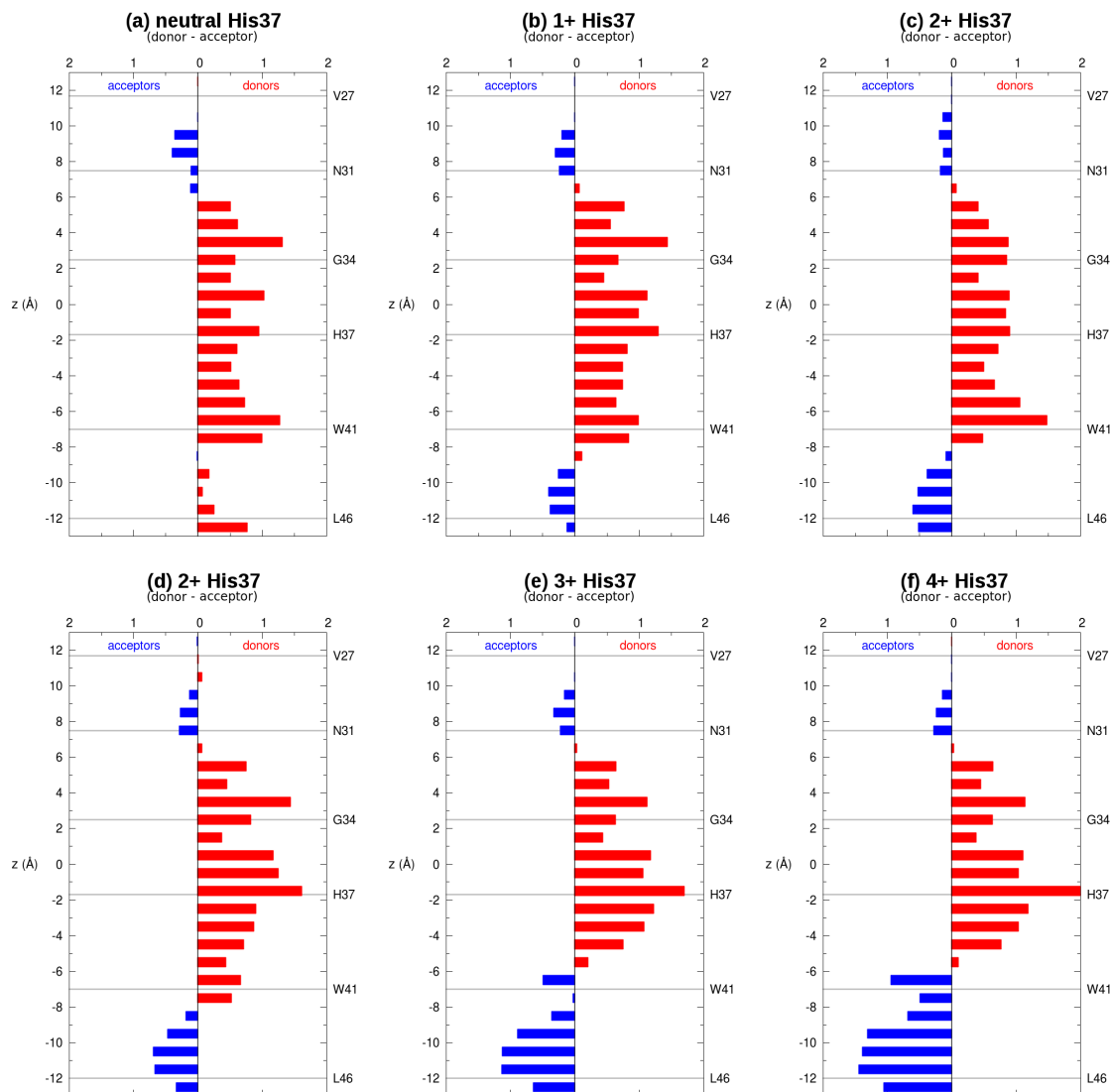


**Figure 2.20.** Difference between the number of water molecules acting as hydrogen bond donors and acceptors at different charge states of the His37 tetrad for the S31N mutant. The (*donor–acceptor*) difference along the M2 pore axis ( $z$ , in Å) is shown. Red bars represent a net number of donors at that pore position and blue bars a net number of acceptors. The position of the pore-lining M2 residues ( $C_{\alpha}$  atom of Val27, Ser31, Gly34, His37, Trp41 and Leu46) is indicated by horizontal grey lines. *Top: a–c*, Difference (*donor–acceptor*) at the 0, 1+ and 2+ charge states, respectively, for the production simulations starting from the cryogenic high pH crystal structure (PDB entry 4QK7). *d–f*, Difference (*donor–acceptor*) at the 2+, 3+ and 4+ charge states, respectively, for the production simulations starting from the cryogenic low pH crystal structure (PDB entry 4QKC).

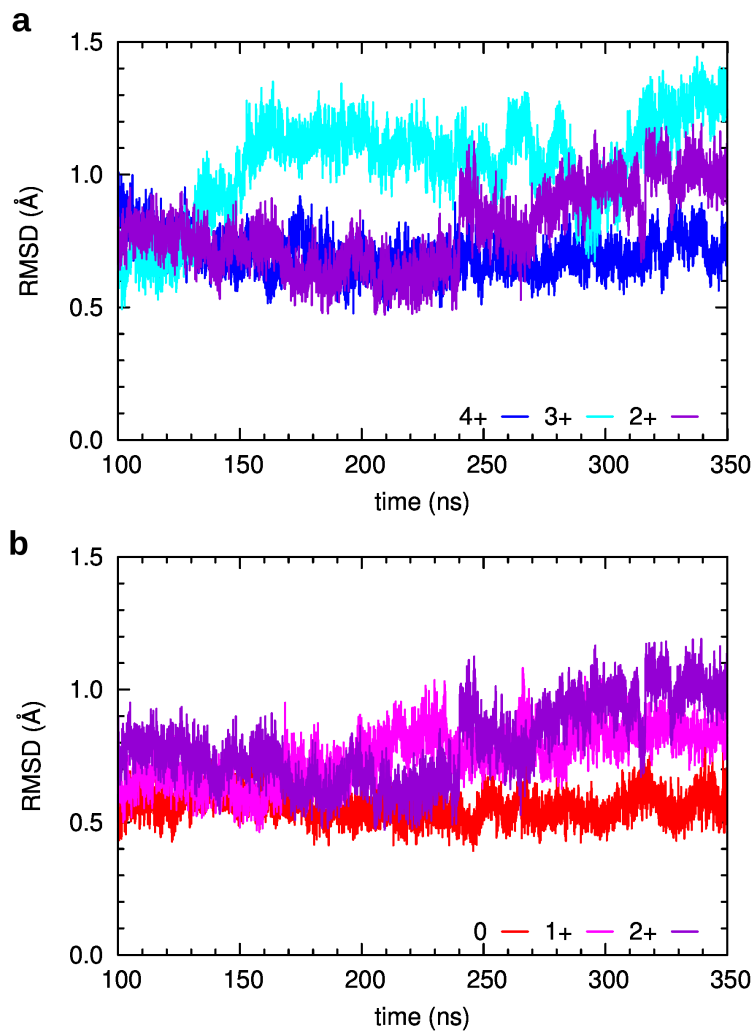


**Figure 2.21.** Evolution of the root mean square deviation (RMSD) of the C $\alpha$  atoms of M2TM along the MD simulations of the D44N mutant. RMSD is calculated with respect to the cryogenic crystal structures. **a**, RMSD for the 4+ (blue), 3+ (cyan) and 2+ (purple) states with respect to the low pH structure (PDB entry 4QKC). **b**, RMSD for neutral (red), 1+ (magenta) and 2+ (purple) states with respect to the high pH structure (PDB entry 4QK7).



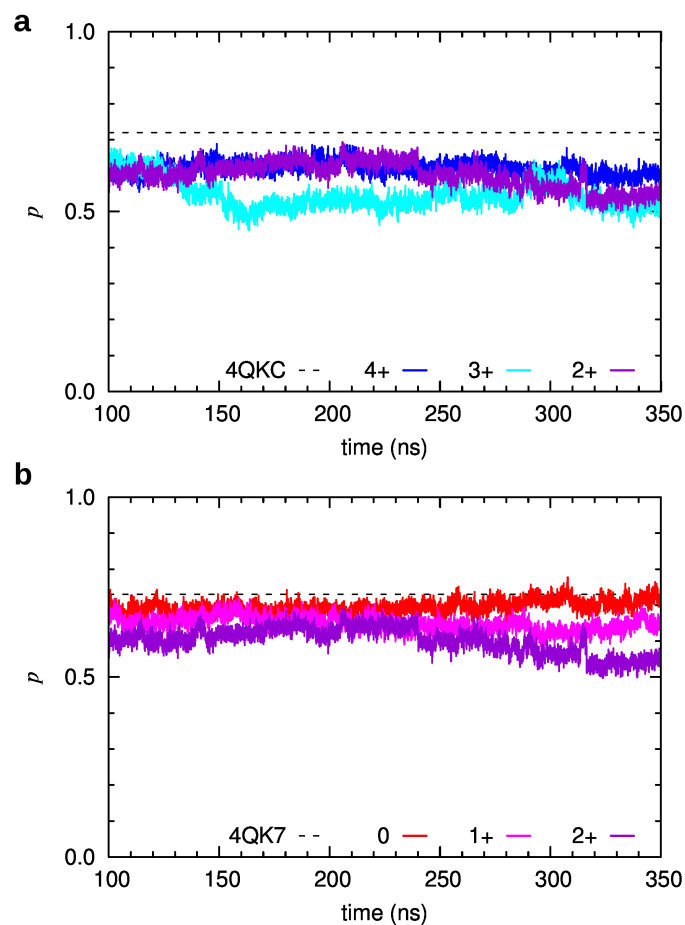


**Figure 2.22. Evolution of the principal component,  $p$ , along the MD simulations of the D44N M2TM mutant.**  $p$  describes the fraction of C-terminally closed *versus* dilated protein conformation. **a**, Principal component for the 4+ (blue), 3+ (cyan) and 2+ (purple) states; the principal component of the cryogenic crystal structure at low pH (PDB entry 4QKC) is shown as a black dashed line. **b**, Principal component for the neutral (red), 1+ (magenta) and 2+ (purple) states; the principal component of the cryogenic crystal structure at high pH (PDB entry 4QK7) is shown as a black dashed line.

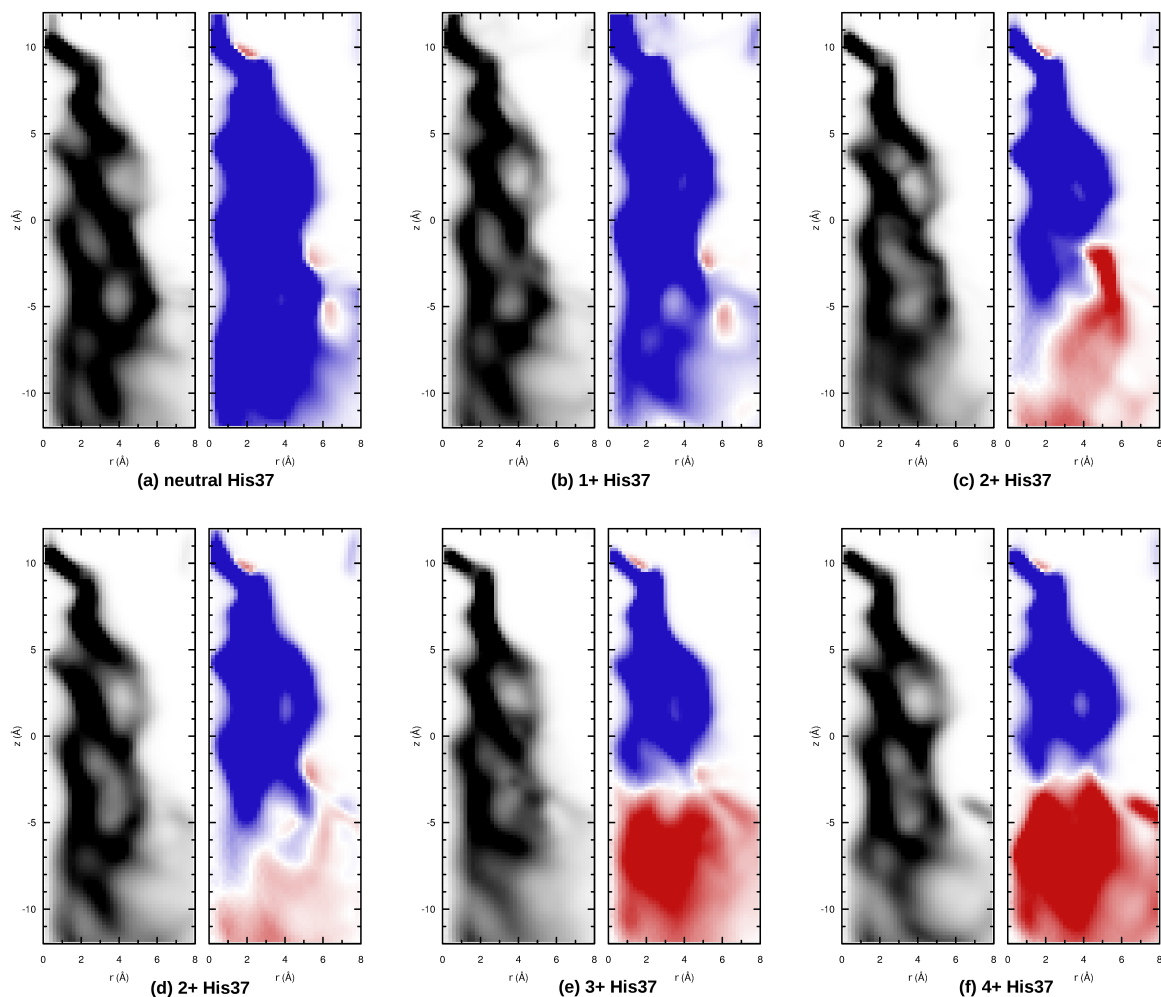


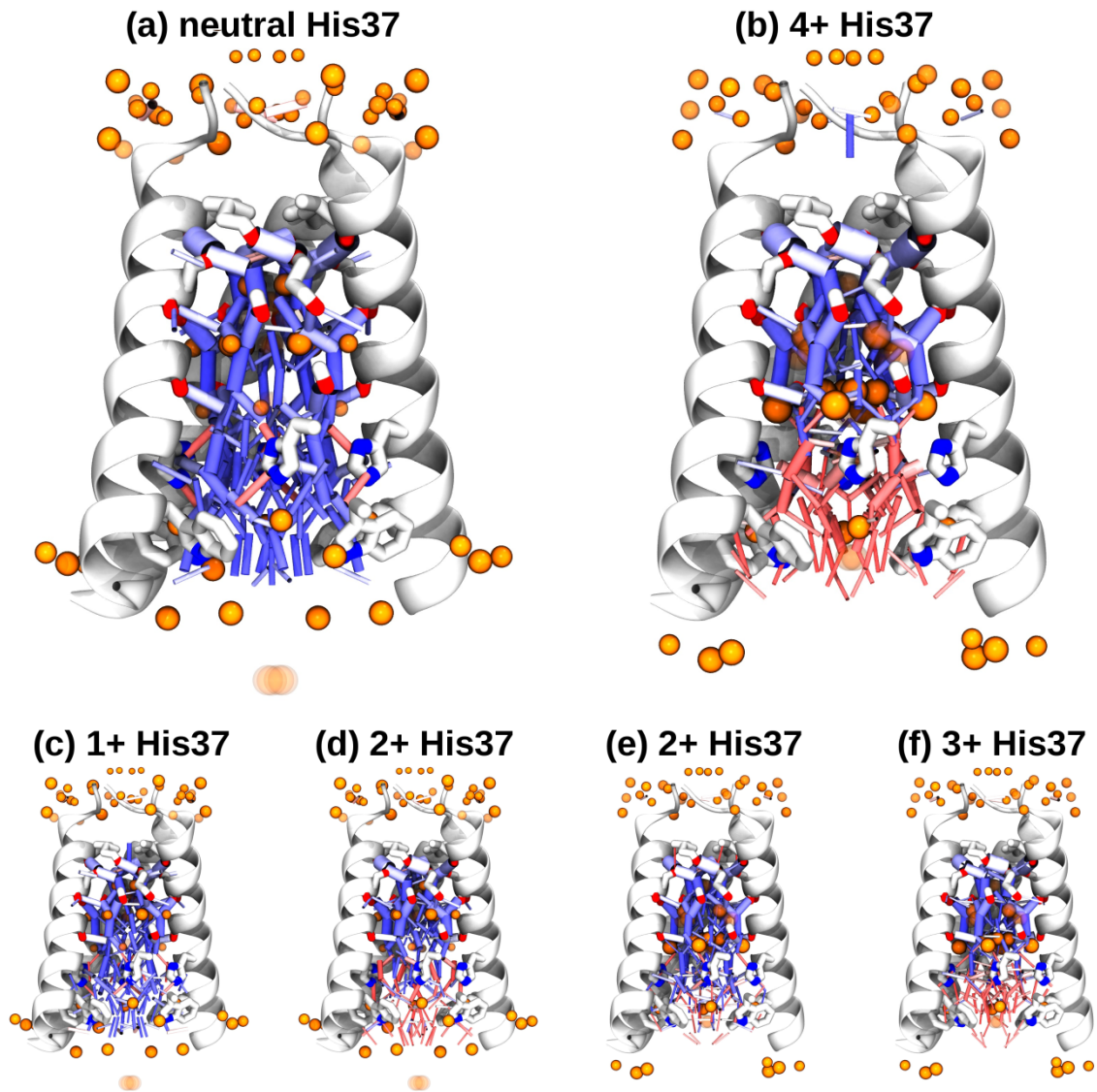
**Figure 2.23. Two-dimensional profile of the hydrogen bond vectors at different charge states of the His37 tetrad for the D44N mutant.** Shown are the density (black,  $\text{\AA}^{-3}$  units) and average orientation (red and blue,  $\text{\AA}^{-2}$  units) of hydrogen bond vectors as a function of the distance from the pore axis,  $r$ , and the displacement along the axis,  $z$ . Blue areas indicate regions populated by outward-oriented H-bonds, red denote inward-oriented H-bonds. *Top: a-c*, Density and average orientation of hydrogen bond vectors at the 0, 1+, 2+ charge states, respectively, started from the high pH cryo structure. *Bottom: d-f*, Density and average orientation of hydrogen bond vectors for at the 2+, 3+ and 4+ charge states, respectively, started from the low pH cryo structure.

**Table 2.4. Average number of hydrogen bonds in the M2 pore at different charge states of the His37 tetrad for the D44N M2 mutant.** The hydrogen bonds are classified as extraviral or intraviral depending on their position (either above or below) with respect to the His37 tetrad. The total number of hydrogen bonds is decomposed in outwards (in blue) or inwards (in red) depending on the hydrogen bond orientation (either towards the viral exterior or interior, respectively).

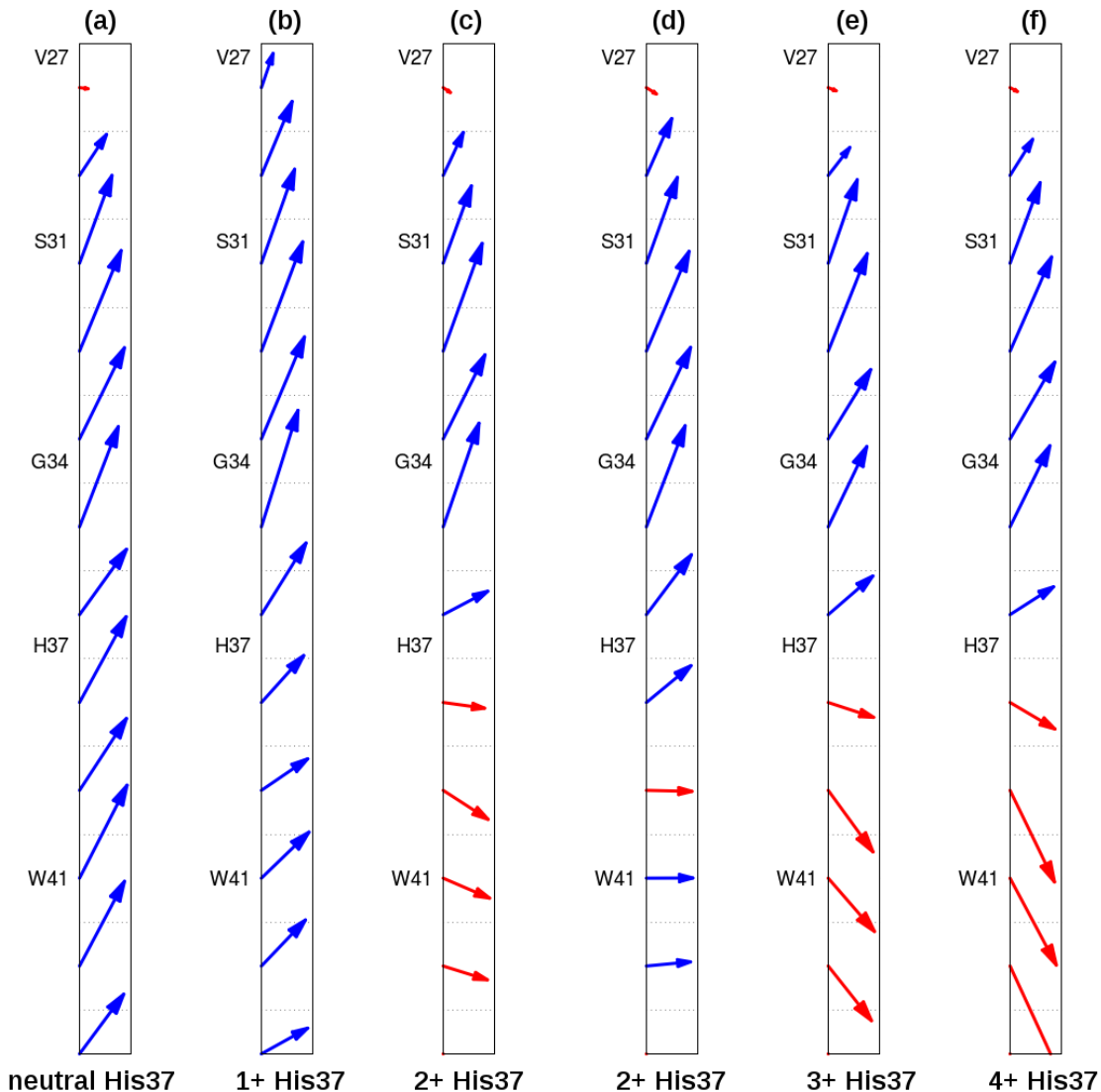
| <b>4QK7-based simulations</b>       |          | <b>neutral His37</b> | <b>1+ His37</b> | <b>2+ His37</b> |
|-------------------------------------|----------|----------------------|-----------------|-----------------|
| <b>extraviral<br/>(above His37)</b> | total    | 45.9 ± 4.9           | 41.6 ± 5.5      | 37.1 ± 4.5      |
|                                     | outwards | 36.5 ± 4.4           | 34.1 ± 4.5      | 27.2 ± 4.0      |
|                                     | inwards  | 9.4 ± 2.8            | 7.6 ± 2.9       | 9.8 ± 2.7       |
| <b>intraviral<br/>(below His37)</b> | total    | 51.9 ± 6.3           | 45.4 ± 6.7      | 42.1 ± 6.4      |
|                                     | outwards | 38.2 ± 5.2           | 27.3 ± 5.2      | 18.4 ± 4.5      |
|                                     | inwards  | 13.7 ± 3.7           | 18.1 ± 4.1      | 23.7 ± 4.5      |

| <b>4QKC-based simulations</b>       |          | <b>2+ His37</b> | <b>3+ His37</b> | <b>4+ His37</b> |
|-------------------------------------|----------|-----------------|-----------------|-----------------|
| <b>extraviral<br/>(above His37)</b> | total    | 40.5 ± 4.5      | 38.3 ± 4.6      | 40.5 ± 4.5      |
|                                     | outwards | 31.4 ± 4.1      | 26.6 ± 4.0      | 28.3 ± 4.0      |
|                                     | inwards  | 9.1 ± 2.7       | 11.7 ± 3.0      | 12.2 ± 3.0      |
| <b>intraviral<br/>(below His37)</b> | total    | 48.1 ± 5.9      | 42.4 ± 6.0      | 49.0 ± 6.1      |
|                                     | outwards | 23.5 ± 4.3      | 14.5 ± 4.0      | 13.1 ± 3.8      |
|                                     | inwards  | 24.6 ± 4.9      | 27.8 ± 5.2      | 35.9 ± 5.7      |



**Figure 2.24. Water wires calculated from the molecular dynamics simulations at different charge states of the His37 tetrad for the D44N mutant.** The oxygen atoms of the water molecules observed in the room temperature X-ray structures are shown as orange van der Waals spheres (orange color), with the diameter proportional to the crystallographic B-factors and transparency reflecting partial occupancy. Hydrogen bonds are represented as sticks, with a color scale denoting their orientation (see panels a-d), and thickness proportional to their population. **a** and **c-d**, Water wires for the 0, 1+ and 2+ charge states, respectively, for the production simulations starting from the cryogenic high pH crystal structure (PDB entry 4QK7). **b** and **d-e**, Water wires at the 4+, 2+ and 3+ charge states, respectively, for the production simulations starting from the cryogenic low pH crystal structure (PDB entry 4QKC).



**Figure 2.25. Average hydrogen bond vectors along the M2 pore at different charge states of the His37 tetrad for the D44N mutant.** The vector direction reflects the net orientation with respect to the pore axis, with the H-bonds pointing to the exterior of the channel (outwards) colored in blue and the ones pointing to the viral interior (inwards) in red. The vector length is proportional to the magnitude of the net hydrogen bond (i.e. the longer, the larger the preference to be oriented in that direction). The hydrogen bonds are averaged over 2 Å bins along the pore axis (delimited by dashed black lines). **a-c**, Average hydrogen bond vectors at the 0, 1+, 2+ charge states, respectively, for the production simulations starting from the high pH cryogenic crystal structure (PDB entry 4QK7). **d-f**, Average hydrogen bond vectors at the 2+, 3+, 4+ charge states, respectively, for the production simulations starting from the low pH cryogenic crystal structure (PDB entry 4QKC).

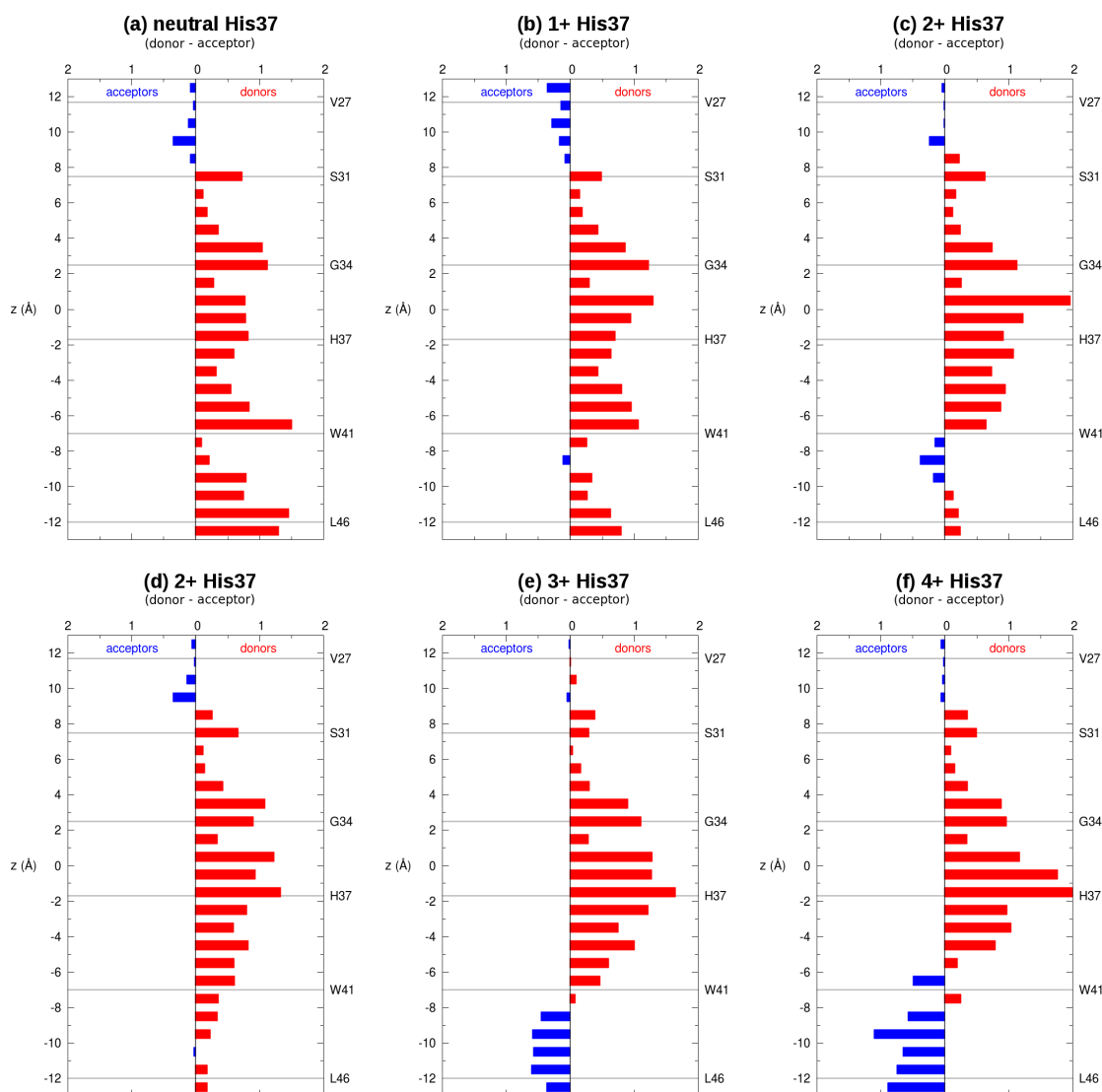


**Figure 2.26.** Difference between the number of water molecules acting as hydrogen bond donors and acceptors at different charge states of the His37 tetrad for the D44N mutant. The (*donor–acceptor*) difference along the M2 pore axis ( $z$ , in Å) is shown. Red bars represent a net number of donors at that pore position and blue bars a net number of acceptors. The position of the pore-lining M2 residues ( $C_{\alpha}$  atom of Val27, Ser31, Gly34, His37, Trp41 and Leu46) is indicated by horizontal grey lines. **Top: a-c**, Difference (*donor–acceptor*) at the 0, 1+ and 2+ charge states, respectively, for the production simulations starting from the cryogenic high pH crystal structure (PDB entry 4QK7). **d-f**, Difference (*donor–acceptor*) at the 2+, 3+ and 4+ charge states, respectively, for the production simulations starting from the cryogenic low pH crystal structure (PDB entry 4QKC).

**Table 2.5. Comparison of the C $\alpha$  RMSD and  $p$  values along the MD simulations of wild-type, S31N and D44N M2TM.**

| <i>4QKC-based simulations</i> |                 |                 |                 |
|-------------------------------|-----------------|-----------------|-----------------|
| <b>RMSD (Å)</b>               | <b>2+ His37</b> | <b>3+ His37</b> | <b>4+ His37</b> |
| <b>wild-type</b>              | 0.77 ± 0.07     | 0.63 ± 0.06     | 0.76 ± 0.07     |
| <b>S31N</b>                   | 0.65 ± 0.07     | 0.67 ± 0.06     | 0.81 ± 0.07     |
| <b>D44N</b>                   | 0.79 ± 0.15     | 1.04 ± 0.18     | 0.70 ± 0.07     |
| <b><math>p</math></b>         | <b>2+ His37</b> | <b>3+ His37</b> | <b>4+ His37</b> |
| <b>wild-type</b>              | 0.60 ± 0.02     | 0.67 ± 0.02     | 0.63 ± 0.02     |
| <b>S31N</b>                   | 0.66 ± 0.02     | 0.68 ± 0.02     | 0.64 ± 0.02     |
| <b>D44N</b>                   | 0.60 ± 0.04     | 0.55 ± 0.04     | 0.62 ± 0.02     |

| <i>4QK7-based simulations</i> |                      |                 |                 |
|-------------------------------|----------------------|-----------------|-----------------|
| <b>RMSD (Å)</b>               | <b>neutral His37</b> | <b>1+ His37</b> | <b>2+ His37</b> |
| <b>wild-type</b>              | 0.75 ± 0.13          | 0.75 ± 0.07     | 1.09 ± 0.09     |
| <b>S31N</b>                   | 0.76 ± 0.06          | 0.72 ± 0.07     | 1.27 ± 0.08     |
| <b>D44N</b>                   | 0.56 ± 0.06          | 0.75 ± 0.10     | 0.65 ± 0.07     |
| <b><math>p</math></b>         | <b>2+ His37</b>      | <b>3+ His37</b> | <b>4+ His37</b> |
| <b>wild-type</b>              | 0.60 ± 0.02          | 0.67 ± 0.02     | 0.63 ± 0.02     |
| <b>S31N</b>                   | 0.66 ± 0.02          | 0.68 ± 0.02     | 0.64 ± 0.02     |
| <b>D44N</b>                   | 0.60 ± 0.04          | 0.55 ± 0.04     | 0.62 ± 0.02     |

## 2.10 Appendix B Detailed Methods

*2.10.1 Synthesis and purification of M2(22-46).* The peptide construct used in this study is M2(22-46) from influenza A/Udorn/307/1972 . The peptide was synthesized on Rink Amide resin using a Quest 210 peptide synthesizer (Argonaut Technologies) at a temperature of 75°C for deprotection and coupling steps. Each residue was deprotected in a solution of 5% w/w piperazine and 0.1 M HOBt. For each coupling reaction, 5 molar equivalents of amino acid were pre-activated with 5 equivalents of HCTU and 10 equivalents of DIEA then this pre-activated mixture was added to the resin. After all of the amino acids were added to the resin, the reaction was cooled to 20°C and the N-terminus of the peptide was acylated by the addition of 20 equivalents of acetic anhydride and 40 equivalents of DIEA. The resin was washed with DCM and hexane then the peptide was cleaved from the resin in a mixture of 94% v/v TFA, 5% TES, and 1% H<sub>2</sub>O. The resin was filtered out from the peptide-containing cleavage solution and washed with TFA, the excess TFA was blown off with a stream of nitrogen gas, then the peptide was precipitated into ether that had been chilled with dry ice. The mass of the resulting cleavage products was then confirmed by MS on a 3200 Q Trap LC/MS/MS (AB Sciex).

The peptide was purified using reverse-phase HPLC on a Varian ProStar purification system using a PROTO300 C4 10  $\mu$ m column (Higgins Analytical Inc.). A gradient combining buffers A (99.9% water and 0.1% TFA) and B' (60% isopropanol, 30% acetonitrile, 10% water, 0.1% TFA) was used to separate and elute the peptide. A high degree of purity was necessary for the crystallization trials; analytical HPLC was used to confirm the degree of purity. The fractions of purified peptide were pooled and dissolved in ethanol. The concentration of peptide in the ethanol stock was determined by measuring the sample's absorbance at 280nm, then the stock solutions of peptide dissolved in ethanol were stored at -80°C.



*2.10.2 Preparation of the lipid cubic phase and crystallization.* The lipid cubic phase was prepared with some modifications to the protocol described by Caffrey and Cherezov.<sup>49</sup> Peptide stock containing  $4.0 \times 10^{-7}$  moles of peptide in ethanol was added to 60mg of monoolein, mixed, then lyophilized overnight. The resulting peptide/monoolein mixture was warmed to 40°C in a water bath and transferred to a gas-tight Hamilton 250  $\mu$ L syringe. 50 mM octylglucopyranoside (OG) in water was added into the syringe at a ratio of 20  $\mu$ L for every 30 mg transferred sample, then the sample was then re-heated to 40°C and connected to a second gas-tight Hamilton syringe using a metal syringe coupler. The sample was pushed back and forth through the syringe coupler to mix; the appearance of the sample became transparent and homogenous after 1-2 minutes of transfer between the two syringes via the syringe coupler.

Crystallization conditions were screened in 96-well plastic plates (Molecular Dimensions) that were set up with a LCP crystallization robot (TTP Labtech) using a protocol that combined 100 nL of monoolein/peptide sample with 1000 nL of screening solution. Square-shaped crystals belonging to space group  $I_4$  formed after 2-4 weeks of incubation at 10°C. These conditions were optimized to grow 20-120  $\mu$ m large crystals using the Hampton Additive screen. The crystals used for data collection at cryogenic conditions were grown in 96-well plates at 10°C then observed and harvested into liquid nitrogen in a 4°C cold room. The conditions that yielded the cryo high pH structure were: 0.18 M  $\text{CaCl}_2$ , 0.09 M Tris pH 8.0, 39.6% v/v PEG 400, 0.01 M  $\beta$ -nicotinamide adenine dinucleotide hydrate additive; the conditions that yielded the cryo low pH structure were: 0.18 M  $\text{CaCl}_2$ , 0.09 M MES pH 5.5, 39.6% v/v PEG 400, 5% v/v Jeffamine M-600 pH 7.0 additive in the presence of amantadine at a 4:1 ratio of Amt to tetramer, though density for the amantadine was not present in the crystal structure under these conditions and low pH crystals without amantadine yielded the same

structure but at slightly lower resolution. Because of the high percentage of PEG 400 in the solution, no additional cryoprotectant was added before the crystals were frozen and stored in liquid nitrogen. The crystals used for room temperature data were grown in 96-well plates at 20°C then were observed, transported to the beam line and harvested at ambient temperature. The conditions that yielded the room temperature high pH structure were: 0.18 M CaCl<sub>2</sub>, 0.09 M Tris pH 8.0, 39.6% v/v PEG 400, 3% w/v xylitol additive; the conditions that yielded the room temperature low pH structure were: 0.18 M CaCl<sub>2</sub>, 0.09 M MES pH 5.5, 39.6% v/v PEG 400, 0.01 M MnCl<sub>2</sub> · 4H<sub>2</sub>O additive.

*2.10.3 Data collection.* All crystallographic data was collected at the Advanced Light Source on beam 8.3.1. The beam size was 100 μm for all data sets; the detector used was a 3 x 3 CCD array (ADSC Q315r). Data from the two cryo condition crystals that diffracted to 1.1 Å were collected at a temperature of < 100K with a 13.0 keV beam and a detector-to-sample distance of 125 mm. The high pH cryo condition crystal (PDB entry 4QK7) was exposed to the beam for 6 seconds per frame and the low pH cryo condition crystal (PDB entry 4QKC) was exposed for 4 seconds per frame; both crystals were oscillated 1 degree during data collection. The room temperature data was collected at 273 K using room temperature data collection techniques; with a 11.111 keV beam and an aluminum foil attenuator for both data sets. The crystals were looped at the beam line and a MiTeGen MicroRT plastic capillary containing 8 μL of precipitant solution mixed with 2 μL deionized water was placed on top of the goniometer base to hydrate the crystals during data collection. The crystals accumulated radiation damage faster under room temperature diffraction conditions, so larger crystals (50-120 μm) were diffracted to obtain complete data sets. The low pH room temperature condition crystal (PDB entry 4QKM) was

exposed to the beam for 3 seconds per frame with a detector-to-sample distance of 125 mm; the high pH room temperature condition crystal (PDB entry 4QKL) was exposed to the beam for one second per frame with a detector-to-sample distance of 150 mm; both crystals were oscillated 1 degree during data collection. The data used to solve the room temperature structures was limited to the first 60 frames to minimize the effects of radiation damage on data quality.

*2.10.4 Data processing, phasing, and refinement.* Data processing was done in iMosflm.<sup>50</sup> Phasing was done by molecular replacement in the Phenix suite using Phaser MR<sup>51</sup> with chain A from PDB entry 3C9J<sup>8</sup> as a search model, then refinement was carried out in Phenix Refine.<sup>17</sup> Protein model manipulation and addition of water and ions were done in Coot,<sup>52</sup> and monoolein molecules were manually fit into Fo-Fc density using both Coot and PyMol.<sup>41</sup> Alternate conformers were predicted using the qFit web server<sup>42</sup> and Ringer,<sup>39</sup> and were also manually added where positive Fo-Fc density indicated they were present. Anisotropic B-factors were used for both cryo conditions (PDB entries 4QK7 and 4QKC) and the low pH room temp condition (PDB entry 4QKM) but not the high pH room temp condition (PDB entry 4QKL).

*2.10.5 Molecular dynamics simulation details.* Classical molecular dynamics (MD) simulations of the hydrated protein crystal were performed to study the network of water molecules confined inside the M2 pore and its response to pH changes (i.e. the protonation state of His37). The initial configurations were built using the two cryo X-ray structures of the transmembrane region of the M2 bundle (M2TM, spanning residues 22-46) reported in this work (4QK7 and 4QKC, at high and low pH, respectively). In order to model the  $I_4$  symmetry of the crystal, two staggered tetramers were included in the simulation box (see **SI Fig. 2.7**), as well as the

crystallographically resolved water molecules, monoolein molecules and calcium and chloride ions. Each of the four cryoprotectant molecules found inside the pore in the X-ray structures was replaced by two water molecules, occupying the same position of the two hydroxyl groups of ethylene glycol. The disordered lipid phase was modeled as heptane, which provides a hydrophobic phase similar to monoolein with the advantage of faster equilibration, in the spirit of the highly mobile membrane mimetic used in another study.<sup>10</sup> A thin layer of water molecules was also added to fill out the unresolved hydrophilic region between the two tetramers, along with additional chloride ions to achieve neutrality. Simulations were performed starting from either the structure solved at low pH or the one at high pH (pH 5.5 and 8.0, respectively) for the five possible protonation states of the His37 tetrad (0, +1, +2, +3 and +4). The neutral histidine residues were set in the  $\epsilon$ -tautomeric state and the histidine charge was increased by protonating one, two (non-adjacent), three or all four histidines, respectively, for each of the two tetramers. Each of the ten resulting systems consists of  $\sim 7,000$  atoms.

The protein was modeled using the CHARMM force field<sup>11,12</sup> with CMAP corrections<sup>13</sup> and the water molecules were described using the TIP3P model.<sup>14</sup> The parameters by Roux and coworkers were used for the chloride<sup>15</sup> and calcium<sup>16</sup> ions. The heptane parameters were taken from the alkane force field.<sup>17,18</sup> Monoolein was parameterized using the CHARMM General Force Field (CGenFF, version 2b7)<sup>19</sup> and the ParamChem server (version 0.9.6 beta).<sup>20-22</sup>

The simulations were performed in the NVT ensemble using the measured crystal lattice dimensions (29.310 Å x 29.310 Å x 67.310 Å for the low pH structure and 29.536 Å x 29.536 Å x 66.853 Å for the high pH) and applying periodic boundary conditions to mimic the crystal environment. Electrostatic interactions were calculated using the particle mesh Ewald (PME) method,<sup>23</sup> with a real space spherical cutoff of 12 Å, an accuracy threshold of  $10^{-6}$  and a fast

Fourier transform (FFT) grid spacing of 0.8 Å (x and y dimensions) or 0.9 Å (z). Lennard-Jones interactions were cut off at 12 Å, with a switching function starting from 10 Å. The equations of motion were solved with the velocity Verlet integrator using a time step of 1.0 fs (equilibration) or 2.0 fs (production runs). The lengths of the bonds involving hydrogen atoms were constrained with the SHAKE method.<sup>24</sup> Each system was run at 310 K using a Langevin temperature coupling scheme,<sup>25</sup> with a thermostat decay time of 1 ps.

The low pH and high pH structures (in the +4 and 0 protonation states, respectively) were pre-equilibrated for ~20 ns by applying harmonic restraining potentials on the position of the non-hydrogen atoms of the peptide backbone, the monoolein molecules and the crystallographic water and ions. The force constant (k) of the harmonic restraints was progressively reduced (from 20 to 2 kcal mol<sup>-1</sup> Å<sup>-2</sup> for the protein, from 10 to 4 kcal mol<sup>-1</sup> Å<sup>-2</sup> for the crystallographic water molecules and from 10 to 1 kcal mol<sup>-1</sup> Å<sup>-2</sup> for the other X-ray-derived moieties) in 0.5 ns steps. The resulting pre-equilibrated configurations of the 4+ and 0 states were used to build the initial models for the other protonation states. Upon change of the His 37 charge, each system was relaxed for ~10 ns using harmonic restraining potentials (with k = 2 kcal mol<sup>-1</sup> Å<sup>-2</sup> for the protein backbone, 4 kcal mol<sup>-1</sup> Å<sup>-2</sup> for the crystallographic water molecules and 1 kcal mol<sup>-1</sup> Å<sup>-2</sup> for monoolein and the X-ray derived ions). Then all harmonic restraints were released<sup>26</sup> and a production trajectory of ~300-450 ns was sampled for each system. All the MD simulations were performed with NAMD (version 2.9)<sup>27</sup> The stability of the tetramer along the MD simulations was confirmed by examining the root mean square deviation (RMSD) of the Cα atoms (see **SI Fig. 2.8**).

Setup of the S31N mutant simulations: Classical MD simulations were performed for the S31N mutant of M2TM in order to assess the effect of the mutation in the number and directionality of the water wires inside the M2 pore. S31N is the most prevalent M2 mutation in circulating viruses and confers amantadine resistance while retaining conduction properties similar to wild-type M2. The initial configurations were built using equilibrated snapshots of the wild-type simulations and mutating *in silico* the residue at position 31 from serine to asparagine. The asparagine side chain was initialized in the same rotameric state as the NMR structure of the M2TM complex with thiophenyl-isoxazole-amantadine ( $\chi_1 \approx -70^\circ$  and  $\chi_2 \approx -30^\circ$ ; PDB code 2LY0). However, after a few nano seconds, it rotates and adopts a different rotameric state, with the amide group perpendicular to the pore axis ( $\chi_1 \approx -80^\circ$  and  $\chi_2 \approx -90^\circ$ ), and this conformation remains stable for the rest of the simulation.

The details of the classical MD simulations of the S31N mutant are identical to the wild-type. S31N M2TM was considered in each of the 5 possible protonation states of the His37 tetrad (0, 1+, 2+, 3+ and 4+). After an initial 20 ns equilibration with the protein backbone restrained, a production trajectory was sampled for 330 ns; only the last 250 ns were considered for the analysis. The stability of the mutant along the MD simulations was confirmed by examining the RMSD of the C $\alpha$  atoms (**SI Fig. 2.15**). Moreover, the protein conformation was maintained during the MD simulations, as can be seen by the stability of the principal component *p* (**SI Fig. 2.16**).

Setup of the D44N mutant simulations: Classical MD simulations were performed for the D44N mutant of M2TM in order to assess the effect of the loss of this C-terminal negative charge on the number and directionality of the water wires inside the M2 pore. The D44N mutation is

present in the A/FPV/Rostock/34 influenza strain and results in enhanced proton conduction and loss of its asymmetry.<sup>28</sup> Moreover, in contrast to the S31N mutant, the D44N mutant is still sensitive to amantadine, since this residue is located far from the drug binding site.

The initial configurations were built using equilibrated snapshots of the wild-type simulations and mutating *in silico* the residue at position 44 from aspartate to asparagine using the *Mutator* plugin of VMD.<sup>32</sup> Four chloride ions were also added for each tetramer in order to maintain neutrality. The details of the classical MD simulations of the D44N mutant are identical to the wild-type. D44N M2TM was considered in each of the 5 possible protonation states of the His37 tetrad (0, 1+, 2+, 3+ and 4+). After an initial 20 ns equilibration with the protein backbone restrained, a production trajectory was sampled for 330 ns; only the last 250 ns were considered for the analysis. The stability of the mutant along the MD simulations was confirmed by examining the RMSD of the C $\alpha$  atoms (**SI Fig. 2.21**). In addition, the partially dilated C-terminal protein conformation was maintained during the MD simulations (**SI Fig. 2.22**). The larger fluctuations of the protein backbone compared to the wild-type and the S31N mutant simulations (Table S5) are probably due to the modification of the protein-protein contacts of the crystal lattice, in which residue 44 is involved. Nevertheless, the structure of D44N M2TM is not significantly altered compared to the wild-type.

Analysis of the MD simulations: *Principal component analysis*. The protein backbone conformation of the crystallographic structures presented in this work lies between the C-terminal closed and dilated structures previously solved by X-ray or NMR (see main text). To characterize the backbone conformation of M2TM, we used the principal component  $p$  introduced in reference.<sup>28</sup> In short, we computed difference vectors between each of the

cryostructures in this work (either at low or at high pH, PDB entries 4QKC and 4QK7, respectively) and the X-ray structure solved at intermediate pH by Acharya and coworkers (PDB entry 3LBW),<sup>29</sup> using the backbone coordinates of M2TM. Then we calculated the scalar product of this vector and the difference vector between the same intermediate pH structure<sup>29</sup> and the X-ray structure solved at low pH by Stouffer et al. (PDB entry 3C9J).<sup>30</sup> The resulting quantity is the principal component  $p$  and it indicates the fraction of C-terminally closed *versus* dilated conformation of each of the two cryostructures. The obtained  $p$  values are 0.72 (low pH) and 0.73 (high pH), indicating that the C-terminus of the current M2TM structures is partially dilated. Moreover, the partially dilated protein conformation is maintained during the MD simulations, as can be shown by the stability of  $p$  as a function of simulation time in **SI Fig. 2.9**.

*Water densities.* Water densities were obtained from the MD simulations using the Volmap plugin<sup>31</sup> in VMD (version 1.9).<sup>32</sup> Each water atom was treated as a normalized isotropic Gaussian density of width equal to 0.532 Å (oxygen) or 0.42 Å (hydrogen), that is their van der Waals radius scaled by 0.35. This radius scaling factor was chosen empirically by applying the Volmap plugin on the recently solved 0.88 Å resolution crystal structure of aquaporin;<sup>33</sup> the calculated density reproduces the experimental density when scaling the atomic radii by 0.35. Besides, this is in line with the electron density of water in simulations being 0.34 e Å<sup>3</sup> for TIP3P waters.<sup>34</sup> The density was weighted by the atomic number ( $z = 8$  or 1, respectively) and summed over all the pore waters using a three dimensional grid with a 0.25 Å bin resolution. The time average was taken over the last ~250 ns of the MD trajectories. Four-fold rotational symmetry was enforced by recalculating the water density after each of the four 90 degree rotations along the pore axis of the homotetramer and averaging the four resulting density maps. The obtained MD water densities are shown in **Fig. 2.4a** and **SI Fig. 2.6**.



*Populations of hydrogen bonds in the M2 pore.* We calculated the populations of hydrogen-bonded water molecules using the following clustering protocol. We defined a hydrogen-bond vector between a donor and an acceptor when the two oxygen atoms are at a distance less than 3.5 Å and the donor-hydrogen-acceptor angle is between 150°-180°. Four-fold rotational symmetry was enforced by recalculating the hydrogen-bond vectors after each of the four 90 degree rotations along the pore axis of the homotetramer. We calculated the clusters of these vectors using g\_cluster (version 4.5.5)<sup>35</sup> over ~250 ns-long MD trajectories (i.e. the first 100 ns were considered as equilibration and discarded). We used a cutoff equal to 1.5 Å to define hydrogen bond vectors as belonging to the same cluster. To obtain the occupancy of a hydrogen bond represented by the centroid of one cluster, we divided the population of the cluster by the total number of MD frames and by 4 (to normalize upon symmetrization), such that the occupancy of a given hydrogen bond is at most 1. Fig. 2.5 and SI Fig. 2.11 are produced by drawing cylinders corresponding to each cluster, with the thickness determined by the corresponding occupancy and the color indicating the orientation (blue for hydrogen bonds oriented towards the exterior of the channel and red if oriented towards the viral interior, see **SI Fig. 2.11**). These figures were made with the VMD program (version 1.9).<sup>32</sup>

*Density and orientation of hydrogen bonds.* The density (in Å<sup>-3</sup>) and orientation (in Å<sup>-2</sup>) of hydrogen bond vectors (SI Fig. 2.10) were calculated over the last ~250 ns of MD trajectory as follows:

1. The frames of the MD simulation are aligned onto the crystal cryostructure (using the backbone atoms of residues 25-46 as reference) to remove diffusive motions of M2TM.
2. The oxygen atoms of all the water molecules forming hydrogen bonds with other water molecules or His37 in the M2 pore are selected and their two cylindrical coordinates ( $z$

and  $r$ ) are computed.  $z$  is the Cartesian coordinate that indicates the displacement along the pore axis (with origin on the center of mass of M2TM 25-46), whereas  $r$  is the radial distance from the pore axis.

3. The corresponding hydrogen bond vectors  $hb(r,z)$  are calculated as the difference between the cylindrical coordinates of the acceptor and the donor.
4. The density of hydrogen bond vectors  $n_{hb}(r,z)$  (shown in black in SI Fig. 2.10) is computed as a two-dimensional histogram of the number of hydrogen bond vectors, with a grid of 0.2 Å spacing. Thereby, we are performing a cylindrical average over  $r$ , that is over the four M2 monomers. The orientation of hydrogen bond vectors  $n_{hb}(r,z)$  (shown in red and blue in SI Fig. 2.10) is computed in a similar way, but considering the direction of the vector, so that a hydrogen bond has a positive contribution if oriented outwards or negative if oriented inwards.
5. The two-dimensional histograms are normalized with weighting factor ( $\frac{1}{2}\pi r$ ) to allow a visual comparison of the density near the pore axis with respect to the density at large values of  $r$ , where atoms are more numerous for geometrical reasons.
6. The normalized density is plotted using a color scale ranging from white ( $0 \text{ \AA}^{-3}$ ) to full black ( $0.05 \text{ \AA}^{-3}$ ), whereas for the normalized orientation color scale spans from full red ( $-0.025 \text{ \AA}^{-2}$ ) to white ( $0 \text{ \AA}^{-2}$ ) and then to full blue ( $+0.025 \text{ \AA}^{-2}$ ).

*Average number of hydrogen bonds.* We calculated the number of hydrogen bonds inside the M2 pore, averaged over the last ~250 ns of the MD trajectory. Only water-water and water-His37 hydrogen bonds were considered and they were classified as extraviral or intraviral depending on whether the donor and acceptor water oxygen atoms were above or below the His37 tetrad (i.e.

extraviral if  $z$  (donor O) and  $z$  (acceptor O)  $>$   $z$  (center of mass of the His37 tetrad) and intraviral if otherwise). Hydrogen bonds are oriented outwards if  $z$  (donor O)  $<$   $z$  (acceptor O), whereas they are oriented inwards if  $z$  (donor O)  $>$   $z$  (acceptor O). This analysis, shown in Supplementary Table S2, is intended to provide a more quantitative picture of the hydrogen bond population displayed in Fig. 2.5 and Supplementary Fig. 2.11.

*Average hydrogen bond vectors along the M2 pore axis.* We calculated the average hydrogen bond vectors along the pore axis ( $z$ ) using the hydrogen bond vectors expressed in spherical coordinates  $hb(r,z)$ , calculated as explained above. These individual vectors were averaged over the last ~250 ns of the MD trajectory and over 2 Å bins along the pore axis;  $hb(r,z)$  is considered to belong to a certain  $z$  slab if the floor of  $z$  (donor O) =  $z$  (slab). The resulting average vectors are shown in SI Fig. 2.12. Their direction reflects the orientation with respect to the pore axis (i.e. upwards indicates a net number of hydrogen bonds directed towards the exterior of the channel and downwards towards the viral interior), whereas their length is proportional to the magnitude of the net hydrogen bond vector (i.e. the longer, the larger the preference to be oriented in that direction). These average hydrogen bond vectors (SI Fig. 2.12) present a one-dimensional, more simplified picture of the two-dimensional histograms in SI Fig. 2.10.

*Average number of donors and acceptors along the pore.* We calculated the difference between the number of water molecules acting as hydrogen bond donors and acceptors along the pore axis  $z$ . Compared to the previous analyses, in which we calculated only the water-water and water-His37 hydrogen bond vectors, here we calculated the number of water molecules donating or accepting hydrogen bonds to or from other water molecules and the protein (i.e. carbonyl oxygen atoms, Ser31 hydroxyl group or Asn31 amide group and His37 imidazole). The (*donor-acceptor*) difference is averaged over the last ~250 ns of the MD trajectory and over 2 Å

bins along the pore axis; a water molecule is considered to belong to a certain  $z$  slab if the floor of  $z$  (oxygen atom) =  $z$  (slab). The average differences along  $z$  are shown as bar graphs in SI Fig. 2.13. A red bar indicates a net number of water molecules acting as H-bond donors, whereas a blue bar represents a net number of water molecules acting as H-bond acceptors.

Control simulations: Besides the production MD described above, we also performed control simulations with all X-ray derived water molecules restrained at their crystallographic positions.

Two types of control simulations were run:

1. “restrained” simulations, in which the cryogenic X-ray structures at high and low pH (PDB entries 4QK7 and 4QKC, respectively) were simulated while applying a restraining harmonic potential on the oxygen atoms of the crystallographic water molecules;
2. “swapped” simulations, where the crystallographic water molecules in the cryogenic high pH structure (PDB entry 4QK7) were replaced by those of the low pH structure (PDB entry 4QKC), and vice versa; the resulting chimeric systems were simulated using a harmonic restraining potential on the grafted water molecules.

The harmonic force constant ( $k$ ) used in both types of control simulations is  $4 \text{ kcal mol}^{-1} \text{ \AA}^{-2}$  (that is, each water oxygen atom can fluctuate  $\pm 0.5 \text{ \AA}$  around its experimental position), except for water molecules 35 and 47 in the high pH structure, for which  $k = 1 \text{ kcal mol}^{-1} \text{ \AA}^{-2}$  ( $\pm 1.1 \text{ \AA}$  oscillations). Water 35 of one M2TM monomer is only  $1.26 \text{ \AA}$  apart from water 47 of another monomer, and either of them can form a H-bond with water 36, indicating that the water sites 35 and 47 are alternatively occupied. The rest of the simulation details are the same as for the production MD (see above). Control simulations were run for all five possible protonation states of the His37 tetrad (0, 1+, 2+, 3+ and 4+) and a trajectory of  $\sim 120 \text{ ns}$  was sampled for each system. For each control simulation, the first  $\sim 20 \text{ ns}$  were discarded as equilibration and the

population of hydrogen bonds was calculated on the last ~100 ns, following the same clustering protocol as for the production simulations (see above). The obtained water wires are shown in SI Fig. 2.14.

The distribution of H-bond donors and acceptors in the restrained simulations (SI Fig. 2.14, panels a-d) is nearly identical to the production MD (Fig. 2.5 and SI Fig. 2.11). Therefore, the computational water model (TIP3P)<sup>14</sup> is able to accurately predict the hydrogens' positions, despite the slight differences between the experimental and calculated water densities. On the other hand, the orientation of hydrogen bonds in the restrained simulations (SI Fig. 2.14, panels a-d) is almost indistinguishable from the swapped simulations (Supplementary Fig. 2.14, panels e-h). This indicates that the hydrogen bond orientation does not depend on the precise position of the water molecules, and it is determined only by the charge state of the His37 tetrad.

## 2.10.6 Appendix B References

- 1 Caffrey, M. & Cherezov, V. Crystallizing membrane proteins using lipidic mesophases. *Nat. Protoc.* **4**, 706-731, doi:10.1038/nprot.2009.31 (2009).
- 2 Battye, T. G. G., Kontogiannis, L., Johnson, O., Powell, H. R. & Leslie, A. G. W. iMOSFLM: a new graphical interface for diffraction-image processing with MOSFLM. *Acta Crystallogr. Sect. D-Biol. Crystallogr.* **67**, 271-281, doi:10.1107/s0907444910048675 (2011).
- 3 McCoy, A. J. *et al.* Phaser crystallographic software. *J. Appl. Crystallogr.* **40**, 658-674, doi:10.1107/s0021889807021206 (2007).
- 4 Stouffer, A. L. *et al.* Structural basis for the function and inhibition of an influenza virus proton channel. *Nature* **451**, 596-U513, doi:10.1038/nature06528 (2008).
- 5 Adams, P. D. *et al.* PHENIX: a comprehensive Python-based system for macromolecular structure solution. *Acta Crystallogr. Sect. D-Biol. Crystallogr.* **66**, 213-221, doi:10.1107/s0907444909052925 (2010).
- 6 Emsley, P., Lohkamp, B., Scott, W. G. & Cowtan, K. Features and development of Coot. *Acta Crystallogr. Sect. D-Biol. Crystallogr.* **66**, 486-501, doi:10.1107/s0907444910007493 (2010).
- 7 Schrodinger, LLC. *The PyMOL Molecular Graphics System, Version 1.3r1* (2010).
- 8 van den Bedem, H., Dhanik, A., Latombe, J. C. & Deacon, A. M. Modeling discrete heterogeneity in X-ray diffraction data by fitting multi-conformers. *Acta Crystallogr. Sect. D-Biol. Crystallogr.* **65**, 1107-1117, doi:10.1107/s0907444909030613 (2009).
- 9 Lang, P. T. *et al.* Automated electron-density sampling reveals widespread conformational polymorphism in proteins. *Protein Sci.* **19**, 1420-1431, doi:10.1002/pro.423 (2010).
- 10 Ohkubo, Y. Z., Pogorelov, T. V., Arcario, M. J., Christensen, G. A. & Tajkhorshid, E. Accelerating membrane insertion of peripheral proteins with a novel membrane mimetic model. *Biophys. J.* **102**, 2130-2139 (2012).
- 11 MacKerell, Jr., A. D., Bashford, D., Bellot, M., Dunbrack, R. L. Jr, Evanseck, J. D., Field, M. J., Fischer, S., Gao, J., Guo, H. & Ha S. All-atom empirical potential for molecular modeling and dynamics studies of proteins. *J. Phys. Chem. B* **102**, 3586-3616 (1998).
- 12 MacKerell, Jr., A. D., Feig, M. and Brooks, III, C. L. Improved treatment of the protein backbone in empirical force fields. *J. Am. Chem. Soc.* **126**, 698-699 (2004).

- 13 Best, R. B., Zhu, X., Shim, J., Lopes, P., Mittal, J., Feig, M. and MacKerell, Jr., A. D.. Optimization of the additive CHARMM all-atom protein force field targeting improved sampling of the backbone phi, psi and sidechain chi1 and chi2 dihedral angle. *J. Chem. Theory Comput.* **8**, 3257-327 (2012).
- 14 Jorgensen, W. L., Chandrasekhar, J., Madura, J. D., Impey, R. W. & Klein, M. L. Comparison of simple potential functions for simulating liquid water. *J. Chem. Phys.* **79**, 926–935 (1983).
- 15 Beglov, D. & Roux, B. Finite Representation of an infinite bulk System: solvent boundary potential for computer simulations. *J. Chem. Phys.* **100**, 9050-9063 (1994).
- 16 Marchand, S. & Roux, B. Molecular dynamics study of calbindin D9k in the apo and singly and doubly calcium-loaded states. *Proteins*, **33**, 265–284 (1998).
- 17 Klauda, J. B., Venable, R. M., Freites, J. A., O'Connor, J. W., Tobias, D. J., Mondragón-Ramírez, C., Vorobyov, I., MacKerell, Jr., A. D. & Pastor, R. W. Update of the CHARMM all-atom additive force field for lipids: validation on six lipid types. *J. Phys. Chem. B* **114**, 7830-7843 (2010).
- 18 Lee, S., Tran, A., Allsopp, M., Lim, J. B., Hénin, J. & Klauda, J. B. CHARMM36 united-atom chain model for lipids and surfactants. *J. Phys. Chem. B* **118**, 547–556 (2014).
- 19 Vanommeslaeghe, K., Hatcher, E., Acharya, C., Kundu, S., Zhong, S., Shim, J., Darian, E., Guvench, O., Lopes, P., Vorobyov, I. & Mackerell, Jr., A. D. CHARMM general force field: a force field for drug-like molecules compatible with the CHARMM all-atom additive biological force fields. *J. Comput. Chem.* **31**, 671–90 (2009).
- 20 Vanommeslaeghe, K. & MacKerell, Jr., A. D. Automation of the CHARMM General Force Field (CGenFF) I: bond perception and atom typing, *J. Chem. Inf. Model.* **52**, 3144-3154 (2012).
- 21 Vanommeslaeghe, K., Raman, E. P. & MacKerell, Jr., A. D. Automation of the CHARMM General Force Field (CGenFF) II: Assignment of bonded parameters and partial atomic charges, *J. Chem. Inf. Model.* **52**, 3155-3168 (2012).
- 22 [www.paramchem.org](http://www.paramchem.org)
- 23 Essman, U., Perera, L., Berkowitz, M. L., Darden, T., Lee, H. & Pedersen, L. G. A smooth particle mesh Ewald method. *J. Chem. Phys.* **103**, 8577–8592 (1995).
- 24 Ryckaert, J.-P., Ciccotti, G. & Berendsen, H. J. C. Numerical integration of the cartesian equations of motion of a system with constraints: molecular dynamics of N-alkanes. *J. Comput. Phys.* **23**, 327– 341 (1977).
- 25 Adelman, S. A. & Doll, J. D. Generalized Langevin equation approach for atom/solid-surface scattering: General formulation for classical scattering off harmonic solids. *J.*

*Chem. Phys.* **64**, 2375-2388 (1976).

- 26 Previous simulations of M2-TM in a membrane (Wei, C. & Pohorille, A. Activation and proton transport mechanism in influenza A M2 channel. *Biophys. J.* **105**, 2036-2045 (2013) and Gkeka, P., Eleftheratos, S., Kolocouris, A & Cournia, Z. Free energy calculations reveal the origin of binding preference for aminoadamantane blockers of influenza. *J. Chem. Theory Comput.* **9**, 1272-1281 (2013)) have shown that anions, such as chloride, can access the interior of the M2 pore. In our crystal environment simulations, entrance of Cl<sup>-</sup> is overestimated due to the limited volume of water between the two staggered tetramers. Therefore, we have used a wall-like restraining potential to penalize the presence of chloride ions inside the pore and thus sample the pore hydration without anion-induced perturbations.
- 27 Phillips, J. C., Braun, R., Wang, W., Gumbart, J., Tajkhorshid, E., Villa, E., Chipot, C., Skeel, R. D., Kalé, L. & Schulten, K. Scalable molecular dynamics with NAMD. *J. Comput. Chem.* **26**, 1781-1802 (2005).
- 28 Ma, C., Fiorin, G., Carnevale, V., Wang, J., Lamb, R. A., Klein, M. L., Wu, Y., Pinto, L. H. & DeGrado, W. F. Asp44 stabilizes the Trp41 gate of the M2 proton channel of influenza A virus. *Structure* **21**, 2033-2041 (2013).
- 29 Acharya, R., Carnevale, V., Fiorin, G., Levine, B.G., Polishchuk, A.L., Balannik, V., Samish, I., Lamb, R.A., Pinto, L.H., DeGrado, W.F. & Klein, M.L. Structure and mechanism of proton transport through the transmembrane tetrameric M2 protein bundle of the influenza A virus. *Proc. Natl. Acad. Sci. USA* **107**, 15075-15080 (2010).
- 30 Stouffer, A.L., Acharya, R., Salom, D., Levine, A.S., Costanzo, L.D., Soto, C.S., Tereshko, V., Nanda, V., Stayrook, S. & DeGrado, W.F. Structural basis for the function and inhibition of an influenza virus proton channel. *Nature* **451**, 596-600 (2008).
- 31 Cohen, J., Arkhipov, A., Braun, R. & Schulten, K. Imaging the migration pathways for O<sub>2</sub>, CO, NO, and Xe inside myoglobin." *Biophysical Journal* **91**, 1844-1857 (2006).
- 32 Humphrey, W., Dalke, A. & Schulten, K. VMD-Visual Molecular Dynamics. *J. Mol. Graphics* **14**, 33-38 (1996).
- 33 Kosinska Eriksson, U., Fischer, G., Friemann, R., Enkavi, G., Tajkhorshid, E. & Neutze, R. Subangstrom resolution X-ray structure details aquaporin-water interactions. *Science*. **340**, 1346-1349 (2013).
- 34 Klauda, J. B., Kucerka, N., Brooks, B. R., Pastor, R. W. & Nagle, J. F. Simulation-based methods for interpreting X-ray data from lipid bilayers. *Biophys. J.* **90**, 2796-2807 (2006).
- 35 Daura, X., Gademann, K., Jaun, B., Seebach, D., van Gunsteren, W. F. & Mark, A. E. Peptide folding: when simulation meets experiment. *Angew. Chem. Int. Ed.* **38**, 236-240 (1999).



## Chapter 3

### **XFEL structures of the influenza M2 proton channel: room temperature water networks and insights into proton conduction**

#### **3.1 Abstract**

The M2 proton channel of influenza A is a drug target that is essential for the reproduction of the flu virus. It is also a model system for the study of selective, unidirectional proton transport across a membrane. Ordered water molecules arranged in “wires” inside the channel pore have been proposed to play a role in both the conduction of protons to the four gating His37 residues and the stabilization of multiple positive charges within the channel. To visualize the solvent in the pore of the channel at room temperature while minimizing the effects of radiation damage, data were collected to a resolution of 1.4 Å using an X-ray free electron laser (XFEL) at three different pH conditions: pH 5.5, pH 6.5, and pH 8.0. Data were collected on the Inward<sub>open</sub> state, which is an intermediate that accumulates at high protonation of the His37 tetrad. At pH 5.5, a continuous hydrogen bonded network of water molecules spans the vertical length of the channel, consistent with a Grotthuss mechanism model for proton transport to the His37 tetrad. This ordered solvent at pH 5.5 could act to stabilize the positive charges that build up on the gating His37 tetrad during the proton conduction cycle. The number of ordered pore waters decreases at pH 6.5 and 8.0, where the Inward<sub>open</sub> state is less stable. These studies provide a graphical view of the response of water to a change in charge within a restricted channel environment.

## 3.2 Significance

The influenza M2 channel is among the smallest proton-selective channels found in nature. High-resolution structures of this channel further our understanding of how protons are transported across a membrane bilayer through a constricted membrane protein environment. This study also has broader implications for the structural interpretation of water in channels using X-ray crystallographic techniques. Previous crystallographic structures determined using synchrotron radiation with cryo-cooling were biased by the low temperature, and room-temperature data collection was limited by radiation damage. These problems have been avoided through room temperature diffraction at an XFEL source.

## 3.3 Introduction

Water molecules in transmembrane protein pores participate in the transport of protons across the membrane bilayer. This process has been extensively studied experimentally and through computational simulations, particularly in small channels such as gramicidin A and influenza A M2. The movement of ions through channels is coupled to the diffusion of water through the pore, but protons are transported at a rate that is faster than the diffusion of  $\text{H}_3\text{O}^+$ .<sup>1,2</sup> Instead of diffusing through channels, protons move concertedly across networks of hydrogen bonded waters through what is known as the Grotthuss mechanism.<sup>3-5</sup> This mechanism of proton transport was initially discovered by the behavior of water in solution, and it has also been proposed to occur within membrane proteins containing water-filled pores.<sup>6-9</sup> The matrix 2 (M2) protein of influenza A is one of the smallest proton-selective channels found in nature. This makes it an ideal system for studying the involvement of water in the selective transport of protons across the membrane.

The M2 protein of influenza A is a tetramer made up of four 97-residue long monomers. M2 is multifunctional, with different functions lying in different regions of the sequence. Residues 1-22 make up a conserved N-terminal domain that assists the incorporation of M2 into the virion,<sup>10</sup> and is absent in influenza B viruses. The transmembrane domain of M2 (residues 22-46) is necessary for tetramerization<sup>11</sup> and forms a proton-selective channel<sup>12-15</sup> that is the target of the adamantane class of drugs, amantadine and rimantadine.<sup>11,16-18</sup> The transmembrane domain of the M2 proton channel (M2TM, residues 22-46) is the smallest construct of M2 that retains the functionally important conductance features of the full-length protein.<sup>16,17</sup> When constructs of varying length are expressed and biosynthetically inserted into cell membranes, there is no experimentally significant difference in their proton conduction properties so long as the full transmembrane conduction domain (M2TM) is included.<sup>16,17,19,20</sup> The regions C-terminal to the TM helices play different important functional roles. An amphiphilic helix formed by residues 46-60 induces membrane curvature and is involved in viral budding and scission,<sup>21-23</sup> and an intrinsically disordered C-terminal tail (residues 62-97) interacts with the matrix 1 protein during the packing and budding of new virus particles.<sup>24,25</sup>

The proton-selective, pH-sensitive gate of the M2 channel consists of residues His37 and Trp41.<sup>26,27</sup> Four gating histidine residues face the pore of the channel; each His within the gate can be protonated, so the gating His tetrad can have a total charge of 0 to +4, with the charge states existing in equilibrium at a given pH (**Fig. 3.1**, top). The pKa values for adding successive protons to the His tetrad have been experimentally determined using solid state NMR of samples in phospholipid bilayers.<sup>28-32</sup> Though there is some variation of the reported pKa values depending on the type of lipid mimetic used, the first two protonation events occur with a pKa > 6, resulting in a +2 to +3 charge on the gating His tetrad at the pH range of an acidifying

endosome. Electrophysiological studies of M2 conductance vs. pH report that a saturation of proton conductance within physiologically relevant pH values occurs at pH  $\sim 5.5$ .<sup>12,27,33-35</sup> Both of the experimentally determined pKa values for the protonation of the third gating His residue occur near the midpoint of this saturation curve. Proton conduction is hypothesized to occur as the gating His tetrad cycles from a +2 to a +3 charge state.

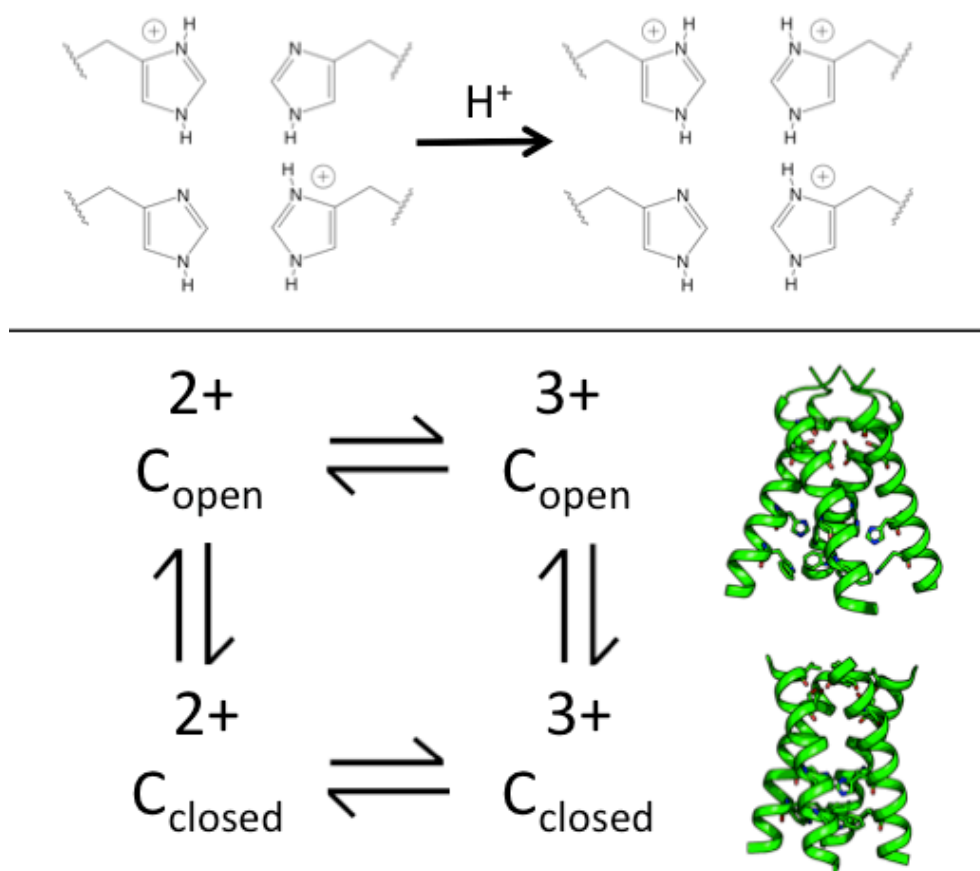


**Figure 3.1. Protonation states of the M2 gating His37 tetrad.** Top: The gating His37 tetrad of the M2 channel can have a charge state ranging from neutral to +4. Shown here is the transition from the 2+ to the 3+ charge state, which is hypothesized to occur during the proton transport cycle. Bottom: The charge states of the His tetrad are in equilibrium, and the Inward<sub>open</sub> conformation is in equilibrium with the Inward<sub>closed</sub> conformation.

Multiple conformations of the M2 conductance domain, which reflect distinct intermediates in the conduction cycle, have been structurally observed by X-ray crystallography.<sup>35-38</sup> In one conformation the C-terminus of the channel is splayed open (Inward<sub>open</sub>); in the other, the C-terminus adopts a more constricted conformation (Inward<sub>closed</sub>). A conformation with hybrid characteristics has also been determined.<sup>35</sup> The Inward<sub>closed</sub> state has been also been characterized by solution NMR<sup>39,40</sup> and solid state NMR<sup>41,42</sup> studies under high pH conditions. The Inward<sub>closed</sub> conformation can transition to the Inward<sub>open</sub> conformation by straightening a kink in the TM helix near Gly34.<sup>40,43,44</sup> This conformational transition provides a pathway for proton transfer past the Trp41 gate into the viral interior. In NMR studies at low pH, both conformations are observed in equilibrium with one another.<sup>40,43,44</sup> Molecular dynamics simulations suggest that the Inward<sub>open</sub> and Inward<sub>closed</sub> conformations are in equilibrium, with the channel becoming more open at the C-terminus as positive charges accumulate on the His37 gate.<sup>45-48</sup>

A recent electrophysiological study<sup>49</sup> using inside-out macro-patches of *Xenopus laevis* oocytes at cytosolic pH values of 5.5, 7.5, and 8.2 has demonstrated the interconversion of the Inward<sub>closed</sub> and the Inward<sub>open</sub> conformations in a transporter-like mechanism (**Fig. 3.1**, bottom). This mechanism also explains the high asymmetry of proton conductance with respect to the proton gradient and the sign of the transmembrane potential.<sup>49</sup> Protons flowing towards the interior of the virus enter via the Inward<sub>closed</sub> state and diffuse to the His37 tetrad, which is likely in a +2 state when the pH<sub>out</sub> is near that of the acidifying endosome (pH 5 – 6). A permeating proton diffuses through the pore and binds to His37, increasing the total charge of the His37 tetrad to a +3 state. This triggers the formation of the Inward<sub>open</sub> state and ultimately the release of the proton into the interior of the virus. Following transfer of the proton into the viral interior,

the protein remains in a meta-stable  $\text{Inward}_{\text{open}}$  state, which must be converted to the  $\text{Inward}_{\text{closed}}$  state in a “recycling step”. This recycling step can limit the rate of proton conduction under some conditions.

Here, we examine solvent ordering of water in the pore of M2 within crystals containing only the  $\text{Inward}_{\text{open}}$  conformation. By collecting structural data at different pH conditions, we probe the structure of the pore’s water network while varying the charge on the gating His37 tetrad. This allows us to access multiple protonation states of His37 in the  $\text{Inward}_{\text{open}}$  state representing the conformation of the His37 tetrad prior to and following the release of a proton into the viral interior. By trapping the  $\text{Inward}_{\text{open}}$  conformation in the crystal lattice, we evaluate the structure of the under-protonated form of His37, which occurs only as a metastable intermediate in membranes. Previously we reported structures of the M2TM solvent network in this  $\text{Inward}_{\text{open}}$  conformation at low and high pH,<sup>37</sup> using a conventional synchrotron X-ray source under cryogenic conditions. The 1.10 Å resolution high and low pH cryogenic structures showed that the waters within the channel form a continuous hydrogen bonding network under both pH conditions. This network could contribute to the stabilization of positive charges in the pore. This structure also supports a Grotthuss mechanism for proton transport, which has been proposed as a possible method of proton transport by quantum mechanical and molecular dynamics simulations on the M2 channel.<sup>36,48,50-52</sup> However, these 1.10 Å structures were collected under cryogenic conditions that could artificially increase the degree of ordering of the water. Indeed, less order was observed at higher temperature,<sup>37</sup> but the diffraction was limited by rapid radiation damage near room temperature. Therefore, the actual arrangement of solvent within the M2 channel pore remained ambiguous.

Here, we have used data collection at an X-ray Free Electron Laser (XFEL) to circumvent these limitations. In XFEL experiments, the energy of the intense X-ray pulses used is large enough to destroy the sample through the effects of radiation damage.<sup>53</sup> However, diffraction occurs on a time scale that is faster than the rate at which radiation damage disrupts the crystal lattice and destroys the sample, effectively giving "diffraction before destruction".<sup>54-56</sup> This allows for data collection at ambient temperature while minimizing the effects of radiation damage on the data. The resulting XFEL datasets provide new high-resolution insights into the involvement of ordered waters in proton transport and the stabilization of positive charges in the M2 channel.

### 3.4 Results and Discussion

*3.4.1 Comparison of low pH XFEL structure to synchrotron structures.* The XFEL structure of M2TM at low pH can be compared to our previous structures collected under the same pH condition using a synchrotron radiation source (**Fig. 3.2**). Within the low pH condition, the previously determined cryogenic synchrotron structure shows the largest number of ordered waters (**Table 3.1**) and also the most extensive hydrogen bonding network, with continuous hydrogen bonds extending throughout the channel from Ser31 to the gating His37 residues. However, the solvent network from the room temperature synchrotron structure contains fewer ordered waters and almost no possible hydrogen bonds to connect those waters. The room temperature XFEL data reveal an intermediate degree of solvent ordering. Fewer ordered waters are observed than in the cryogenic structure. But, unlike the room temperature synchrotron structure, the XFEL data reveals a continuous hydrogen bonding network that spans the vertical length of the channel pore.

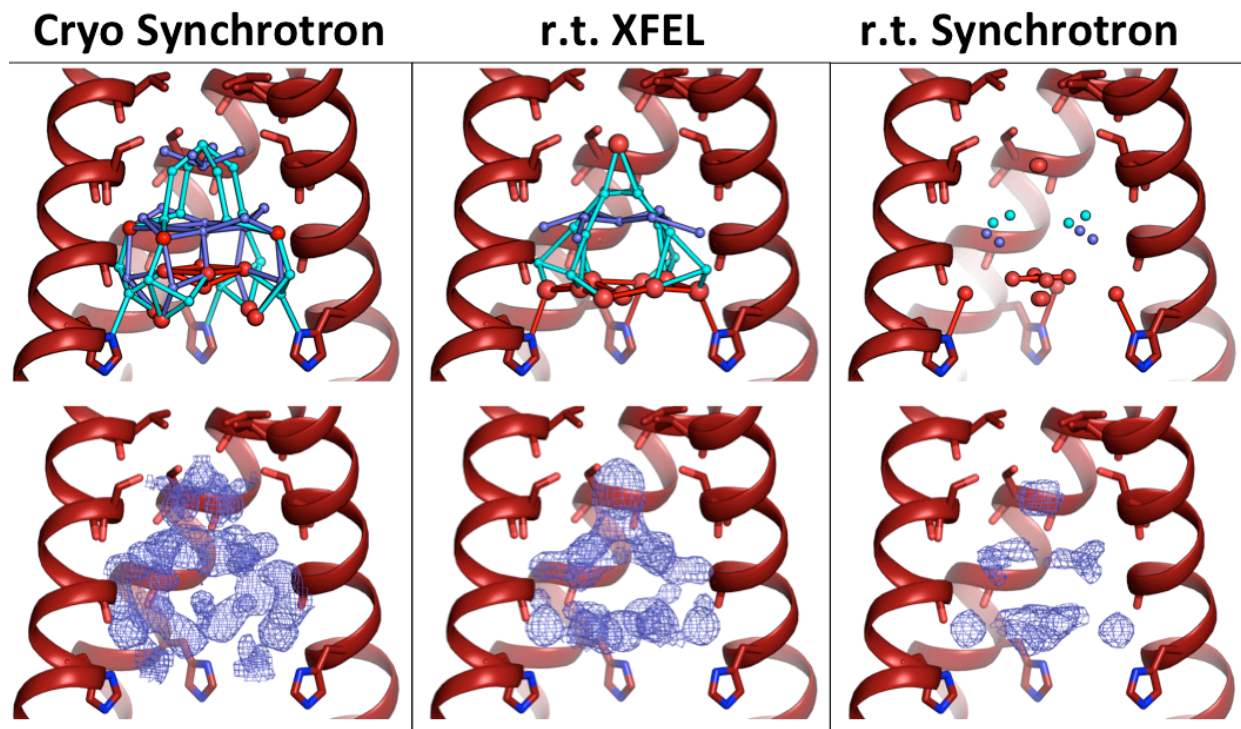


**Figure 3.2. Low pH M2TM crystal structures.** Low pH (pH 5.5) structures of M2TM under cryogenic synchrotron (4QKC, left), room temperature XFEL (5JOO, center), and room temperature (r.t.) synchrotron (4QKM, right) diffraction conditions. **Top:** The front helix of each tetramer has been removed; waters are modeled as spheres, with red spheres representing full-occupancy waters and light and dark blue spheres representing half-occupancy waters in alternate occupancy networks A and B. Waters within hydrogen bonding distance of each other are connected by sticks. The number of ordered waters decreases moving from left to right across the figure. **Bottom:** Electron density for the pore solvent network (blue mesh) is shown to a contour of  $0.5 \sigma$ . The largest amount of ordered density is present in the cryogenic synchrotron data collection condition. The volume and shape of the solvent density for the room temperature structures collected using XFEL and synchrotron sources is similar.



**Table 3.1. Number of ordered waters in M2 pore.** Number of modeled waters in the pore region (Val27-His37) of M2 for the structures collected under cryogenic synchrotron, room temperature synchrotron, and room temperature XFEL diffraction conditions. Total waters are equal to the number of full occupancy waters plus one half the number of half occupancy waters. For waters located on the fourfold axis of symmetry at the center of the channel, one full occupancy water is equivalent to four 0.25 occupancy waters, and one half occupancy water is equivalent to four 0.125 occupancy waters.

|   | Full occupancy | Half occupancy | Total |
|---|----------------|----------------|-------|
| <b>XFEL room temperature low pH (5JOO)</b>          | 10             | 21             | 20.5  |
| <b>XFEL room temperature intermediate pH (5UM1)</b> | 10             | 8              | 14    |
| <b>XFEL room temperature high pH (5TTC)</b>         | 9              | 4              | 11    |
| <b>Cryogenic low pH (4QKC)</b>                      | 13             | 34             | 30    |
| <b>Cryogenic high pH (4QK7)</b>                     | 9              | 34             | 28    |
| <b>Room temperature low pH (4QKM)</b>               | 10             | 8              | 14    |
| <b>Room temperature high pH (4QKL)</b>              | 15             | 8              | 19    |

The room temperature data from both XFEL and synchrotron sources have pore solvent electron density with a similar shape. In both density maps, there are three layers of solvent density arranged in a pyramid-like shape. This pattern differs from the density observed in the cryogenic synchrotron structure, which contains a larger volume of electron density from ordered solvent. The topmost layer of waters near Ser31 consists of a single full-occupancy water at the center of the channel, which is observed in both of the room temperature structures. Similarly, in the middle solvent layer near Gly34 and the bottom layer immediately above His37, the waters are located in similar positions. However, the XFEL structure can be modeled with additional ordered waters in these layers.

*3.4.2 Comparison of high pH XFEL structure to synchrotron structures.* The trends observed comparing the high pH datasets from XFEL and synchrotron sources are similar to those

observed at low pH (**Fig. 3.3**). Again, the cryogenic synchrotron structure contains the largest number of modeled ordered waters (**Table 3.1**) and, correspondingly, the largest volume of solvent electron density. In both room temperature structures, the waters are separated into three layers. Here, a slightly larger number of ordered waters is present in the room temperature synchrotron structure relative to the room temperature XFEL structure. The total number of ordered solvent molecules and the shape of their resulting electron density is similar for both of the room temperature datasets.

The high pH XFEL structure has a solvent network that consists of mostly full occupancy waters. These are again separated into three layers, but here there are no hydrogen bonds vertically connecting the layers. The only hydrogen bonds that can be formed within the pore water network are between the waters in the bottom layer above the His37 gate. These waters are not within hydrogen bonding distance of the His37 sidechains.

*3.4.3 XFEL datasets avoid artifacts from both cryocooling and radiation damage.* Our new data suggest that the previous structures collected at a conventional synchrotron X-ray source likely suffer from experimental artifacts. In both high and low pH conditions, the volume of ordered solvent observed at cryogenic temperatures is much higher than the amount observed in any of the room temperature structures. This reflects tightened enthalpically favored water distributions within the pore induced by freezing the crystals at 100 K.<sup>57</sup> The decreased solvent ordering when diffracting at room temperature using a synchrotron source likely reflects resolution-limiting radiation damage. Collecting room temperature data using an XFEL source avoids the effects of both sets of potential experimental artifacts.

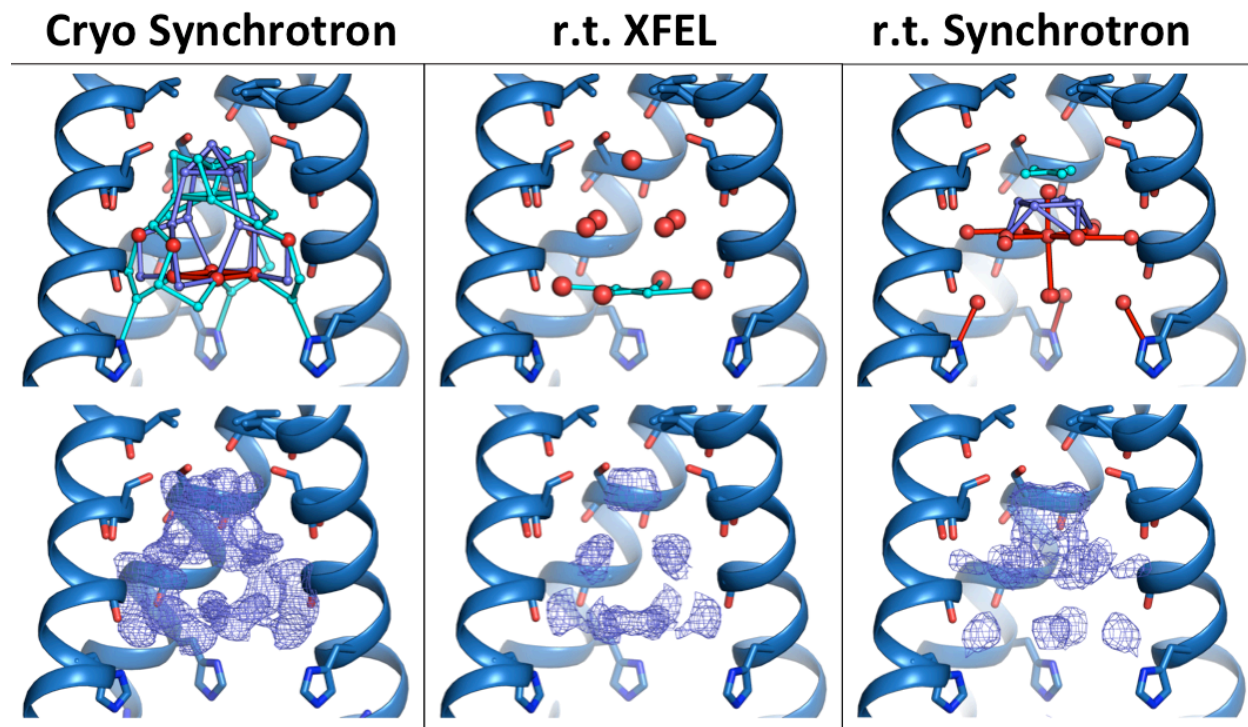


**Figure 3.3. High pH M2TM crystal structures.** High pH (pH 8.0) structures of M2TM under cryogenic synchrotron (4QK7, left), room temperature (r.t.) XFEL (5TTC, center), and room temperature synchrotron (4QKL, right) diffraction conditions, shown as described in Figure 1. **Top:** The largest number of ordered waters is found in the cryogenic synchrotron diffraction condition; fewer ordered waters are present at room temperature. **Bottom:** The largest amount of ordered solvent electron density is observed under cryogenic diffraction conditions; the volume and shape of the solvent density for the two room temperature conditions is similar.

*3.4.4 Continuous hydrogen bonding network at low pH.* In the low pH XFEL structure, the ordered waters within the pore form three layers (**Fig. 3.4**): a top layer near Ser31, a middle layer near Gly34, and a bottom layer above the His37 gate. The top and bottom layers consist of mostly full-occupancy waters, while many of the waters in the middle layer are modeled as partial occupancy. In the topmost layer of waters, the Ser31 sidechain is not within hydrogen bonding distance of the single water, which is consistent with the fact that this residue can accept a wide range of substitutions to small polar residues with retention of the proton conduction activity.<sup>58</sup> In the bottom layer, the pore waters are positioned to act as either hydrogen bond

donors or acceptors immediately above His37. The hydrogen bonding interactions formed by the waters in the bottom solvent layer could stabilize positive charges on the gating His residues, or they could connect the hydrogen-bonded water wire formed by alternate occupancy network A to a neutral His residue. The pore solvent network has more hydrogen bond donating interactions with the protein than potential hydrogen bond accepting interactions, which is consistent with our previously observed structures.<sup>37</sup>

The partial occupancy solvent molecules of the low pH XFEL structure can be grouped into two self-consistent "alternate occupancy" networks. "A" and "B" are the minimum number of networks needed to explain the crystallographic positions of the half-occupancy waters within the symmetry constraints of the I4 space group; the waters within network "A" are too close to those in network "B" for both to coexist simultaneously. The previously collected single-crystal synchrotron data on this crystal form<sup>37</sup> have been refined with P1 symmetry with no differences observed in the electron density for the protein or the pore water network. From this we conclude that any possible asymmetric structural features in the water network are averaged within the crystal lattice.

The hydrogen bonds that can be formed by waters from alternate occupancy networks A and B are shown in **Figure 3.4**. Note that, in the middle layer of waters within network A, 90° rotation about the four-fold crystallographic axis of symmetry produces two clashing interactions and two hydrogen bonds. The waters modeled in this location likely exist as a dimer whose electron density is averaged across the fourfold axis of symmetry. Within alternate occupancy network A, a continuous chain of hydrogen bonds connects waters from the top of the water network to the gating His37 residues. By contrast, the waters in alternate occupancy network B do not form hydrogen bonds to vertically connect the three layers of waters. The chain of

hydrogen bonds that spans the length of the channel from Ser31 to the gating His37 residues in alternate occupancy network A is consistent with a continuous pathway for a proton to be shuttled from the top of the network to the gating His37 residues via the Grotthuss transport mechanism.

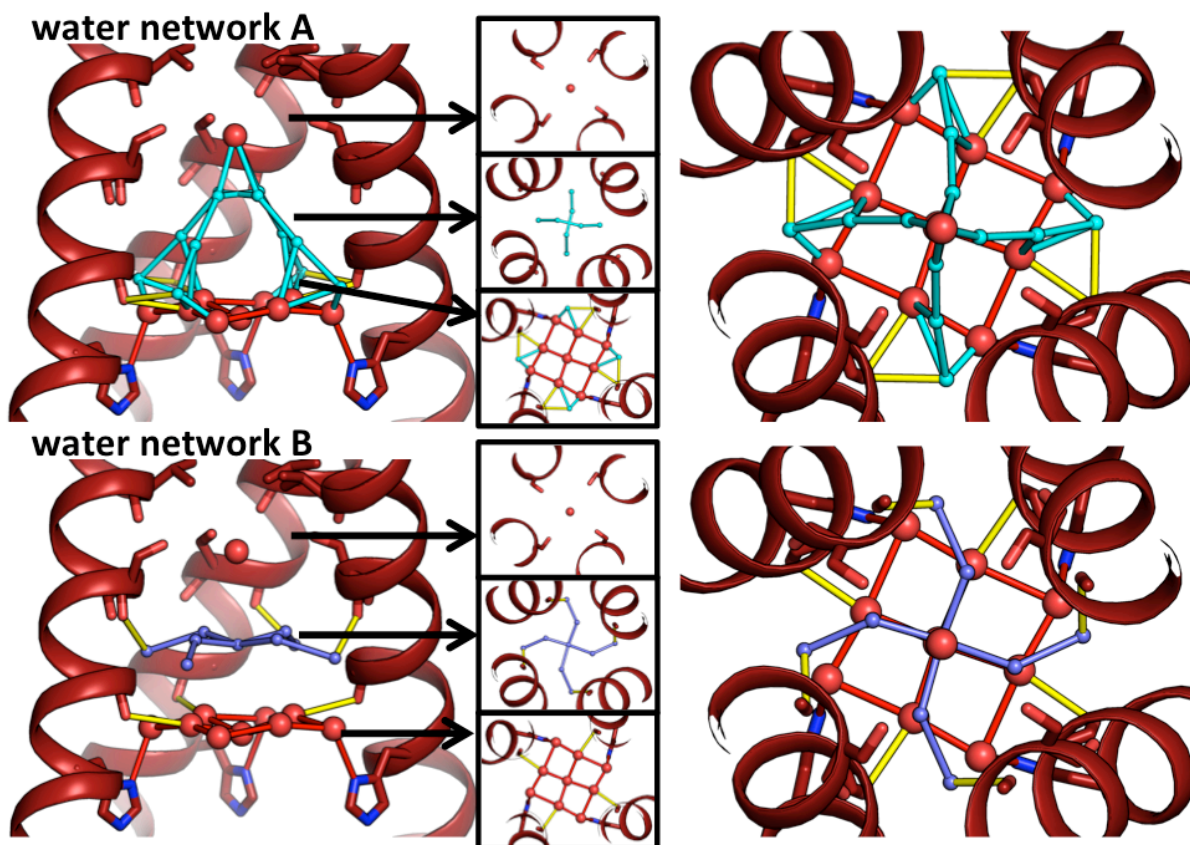


**Figure 3.4. Alternate occupancy water networks in the low pH (pH 5.5) room temperature XFEL structure (5JOO).** Full occupancy waters are red, waters from alternate occupancy network A are cyan, and waters from alt. occ. network B are dark blue. Waters within hydrogen bonding distance of each other are connected by sticks; yellow sticks indicate hydrogen bonds that can be made between the solvent network and protein carbonyls. **Left:** Side view of solvent from alternate occupancy network A (top) and B (bottom), with top-down views of the three layers of water in the pore. **Right:** Top-down view of all three layers of water in alternate occupancy network A (top) and B (bottom).

The two alternative networks discussed above represent only two possible interpretations of the ensemble average of all possible water networks within the channel averaged by the fourfold symmetry of the crystal lattice. To examine all possible symmetric and asymmetric water networks that contribute to the observed density, we used graph theory to extract all possible water networks from the crystallographic water positions from the low pH XFEL structure. Each water molecule represented a node in the graph, and all possible cliques were extracted and filtered for symmetry and total occupancy. We identified 11 unique hydrogen bonding networks (Figs. 3.5, 3.6), among which only 2 formed a continuous water wire that would connect a potential hydronium molecule at the top of the water network to one of the four gating His37 residues.

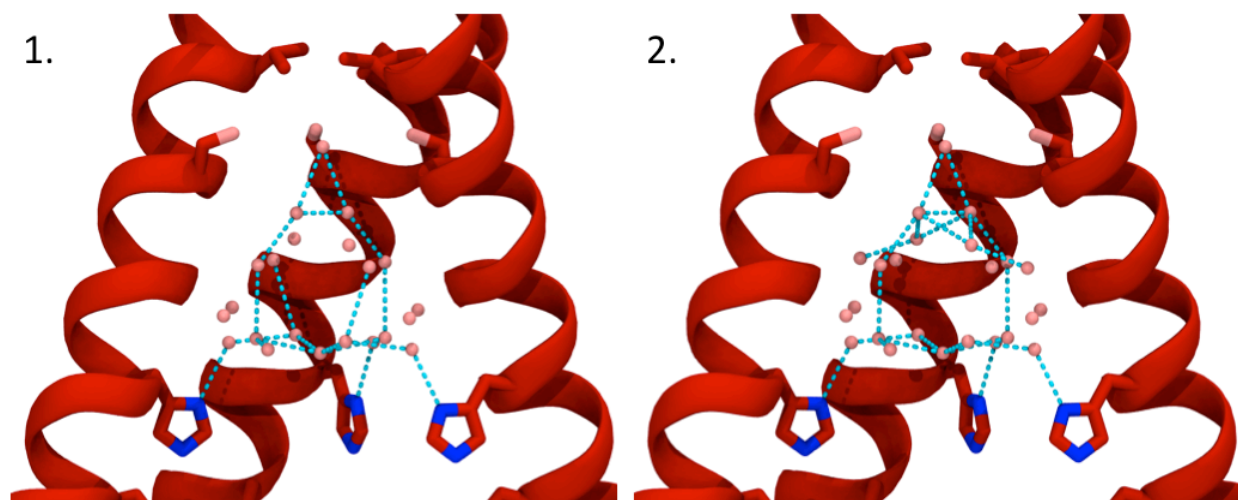


**Figure 3.5. Possible water networks forming continuous hydrogen bonds to His37.** Possible water networks #1 and #2 form a continuous chain of hydrogen bonds from the top of the water network to the gating His37 residues.

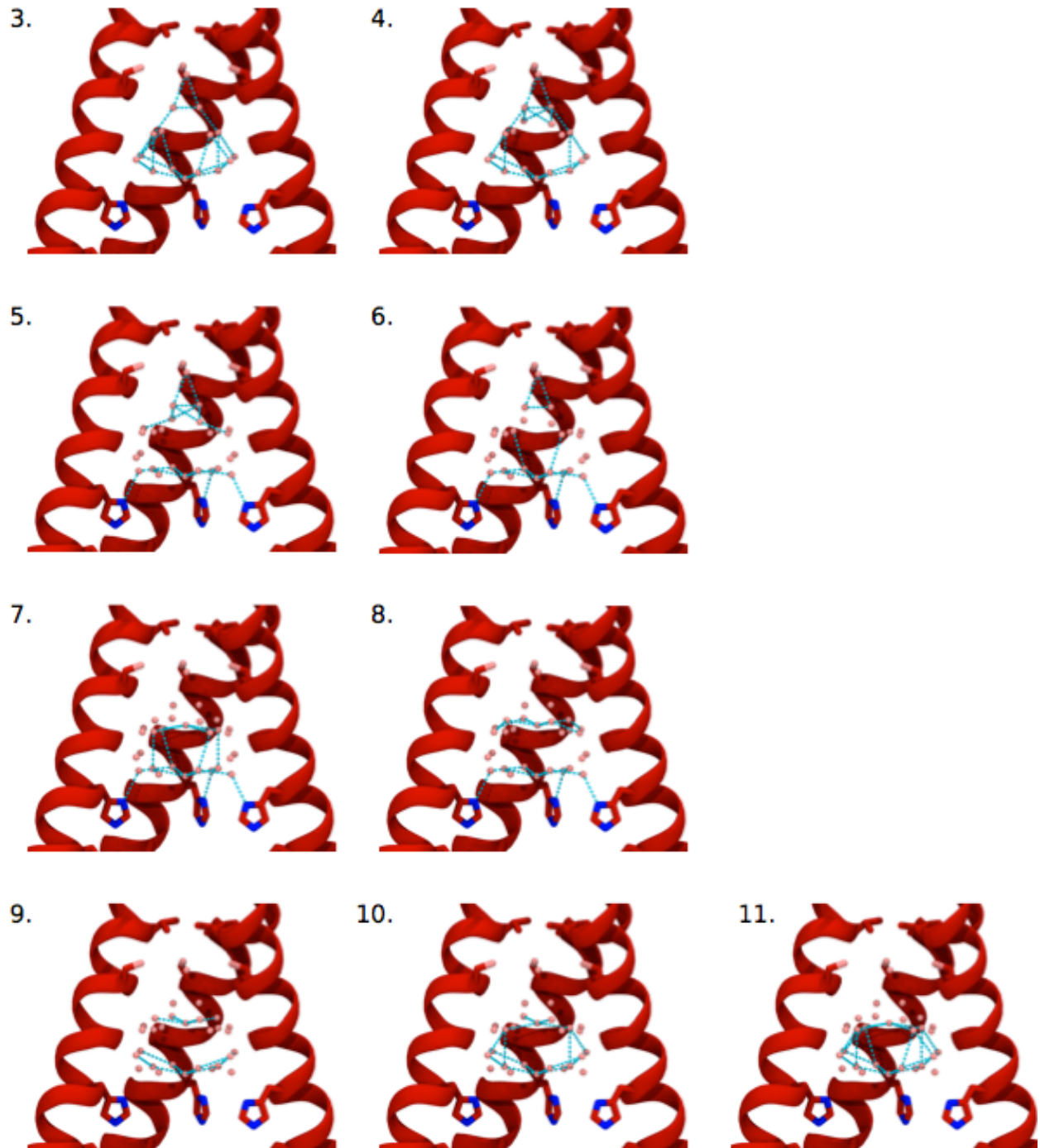


**Figure 3.6. Possible water networks not forming continuous hydrogen bonds to His37.** Possible water networks #3-11 form hydrogen bonds that do not continuously link the top of the water network to the gating His37 residues.



*3.4.5 Intermediate pH XFEL structure compared to previous structures.* The intermediate pH (6.5) XFEL structure can be compared to a previous structure collected at a conventional synchrotron source under cryogenic diffraction conditions; in the structure from Acharya et al.,<sup>36</sup> the channel adopts the Inward<sub>closed</sub> conformation. Comparison of the two structures reveals that the same general arrangement of solvent layers is observed in both conformational states, although the solvent molecules hydrogen bonded to His37 move away from the central axis by 1.4 Å of the channel in the Inward<sub>open</sub> state (**Fig. 3.7**). The radial distances increase from 3.2 Å in the Inward<sub>closed</sub> conformation to 4.6 Å in the Inward<sub>open</sub> conformation. Thus, as the C-terminus of the channel dilates to form the Inward<sub>open</sub> conformation, the solvent network within the channel also expands. Interestingly, the degree of dilation is close to the van der Waals radius of a single water molecule.

*3.4.6 XFEL structures at low, intermediate, and high pH.* The maximally conducting low pH 5.5 condition has the largest volume of ordered solvent electron density, the largest number of ordered waters (**Table 3.1**), and also the most extensive hydrogen bonding network, with solvent ordering decreasing at intermediate and high pH (**Fig. 3.8**). A continuous hydrogen bonding network is only observed in the low pH condition and could be consistent with a Grothuss transport mechanism for proton transport when the channel is at maximally conducting pH conditions. The intermediate pH 6.5 condition shows fewer ordered waters relative to the low pH state. At intermediate pH, the hydrogen bonding network spans roughly half of the vertical length of the channel pore. The solvent network in the high pH 8.0 condition has more diffuse electron density and the fewest number of ordered waters; at high pH, these waters do not make any hydrogen bonds in a vertical direction. Examining the bottom water layer just above the



gating His37 residue reveals that hydrogen bonds between His37 and solvent are only observed in the low pH condition. At low pH, both the delta and epsilon nitrogen are within 3 Å of an ordered water molecule, but, at intermediate and high pH, the bottom layer of solvent is too far away from His37 for a hydrogen bond to be formed (**Fig. 3.9**).

*3.4.7 Implications for proton conduction.* The conduction of protons through the M2 channel conforms to a transporter-like mechanism in which protonation leads to a conformational change from the Inward<sub>closed</sub> to the Inward<sub>open</sub> state. When a proton passes to the other side of the His37 gate, deprotonation occurs and channel cycles from the Inward<sub>open</sub> state back to its initial Inward<sub>closed</sub> conformation. Electrophysiological studies have resolved intermediates in the mechanism that reflect these two limiting conformational states (Inward<sub>open</sub> and Inward<sub>closed</sub>) at two different protonation states.<sup>49</sup> These states differ in the ease of proton diffusion through the N-terminal as well as the C-terminal ends of the channel, which can be understood in terms of reciprocal opening of the His37 tetrad in parallel with the closing of the Val27 gate.

Under physiological conditions in the acidifying endosome, the protein is predominantly in the Inward<sub>closed</sub> state with an open Val27 gate. This allows rapid equilibration of the His37 gate with the external pH ( $\text{pH}_{\text{out}}$ ), but not the  $\text{pH}_{\text{in}}$ . As the pH decreases, His37 reaches a threshold protonation state (probably to +3), which destabilizes packing of His37 residues in the Inward<sub>closed</sub> state and enables transient population of a Inward<sub>open</sub> conformation. The Inward<sub>open</sub> conformation can now equilibrate with the higher  $\text{pH}_{\text{in}}$  leading to the formation of a *metastable* Inward<sub>open</sub> conformation with one fewer proton bound to the His37 tetrad. The process of inward deprotonation of His37 and recycling of the Inward<sub>open</sub> conformation to the Inward<sub>closed</sub> conformation is sufficiently slow to constitute the rate-limiting step under some conditions.

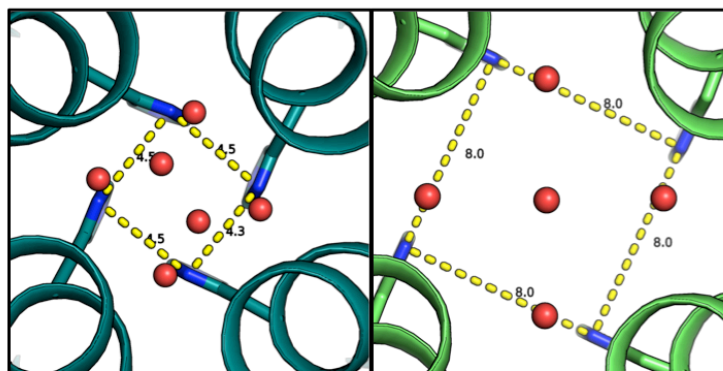


**Figure 3.7. Solvent layer above His37 expands in Inward<sub>open</sub> conformation.** Solvent layer above His37 in the cryogenic structure of the Inward<sub>closed</sub> conformation at pH 6.5 (3LBW,<sup>36</sup> left) and the room temperature XFEL structure at pH 6.5. The distance between the His37 residues increases from 4.5 Å to 8.0 Å and the water network expands.

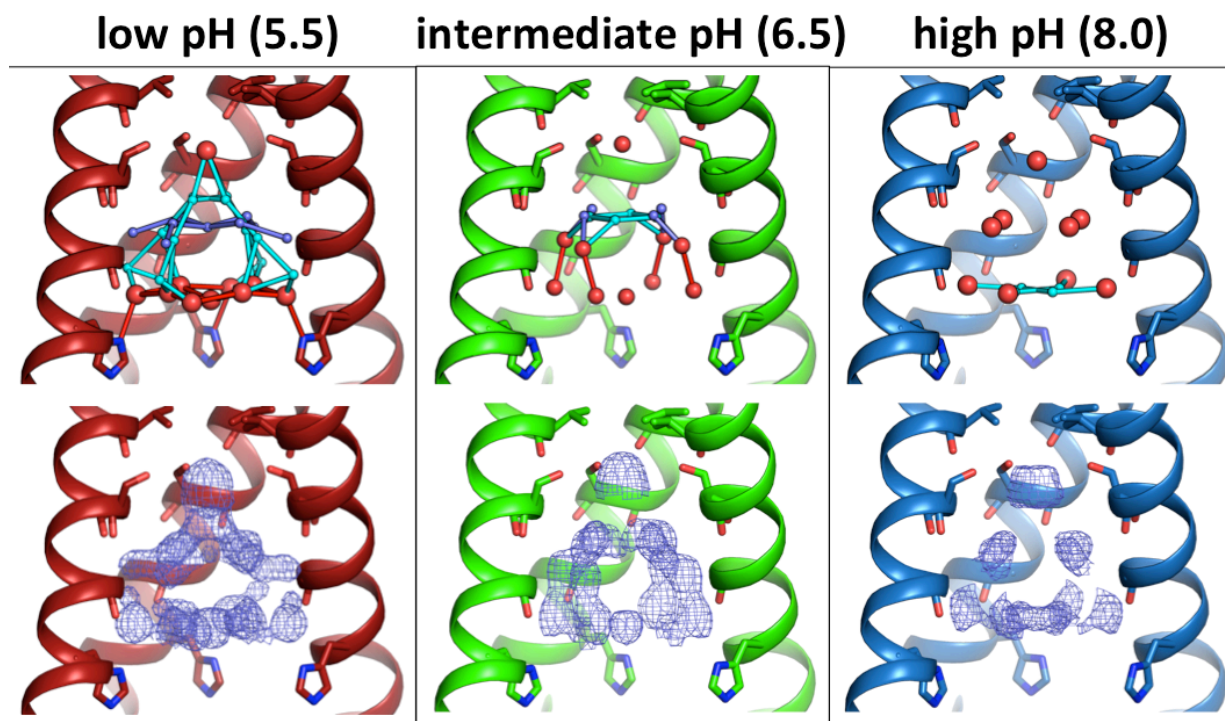


**Figure 3.8. Room temperature XFEL structures of M2TM under all pH conditions.** Low (pH 5.5, 5JOO, red), intermediate (pH 6.5, 5UM1, green), and high (pH 8.0, 5TTC, blue) pH structures are shown as described in Figure 1. **Top:** The most ordered waters are observed under the low pH condition, with fewer waters present at intermediate pH and the smallest number of ordered waters at high pH. Moving from low to high pH, the number of half occupancy waters decreases and the hydrogen bonding network becomes less complex. **Bottom:** The same trend is observed from the electron density maps; the largest volume of solvent density is at low pH, the smallest volume is at high pH.

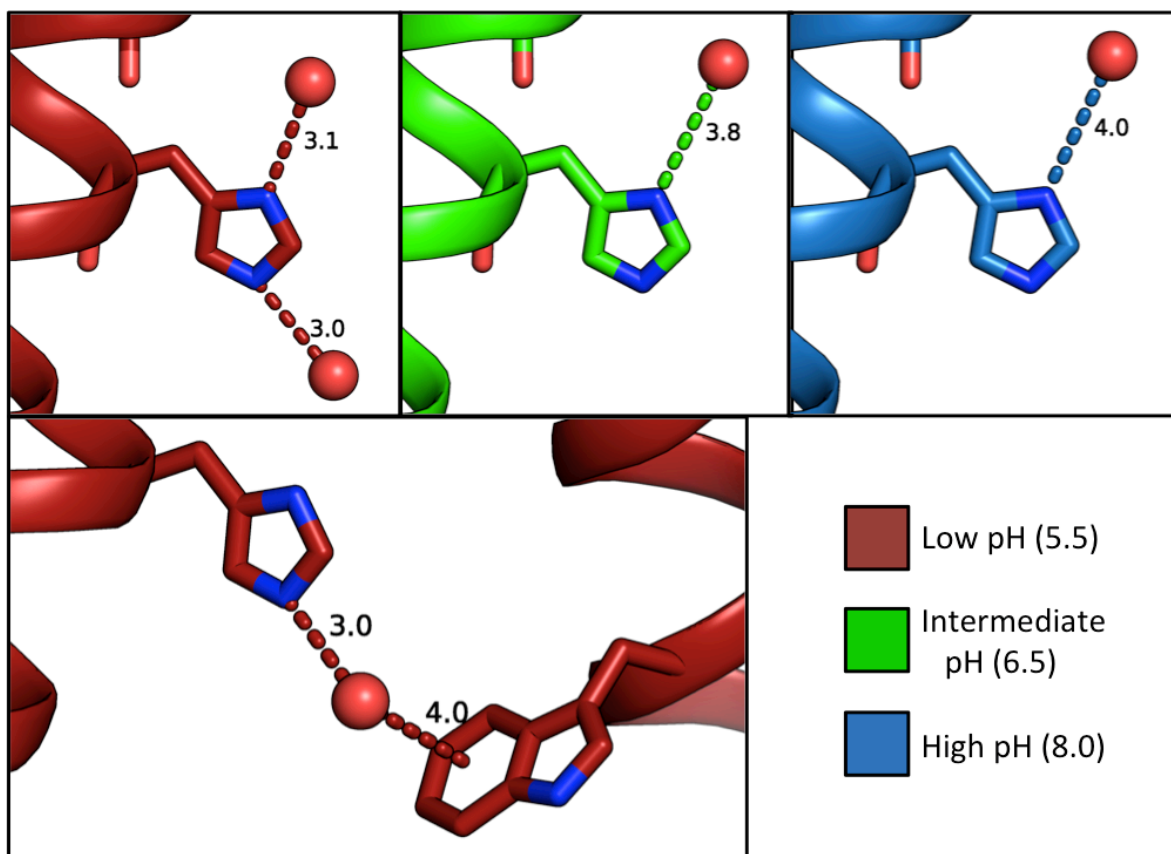


**Figure 3.9. Distance of water from gating His37 residues in all XFEL structures.** Distance of waters from His37 residues in XFEL structures at low (5.5), intermediate (6.5), and high (8.0) pH, measured in Angstroms (Å). Top: Side view of one monomer; only the waters in the low pH XFEL structure are close enough to form hydrogen bonds with His37. Bottom: In the low pH XFEL structure, the water hydrogen bonding to the epsilon nitrogen of His37 is positioned close enough to the Trp41 of an adjacent monomer to form a cation- $\pi$  interaction.

The ability to crystallize M2TM in the Inward<sub>open</sub> configuration over a wide range of pH conditions allows us to examine the protonated state of His37 after the conformational transition from the Inward<sub>closed</sub> state, as well as the metastable intermediate that occurs following release of the proton to the interior of the virus.

At low pH, the solvent is well ordered and there are multiple pathways to enable rapid proton diffusion and enthalpic stabilization throughout the lumen of the channel reaching to Val27, particularly in the vicinity of His37 and Gly34. This finding is consistent with solid state

NMR,<sup>59</sup> MD,<sup>45</sup> and 2D IR studies,<sup>60</sup> which show increased hydration and proton diffusion when the His37 tetrad is highly protonated. By contrast, the extent of ordered solvent decreases as the pH is increased (**Fig. 3.8, Table 3.1**). These findings clearly show that the water structure seen in the low pH form of the Inward<sub>open</sub> state plays an important role in stabilizing charge in the highly protonated His37 state. Furthermore, these findings indicate that this stabilizing network is lost following the loss of a proton to create the metastable deprotonated state. This loss of specific hydration might contribute to lowering the activation energy for returning to the resting Inward<sub>closed</sub> state during the conduction cycle.

### 3.5 Materials and Methods

The M2TM transmembrane domain (residues 22-46) was reconstituted into the lipid cubic phase (LCP)<sup>61</sup> and I4 crystals were grown as previously described.<sup>37</sup> M2 crystals in concentrations ranging from 10<sup>6</sup>-10<sup>9</sup> crystals per mL grew in a sponge phase slurry and were pooled into milliliter quantities (**Fig. 3.10**), then monoolein was added to increase the viscosity of the sample. Preliminary diffraction experiments were carried out at the Linac Coherent Light Source (LCLS) to diffract mounted single crystals and microcrystals grown on grids.<sup>62</sup>

XFEL data collection techniques were used to obtain room temperature structures of the M2 channel with minimal radiation damage. By using serial diffraction techniques, we are able to observe the ensemble average of the M2 channel's water network over tens of thousands of crystals per dataset. The XFEL datasets described in this paper were collected using a Diverse Application Platform for Hard X-ray Diffraction in SACLA (DAPHNIS)<sup>63</sup> at SPring-8 Angstrom Compact free-electron LAsER (SACLA) beamline BL3 using a 1.1587 Å beam with a pulse rate of 30 Hz and a MPCCD detector. An LCP injection system<sup>64</sup> was used to continuously deliver

sample to the XFEL beam. Three pH conditions were examined: pH 5.5 "low pH" state, PDB code 5JOO; pH 6.5 "intermediate pH" state, PDB code 5UM1; and pH 8.0 "high pH" state, PDB code 5TTC.

Frames of data containing diffraction patterns were identified using Cheetah.<sup>65,66</sup> Indexing and integration were done using cctbx.xfel.<sup>67</sup> Postrefinement and merging were carried out in cctbx.prime<sup>68</sup> (**Table 3.2**), and the Brehm & Diederichs algorithm<sup>69</sup> was used to resolve the indexing ambiguity resulting from the I4 space group of the diffracted crystals (**Table 3.3**). Molecular replacement and refinement were performed using Phenix<sup>70</sup> (**Table 3.4**).

The high and low pH datasets are complete to a resolution of 1.40 Å, which was the detector-limited resolution. The intermediate pH condition was truncated to 1.45 Å because the crystals at this pH condition diffracted to a slightly lower resolution on average.  $CC_{1/2}$  and paired refinement<sup>71,72</sup> were used to determine the maximum resolution.

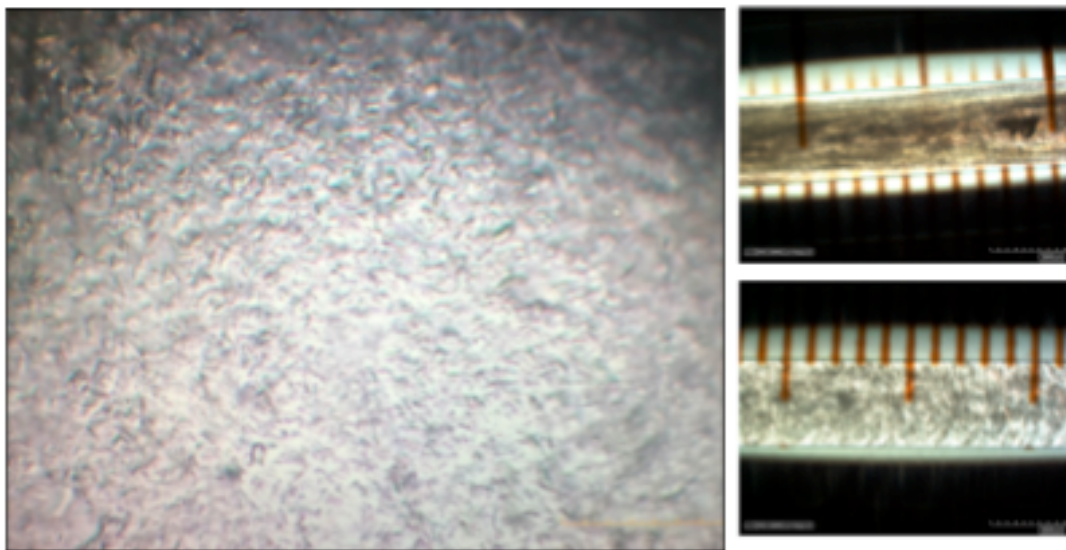


**Figure 3.10. High concentration solution of M2TM microcrystals.** Left: visible light image of square M2TM(22-46) microcrystals at a concentration of over  $1 \times 10^9$  per mL. Right: visible light image of glass syringes full of pooled M2 microcrystals.

**Table 3.2. Data processing statistics for room temperature XFEL datasets.** Note that post-refinement with Prime calculates  $I/s(I)$  after the integrated intensities are post-refined and merged; scale/partiality factors are applied the standard deviations of individual partial observations ( $\text{sigI}$ ) including inflation factors (Uervirojnangkoorn *et al.* 2015, Equation 21).<sup>68</sup> This is different from sigma values from CrystFEL, which are calculated as population sigma, not by error propagation from sigmas of individual partial observations. This results in results in lower  $I/s(I)$  in the highest resolution shell when compared to traditional methods of refinement. As a result,  $I/s(I)$  is not an appropriate statistic in this shell. Data in successively higher resolution shells were included in a series of refinements as long as  $CC_{1/2}$  was greater than 0.50, and an improvement in  $R_{\text{free}}$  was observed following the procedure of Karplus and Diederichs.<sup>71</sup>

|                                      | <b>low pH (5.5)</b>      | <b>intermediate pH (6.5)</b> | <b>high pH (8.0)</b>     |
|--------------------------------------|--------------------------|------------------------------|--------------------------|
| <b>PDB code</b>                      | 5JOO                     | 5UM1                         | 5TTC                     |
| <b>Space group</b>                   | I4                       | I4                           | I4                       |
| <b>Unit cell (Å)</b>                 | 30.1, 30.1, 67.4         | 29.9, 29.9, 67.8             | 29.8, 29.8, 68.0         |
| <b>Resolution range (Å)</b>          | 1.4-27.45<br>(1.40-1.42) | 1.45-27.35<br>(1.45-1.48)    | 1.4-27.32<br>(1.40-1.42) |
| <b>No. of frames</b>                 | 34,113                   | 29,173                       | 64,249                   |
| <b>Unique reflections</b>            | 5922                     | 5297                         | 5886                     |
| <b>Completeness (%)</b>              | 100                      | 100                          | 100                      |
| <b>Redundancy</b>                    | 622.87 (177.22)          | 624.00 (92.86)               | 1356.36 (73.57)          |
| <b><math>CC_{1/2}</math></b>         | 0.9540 (0.5266)          | 0.9228 (0.5020)              | 0.9996 (0.3075)          |
| <b><math>R_{\text{split}}</math></b> | 0.1172 (0.6464)          | 0.1016 (0.7420)              | 0.0235 (0.1724)          |

**Table 3.3. Twin fractions.** Estimated twin fractions for room temperature XFEL datasets after correction of indexing ambiguity.

|                                  | <b>low pH (5.5)</b> | <b>intermediate pH (6.5)</b> | <b>high pH (8.0)</b> |
|----------------------------------|---------------------|------------------------------|----------------------|
| <b>Britton analyses</b>          | 0.057               | 0.091                        | 0.072                |
| <b>H-test</b>                    | 0.185               | 0.244                        | 0.166                |
| <b>Maximum likelihood method</b> | 0.026               | 0.068                        | 0.043                |

**Table 3.4. Refinement statistics for room temperature XFEL structures.**

|  | <b>low pH (5.5)</b> | <b>intermediate<br/>pH (6.5)</b> | <b>high pH (8.0)</b> |
|--|---------------------|----------------------------------|----------------------|
| <b>PDB code</b>                              | 5J00                | 5UM1                             | 5TTC                 |
| <b>Resolution range (Å)</b>                  | 21.25 - 1.40        | 21.13 - 1.45                     | 21.09 - 1.40         |
| <b>Reflections refined against</b>           | 5,401               | 4,643                            | 5,885                |
| <b>Completeness (working + test)<br/>(%)</b> | 94.06               | 87.8                             | 99.98                |
| <b>R<sub>work</sub></b>                      | 0.2043              | 0.2128                           | 0.1981               |
| <b>R<sub>free</sub></b>                      | 0.2373              | 0.2296                           | 0.2289               |
| <b>No. of non-hydrogen atoms</b>             | 226                 | 218                              | 221                  |
| <b>Macromolecules</b>                        | 192                 | 192                              | 192                  |
| <b>Ligands</b>                               | 7                   | 7                                | 7                    |
| <b>Water</b>                                 | 25                  | 20                               | 20                   |
| <b>Ramachandran plot favored<br/>(%)</b>     | 100                 | 100                              | 100                  |
| <b>RMS deviations (bonds (Å))</b>            | 0.003               | 0.003                            | 0.003                |
| <b>RMS deviations (angles (°))</b>           | 0.622               | 0.572                            | 0.622                |
| <b>Average B-factor (Å<sup>2</sup>)</b>      | 21.5                | 27.8                             | 21.2                 |
| <b>Macromolecules (Å<sup>2</sup>)</b>        | 19                  | 26.7                             | 19.3                 |
| <b>Ligands (Å<sup>2</sup>)</b>               | 18.4                | 26                               | 17.4                 |
| <b>Solvent (Å<sup>2</sup>)</b>               | 40.4                | 39.2                             | 38.8                 |

### 3.6 Acknowledgements

J.L.T, W.F.D, and experimental work were supported by NIH grant GM122603 and GM117593. N.K.S. acknowledges NIH GM117126 for computational methods. R.A.W. is supported by the NSF GRFP; J.S.F. is a Searle Scholar, Pew Scholar, and Packard Fellow, and is supported by NIH OD009180, NIH GM110580, and NSF STC-1231306. S.I.; O.N., and F.Y. were supported by the X-ray Free-Electron Laser Priority Strategy Program (MEXT). Use of the LCP crystallization robot was made possible by NCRN grant 1S10RR027234-01. Preliminary XFEL diffraction experiments were carried out at LCLS XPP (PCS proposal LG53). Use of the Linac Coherent Light Source (LCLS), SLAC National Accelerator Laboratory, is supported by the U.S. Department of Energy, Office of Science, Office of Basic Energy Sciences under Contract No.

DE-AC02-76SF00515. The XFEL datasets described in this paper were collected at BL3 of SACLA with the approval of the Japan Synchrotron Radiation Research Institute (JASRI) (Proposal No. 2015A8048, 2015B8028, 2016A8030). We acknowledge computational support from SACLA HPC system and Mini-K supercomputer system.

### **3.7 Detailed Methods**

*3.7.1 Peptide synthesis, purification, and reconstitution into lipid.* Influenza A M2TM(22-46) (Ac-SSDPLVVAASIIGILHLILWILDRL-NH<sub>3</sub>) was manually synthesized, purified, and reconstituted into the lipid cubic phase, then crystals were grown as previously described.<sup>37</sup>

*3.7.2 Microcrystal optimization.* Large concentrations of microcrystals are needed for XFEL experiments. Attempts were made to scale up crystal growth in syringes according to Cherezov's method,<sup>73</sup> but under these conditions the lipid cubic phase remained separated from the precipitant solution and did not expand into the sponge phase that is necessary for I4 symmetry M2 crystals to form. Instead, a new protocol was made to increase the scale of the crystal drops from the initial 96-well conditions. First, the concentration of peptide in the lipid cubic phase was increased from the initial condition of approximately 1 mM peptide in LCP to approximately 12 mM peptide in LCP. One microliter of LCP was dispensed onto a screw-cap crystallization support (Qiagen), then 2 microliters of crystallization solution were added on top of the LCP. The crystallization support was screwed into the well to create a hanging drop above an empty reservoir. Exposing the hanging drop to the air inside the sealed crystallization well allowed the lipid cubic phase to expand into the sponge phase and create a high concentration of M2 crystals. The solution containing these crystals was pipetted into syringes and stored at -20 °C.



The composition of the crystal solution was as follows:

Lipid Cubic Phase (LCP): 60% monoolein, 40% 50 mM OG in water, 12 mM M2TM(22-46)

precipitant solution: 0.2 M CaCl<sub>2</sub>, 44% PEG 400, plus either 0.1 M Tris pH 8.0 or 0.1 M Tris pH 6.5 or 0.1 M MES pH 5.5, depending on the desired pH condition. Crystals formed at a LCP:ppt solution ratio of 1:2.

Because crystals formed after the lipid cubic phase transitioned into a sponge phase with an oil-like consistency, the sample's viscosity was increased to make it compatible with an LCP injection system. Monoolein was added to the crystal-containing solution at a 1:1 to 2:1 ratio and mixed using a metal syringe coupler. The crystals within the sample were stable after the addition of monoolein, with no damage to the crystals observed immediately after mixing or after storing the sponge phase/ monoolein mixture for multiple days. Before data collection, the pH of the sample was confirmed using a pH meter and pH paper. For the high pH sample, the pH was adjusted by adding Tris pH 8.5 precipitant solution (described above) and using a syringe coupler to homogenize the sample.

*3.7.3 XFEL data collection.* Preliminary data were collected at the Linac Coherent Light Source (LCLS) in SLAC National Accelerator Laboratory, CA; this data consisted of frames of data from fixed target data collection and also frames of data from crystallization on goniometer-mountable grids.<sup>62</sup>

Data collection was carried out at ambient temperature (20 °C) at SACLA in Hyogo, Japan using SACLA BL3. Data were collected continuously with a pulse repetition rate of 30 Hz in a helium chamber using an LCP injector to flow crystals to the beam. The injector nozzle size was 100 μm and the sample flow rate was 0.42 μL/min. The beam size used was 1.5 microns; the

beam stop was 3 mm. For the low and intermediate pH datasets, the beam energy was 10.7 keV, which in combination with the MultiPort Charged Coupled Device detector (MPCCD) geometry limited the resolution of the data to 1.4 Å. Hit rates ranged from 3-10% for these samples. The high pH data set was collected using SACLA's LCP injection system in a He chamber with a beam energy of 10.5 keV. Hit rates ranged from 30% to 70% because of the high pH sample's large concentration of crystals. A portion of the diffraction from each dataset was collected using a 0.025 mm Al attenuator so that low resolution spots could be observed without saturating the detector signal.

*3.7.4 Data processing.* Frames of data containing diffraction were identified using Cheetah.<sup>65,66</sup> Indexing and integration were done using *cctbx.xfel*<sup>67</sup> on dark-subtracted images. The Brehm & Diederichs algorithm<sup>69</sup> was used to resolve the indexing ambiguity resulting from the I4 space group of the diffracted crystals. Table S3 lists the predicted twin fraction for the datasets after this correction was applied. The number of frames used for data processing in each pH condition is as follows: 34,113 frames at low pH, 29,173 frames at intermediate pH, and 64,249 frames at high pH. Post-refinement and merging were carried out with *cctbx.prime*.<sup>68</sup> Resolution cut-offs were determined by monitoring  $CC_{1/2}$  and  $R_{\text{free}}$  in paired refinements following the procedure of Karplus and Diederichs.<sup>71</sup> For the high and low pH conditions, the 1.40 Å resolution cutoff was limited only by the detector. The intermediate pH condition data were truncated to 1.45 Å because the crystals prepared in this pH condition diffracted to a slightly lower resolution on average.

*3.7.5 Molecular replacement and refinement.* Molecular replacement and refinement were carried out in Phenix.<sup>70</sup> The model used for molecular replacement was PDB structure 4QK7. The inclusion of alternate side chain conformers did not significantly improve the fit of the model to the electron density, so these were omitted in the final model. Waters were added to the model where positive Fo-Fc indicated they should be; those that occupied smaller Fo-Fc density peaks were modeled as half occupancy, creating alternate occupancy water networks A and B. Solvent and ions located on the axis of fourfold symmetry at the center of the channel were modeled as having an occupancy of 0.25.

R and free R factors are poorer for the XFEL structures relative to previous structures from synchrotron diffraction experiments because of the difficulty of getting good intensity estimates from serial diffraction. The same effect can be seen in Uervirojnangkoorn et al. 2015,<sup>68</sup> where myoglobin data at 1.45 Å yields R-factors comparable with the ones presented in this work. The higher level of detail that we claim to observe is an increased volume of electron density in the RT XFEL structures relative to the RT synchrotron structures, which is likely an effect of minimizing radiation damage.

### *3.7.6 RMSDs to previous structures.*

Monomer RMSDs:

low pH: 5JOO to 4QKM (0.091 Å), 5JOO to 4QKC (0.155 Å)

high pH: 5TTC to 4QKL (0.081 Å), 5TTC to 4QK7 (0.179 Å)

Tetramer RMSDs:

low pH: 5JOO to 4QKM (0.194 Å), 5JOO to 4QKC (0.192 Å)

high pH: 5TTC to 4QKL (0.147 Å), 5TTC to 4QK7 (0.241 Å)

*3.7.7 Analysis of hydrogen bonding networks in the low pH XFEL structure.* The water network analysis at low pH was carried using the NetworkX library in Python.<sup>74</sup> Each water molecule corresponded to one node in the graph. An edge connected two nodes if they were at least 2.6 Å apart. The largest cliques that contained water molecules with partial occupancy was then extracted. The corresponding networks were finally filtered for symmetry and consistent total occupancy.

### 3.8 References

- 1 Levitt, D. G., Elias, S. R. & Hautman, J. M. Number of water molecules coupled to the transport of sodium, potassium and hydrogen ions via gramicidin, nonactin or valinomycin. *Biochimica et Biophysica Acta (BBA) - Biomembranes* **512**, 436-451, doi:[http://dx.doi.org/10.1016/0005-2736\(78\)90266-3](http://dx.doi.org/10.1016/0005-2736(78)90266-3) (1978).
- 2 Rosenberg, P. A. & Finkelstein, A. Interaction of ions and water in gramicidin A channels: streaming potentials across lipid bilayer membranes. *The Journal of General Physiology* **72**, 327 (1978).
- 3 Agmon, N. The Grotthuss mechanism. *Chemical Physics Letters* **244**, 456-462, doi:[http://dx.doi.org/10.1016/0009-2614\(95\)00905-J](http://dx.doi.org/10.1016/0009-2614(95)00905-J) (1995).
- 4 Bernal, J. D. & Fowler, R. H. A Theory of Water and Ionic Solution, with Particular Reference to Hydrogen and Hydroxyl Ions. *The Journal of Chemical Physics* **1**, 515-548, doi:10.1063/1.1749327 (1933).
- 5 de Grotthuss, C. J. T. Mémoire sur la décomposition de l'eau et des corps qu'elle tient en dissolution à l'aide de l'électricité galvanique. *Annales de Chimie* **LVIII**, 54-74 (1806).
- 6 Brewer, M. L., Schmitt, U. W. & Voth, G. A. The formation and dynamics of proton wires in channel environments. *Biophys. J.* **80**, 1691-1702 (2001).
- 7 Day, T. J. F., Schmitt, U. W. & Voth, G. A. The Mechanism of Hydrated Proton Transport in Water. *J. Am. Chem. Soc.* **122**, 12027-12028, doi:10.1021/ja002506n (2000).
- 8 Nagle, J. F. & Morowitz, H. J. Molecular mechanisms for proton transport in membranes. *Proceedings of the National Academy of Sciences* **75**, 298-302 (1978).
- 9 Pomès, R. & Roux, B. Structure and dynamics of a proton wire: a theoretical study of H<sup>+</sup> translocation along the single-file water chain in the gramicidin A channel. *Biophys. J.* **71**, 19-39, doi:[http://dx.doi.org/10.1016/S0006-3495\(96\)79211-1](http://dx.doi.org/10.1016/S0006-3495(96)79211-1) (1996).
- 10 Park, E. K., Castrucci, M. R., Portner, A. & Kawaoka, Y. The M2 Ectodomain Is Important for Its Incorporation into Influenza A Virions. *J. Virol.* **72**, 2449-2455 (1998).
- 11 Salom, D., Hill, B. R., Lear, J. D. & DeGrado, W. F. pH-Dependent Tetramerization and Amantadine Binding of the Transmembrane Helix of M2 from the Influenza A Virus. *Biochemistry* **39**, 14160-14170 (2000).
- 12 Chizhnikov, I. V. *et al.* Selective proton permeability and pH regulation of the influenza virus M2 channel expressed in mouse erythroleukaemia cells. *J. Physiol.-London* **494**, 329-336 (1996).

- 13 Lin, T. I. & Schroeder, C. Definitive assignment of proton selectivity and attoampere unitary current to the M2 ion channel protein of influenza A virus. *J. Virol.* **75**, 3647-3656, doi:10.1128/jvi.75.8.3647-3656.2001 (2001).
- 14 Mould, J. A. *et al.* Permeation and activation of the M-2 ion channel of influenza A virus. *J. Biol. Chem.* **275**, 31038-31050, doi:10.1074/jbc.M003663200 (2000).
- 15 Shimbo, K., Brassard, D. L., Lamb, R. A. & Pinto, L. H. Ion selectivity and activation of the M2 ion channel of influenza virus. *Biophys. J.* **70**, 1335-1346 (1996).
- 16 Duff, K. C. & Ashley, R. H. The transmembrane domain of influenza A M2 protein forms amantadine-sensitive proton channels in planar lipid bilayers. *Virology* **190**, 485-489, doi:[http://dx.doi.org/10.1016/0042-6822\(92\)91239-Q](http://dx.doi.org/10.1016/0042-6822(92)91239-Q) (1992).
- 17 Ma, C. L. *et al.* Identification of the functional core of the influenza A virus A/M2 proton-selective ion channel. *Proc. Natl. Acad. Sci. U. S. A.* **106**, 12283-12288, doi:10.1073/pnas.0905726106 (2009).
- 18 Pinto, L. H. & Lamb, R. A. Controlling influenza virus replication by inhibiting its proton channel. *Mol. Biosyst.* **3**, 18-23, doi:10.1039/b611613m (2007).
- 19 Holsinger, L. J., Nichani, D., Pinto, L. H. & Lamb, R. A. Influenza A virus M2 ion channel protein: a structure-function analysis. *J. Virol.* **68**, 1551-1563 (1994).
- 20 Wang, C., Lamb, R. A. & Pinto, L. H. Direct Measurement of the Influenza A Virus M2 Protein Ion Channel Activity in Mammalian Cells. *Virology* **205**, 133-140, doi:<http://dx.doi.org/10.1006/viro.1994.1628> (1994).
- 21 Roberts, K. L., Leser, G. P., Ma, C. & Lamb, R. A. The Amphipathic Helix of Influenza A Virus M2 Protein Is Required for Filamentous Bud Formation and Scission of Filamentous and Spherical Particles. *J. Virol.* **87**, 9973-9982, doi:10.1128/jvi.01363-13 (2013).
- 22 Rossman, J. S., Jing, X., Leser, G. P. & Lamb, R. A. Influenza Virus M2 Protein Mediates ESCRT-Independent Membrane Scission. *Cell* **142**, 902-913, doi:10.1016/j.cell.2010.08.029 (2010).
- 23 Schmidt, N. W., Mishra, A., Wang, J., DeGrado, W. F. & Wong, G. C. L. Influenza Virus A M2 Protein Generates Negative Gaussian Membrane Curvature Necessary for Budding and Scission. *J. Am. Chem. Soc.* **135**, 13710-13719, doi:10.1021/ja400146z (2013).
- 24 Martin, K. & Helenius, A. Nuclear transport of influenza virus ribonucleoproteins: The viral matrix protein (M1) promotes export and inhibits import. *Cell* **67**, 117-130, doi:10.1016/0092-8674(91)90576-k (1991).

- 25 McCown, M. F. & Pekosz, A. Distinct Domains of the Influenza A Virus M2 Protein Cytoplasmic Tail Mediate Binding to the M1 Protein and Facilitate Infectious Virus Production. *J. Virol.* **80**, 8178-8189, doi:10.1128/jvi.00627-06 (2006).
- 26 Tang, Y. J., Zaitseva, F., Lamb, R. A. & Pinto, L. H. The gate of the influenza virus M-2 proton channel is formed by a single tryptophan residue. *J. Biol. Chem.* **277**, 39880-39886, doi:10.1074/jbc.M206582200 (2002).
- 27 Wang, C., Lamb, R. A. & Pinto, L. H. Activation of the M2 ion channel of influenza virus: a role for the transmembrane domain histidine residue. *Biophys J* **69**, 1363-1371 (1995).
- 28 Colvin, M. T., Andreas, L. B., Chou, J. J. & Griffin, R. G. Proton Association Constants of His 37 in the Influenza-A M2(18-60) Dimer-of-Dimers. *Biochemistry* **53**, 5987-5994, doi:10.1021/bi5005393 (2014).
- 29 Hu, F. H., Schmidt-Rohr, K. & Hong, M. NMR detection of pH-dependent histidine-water proton exchange reveals the conduction mechanism of a transmembrane proton channel. *J. Am. Chem. Soc.* **134**, 3703-3713, doi:10.1021/ja2081185 (2012).
- 30 Hu, J. *et al.* Histidines, heart of the hydrogen ion channel from influenza A virus: Toward an understanding of conductance and proton selectivity. *Proc. Natl. Acad. Sci. U. S. A.* **103**, 6865-6870, doi:10.1073/pnas.0601944103 (2006).
- 31 Liao, S. Y., Yang, Y., Tietze, D. & Hong, M. The Influenza M2 Cytoplasmic Tail Changes the Proton-Exchange Equilibria and the Backbone Conformation of the Transmembrane Histidine Residue to Facilitate Proton Conduction. *J. Am. Chem. Soc.* **137**, 6067-6077, doi:10.1021/jacs.5b02510 (2015).
- 32 Miao, Y., Fu, R., Zhou, H.-X. & Cross, T. A. Dynamic Short Hydrogen Bonds in Histidine Tetrad of Full-Length M2 Proton Channel Reveal Tetrameric Structural Heterogeneity and Functional Mechanism. *Structure* **23**, 2300-2308, doi:10.1016/j.str.2015.09.011 (2015).
- 33 Leiding, T., Wang, J., Martinsson, J., DeGrado, W. F. & Arskold, S. P. Proton and cation transport activity of the M2 proton channel from influenza A virus. *Proc. Natl. Acad. Sci. U. S. A.* **107**, 15409-15414, doi:10.1073/pnas.1009997107 (2010).
- 34 Pielak, R. M. & Chou, J. J. Kinetic Analysis of the M2 Proton Conduction of the Influenza Virus. *J. Am. Chem. Soc.* **132**, 17695-17697, doi:10.1021/ja108458u (2010).
- 35 Stouffer, A. L. *et al.* Structural basis for the function and inhibition of an influenza virus proton channel. *Nature* **451**, 596-U513, doi:10.1038/nature06528 (2008).
- 36 Acharya, R. *et al.* Structure and mechanism of proton transport through the transmembrane tetrameric M2 protein bundle of the influenza A virus. *Proc Natl Acad Sci U S A* **107**, 15075-15080, doi:10.1073/pnas.1007071107 (2010).

- 37 Thomaston, J. L. *et al.* High-resolution structures of the M2 channel from influenza A virus reveal dynamic pathways for proton stabilization and transduction. *Proceedings of the National Academy of Sciences* **112**, 14260-14265, doi:10.1073/pnas.1518493112 (2015).
- 38 Thomaston, J. L. & DeGrado, W. F. Crystal structure of the drug-resistant S31N influenza M2 proton channel. *Protein Sci.* **25**, 1551-1554, doi:10.1002/pro.2937 (2016).
- 39 Schnell, J. R. & Chou, J. J. Structure and mechanism of the M2 proton channel of influenza A virus. *Nature* **451**, 591-U512, doi:10.1038/nature06531 (2008).
- 40 Wang, J. *et al.* Structure and inhibition of the drug-resistant S31N mutant of the M2 ion channel of influenza A virus. *Proc Natl Acad Sci U S A* **110**, 1315-1320, doi:10.1073/pnas.1216526110 (2013).
- 41 Cady, S. D. *et al.* Structure of the amantadine binding site of influenza M2 proton channels in lipid bilayers. *Nature* **463**, 689-U127, doi:10.1038/nature08722 (2010).
- 42 Sharma, M. *et al.* Insight into the mechanism of the influenza a proton channel from a structure in a lipid bilayer. *Science* **330**, 509-512, doi:10.1126/science.1191750 (2010).
- 43 Hu, F., Luo, W., Cady, S. D. & Hong, M. Conformational Plasticity of the Influenza A M2 Transmembrane Helix in Lipid Bilayers Under Varying pH, Drug Binding and Membrane Thickness. *Biochimica et biophysica acta* **1808**, 415-423, doi:10.1016/j.bbamem.2010.09.014 (2011).
- 44 Li, C., Qin, H., Gao, F. P. & Cross, T. A. Solid-state NMR characterization of conformational plasticity within the transmembrane domain of the influenza A M2 proton channel. *Biochim Biophys Acta* **1768**, 3162-3170 (2007).
- 45 Khurana, E. *et al.* Molecular dynamics calculations suggest a conduction mechanism for the M2 proton channel from influenza A virus. *Proceedings of the National Academy of Sciences* **106**, 1069-1074, doi:10.1073/pnas.0811720106 (2009).
- 46 Liang, R., Li, H., Swanson, J. M. J. & Voth, G. A. Multiscale simulation reveals a multifaceted mechanism of proton permeation through the influenza A M2 proton channel. *Proc. Natl. Acad. Sci. U. S. A.* **111**, 9396-9401, doi:10.1073/pnas.1401997111 (2014).
- 47 Liang, R. *et al.* Acid activation mechanism of the influenza A M2 proton channel. *Proceedings of the National Academy of Sciences* **113**, E6955-E6964, doi:10.1073/pnas.1615471113 (2016).



- 48 Yi, M., Cross, T. A. & Zhou, H. X. A secondary gate as a mechanism for inhibition of the M2 proton channel by amantadine. *J Phys Chem B* **112**, 7977-7979, doi:10.1021/jp800171m (2008).
- 49 DiFrancesco, M. L., Hansen, U.-P., Thiel, G., Moroni, A. & Schroeder, I. Effect of Cytosolic pH on Inward Currents Reveals Structural Characteristics of the Proton Transport Cycle in the Influenza A Protein M2 in Cell-Free Membrane Patches of *Xenopus* oocytes. *PLoS One* **9**, e107406, doi:10.1371/journal.pone.0107406 (2014).
- 50 Carnevale, V., Fiorin, G., Levine, B. G., DeGrado, W. F. & Klein, M. L. Multiple proton confinement in the M2 channel from the influenza A virus. *J Phys Chem C* **114**, 20856-20863, doi:Doi 10.1021/Jp107431g (2010).
- 51 Chen, H., Wu, Y. & Voth, G. A. Proton transport behavior through the influenza A M2 channel: insights from molecular simulation. *Biophys. J.* **93**, 3470-3479, doi:10.1529/biophysj.107.105742 (2007).
- 52 Wei, C. & Pohorille, A. Activation and proton transport mechanism in influenza A M2 channel. *Biophys J* **105**, 2036-2045, doi:10.1016/j.bpj.2013.08.030 (2013).
- 53 Lomb, L. *et al.* Radiation damage in protein serial femtosecond crystallography using an x-ray free-electron laser. *Physical review. B, Condensed matter and materials physics* **84**, 214111, doi:10.1103/PhysRevB.84.214111 (2011).
- 54 Barty, A. *et al.* Self-terminating diffraction gates femtosecond X-ray nanocrystallography measurements. *Nature photonics* **6**, 35-40, doi:10.1038/nphoton.2011.297 (2012).
- 55 Chapman, H. N. *et al.* Femtosecond X-ray protein nanocrystallography. *Nature* **470**, 73-77, doi:10.1038/nature09750 (2011).
- 56 Neutze, R., Wouts, R., van der Spoel, D., Weckert, E. & Hajdu, J. Potential for biomolecular imaging with femtosecond X-ray pulses. *Nature* **406**, 752-757 (2000).
- 57 Halle, B. Biomolecular cryocrystallography: structural changes during flash-cooling. *Proc Natl Acad Sci U S A* **101**, 4793-4798, doi:10.1073/pnas.0308315101 (2004).
- 58 Balannik, V. *et al.* Functional Studies and Modeling of Pore-Lining Residue Mutants of the Influenza A Virus M2 Ion Channel. *Biochemistry* **49**, 696-708, doi:10.1021/bi901799k (2010).
- 59 Hu, F. H., Luo, W. B. & Hong, M. Mechanisms of proton conduction and gating in influenza M2 proton channels from solid-state NMR. *Science* **330**, 505-508, doi:DOI 10.1126/science.1191714 (2010).

- 60 Ghosh, A., Qiu, J., DeGrado, W. F. & Hochstrasser, R. M. Tidal surge in the M2 proton channel, sensed by 2D IR spectroscopy. *Proc. Natl. Acad. Sci. U. S. A.* **108**, 6115-6120, doi:10.1073/pnas.1103027108 (2011).
- 61 Jason, B., Hesson, C. & Martin, C. The Temperature-Composition Phase Diagram and Mesophase Structure Characterization of the Monoolein/Water System. *J. Phys. II France* **6**, 723-751 (1996).
- 62 Baxter, E. L. *et al.* High-density grids for efficient data collection from multiple crystals. *Acta Crystallographica Section D* **72**, 2-11, doi:doi:10.1107/S2059798315020847 (2016).
- 63 Tono, K. *et al.* Diverse application platform for hard X-ray diffraction in SACLA (DAPHNIS): application to serial protein crystallography using an X-ray free-electron laser. *Journal of Synchrotron Radiation* **22**, 532-537, doi:10.1107/s1600577515004464 (2015).
- 64 Weierstall, U. *et al.* Lipidic cubic phase injector facilitates membrane protein serial femtosecond crystallography. *Nature Communications* **5**, 3309, doi:10.1038/ncomms4309 (2014).
- 65 Barty, A. *et al.* Cheetah: software for high-throughput reduction and analysis of serial femtosecond X-ray diffraction data. *J. Appl. Crystallogr.* **47**, 1118-1131, doi:10.1107/s1600576714007626 (2014).
- 66 Nakane, T. *et al.* Data processing pipeline for serial femtosecond crystallography at SACLA. *J. Appl. Crystallogr.* **49**, 1035-1041, doi:doi:10.1107/S1600576716005720 (2016).
- 67 Sauter, N. K., Hattne, J., Grosse-Kunstleve, R. W. & Echols, N. New Python-based methods for data processing. *Acta Crystallographica Section D: Biological Crystallography* **69**, 1274-1282, doi:10.1107/s0907444913000863 (2013).
- 68 Uervirojnangkoorn, M. *et al.* Enabling X-ray free electron laser crystallography for challenging biological systems from a limited number of crystals. *eLife* (2015).
- 69 Brehm, W. & Diederichs, K. Breaking the indexing ambiguity in serial crystallography. *Acta Crystallographica Section D 1399-0047* **70**, 101-109 (2014).
- 70 Adams, P. D. *et al.* PHENIX: a comprehensive Python-based system for macromolecular structure solution. *Acta Crystallogr. Sect. D-Biol. Crystallogr.* **66**, 213-221, doi:10.1107/s0907444909052925 (2010).
- 71 Karplus, P. A. & Diederichs, K. Linking Crystallographic Model and Data Quality. *Science* **336**, 1030 (2012).

- 72 Lyubimov, A. Y. *et al.* Advances in X-ray free electron laser (XFEL) diffraction data processing applied to the crystal structure of the synaptotagmin-1 / SNARE complex. *eLife* **5**, e18740, doi:10.7554/eLife.18740 (2016).
- 73 Liu, W., Ishchenko, A. & Cherezov, V. Preparation of microcrystals in lipidic cubic phase for serial femtosecond crystallography. *Nat. Protocols* **9**, 2123-2134, doi:10.1038/nprot.2014.141 (2014).
- 74 Hagberg, A. A. S., Daniel A.; Swart, Pieter J. . Exploring network structure, dynamics, and function using NetworkX. *Proceedings of the 7th Python in Science Conference (SciPy2008)*, pp. 11--15 (Aug 2008).

## Chapter 4

### **Inhibitors of the M2 proton channel engage and disrupt transmembrane networks of hydrogen-bonded waters**

#### **4.1 Abstract**

Water-mediated interactions play key roles in drug binding. In protein sites with sparse polar functionality, a small-molecule approach is often viewed as insufficient to achieve high affinity and specificity. Here, we show that small molecules can enable potent inhibition by targeting key waters. X-ray crystal structures of the influenza A M2 proton channel with bound inhibitors reveal that ammonium groups bind to water-lined sites that are hypothesized to stabilize transient hydronium ions formed in the proton-conduction mechanism. Furthermore, the ammonium and adamantyl groups of the adamantyl-amine class of drugs are free to rotate in the channel, minimizing the entropic cost of binding. These drug-bound complexes provide the first high-resolution structures of drugs that interact with and disrupt the “water-wires” that are widely utilized throughout nature to facilitate proton diffusion within proteins.

#### **4.2 Introduction**

Protein channels and water-filled pores present a particularly challenging target for drug design. Typically, drugs bind their targets at extended allosteric or substrate-binding sites, lined with multiple functional groups capable of forming numerous protein-small molecule interactions. Often structural and functional water molecules play critical roles in drug interactions.<sup>1,2</sup> Water is also an important component in channels, but these proteins often have very constricted cavities with only sparse polar functionality available for drug design. The natural substrate in such cases can be as small as a single proton. Nevertheless, potent inhibitors

of channels can still be achieved, possibly by targeting water molecules that serve to hydrate charged groups during ion conduction. Examples of this include channel-blockers such as the chloride channel blocker, picrotoxin,<sup>3</sup> or the adamantyl-amine class of influenza A virus matrix 2 (M2) proton channel inhibitors (**Fig. 4.1**).<sup>4,5</sup> These compounds achieve high affinity, ligand efficiency, and biologically useful specificity, despite their relatively small size and low molecular weights (e.g., the M.W. of amantadine is 151 g/mol). Here we use X-ray crystallography to show the role of water in the binding and the mechanism of action of the adamantyl-amine class of M2 inhibitors. The hydrophobic groups of these molecules displace waters from the portion of the pore that faces the viral exterior, while the drug's positively charged ammonium group locks into water networks that normally hydrate and stabilize protons as they diffuse through the pore. Intriguingly, the  $\alpha$ -helical pore-lining carbonyl groups are physicochemical chameleons that are easily dehydrated to hydrophobically stabilize the binding of apolar groups from M2 inhibitors in the drug-bound form, and yet are also able to form stabilizing interactions with cations through water-mediated polar interactions in the drug-free form. We also elucidate several features of adamantane, which explain its increasingly successful use in drug design.<sup>6</sup>

Influenza virus infections are perennial problems. The 2017-2018 influenza season is a timely reminder of the devastating impact of influenza: between October 1, 2017 and April 30, 2018, 30,451 laboratory-confirmed influenza-associated hospitalizations have been reported in the United States.<sup>7</sup> Moreover, 2018 marks the 100-year anniversary of the 1918 Spanish Flu, which infected an estimated one-third of the human population and killed approximately 50 million people.<sup>8</sup> In recent years, resistance to the adamantyl-amine class of drugs has become widespread, leaving the neuraminidase inhibitor oseltamivir (Tamiflu) as the sole orally

bioavailable anti-influenza medication.<sup>9</sup> Thus, elucidating the structural mechanism of inhibition of adamantyl-amines has specific relevance to the design of new compounds to target drug-resistant influenza infections, as well as general relevance to the design of drugs that bind to the water-filled pores of channel proteins.

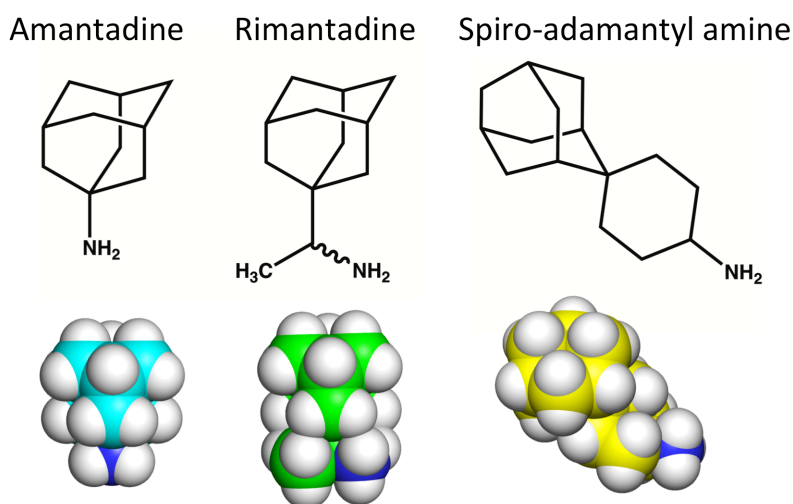


**Figure 4.1. Structures and space-filling models of amantadine, rimantadine, and spiro-adamantyl amine.** Chemical structures and space-filling models of amantadine (cyan), rimantadine (green), and spiro-adamantyl amine (yellow).

The M2 protein is a homotetrameric channel that serves several different functions during the life cycle of the virus,<sup>10-14</sup> which enters the cell via receptor-mediated endocytosis. The transmembrane (TM) domain (residues 23-46) transports protons from the low pH conditions of the endosome into the viral interior. The resulting drop in the intra-viral pH triggers the dissociation of viral ribonucleoproteins (RNPs) from the matrix 1 protein.<sup>15</sup> M2's extracellular domain (residues 1-22) aids incorporation of M2 into the virion, but this domain is absent in influenza B viruses.<sup>16</sup> An amphiphilic helix in the cytosolic tail of M2 (residues 46-60) assists viral budding and membrane scission, and a disordered domain at the C-terminus is involved in

virus assembly through interactions with M1.<sup>15</sup> The TM domain is the minimal construct needed for selective proton transport and amantadine binding.<sup>17-20</sup> The rate of conductance of the M2 TM domain and its ability to be inhibited by amantadine are nearly identical to the full-length protein when the proteins are expressed in frog oocytes or reconstituted in phospholipid vesicles.<sup>18,21</sup> In fact, the conductance rate differences between different-length constructs (when expressed or reconstituted under identical conditions) are smaller than those seen between point mutants found in different strains of the virus.<sup>22</sup> Thus, much crystallographic work has focused on the TM domain, because the extra-membrane domains appear to impede crystallization.

The structure of M2 has been studied using solution NMR, solid state NMR (SSNMR), and X-ray crystallography. Two conformational states of the conductance domain have been observed, in which the C-terminus is either largely closed or open to the viral interior (Inward<sub>closed</sub> and Inward<sub>open</sub>, respectively). The Inward<sub>closed</sub> state has been characterized through solution NMR,<sup>23,24</sup> SSNMR,<sup>25,26</sup> and X-ray crystallography.<sup>27</sup> The Inward<sub>open</sub> state has been characterized primarily through X-ray crystallography,<sup>20,28-30</sup> with conformational equilibria between the multiple states at low pH resulting in peak broadening in NMR studies.<sup>23,24,31</sup> The various crystallographic structures of the Inward<sub>open</sub> state are in good agreement with molecular dynamics simulations that quantitatively explain experimental conductance curves.<sup>32</sup> The degree of protonation of His37 near the C-terminal region of the pore defines the stability of the Inward<sub>open</sub> and Inward<sub>closed</sub> states. This residue also serves as a selectivity filter and proton shuttle that imbues M2 with its strong proton-selectivity.<sup>33,34</sup> The conductance mechanism involves a transporter-like cycling between different protonation states and the two conformations.<sup>35</sup>

Previously, structure-based approaches have been used to inform the design of M2 inhibitors that are effective against wild type and amantadine-resistant strains of the virus.<sup>36,37</sup>

However, high-resolution structural studies of M2 bound to inhibitors, particularly with high enough resolution to examine the critical role of water in drug binding, have been lacking. The only previous drug-bound structures were obtained at relatively low resolution by solution or solid state NMR,<sup>38,39</sup> and the sole crystal structure was solved at a diffraction limit of 3.5 Å.<sup>20</sup> These studies have been sufficient to locate the drug's general location, but not its engagement of the pore-lining residues and water molecules in the channel. Here, we report crystallographic structures of rimantadine bound to both the Inward<sub>open</sub> and Inward<sub>closed</sub> states of the wild-type (WT) M2 channel. We also determine structures of amantadine and a novel spiro-adamantyl amine inhibitor (**Fig. 4.1**) bound to the Inward<sub>closed</sub> states of WT M2 channel. These drug-bound structures describe the mechanism of binding and inhibition and inform the future design of drugs that interact with and disrupt the “water-wires” that are widely utilized throughout nature to facilitate proton diffusion within proteins.<sup>40</sup>

### 4.3 Results and Discussion

*4.3.1 The adamantane groups of rimantadine and amantadine snip water-wires, while the ammonium group engages the remaining water networks in the Inward<sub>closed</sub> state.* Using lipid cubic phase (LCP) crystallization techniques,<sup>41</sup> we have solved X-ray crystal structures of the M2 TM domain (residues 22-46) (M2TM) in the Inward<sub>closed</sub> state bound to rimantadine (PDB code 6BKL, 2.00 Å resolution) and amantadine (PDB code 6BKK, 2.00 Å resolution) (**Fig. 4.2a,b**). In both structures, the electron density (**Fig. 4.3**) unambiguously defines the positions of the drug and surrounding water molecules. A Polder omit map,<sup>42</sup> which is calculated by removing the drug and solvent from the model, shows good density for the drugs at a contour of 3 σ (**Fig. 4.3**, green mesh). For each complex, the hydrophobic adamantane moiety points upward towards the



N-terminus on the exterior of the virus, while the ammonium group is directed downwards in the aqueous pore towards His37. The adamantane is bound in a predominantly hydrophobic pocket, lined by the sidechains and mainchains of Val27, Ala30, and Ser31. The hydroxyl of Ser31 forms an internal hydrogen bond to a mainchain carbonyl of Val27, increasing the effective hydrophobicity of the environment. Rimantadine is a racemic drug, and the ligand electron density strongly suggests that the bound drug consists of an equimolar mixture of both the R and S enantiomers, which were hence each modeled at half occupancy. Indeed, the two enantiomers have been shown to have equal potency in *in vitro* electrophysiology and cellular antiviral plaque assays.<sup>43</sup>

In previous high-resolution crystallographic and molecular dynamics investigations of M2's TM domain in the drug-free form, continuous water-wires were found to span the pore from the exterior vestibule near Val27 to His37.<sup>28,30,44</sup> The carbonyl groups of Val27, Ala30, and Gly34 form hydrogen bonds to successive layers of waters. Additional “bridging” waters bridge the carbonyl-associated waters to form continuous water-wires from the Val27 to His37 (**Fig. 4.2e**). In both the amantadine- and rimantadine-bound structures, the adamantane cage fits snugly into the top of the pore, displacing the layer of waters near Val27 (**Fig. 4.4a,d**). Thus, the drug dehydrates the upper portion of the pore, snipping the continuous water wires seen in the drug-free state.

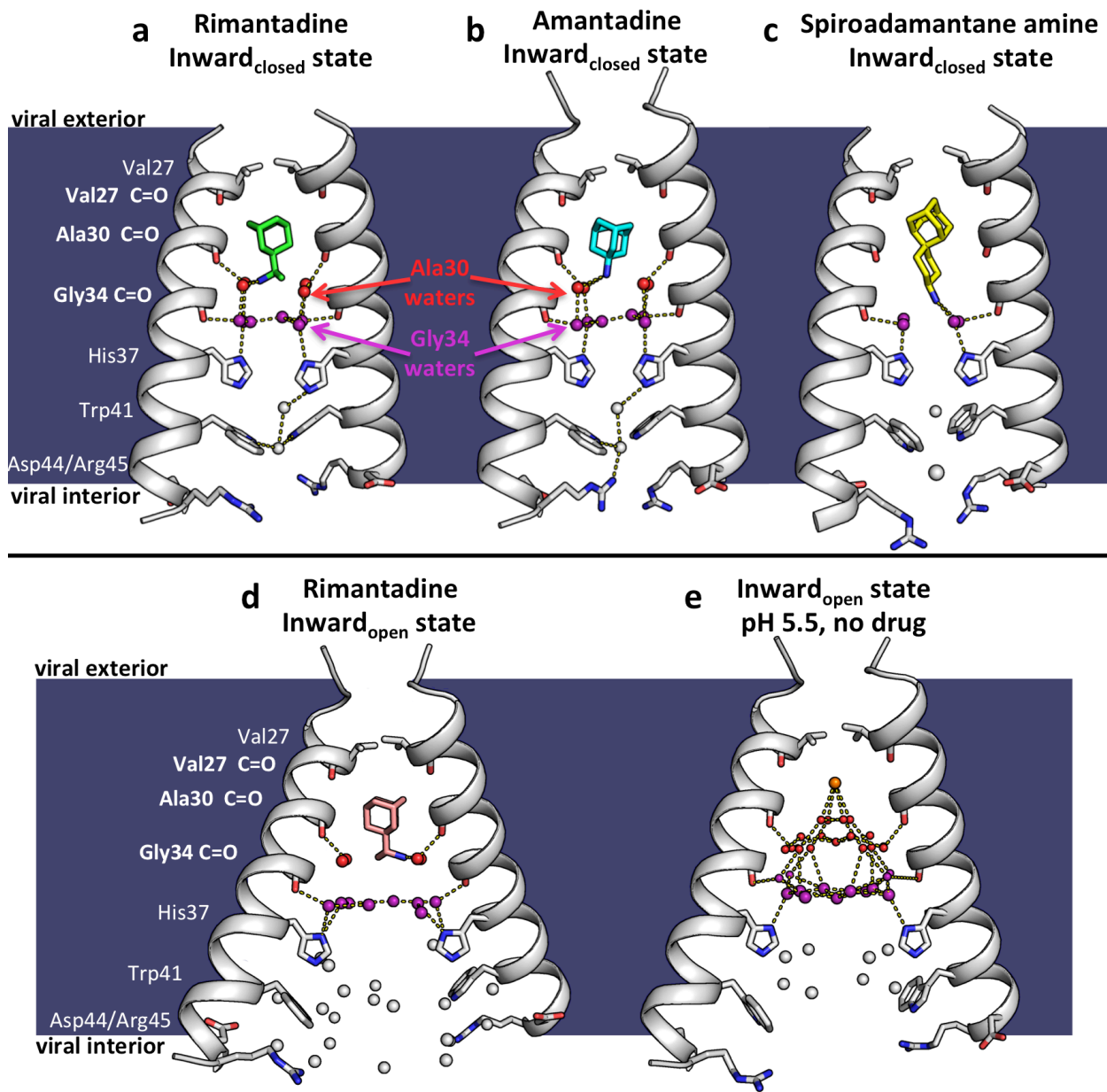


**Figure 4.2. X-ray crystal structures of the M2 proton channel bound to drugs and inhibitors.** The M2 channel is a homotetramer, but here the front and back monomers have been removed to show the contents of the channel pore. Hydrogen bonds are shown as yellow dashes. The layer of waters forming H-bonds to Ala30 carbonyls ("Ala30 layer") is shown as red spheres; the layer of waters forming H-bonds to Gly34 carbonyls ("Gly34 layer") is shown as purple spheres. Top, left to right: a. M2 bound to rimantadine in the Inward<sub>closed</sub> state; PDB code 6BKL, 2.00 Å resolution, monomer subunits F and H; b. M2 bound to amantadine in the Inward<sub>closed</sub> state; 6BKK, 2.00 Å resolution, monomers B and D; c. M2 bound to spiro-adamantyl amine in the Inward<sub>closed</sub> state; 6BMZ, 2.63 Å resolution, monomers B and D. Bottom, left to right: d. M2 bound to rimantadine in the Inward<sub>open</sub> state; 6BOC, 2.25 Å resolution, monomers B and D; e. Previously solved structure of M2 in the Inward<sub>open</sub> state at pH 5.0 in the absence of bound drug,<sup>30</sup> 5JOO, 1.41 Å resolution.

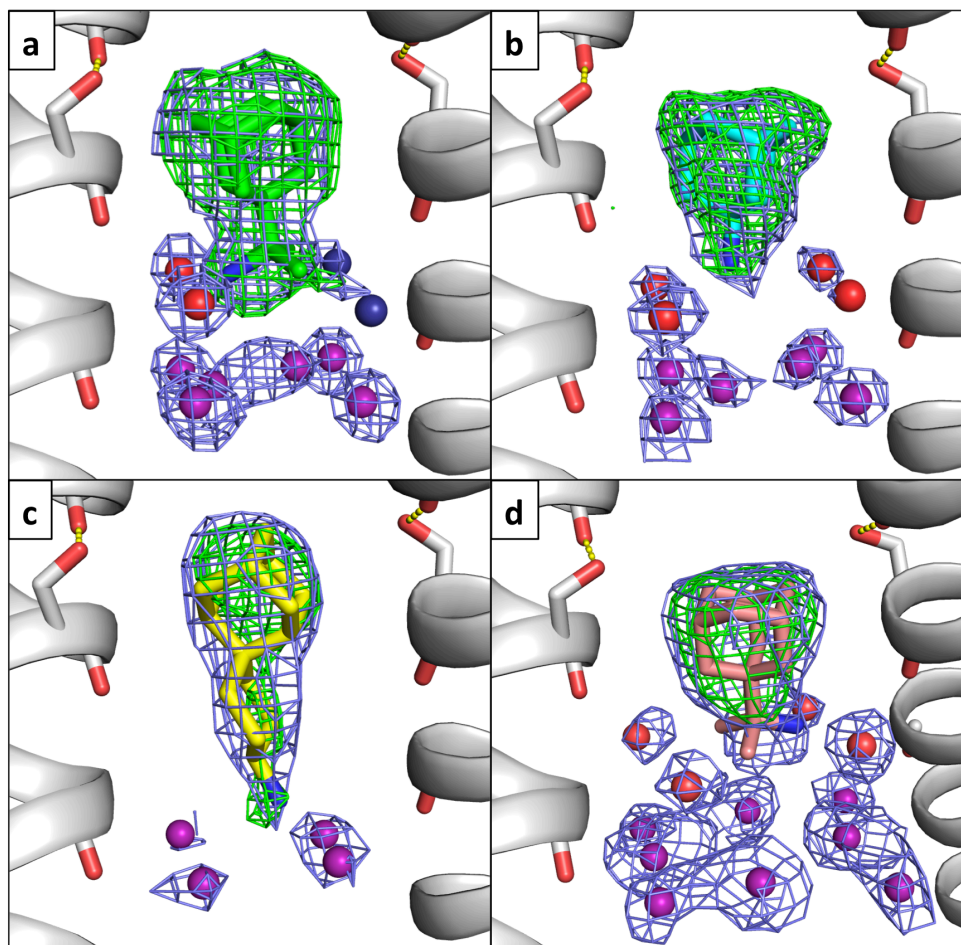


**Figure 4.3. Electron density in channel pore above the gating His37 residues.** Blue mesh is 2Fo-Fc density shown at a contour of 1  $\sigma$ , green mesh is a Polder omit map shown to a contour of 3  $\sigma$ . Ala30 water layer is shown as red spheres, Gly34 water layer is shown as purple spheres. Partial occupancy waters are shown as dark blue spheres. The hydrogen bond between Ser31 and the Val27 carbonyl is shown. a. Rimantadine-bound Inward<sub>closed</sub> state (green, 6BKL, monomers F and H). b. Amantadine-bound Inward<sub>closed</sub> state (cyan, 6BKK, monomers B and D). c. Spiro-adamantyl amine-bound Inward<sub>closed</sub> state (yellow, 6BMZ, monomers B and D). d. Rimantadine-bound Inward<sub>open</sub> state (pink, 6BOC, monomers B and D). Note that, in the rimantadine-bound structures (a,d), the bound rimantadine has been modeled as a superposition of the R and S enantiomers, with both at half occupancy. In the rimantadine-bound Inward<sub>closed</sub> structure, two of the waters in the Ala30 layer have been also modeled as half-occupancy due to steric clashes with the rimantadine methyl group. Also note the difference in the shape of 2Fo-Fc electron density corresponding to bridging waters in the Gly34 layer in the amantadine- and rimantadine- bound Inward<sub>closed</sub> state structures (a, b); these waters are two clearly defined spheres when amantadine binds to one of the tetramers (monomers A,B,C,D), though this density consists of just one water in the second tetramer within the asymmetric unit (monomers E,F,G,H); the bridging water density is elongated when rimantadine binds. This is likely caused by a racemic mixture of rimantadine enantiomers resulting in two water structures that are averaged in the electron density.

In contrast to the disruption of the waters adjacent to Val27, the lower two water layers remain similar to the drug-free state.<sup>27</sup> The ammonium group is positioned proximal to the four waters comprising the Ala30 layer (**Fig. 4.4b,e**), followed by the Gly34 water layer consisting of four carbonyl-associated and two bridging water molecules (**Fig. 4.4c,f**). The B-factors of the waters bound directly to Ala30 and Gly34 backbone carbonyls are generally similar to those of the backbone atoms, indicating that they are tightly associated, while the bridging waters show greater disorder. The overall water arrangement is strikingly similar to that observed in the crystal structure of the Inward<sub>closed</sub> conformation of M2TM in the absence of drug (3LBW), indicating that the water structure that stabilizes the ammonium group is largely pre-organized. This same pathway would appear ideally oriented for stabilizing and facilitating proton transfer and diffusion through this region of the channel in the absence of inhibitor. This arrangement is also in good agreement with earlier MD simulations of the water in a model of the amantadine complex based on the structure of the drug-free structure (PDB: 3LBW).<sup>27</sup>

While the overall structure of the tetramer and pore waters is largely symmetrical, the placement of the drug within the pore deviates slightly from four-fold rotational symmetry. The rimantadine- and amantadine-bound M2 crystals presented here belong to the P2<sub>1</sub> space group, with two crystallographically distinct tetramers per asymmetric unit. Both drugs adopt similar asymmetric orientations in each of the two amantadine and rimantadine complexes. Their ammonium groups have three hydrogen-bond donating protons, which cannot form symmetrical interactions with each of the four Ala30 waters without breaking symmetry. Thus, the drugs tilt slightly within the site, displacing the ammonium group away from the central axis towards two of the Ala30 waters. The angle of tilt of the adamantyl 3-fold axis of symmetry relative to the channel's four-fold axis of symmetry is  $11.3^\circ \pm 0.7$  for the amantadine-bound structure and  $11^\circ \pm$

3 for the rimantadine bound structure, in good agreement with the value of  $13^\circ$  measured by SSNMR for amantadine.<sup>39</sup>

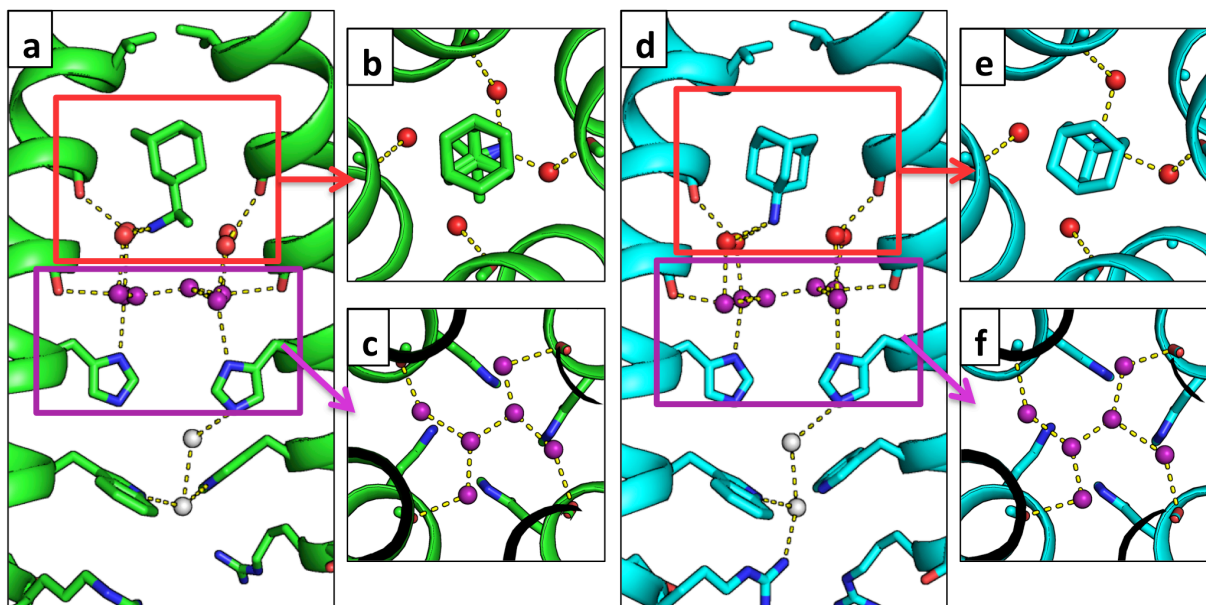


**Figure 4.4. Water-mediated hydrogen bonds facilitate the binding of rimantadine and amantadine to the M2 pore.** In both the rimantadine-bound (6BKL, green) and amantadine-bound (6BKK, cyan) structures of the  $\text{Inward}_{\text{closed}}$  conformation, the drug ammonium group is positioned to H-bond with two of the four waters in the Ala30 water layer, shown as red spheres. The Gly34 water layer is shown as purple spheres. H-bonds are shown as yellow dashes. Amantadine and rimantadine bind asymmetrically and form hydrogen bonds with two of the four waters in the top solvent layer. a,d: Side view of rimantadine (a, monomer subunits F and H) and amantadine (d, monomers B and D) binding. b,e: Top-down view of rimantadine (b, monomers E,F,G,H) and amantadine (e, monomers A,B,C,D) binding to the Ala30 water layer in the pore of the M2 channel. c,f: Top-down view of the Gly34 water layer.

4.3.2 *The spiro-adamantyl amine inhibitor additionally displaces a second layer of water molecules in the  $\text{Inward}_{\text{closed}}$  state.* Spiro-adamantyl amine derivatives are excellent inhibitors of the wild-type M2 channel and also the V27A drug-resistant mutants as assessed by antiviral plaque assay and electrophysiological assays.<sup>45,46</sup> Moreover, these compounds have also been shown to rescue mice from lethal influenza infection.<sup>47</sup> The more extended scaffold of the

spiro-adamantyl amine (**Fig. 4.1**) was designed to exclude more water from the channel and to bind with their ammonium groups deeper in the wild-type channel relative to the ammonium position of amantadine.<sup>46</sup> However, this extended scaffold results in a compound that is more hydrophobic than amantadine; the calculated LogP of spiro-adamantyl amine is 3.08, versus cLogP = 1.17 for amantadine. The X-ray crystal structure of spiro-adamantyl amine bound to the Inward<sub>closed</sub> conformation (**Fig. 4.2c**) solved here at a resolution of 2.63 Å (PDB code 6BMZ) shows that the drug indeed projects more deeply into the channel. The longer spiro-adamantyl amine compound displaces the waters of the Ala30 water layer (**Fig. 4.5a,b**) previously observed in the amantadine- and rimantadine-bound structures, and the ammonium group of the spiro-adamantyl amine is positioned to form H-bonds with the four carbonyl-associated waters in the Gly34 solvent layer.

Interestingly, the adamantane groups are oriented differently in the channel in the spiro-adamantyl amine versus the amantadine and rimantadine complexes. The adamantyl group projects one of its methylene groups along its own pseudo- two-fold symmetry axis towards the top of the channel in the spiro-adamantyl amine complex. By contrast, a tertiary center along the three-fold axis of adamantane projects upward in the amantadine and rimantadine complexes (**Fig. 4.5a-c**). This result highlights the near-spherical nature of the adamantane group and helps explain its versatility in drug design.<sup>6</sup>

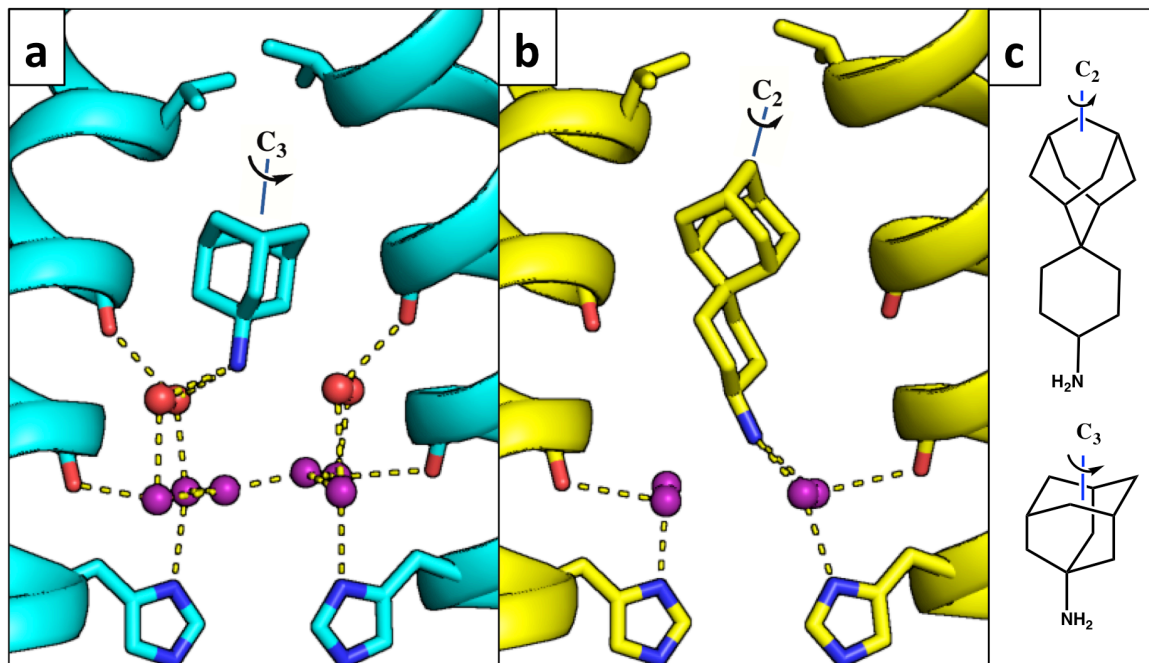


**Figure 4.5. Binding of spiro-adamantyl amine to the Inward<sub>closed</sub> state.** Hydrogen bonds are shown as yellow dashes. a,b: Side view of (a) amantadine-bound Inward<sub>closed</sub> M2 structure (6BKK, cyan, monomers B and D) and (b) the spiro-adamantyl amine-bound Inward<sub>closed</sub> M2 structure (6BMZ, yellow, monomers B and D). The spiro-adamantyl amine inhibitor binds with its ammonium group deeper in the channel. The Ala30 water layer (red) is completely displaced, and the inhibitor ammonium group is within H-bonding distance of the Gly34 water layer (purple). c: Chemical structures of spiro-adamantyl amine (top) and amantadine (bottom), showing adamantyl C2 and C3 symmetry axes.

4.3.3 Structure of rimantadine bound to M2 in the Inward<sub>open</sub> state. Effective blockers of M2 inhibit proton conductance at both high and low pH with the same or only slight reductions in potency (less than two-fold) at lower pH.<sup>5,18</sup> This versatility is likely an important property for drugs that need to remain bound as the pH of the endosome decreases prior to fusion of the viral and endosomal membranes. Nevertheless, this finding runs contrary to early biophysical studies, which appeared to show that amantadine bound the channel only under conditions in which the His residues are in the neutral state<sup>19,48</sup> and that the amantadine dissociated at lower pH. However, these early studies focused on spectroscopic signatures of only the Inward<sub>closed</sub> state



suggesting that the drug must also bind to another conformational form at low pH. Thus, it was important to determine structures of drugs bound to the Inward<sub>open</sub> state in addition to the Inward<sub>closed</sub> conformational state.

We solved the structure of rimantadine bound to the Inward<sub>open</sub> state of the M2 channel (**Fig. 4.2d**) to a resolution of 2.25 Å (PDB code 5BOC). The helices, which bend slightly at Gly34 in the Inward<sub>closed</sub> rimantadine complex (**Fig. 4.2a**), straighten in the Inward<sub>open</sub> rimantadine complex. This conformational change increases the diameter of the bottom of the channel while slightly constricting the upper portion of the channel. The newly solved structure of rimantadine bound to the Inward<sub>open</sub> state is in good agreement with a previously solved low-resolution (3.5 Å) structure of the Inward<sub>open</sub> amantadine complex (3C9J)<sup>20</sup> (C $\alpha$  RMSD = 0.98 Å). The adamantane drugs are observed to bind to the same position in both structures (**Fig. 4.6**). However, the water molecules, which were not resolved in the low-resolution amantadine complex (3C9J), are now well defined in the current rimantadine complex (5BOC).

Hydrogen-bonded networks of water molecules play a similar role in stabilizing the Inward<sub>open</sub> and Inward<sub>closed</sub> rimantadine complexes (**Fig. 4.2a,d**). In both complexes, the ammonium group is proximal to the four Ala30 carbonyl-associated water molecules, and the Gly34 waters are retained. However, the increased radius of the channel near the C-terminus of the Inward<sub>open</sub> complex leads to an increase in the number of the bridging waters in the Gly34 layer, and a progressive opening of a channel from His37 downward. The structures of the Inward<sub>open</sub> and Inward<sub>closed</sub> complexes are consistent with the known pH-independent binding of the drugs to the channel, which now can be understood in terms of the affinity of the individual conformational forms for drugs at a given pH (**Fig. 4.7**). The Inward<sub>closed</sub> drug-bound conformation is stable at high pH where the overall charge on His37 is 0 or at most +1. At lower



pH, His37 residues are protonated, leading to repulsion between the imidazolium cations as well as the ammonium group of the drug in the highly restricted environment of the channel. However, at low pH, charge repulsions between protonated His37 groups as well as their interaction with the drug ammonium group would be more easily electrostatically screened in the solvent-exposed end of the  $\text{Inward}_{\text{closed}}$  conformation. Thus, the structures of the  $\text{Inward}_{\text{open}}$  and  $\text{Inward}_{\text{closed}}$  complexes explain how the drugs can inhibit over a wide range of pH with similar affinity.<sup>5,18</sup>

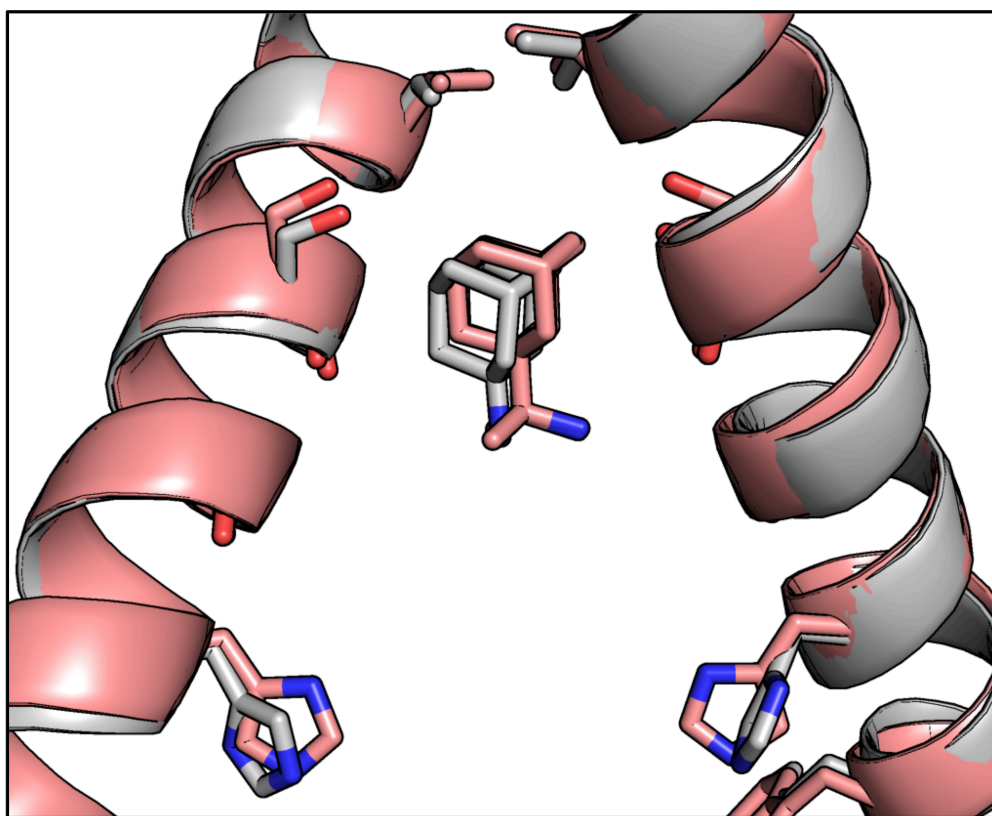


**Figure 4.6. Aligned rimantadine-bound  $\text{Inward}_{\text{open}}$  (6BOC, pink) and amantadine-bound  $\text{Inward}_{\text{open}}$  (3C9J, gray) structures.** The position of the bound rimantadine group is in good agreement with the previously observed binding position of amantadine. Note that the His37 rotamers in structure 3C9J are not meaningfully different, as these side chains were fit to 3.5 Å resolution electron density.

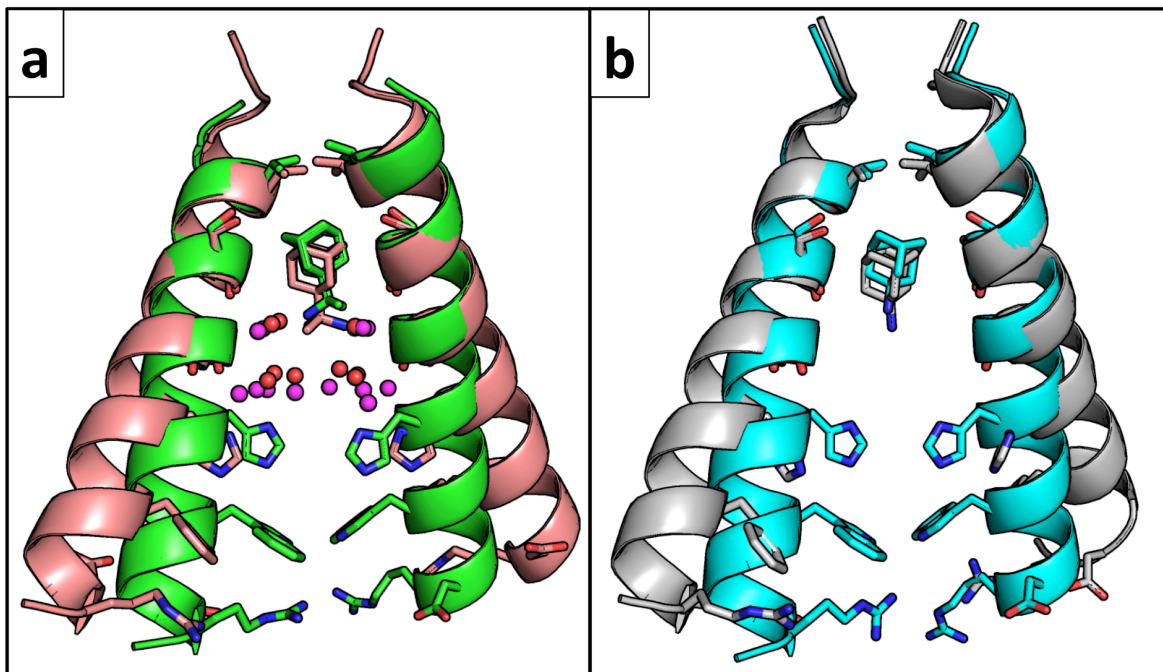


**Figure 4.7. Alignment of Inward<sub>open</sub> and Inward<sub>closed</sub> structures showing rimantadine and amantadine binding.** A: Rimantadine-bound Inward<sub>open</sub> (6BOC, pink with waters shown as magenta spheres) and Inward<sub>closed</sub> (6BKL, green with waters shown as red spheres) structures. B. Previously solved amantadine-bound Inward<sub>open</sub> structure (3C9J, gray)<sup>20</sup> and the amantadine-bound Inward<sub>closed</sub> structure (6BKK, cyan). In the Inward<sub>open</sub> conformation, the top of the pore near Val27 is constricted and adamantane drugs bind slightly deeper in the channel pore.

*4.3.4 Structural mechanism of drug-binding and channel inhibition.* The binding of the adamantane drugs to M2 presents particularly interesting problems for understanding the mechanism of drug action against channels in general as well as the design of drugs to address drug resistance in strains of M2 in particular. We hypothesize that amantadine acts as a *mechanism-based inhibitor*. The amantadine ammonium group exploits the channel's essential capability of stabilizing an excess hydrated proton. Thus, the ammonium groups do not form H-bonds with pore-facing carbonyl groups; instead they are hydronium mimics that interact with functional water networks connected directly to the proton-shuttling and gating residue, His37. This hypothesis is consistent with the fact that replacing the ammonium group of

amantadine with hydroxyl strongly decreases antiviral activity.<sup>49</sup> Moreover, the large adamantane displaces loosely bound waters near the top of the pore, thereby stabilizing the complex through hydrophobic van der Waals interactions, while also inhibiting conduction by occluding entry of protons into the pore. The more extended spiro-adamantyl amine places its ammonium group further down the channel into a lower site lined by four water molecules that simultaneously receive hydrogen bonds from both the carbonyl of Gly34 and the imidazole of His37.

Interestingly, our structures show that the pore-lining carbonyl groups act as physicochemical chameleons that stabilize hydrated cations through polar interactions in some complexes (e.g. the Ala30 carbonyls in structures 6BKL, 6BKK), but hydrophobically stabilize apolar aliphatic groups in others (e.g. the Ala30 carbonyls in structure 6BMZ). This behavior is consistent with the known tendency of the carbonyl groups of helices to form a single strong helical hydrogen bond with an amide at position *i-4* when in the hydrophobic core of a protein, but to form an additional hydrogen bond to water molecules when exposed to water.<sup>50</sup> The ability to switch between these two states offers intriguing and potentially generalizable possibilities for small molecule drug design.

*4.3.5 Explaining the effectiveness of adamantane as a substituent for drug design.* Adamantane derivatives are commonly used in drugs that treat influenza (amantadine, rimantadine), Alzheimer's disease (memantine), and diabetes (saxagliptin, vildagliptin), among other uses.<sup>6</sup> The adamantyl group has been referred to as a "lipophilic bullet"<sup>6</sup> that can be added onto drugs to increase their hydrophobicity and structural stability. The adamantane drugs are hydrophobic, though less so than one would expect based on the number of carbons they contain. Adamantane has ten carbons contained within four inter-connected cyclohexane rings that form a cage with a

greatly reduced apolar surface area when compared to the corresponding unbranched alkane. In fact, the hydrophobicity of adamantane ( $\text{LogP} = 3.98$ ) is far smaller than that of n-decane ( $\text{LogP} = 5.98$ ), and instead is similar to n-hexane ( $\text{LogP} = 3.87$ ).<sup>51</sup> The decreased hydrophobicity of adamantane is a simple consequence of its highly compact, highly cross-linked structure. For example, the solvent accessible surface area of adamantane is  $262 \text{ \AA}^2$  while that of n-decane in an extended conformation  $361 \text{ \AA}^2$ .

A second attractive feature of adamantane is that it has no rotatable bonds and hence it loses very little conformational entropy when it binds into a protein pocket. By comparison, an alkane of similar hydrophobicity such as n-pentane could lose up to 2.6 kcal/mol ( $\text{DS} = 4 \times \text{RT} \ln[3]$ ) associated with the three rotamers of each of its four rotatable bonds) when immobilized in a receptor-binding site. Moreover, adamantane has a very smooth surface (**Fig. 4.1**), which allows it to rotate extremely rapidly about its C3 axis, even in the crystalline state at room temperature.<sup>52</sup> Due to this rapid rotational averaging, adamantane effectively has a smooth ellipsoidal shape with a round cross-section that belies its jagged appearance when drawn as a stick figure in two dimensions. Thus, the apparent mismatch between the C3 structural symmetry of amantadine and the M2 tetramer is an artifact of considering the complex as a static object. The smooth cross-section of the adamantane ring also assures a low torsional barrier for rotation of the amantadine C1-N bond, which again contributes to minimal loss in configurational entropy of binding. In summary, adamantane is a highly rigid group with a hydrophobicity similar to n-hexane, which can contribute to binding with a greatly lower conformational entropy loss than an unbranched alkane.

*4.3.6 Molecular dynamics confirm the structural mechanism of drug binding and inhibition.* To test and further refine these conclusions we turned to all-atom molecular dynamics simulations of the M2 channel in a POPC (200 lipid molecules) bilayer (see SI). We examined the amantadine and spiro-adamantyl amine complexes in the neutral Inward<sub>closed</sub> conformation to allow a comparison of the two distinct drug classes in the same conformation of the channel. The simulated complexes were structurally stable and showed no large conformational changes over 200 nsec (C $\alpha$  RMSD to the crystallographic structures  $\leq 1$  Å, **SI Table 4.2**, **SI Fig. 4.10**). In accord with SSNMR measurements,<sup>39</sup> amantadine undergoes rapid rotation about its major axis (correlation,  $t_c = 40$  psec) (**SI Fig. 4.11**). Torsional averaging about the C1-NH<sub>2</sub> bond of the drug also occurs with  $t_c = 30$  psec. Also in agreement with SSNMR, the main axis of the drug undergoes rapid motion within a cone (mean tilt =  $9 \pm 5^\circ$ , **SI Fig. 4.12**) rather than being fixed in one single orientation. Thus, the fixed asymmetric orientation seen in the cryo-cooled crystal structure represents a single snapshot of the time-averaged structure seen by SSNMR and MD simulations.

Although the water molecules undergo rapid motions in the channel, their average positions are in excellent ( $< 1$  Å) agreement with the positions seen in the crystal structure of the corresponding amantadine complex. As in the crystallographic structure, the waters form tight clusters within hydrogen-bonding distance of the Ala30 and Gly34 carbonyls, with more diffuse density in the region bridging between the four Gly34 waters (**Fig. 4.8** and **SI Fig. 4.13**). Examination of the probability density function for the amine-water interaction (**SI Fig. 4.14**), showed that, on average, three to four waters are within hydrogen bonding distance of the amine, and that other features of the water are in quantitative agreement with the crystallographic structure. In summary, the MD simulations of the amantadine Inward<sub>closed</sub> complex are in

excellent agreement with the crystallographic structure, and confirm the expectation that the complex is entropically stabilized by rapid axial rotation and torsional motions of the bound amantadine.

Simulations of the spiro-adamantyl amine complex were similarly in good agreement with SSNMR<sup>46</sup> and crystallographic structures. The drug undergoes rapid rigid-body and torsional rotations about its pseudo-C2 axis ( $t_c = 190$  and  $70$  psec, respectively) (**SI Fig. 4.15**), similar to the rotation of amantadine about its C3 axis. The water density obtained from the ensemble-averaged structures also matches the crystallographic structure (**Fig. 4.8** and **SI Figs. 4.13, 4.16**), with dense clusters of water seen near the carbonyls of Gly34. Throughout the simulations of M2 bound to amantadine and M2 bound to spiro-adamantyl amine, the ammonium group remained near the center of the channel, within  $1 \text{ \AA}$  of its position in the starting crystallographic structures (**SI Fig. 4.17**).

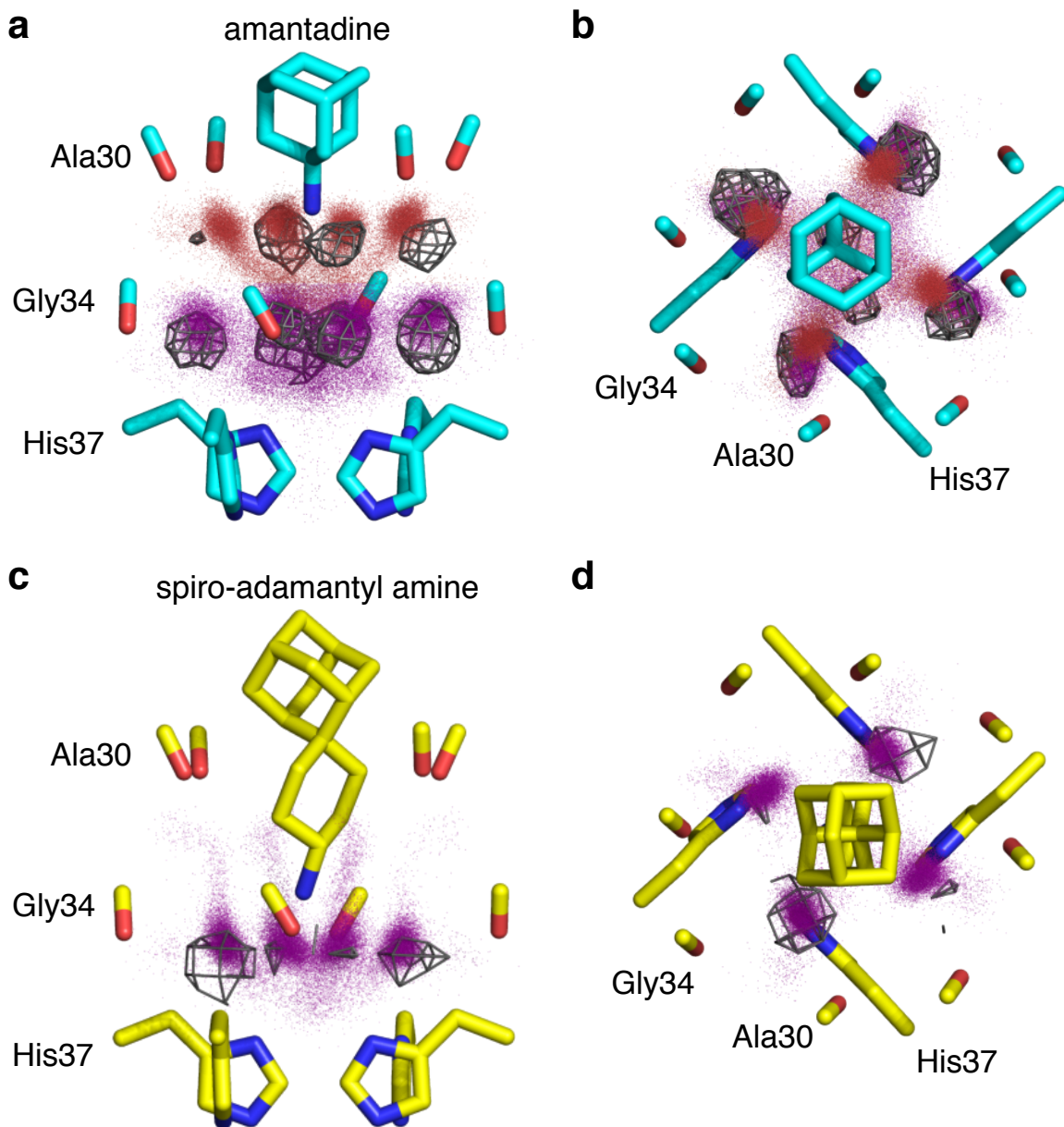


**Figure 4.8. Molecular dynamics simulations reproduce the positions of the crystallographic waters.** X-ray crystal structures are shown as sticks. Red and purple dots are water oxygen positions from MD snapshots of the largest amine clusters. Gray wireframe shows 1 $\sigma$  contours of water electron density from the X-ray crystal structure. a,c: Side views. b,d: Top views. See supplement for details of the simulations and treatment of the data.

*4.3.7 Implications for the design of drugs that target influenza A virus.* M2 undergoes changes in conformation and the protonation state of the gating His37 tetrad as the pH of the endosome gradually decreases. Thus, a successful drug must inhibit the channel over a wide range of pH and conformational states. If drugs such as amantadine and rimantadine bound exclusively to the Inward<sub>closed</sub> state, then one would expect that the drug would dissociate as the pH was lowered below the pKa of the His37 residues (Le Chatlier's principle). However, the affinity of amantadine is relatively invariant with pH between neutral pH and acidic endosomal pH, as assessed by electrophysiological measurements at pH as low as 5.5.<sup>5,18</sup> It was therefore important to define the mode of inhibition of drugs when bound to the Inward<sub>open</sub> form of the channel, which is the more stable form in native membranes at low pH.<sup>35</sup> The crystal structures shown here define similar modes of drug binding in both forms, with the ammonium group engaged in hydrogen bonds with functional water wires near the lower reaches of the channel and the adamantane cage displacing water from the hydrophobic region near Val27. Thus, the ability of drugs to bind over a range of pH and conformational states appears to be important for viral inhibition. Along these lines, it is noteworthy that a series of inhibitors that appear to bind the S31N variant of M2's TM domain exclusively in the Inward<sub>open</sub> state (with a straight helix lacking the kink that allows formation of the inwardly closed state) are very weak inhibitors of this protein's proton channel activity, and they are also inactive in antiviral assays.<sup>53</sup>

The structures presented here should also inform the design of compounds that inhibit M2 mutants from amantadine- and rimantadine-resistant forms of the virus. These mutants cluster in the upper portion of the channel between residues 26-31, disrupting the hydrophobic adamantane-binding site, while the pore-lining residues that are important for water-mediated conduction (Ala30, Gly34, His37) remain unchanged in more than 99% of the virus identified in



humans, pigs and animals to date.<sup>54</sup> Here, we show that inhibitors can be designed by either hydrogen-bonding to the Ala30-associated waters in the amantadine and rimantadine complexes, or by displacing these same water molecules in the spiro-adamantyl amine complex. The structures presented here will provide critical information to aid in the design of inhibitors that also displace waters that associate with the absolutely conserved His37 imidazole and Gly34 carbonyls. Such compounds might be able to bind lower in the channel, avoiding the more resistance-prone upper region of the pore altogether.

#### 4.4 Methods

M2TM peptide was synthesized and purified as previously described<sup>28,29</sup> and reconstituted into the lipid cubic phase with some modifications to the protocol described by Caffrey and Cherezov.<sup>41</sup> Amantadine, rimantadine, and spiro-adamantyl amine<sup>46</sup> were co-crystallized with M2TM. Crystallization conditions were tested in plastic 96-well LCP trays (Laminex) using a LCP crystallization robot (TTP Labtech). Trays were screened using visible light and UV images (**Fig. 4.9**). Crystals were harvested from the 96-well sandwich trays then frozen in liquid nitrogen. Data were collected at Advanced Light Source (ALS) beam 8.3.1. Data collection, processing (**Table 4.1**), model building, refinement (**Table 4.2**), and MD simulations were carried out as described in the supplement.

*4.4.1 Data availability.* Atomic coordinates and structure factors have been deposited to the Protein Data Bank with the following accession codes: 6BKK, 6BKL, 6BOC, 6BMZ.

## 4.5 Acknowledgements

The authors would like to thank Pil Seok Chae (Hanyang University, Seoul, South Korea) for providing DMNG detergent. J.L.T., W.F.D., and N.F.P. were supported by NIH Grants GM122603 and GM117593. N.F.P. was supported by a T32 grant from NIH: 4 T32 HL 7731-25. J. W. was supported by the NIH grant AI119187. Use of the LCP crystallization robot was made possible by National Center for Research Resources Grant 1S10RR027234-01. Data collection was carried out at ALS 8.3.1. Beamline 8.3.1 at the Advanced Light Source is operated by the University of California Office of the President, Multicampus Research Programs and Initiatives grant MR-15-328599 and NIGMS grants P30 GM124169 and R01 GM124149. J.L.T. thanks George Meigs and James Holton at ALS 8.3.1 for support during data collection. A.K. thanks Chiesi Hellas, which supported this research (SARG No 10354).

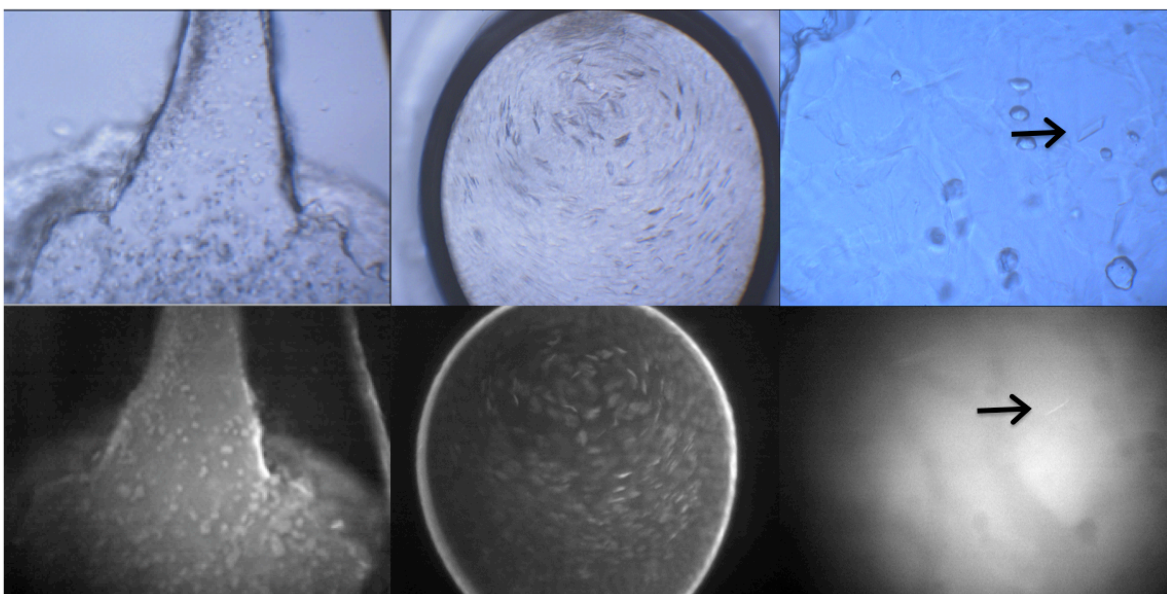


**Figure 4.9. Crystals of M2TM bound to drugs and inhibitors.** Visible light (top) and UV (bottom) images of M2 crystals. Square-shaped plates of M2TM bound to drugs and inhibitors form in the lipid cubic phase.

**Table 4.1. Data processing statistics.** Data processing statistics for M2 bound to amantadine (6BKK), rimantadine (6BKL), and spiro-adamantyl amine (6BMZ) in the Inward<sub>closed</sub> conformation, and M2 bound to rimantadine (6BOC) in the Inward<sub>open</sub> conformation. Data processing was carried out in Aimless,<sup>55</sup> with space group validation in Zanuda.<sup>56</sup>

| <b>Structure</b>                    | <b>6BKK</b>                   | <b>6BKL</b>                   | <b>6BMZ</b>                                   | <b>6BOC</b>                   |
|-------------------------------------|-------------------------------|-------------------------------|---|-------------------------------|
| <b>Space group</b>                  | P2 <sub>1</sub>               | P2 <sub>1</sub>               | P2 <sub>1</sub> 2 <sub>1</sub> 2 <sub>1</sub> | P2                            |
| <b>Cell dimensions (Å)</b>          |                               |                               |   |                               |
| <b>a,b,c (Å)</b>                    | 44.22,<br>52.05, 48.72        | 36.46,<br>47.84, 48.53        | 49.62,<br>72.59, 99.25                        | 34.05,<br>34.02, 72.09        |
| <b>a, b, g (°)</b>                  | 90.00,<br>108.2, 90.00        | 90.00,<br>96.76, 90.00        | 90.00,<br>90.00, 90.00                        | 90.00,<br>90.23, 90.00        |
| <b>Resolution (Å)</b>               | 52.05 - 2.00<br>(2.05 - 2.00) | 48.19 - 2.00<br>(2.05 - 2.00) | 72.59 - 2.63<br>(2.76 - 2.63)                 | 36.04 - 2.25<br>(2.32 - 2.25) |
| <b>Completeness (%)</b>             | 93.5 (88.8)                   | 93.3 (90.8)                   | 99.3 (98.9)                                   | 98.3 (96.3)                   |
| <b>Number of unique reflections</b> | 13454 (942)                   | 10589 (754)                   | 11007<br>(1442)                               | 7894 (695)                    |
| <b>Average redundancy</b>           | 2.2 (2.1)                     | 4.8 (4.5)                     | 7.0 (6.9)                                     | 3.2 (3.3)                     |
| <b>Rmerge</b>                       | 0.164<br>(0.808)              | 0.114<br>(0.348)              | 0.154<br>(0.608)                              | 0.203<br>(0.463)              |
| <b>CC(1/2)</b>                      | 0.974<br>(0.508)              | 0.994<br>(0.959)              | 0.997<br>(0.920)                              | 0.957<br>(0.791)              |
| <b>Average I/sigI</b>               | 4.6 (2.2)                     | 7.1 (2.9)                     | 8.7 (3.0)                                     | 4.2 (2.1)                     |

**Table 4.2. Refinement statistics.** Refinement statistics for M2 bound to amantadine (6BKK), rimantadine (6BKL), and spiro-adamantyl amine (6BMZ) in the Inward<sub>closed</sub> conformation, and M2 bound to rimantadine in the Inward<sub>open</sub> conformation (6BOC). Refinement was carried out in PHENIX.refine<sup>57</sup> with model-building in Coot<sup>58</sup> and PyMOL.<sup>59</sup>

| <b>Structure</b>                             | <b>6BKK</b>                      | <b>6BKL</b>                      | <b>6BMZ</b>                      | <b>6BOC</b>                   |
|--|----------------------------------|----------------------------------|----------------------------------|-------------------------------|
| <b>Resolution (Å)</b>                        | 46.29 - 1.995<br>(2.066 - 1.995) | 48.19 - 1.995<br>(2.066 - 1.995) | 44.38 - 2.634<br>(2.728 - 2.634) | 34.05 - 2.25<br>(2.33 - 2.25) |
| <b>Number of reflections refined against</b> | 13419 (1269)                     | 10543 (1022)                     | 10945 (1075)                     | 7886 (747)                    |
| <b>Completeness (working + test) (%)</b>     | 92.83 (89.05)                    | 92.24 (89.81)                    | 98.49 (98.53)                    | 97.74 (95.77)                 |
| <b>Rwork</b>                                 | 0.2271<br>(0.2443)               | 0.1863<br>(0.2019)               | 0.2255<br>(0.2608)               | 0.2600<br>(0.2785)            |
| <b>Rfree</b>                                 | 0.2703<br>(0.3112)               | 0.2439<br>(0.2892)               | 0.2767<br>(0.3376)               | 0.2815<br>(0.4070)            |
| <b>Number of non-hydrogen atoms</b>          | 1680                             | 1538                             | 3115                             | 849                           |
| <b>Macromolecules</b>                        | 1536                             | 1452                             | 2964                             | 768                           |
| <b>Ligands</b>                               | 39                               | 52                               | 84                               | 44                            |
| <b>Water</b>                                 | 105                              | 34                               | 67                               | 37                            |
| <b>Ramachandran favored (%)</b>              | 100                              | 100                              | 99.14                            | 100                           |
| <b>RMS(bonds)</b>                            | 0.001                            | 0.007                            | 0.002                            | 0.015                         |
| <b>RMS(angles)</b>                           | 0.33                             | 0.75                             | 0.44                             | 1.23                          |
| <b>Average B-factor</b>                      | 15.95                            | 28.49                            | 29.20                            | 32.96                         |
| <b>Macromolecules</b>                        | 14.99                            | 28.41                            | 28.83                            | 31.85                         |
| <b>Ligands</b>                               | 21.01                            | 26.92                            | 32.62                            | 42.70                         |
| <b>Water</b>                                 | 28.14                            | 34.42                            | 41.39                            | 44.62                         |

## 4.6 References

- 1 Leidner, F., Kurt Yilmaz, N., Paulsen, J., Muller, Y. A. & Schiffer, C. A. Hydration structure and dynamics of inhibitor-bound HIV-1 protease. *Journal of Chemical Theory and Computation* **14**, 2784-2796, doi:10.1021/acs.jctc.8b00097 (2018).
- 2 Spyrakis, F. *et al.* The roles of water in the protein matrix: a largely untapped resource for drug discovery. *Journal of Medicinal Chemistry* **60**, 6781-6827, doi:10.1021/acs.jmedchem.7b00057 (2017).
- 3 Olsen, R. W. Picrotoxin-like channel blockers of GABAA receptors. *Proceedings of the National Academy of Sciences* **103**, 6081 (2006).
- 4 Hay, A. J., Wolstenholme, A. J., Skehel, J. J. & Smith, M. H. The molecular basis of the specific anti-influenza action of amantadine. *The EMBO Journal* **4**, 3021-3024 (1985).
- 5 Wang, C., Takeuchi, K., Pinto, L. H. & Lamb, R. A. Ion-channel activity of influenza-A virus M(2) protein - characterization of the amantadine block. *Journal of Virology* **67**, 5585-5594 (1993).
- 6 Wanka, L., Iqbal, K. & Schreiner, P. R. The lipophilic bullet hits the targets: medicinal chemistry of adamantane derivatives. *Chemical Reviews* **113**, 3516-3604, doi:10.1021/cr100264t (2013).
- 7 CDC. Situation Update: Summary of Weekly FluView Report. (2018).
- 8 Taubenberger, J. K. & Morens, D. M. 1918 influenza: the mother of all pandemics. *Emerging Infectious Diseases* **12**, 15-22 (2006).
- 9 Shaw, M. L. The next wave of influenza drugs. *ACS Infectious Diseases* **3**, 691-694, doi:10.1021/acsinfecdis.7b00142 (2017).
- 10 Chizhmakov, I. V. *et al.* Selective proton permeability and pH regulation of the influenza virus M2 channel expressed in mouse erythroleukaemia cells. *Journal of Physiology-London* **494**, 329-336 (1996).
- 11 Lin, T. I. & Schroeder, C. Definitive assignment of proton selectivity and attoampere unitary current to the M2 ion channel protein of influenza A virus. *Journal of Virology* **75**, 3647-3656, doi:10.1128/jvi.75.8.3647-3656.2001 (2001).
- 12 Mould, J. A. *et al.* Permeation and activation of the M-2 ion channel of influenza A virus. *Journal of Biological Chemistry* **275**, 31038-31050, doi:10.1074/jbc.M003663200 (2000).

- 13 Pinto, L. H., Holsinger, L. J. & Lamb, R. A. Influenza virus M2 protein has ion channel activity. *Cell* **69**, 517-528, doi:[http://dx.doi.org/10.1016/0092-8674\(92\)90452-I](http://dx.doi.org/10.1016/0092-8674(92)90452-I) (1992).
- 14 Shimbo, K., Brassard, D. L., Lamb, R. A. & Pinto, L. H. Ion selectivity and activation of the M2 ion channel of influenza virus. *Biophysical Journal* **70**, 1335-1346 (1996).
- 15 Martin, K. & Helenius, A. Nuclear transport of influenza virus ribonucleoproteins: The viral matrix protein (M1) promotes export and inhibits import. *Cell* **67**, 117-130, doi:[http://dx.doi.org/10.1016/0092-8674\(91\)90576-K](http://dx.doi.org/10.1016/0092-8674(91)90576-K) (1991).
- 16 Park, E. K., Castrucci, M. R., Portner, A. & Kawaoka, Y. The M2 ectodomain is important for its incorporation into influenza A virions. *Journal of Virology* **72**, 2449-2455 (1998).
- 17 Duff, K. C. & Ashley, R. H. The transmembrane domain of influenza A M2 protein forms amantadine-sensitive proton channels in planar lipid bilayers. *Virology* **190**, 485-489, doi:[http://dx.doi.org/10.1016/0042-6822\(92\)91239-Q](http://dx.doi.org/10.1016/0042-6822(92)91239-Q) (1992).
- 18 Ma, C. L. *et al.* Identification of the functional core of the influenza A virus A/M2 proton-selective ion channel. *Proceedings of the National Academy of Sciences* **106**, 12283-12288, doi:10.1073/pnas.0905726106 (2009).
- 19 Salom, D., Hill, B. R., Lear, J. D. & DeGrado, W. F. pH-Dependent tetramerization and amantadine binding of the transmembrane helix of M2 from the influenza A virus. *Biochemistry* **39**, 14160-14170 (2000).
- 20 Stouffer, A. L. *et al.* Structural basis for the function and inhibition of an influenza virus proton channel. *Nature* **451**, 596-U513, doi:10.1038/nature06528 (2008).
- 21 Tobler, K., Kelly, M. L., Pinto, L. H. & Lamb, R. A. Effect of cytoplasmic tail truncations on the activity of the M(2) ion channel of influenza A virus. *Journal of Virology* **73**, 9695-9701 (1999).
- 22 Balannik, V. *et al.* Functional studies and modeling of pore-lining residue mutants of the influenza A virus M2 ion channel. *Biochemistry* **49**, 696-708, doi:10.1021/bi901799k (2010).
- 23 Schnell, J. R. & Chou, J. J. Structure and mechanism of the M2 proton channel of influenza A virus. *Nature* **451**, 591-U512, doi:10.1038/nature06531 (2008).
- 24 Wang, J. *et al.* Structure and inhibition of the drug-resistant S31N mutant of the M2 ion channel of influenza A virus. *Proc Natl Acad Sci U S A* **110**, 1315-1320, doi:10.1073/pnas.1216526110 (2013).
- 25 Hu, F. H., Schmidt-Rohr, K. & Hong, M. NMR detection of pH-dependent histidine-water proton exchange reveals the conduction mechanism of a transmembrane proton

- channel. *Journal of the American Chemical Society* **134**, 3703-3713, doi:10.1021/ja2081185 (2012).
- 26 Sharma, M. *et al.* Insight into the mechanism of the influenza A proton channel from a structure in a lipid bilayer. *Science* **330**, 509-512, doi:10.1126/science.1191750 (2010).
- 27 Acharya, R. *et al.* Structure and mechanism of proton transport through the transmembrane tetrameric M2 protein bundle of the influenza A virus. *Proceedings of the National Academy of Sciences* **107**, 15075-15080, doi:10.1073/pnas.1007071107 (2010).
- 28 Thomaston, J. L. *et al.* High-resolution structures of the M2 channel from influenza A virus reveal dynamic pathways for proton stabilization and transduction. *Proceedings of the National Academy of Sciences* **112**, 14260-14265, doi:10.1073/pnas.1518493112 (2015).
- 29 Thomaston, J. L. & DeGrado, W. F. Crystal structure of the drug-resistant S31N influenza M2 proton channel. *Protein Science* **25**, 1551-1554, doi:10.1002/pro.2937 (2016).
- 30 Thomaston, J. L. *et al.* XFEL structures of the influenza M2 proton channel: Room temperature water networks and insights into proton conduction. *Proceedings of the National Academy of Sciences* (2017).
- 31 Li, C., Qin, H., Gao, F. P. & Cross, T. A. Solid-state NMR characterization of conformational plasticity within the transmembrane domain of the influenza A M2 proton channel. *Biochim Biophys Acta* **1768**, 3162-3170 (2007).
- 32 Liang, R., Li, H., Swanson, J. M. J. & Voth, G. A. Multiscale simulation reveals a multifaceted mechanism of proton permeation through the influenza A M2 proton channel. *Proceedings of the National Academy of Sciences of the United States of America* **111**, 9396-9401, doi:10.1073/pnas.1401997111 (2014).
- 33 Hu, J. *et al.* Histidines, heart of the hydrogen ion channel from influenza A virus: Toward an understanding of conductance and proton selectivity. *Proceedings of the National Academy of Sciences of the United States of America* **103**, 6865-6870, doi:10.1073/pnas.0601944103 (2006).
- 34 Venkataraman, P., Lamb, R. A. & Pinto, L. H. Chemical rescue of histidine selectivity filter mutants of the M2 ion channel of influenza A virus. *Journal of Biological Chemistry* **280**, 21463-21472 (2005).
- 35 DiFrancesco, M. L., Hansen, U.-P., Thiel, G., Moroni, A. & Schroeder, I. Effect of cytosolic pH on inward currents reveals structural characteristics of the proton transport cycle in the influenza A protein M2 in cell-free membrane patches of xenopus oocytes. *PLoS ONE* **9**, e107406, doi:10.1371/journal.pone.0107406 (2014).

- 36 Alhadeff, R., Assa, D., Astrahan, P., Krugliak, M. & Arkin, I. T. Computational and experimental analysis of drug binding to the Influenza M2 channel. *Biochim Biophys Acta* **1838**, 1068-1073, doi:10.1016/j.bbamem.2013.07.033 (2014).
- 37 Wang, J., Li, F. & Ma, C. Recent progress in designing inhibitors that target the drug-resistant M2 proton channels from the influenza A viruses. *Peptide Science* **104**, 291-309, doi:10.1002/bip.22623 (2015).
- 38 Cady, S. D., Mishanina, T. V. & Hong, M. Structure of amantadine-bound M2 transmembrane peptide of influenza A in lipid bilayers from magic-angle-spinning solid-state NMR: The role of Ser31 in amantadine binding. *Journal of Molecular Biology* **385**, 1127-1141, doi:10.1016/j.jmb.2008.11.022 (2009).
- 39 Cady, S. D. *et al.* Structure of the amantadine binding site of influenza M2 proton channels in lipid bilayers. *Nature* **463**, 689-U127, doi:10.1038/nature08722 (2010).
- 40 Day, T. J. F., Schmitt, U. W. & Voth, G. A. The mechanism of hydrated proton transport in water. *Journal of the American Chemical Society* **122**, 12027-12028, doi:10.1021/ja002506n (2000).
- 41 Caffrey, M. & Cherezov, V. Crystallizing membrane proteins using lipidic mesophases. *Nature Protocols* **4**, 706-731, doi:10.1038/nprot.2009.31 (2009).
- 42 Liebschner, D. *et al.* Polder maps: improving OMIT maps by excluding bulk solvent. *Acta Crystallographica. Section D, Structural Biology* **73**, 148-157, doi:10.1107/S2059798316018210 (2017).
- 43 Drakopoulos, A. *et al.* Affinity of rimantadine enantiomers against influenza A/M2 protein revisited. *ACS Medicinal Chemistry Letters* **8**, 145-150, doi:10.1021/acsmchemlett.6b00311 (2017).
- 44 Liang, R. *et al.* Acid activation mechanism of the influenza A M2 proton channel. *Proceedings of the National Academy of Sciences* **113**, E6955 (2016).
- 45 Balgi, A. D. *et al.* Inhibitors of the influenza A virus M2 proton channel discovered using a high-throughput yeast growth restoration assay. *PLoS ONE* **8**, e55271, doi:10.1371/journal.pone.0055271 (2013).
- 46 Wang, J. *et al.* Molecular dynamics simulation directed rational design of inhibitors targeting drug-resistant mutants of influenza A virus M2. *Journal of the American Chemical Society* **133**, 12834-12841, doi:Doi 10.1021/Ja204969m (2011).
- 47 Hu, Y. *et al.* An M2-V27A channel blocker demonstrates potent in vitro and in vivo antiviral activities against amantadine-sensitive and -resistant influenza A viruses. *Antiviral Research* **140**, 45-54, doi:<http://dx.doi.org/10.1016/j.antiviral.2017.01.006> (2017).



- 48 Hu, J. *et al.* Backbone structure of the amantadine-blocked trans-membrane domain M2 proton channel from influenza A virus. *Biophysical Journal* **92**, 4335-4343, doi:10.1529/biophysj.106.090183 (2007).
- 49 Kolocouris, A. *et al.* Comparisons of the influenza virus A M2 channel binding affinities, anti-influenza virus potencies and NMDA antagonistic activities of 2-alkyl-2-aminoadamantanes and analogues. *Bioorganic & Medicinal Chemistry Letters* **18**, 6156-6160, doi:<https://doi.org/10.1016/j.bmcl.2008.10.003> (2008).
- 50 Walsh, S. T. R. *et al.* The hydration of amides in helices; a comprehensive picture from molecular dynamics, IR, and NMR. *Protein Science : A Publication of the Protein Society* **12**, 520-531 (2003).
- 51 Raska, I. & Toropov, A. Comparison of QSPR models of octanol/water partition coefficient for vitamins and non vitamins. *European Journal of Medicinal Chemistry* **41**, 1271-1278, doi:<https://doi.org/10.1016/j.ejmech.2006.06.006> (2006).
- 52 Vijayakumar, V., Alka, B. G., Godwal, B. K. & Sikka, S. K. Pressure induced phase transitions and equation of state of adamantane. *Journal of Physics: Condensed Matter* **13**, 1961 (2001).
- 53 Tzitzoglaki, C. *et al.* Binding and proton blockage by amantadine variants of the influenza M2WT and M2S31N explained. *Journal of Medicinal Chemistry* **60**, 1716-1733, doi:10.1021/acs.jmedchem.6b01115 (2017).
- 54 Durrant, M. G., Eggett, D. L. & Busath, D. D. Investigation of a recent rise of dual amantadine-resistance mutations in the influenza A M2 sequence. *BMC Genetics* **16**, S3, doi:10.1186/1471-2156-16-S2-S3 (2015).

## 4.7 Appendix C, Supplemental Information Figures and Tables

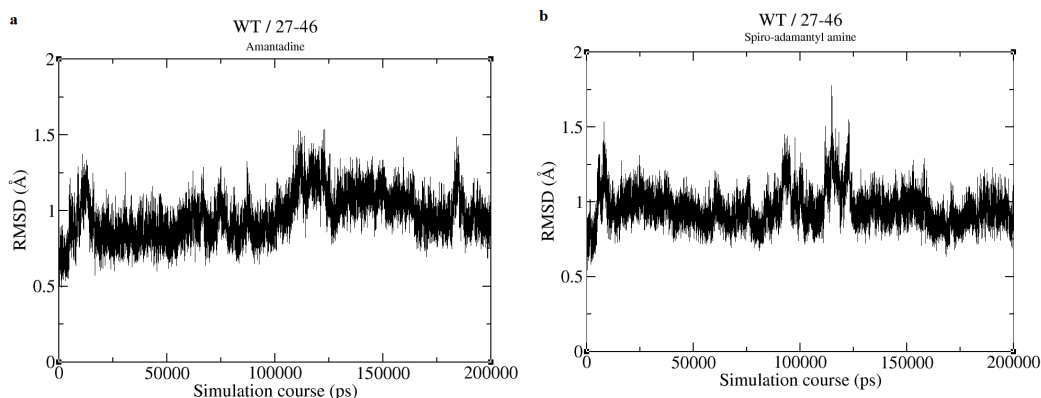


**Figure 4.10. C $\alpha$  atom RMSD during MD simulations.** Root-mean-square deviation (RMSD) for C $\alpha$  atoms of M2TM relative to the initial structure for MD simulations of amantadine and spiro-adamantyl amine complexes (PDB IDs: 6BKK and 6BMZ respectively), after root-mean-square fitting of C $\alpha$  atoms of M2TM; values in Å. The tetramer observed in the X-ray crystal structure was maintained for all 200 ns of simulation time

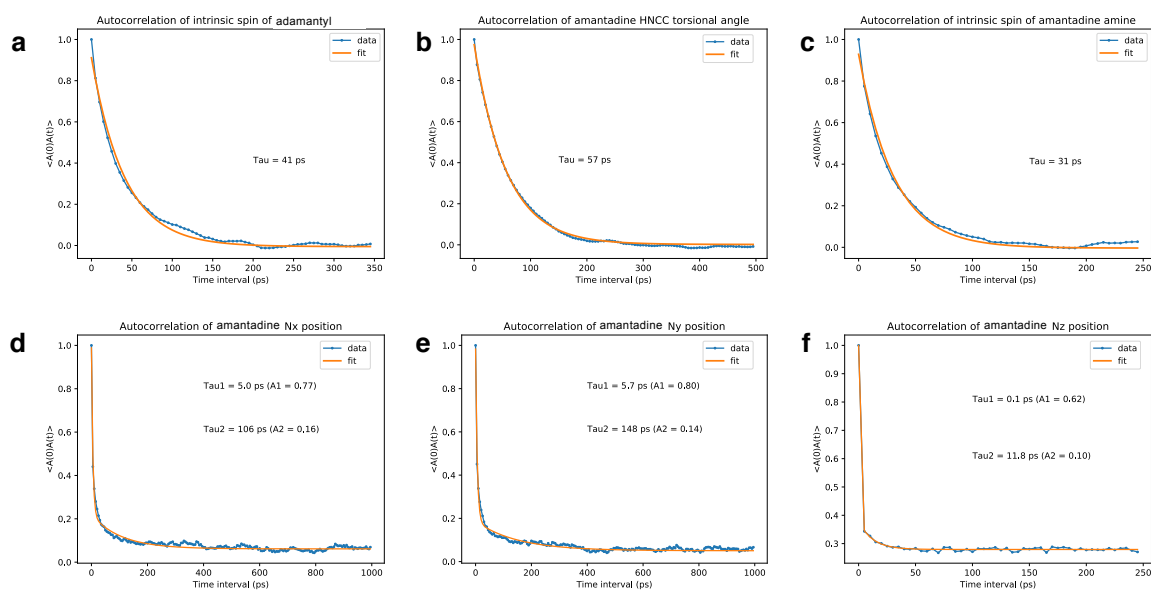


**Figure 4.11. Autocorrelation of amantadine rotation and displacement.** Correlation decay times are labeled in the insets, with corresponding amplitudes for bi-exponential fits.

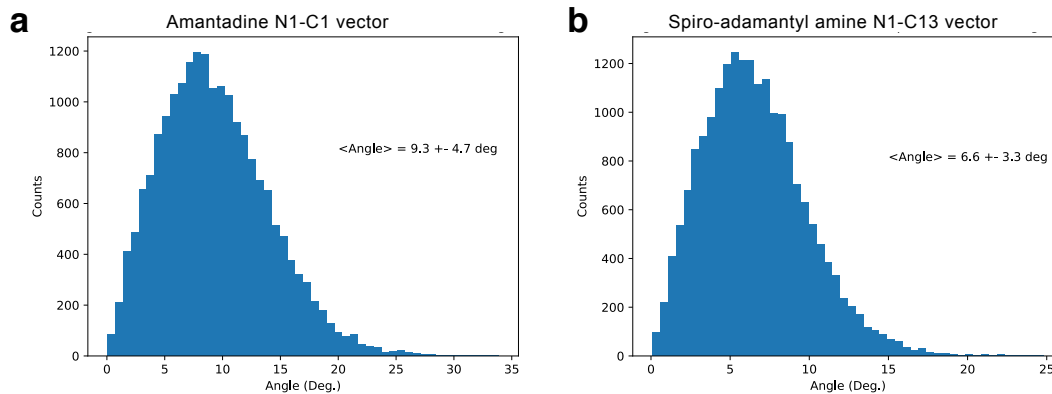


**Figure 4.12. Amantadine tilt in MD simulation.** Histograms from 20,000 MD snapshots (5ps intervals) of amantadine tilt angle relative to M2 tetramer long axis.

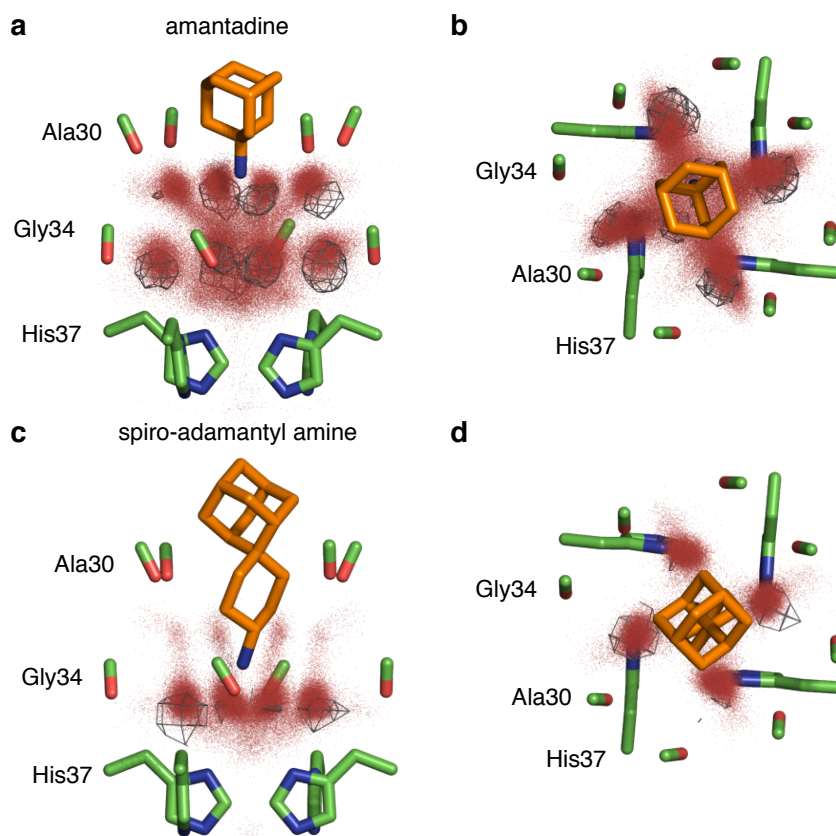


**Figure 4.13. Molecular dynamics reproduces the positions of the crystallographic waters, all snapshots.** The X-ray crystal structure is shown as sticks. Red dots are water oxygen positions from 20,000 molecular dynamics snapshots. Gray wireframe shows  $1\sigma$  contours of water electron density from the X-ray crystal structure. a,c: Side views. b,d: Top views.

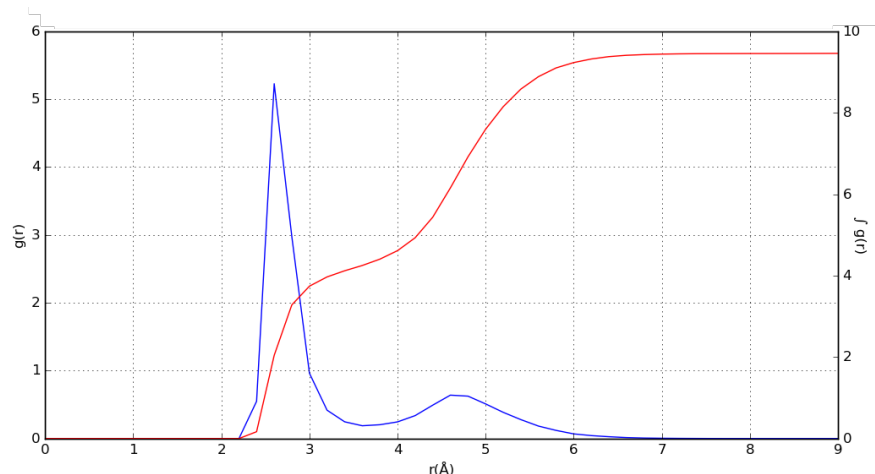


**Figure 4.14. Water RDF from MD simulation of amantadine bound to M2 in the  $\text{Inward}_{\text{closed}}$  state.** Radial distribution function (RDF) between amantadine amino group and water oxygen atoms, extracted from a 200 ns simulation. The RDF  $g(r)$  function (right axis) shows a strong peak near 2.7 Å, associated with waters forming hydrogen bonds to the ammonium group. The cumulative integrated intensity ( $Sg(r)$ , right axis) indicates that 3.5 to 4 waters are associated with the ammonium, on average. The second broad peak near 4.8 Å represents the bridging and Gly34 waters, and integrate to approximately five to six waters, in good agreement with the crystallographic structure.

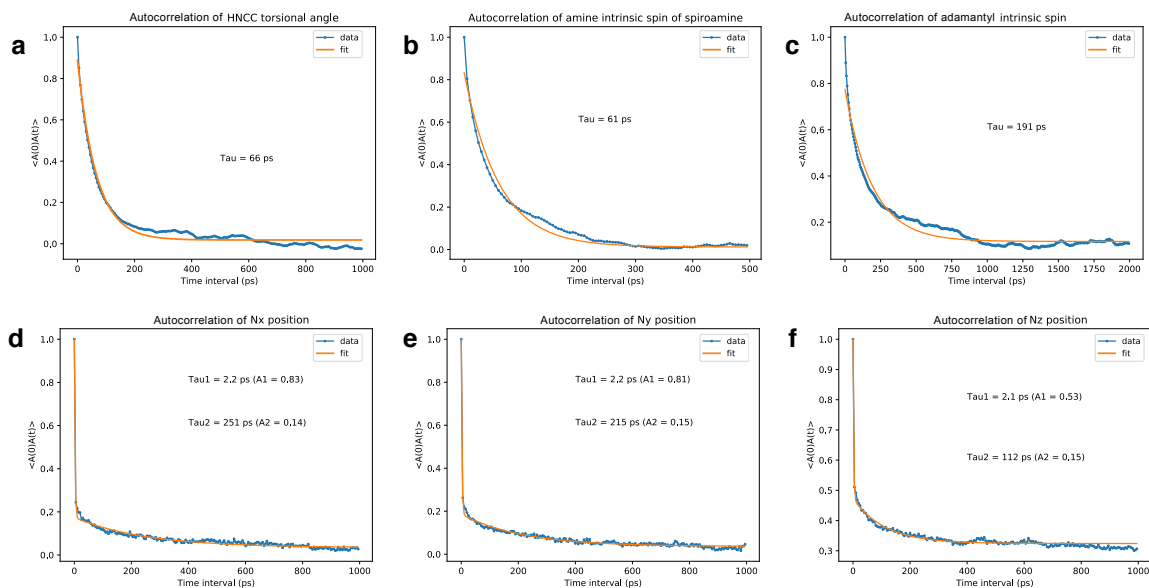


**Figure 4.15. Autocorrelation of spiro-adamantyl amine rotation and displacement.** Correlation decay times are labeled in the insets, with corresponding amplitudes for bi-exponential fits.

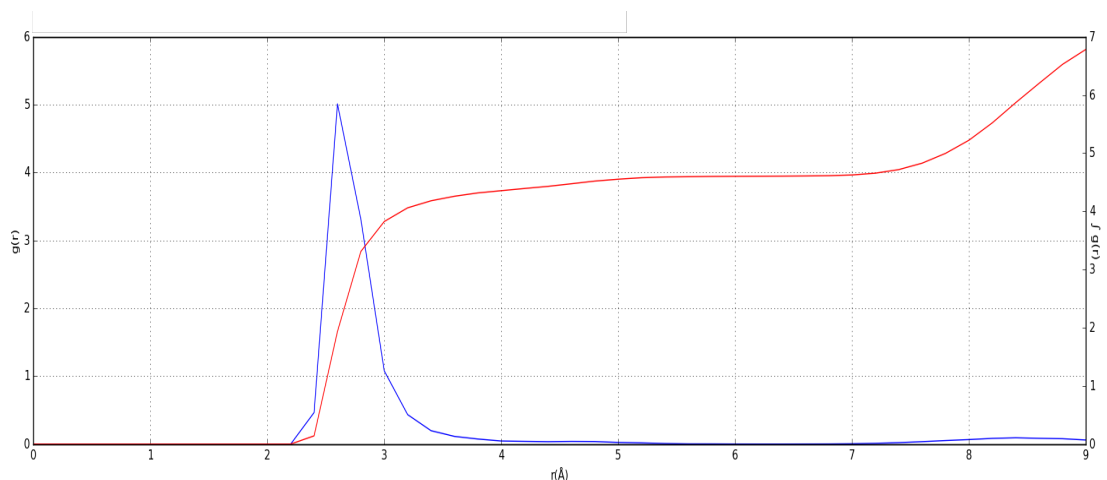


**Figure 4.16. Water RDF from MD simulation of spiro-adamantyl amine bound to M2 in the Inward<sub>closed</sub> state.** RDF between Spiro-adamantyl amine amino group and water oxygens, extracted from a 200 ns simulation. Four waters are observed associated with the ammonium group, in agreement with the crystal structure. The second peak near 8 Å reflect more distant waters between His37 and Trp41 at the C-terminus of the channel.

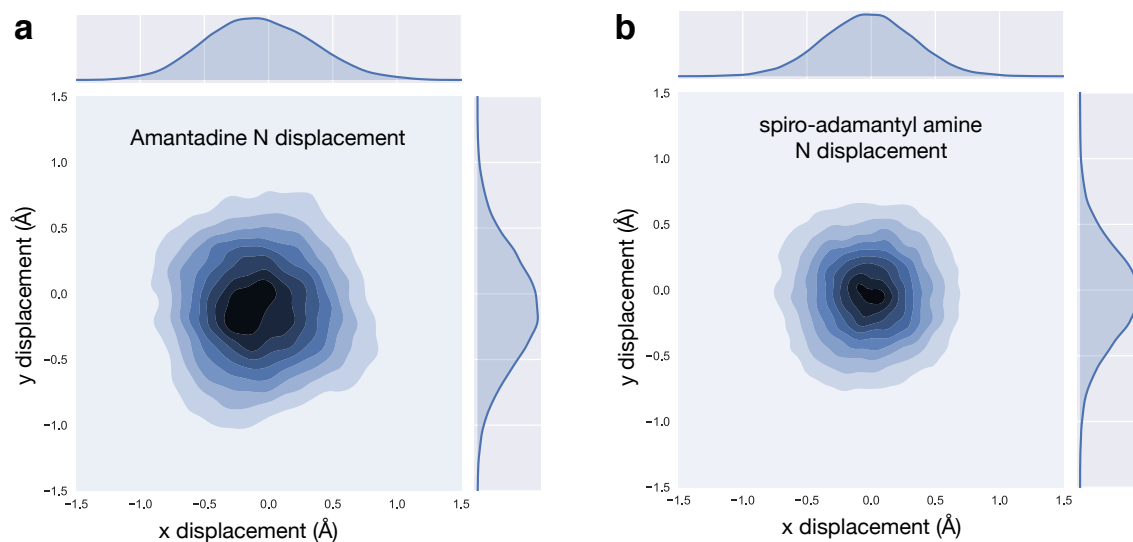


**Figure 4.17. KDE for amine displacement of amantadine and spiro-adamantyl amine.** Kernel density estimate (KDE) of the amine N displacement of amantadine (a) and spiro-adamantyl amine (b) in the x-y plane (orthogonal to bundle long-axis). Darker shading represents higher density, e.g., near (-0.3, -0.3) in (a) showing the amine N spends a substantial amount of time off-center. KDEs are derived from 20,000 snapshots (5 ps intervals) of the MD simulation.

**Table 4.3. Structural and dynamic measures from 250 ns MD trajectories of M2TM-ligand complexes in POPC bilayer at high pH.**

<sup>1</sup> Root-mean-square deviation (RMSD) for C $\alpha$  atoms of M2TM tetramer, residues 27-46, relative to the initial structure (PDB entry: 6BKK, 6BKL, 6BMZ respectively) after root-mean-square fitting of C $\alpha$  atoms; in Å. ; <sup>2-5</sup> Root-mean-square deviation (RMSD) for C $\alpha$  atoms of M2TM helix A-D, residues 27-46, relative to the initial structure (PDB entry: 6BKK, 6BKL, 6BMZ respectively) after root-mean-square fitting of C $\alpha$  atoms; in Å; <sup>6</sup> Angle between the adamantane C3 symmetry axis vector and the normal to the membrane; in degrees; <sup>7</sup> Angle between the adamantane C2 symmetry axis vector and the normal to the membrane; in degrees; <sup>8</sup> Mean distance between center of mass of V27 and centers of mass of adamantane calculated using Gromacs tools; in Å; <sup>9</sup> Mean distance between center of mass of A30 and centers of mass of adamantane calculated using Gromacs tools; in Å; <sup>10</sup> Mean distance between center of mass of G34 and centers of mass of adamantane calculated using Gromacs tools; in Å; <sup>11</sup> Mean number of H-bonds between ligand's ammonium group and waters; <sup>12</sup> Mean distance in Å between the ligand N and the nearest Cl<sup>-</sup>.

| Ligand                | RMSD (C $\alpha$ 27-46) <sup>1</sup> | RMSD Achain (C $\alpha$ 27-46) <sup>2</sup> | RMSD Bchain (27-46) <sup>3</sup> | RMSD Cchain (27-46) <sup>4</sup> | RMSD Dchain (27-46) <sup>5</sup> |
|-----------------------|--------------------------------------|---|----------------------------------|----------------------------------|----------------------------------|
| Amt                   | 0.90 ± 0.2                           | 0.76 ± 0.1                                  | 0.75 ± 0.1                       | 0.64 ± 0.1                       | 0.62 ± 0.1                       |
| Rim-R                 | 0.97 ± 0.2                           | 0.60 ± 0.1                                  | 0.53 ± 0.1                       | 0.66 ± 0.1                       | 1.03 ± 0.2                       |
| Rim-S                 | 0.77 ± 0.2                           | 0.61 ± 0.1                                  | 0.56 ± 0.1                       | 0.64 ± 0.1                       | 0.55 ± 0.1                       |
| Spiro-adamantyl amine | 0.96 ± 0.2                           | 0.60 ± 0.1                                  | 0.62 ± 0.1                       | 0.58 ± 0.1                       | 0.93 ± 0.2                       |

| Ligand                | Ligand tilt             | V27-Ad <sup>8</sup> | A30-Ad <sup>9</sup> | G34-Ad <sup>10</sup> | H-bonds <sup>11</sup> | Cl-N distance <sup>12</sup> |
|-----------------------|-------------------------|---------------------|---------------------|----------------------|-----------------------|-----------------------------|
| Amt                   | 11.5 ± 6.1 <sup>6</sup> | 4.5 ± 0.3           | 0.7 ± 0.3           | 5.2 ± 0.3            | 2.8 ± 0.4             | 51.0 ± 10.7                 |
| Rim-R                 | 21.7 ± 7.7 <sup>6</sup> | 4.2 ± 0.3           | 1.1 ± 0.3           | 5.7 ± 0.3            | 3.0 ± 1.1             | 47.2 ± 10.1                 |
| Rim-S                 | 17.4 ± 5.7 <sup>6</sup> | 4.3 ± 0.3           | 1.0 ± 0.3           | 5.5 ± 0.3            | 2.9 ± 1.1             | 47.1 ± 10.4                 |
| Spiro-adamantyl amine | 8.2 ± 4.1 <sup>7</sup>  | 4.3 ± 0.3           | 1.0 ± 0.3           | 5.4 ± 0.3            | 2.7 ± 0.5             | 49.0 ± 10.6                 |

## 4.8 Appendix D, Detailed Methods

*4.8.1 Experimental methods.* The construct of M2 used in this study was Influenza A/Udorn/1972 M2 wild-type, residues 22-46. The peptide was chemically synthesized and purified as previously described,<sup>28,29</sup> with acetylation of the N-terminus and amidation of the C-terminus:

Ace-SSDPLVVAASIIGILHLILWILDRL-NH<sub>2</sub>

The peptide sample was reconstituted into the lipid cubic phase (LCP) with some modifications to Caffrey and Cherezov's protocol.<sup>41</sup> Dry peptide was dissolved in ethanol and added directly to monoolein powder. Excess ethanol was blown off with nitrogen gas, and the sample was left under vacuum (<100 mTorr) overnight to remove the remaining solvent.

The drugs and inhibiting compounds used in this study were amantadine (1-adamantylamine HCl, Aldrich), rimantadine (1-(1-adamantyl)ethylamine HCl, Aldrich), and spiro adamantyl amine "Compound 9" from Wang et al. 2011.<sup>46</sup>

The lipid cubic phase was made by mixing 30 mg of peptide/monoolein sample with 20  $\mu$ L of 50 mM detergent solution. The detergent used in this study was decyl maltose neopentyl glycol (DMNG, MW = 949.08); MNG detergents have been observed to stabilize membrane proteins for crystallization trials.<sup>60,61</sup> DMNG detergent was synthesized by the Pil Seok Chae group (Hanyang University, Seoul, South Korea). Plastic 96-well LCP sandwich trays (Laminex, 200 micron base) containing drops of LCP plus precipitant solution were used to screen crystallization conditions using a LCP crystallization robot (TTP Labtech). Trays were screened using visible-light and UV imaging. Crystals were harvested from 96-well trays and frozen in liquid nitrogen for transport and data collection.

The crystals formed by these conditions were thin, square-shaped plates. Though a detergent amphiphile was present in the crystallization conditions, the protein-containing lipid cubic phase remained separate from the precipitant solution and did not swell into the sponge phase. The crystallization conditions yielding the deposited PDB structures are as follows:

**6BKK:** 100 nL LCP + 1  $\mu$ L precipitant solution. LCP: 60 mg monoolein,  $1.6 \times 10^{-6}$  moles M2TM (EtOH stock),  $6.4 \times 10^{-6}$  amantadine (EtOH stock) (4:1 ratio of amantadine:M2 monomer); 40  $\mu$ L of 50 mM DMNG detergent in water. Precipitant solution: 0.1 M NaCl, 0.02 M sodium citrate pH 5.6, 11% w/v PEG 3350. Crystals grew at 20 °C. Thin square plates formed after 9 months and grew to 100  $\mu$ m in size.

**6BKL:** 100 nL LCP + 0.5  $\mu$ L precipitant solution. LCP: 60 mg monoolein,  $1.6 \times 10^{-6}$  moles M2TM (EtOH stock),  $6.4 \times 10^{-6}$  moles rimantadine (EtOH stock) (4:1 ratio of rimantadine:M2 monomer); 40  $\mu$ L of 50 mM DMNG detergent in water. Precipitant solution: 0.2 M MgCl<sub>2</sub>, 0.1 M sodium acetate / acetic acid pH 4.5, 20% w/v PEG 8000. Plates were incubated at 20 °C. Thin square plates formed after 1 month and grew to 75  $\mu$ m in size.

**6BMZ:** 100 nL LCP + 0.5  $\mu$ L precipitant solution. LCP: 60 mg monoolein,  $1.6 \times 10^{-6}$  moles M2TM (EtOH stock),  $6.4 \times 10^{-6}$  moles spiro-adamantyl amine (EtOH stock) (4:1 ratio of inhibitor:M2 monomer); 40  $\mu$ L of 50 mM DMNG detergent in water. Precipitant solution: 0.1 M HEPES pH 7.0, 30% v/v PEG 400. Plates were incubated at 20 °C. Thin square plates formed after 1 week and grew to 50  $\mu$ m in size.

**6BOC:** 100 nL LCP + 0.5  $\mu$ L precipitant solution. LCP:  $2.4 \times 10^{-6}$  moles M2TM (EtOH stock),  $9.6 \times 10^{-6}$  moles rimantadine (EtOH stock) (4:1 ratio of rimantadine:M2 monomer); 40  $\mu$ L of 50 mM DMNG detergent in water. Precipitant solution: 0.18 M LiSO<sub>4</sub>, 4% v/v



(±)-1,3-butanediol, 0.09 M sodium citrate pH 3.5 (adjusted w/ HCl), 25.2% v/v PEG 400. Thin square plates formed after 2 weeks and grew to 300  $\mu\text{m}$  in size.

Data were collected at Advanced Light Source (ALS) beam 8.3.1. 6BKK, 6BKL, and 6BMZ were collected using a Q315 detector. 6BOC was collected using a Pilatus 6M detector.

Data collection parameters were as follows:

**6BKK:** E = 11111 eV, d = 250 mm, oscillation = 1°, t = 2 s, 115 frames.

**6BKL:** E = 11111 eV, d = 250 mm, oscillation = 1°, t = 1 s, 360 frames.

**6BMZ:** E = 11111 eV, d = 350 mm, oscillation = 1°, t = 1 s, 200 frames.

**6BOC:** E = 11111 eV, d = 300 mm, oscillation = 0.7°, t = 0.2 s, 300 frames.

Indexing and integration were carried out in MOSFLM,<sup>62</sup> and the data were scaled and merged using Aimless<sup>55</sup> in the CCP4 suite.<sup>63,64</sup> Molecular replacement was done using Phaser<sup>65</sup> with previously solved structures as search models (3LBW<sup>27</sup> for the Inward<sub>closed</sub> state, 4QK7<sup>28</sup> for the Inward<sub>open</sub> state). Zanuda<sup>56</sup> was used to aid in space group determination. Refinement was carried out in PHENIX,<sup>57</sup> with model building in Coot<sup>58</sup> and PyMOL.<sup>59</sup>

The tilts of amantadine and rimantadine adamantyl groups relative to the channel's central axis for structures 6BKK and 6BKL were calculated as the angle between two vectors: the channel central axis vector, and the adamantyl 3-fold axis vector. The channel central axis vector consists of the averaged C $\alpha$  coordinates for all four monomers of the tetramer at two different residues, Leu26 and His37. The adamantyl 3-fold axis vector consists of the averaged coordinates of three symmetrically equivalent adamantyl carbons (atom names C2, C4, and C6 for amantadine, and atom names CG1, CG2, and CG3 for rimantadine), and the coordinates of an

atom at the center of the 3-fold axis (atom name C10 for amantadine, and atom name CD for rimantadine).

*4.8.2 Molecular dynamics methods.* The M2TM complexes were embedded in a POPC lipid bilayer extending 30 Å beyond the solutes. The number of lipids added was ~ 200. The bilayer was then solvated by a 30-Å-thick layer of waters. Na<sup>+</sup> and Cl<sup>-</sup> ions were placed in the water phase to neutralize the systems and to reach the experimental salt concentration of 0.150 M NaCl. The total number of ions was ~ 80000. Membrane creation and system solvation were conducted with the “System Builder” utility of Desmond. The OPLS 2005 force field<sup>66-68</sup> was used to model all protein and ligand interactions, and the TIP3P<sup>69</sup> model was used for water. The particle mesh Ewald method (PME)<sup>70,71</sup> was employed to calculate long-range electrostatic interactions with a grid spacing of 0.8 Å. Van der Waals and short range electrostatic interactions were smoothly truncated at 9.0 Å. The Nosé-Hoover thermostat<sup>72</sup> was utilized to maintain a constant temperature in all simulations, and the Martyna-Tobias-Klein method<sup>72</sup> was used to control the pressure. Periodic boundary conditions were applied (90×90×105)Å<sup>3</sup>. The equations of motion were integrated using the multistep RESPA integrator with an inner time step of 2 fs for bonded interactions and non-bonded interactions within a cutoff of 9 Å. An outer time step of 6.0 fs was used for non-bonded interactions beyond the cut-off. Each system was equilibrated in MD simulations with a modification of the default protocol provided in Desmond, which consists of a series of restrained minimizations and MD simulations designed to relax the system, while not deviating substantially from the initial coordinates. First, two rounds of steepest descent minimization were performed with a maximum of 2000 steps with harmonic restraints of 50 kcal mol<sup>-1</sup> Å<sup>-2</sup> applied on all solute atoms, followed by 10000 steps of minimization without restraints.

The first simulation was run for 200 ps at a temperature of 10 K in the NVT ensemble with solute heavy atoms restrained with a force constant of  $50 \text{ kcal mol}^{-1} \text{ \AA}^{-2}$ . The temperature was then raised during a 200 ps MD simulation to 310 K in the NVT ensemble with the force constant retained. The heating was followed by equilibration runs. First, two stages of NPT equilibration were performed, one with the heavy atoms of the system restrained for 1 ns and one for solvent and lipids for 10 ns, with a force constant of  $10 \text{ kcal/mol/\AA}^2$  for the harmonic constraints, respectively. A NPT simulation followed with the  $C_\alpha$  atoms restrained for 1 ns with a force constant of  $2 \text{ kcal/mol/\AA}^2$ . The above-mentioned equilibration was followed by a 250 ns NPT simulation without restraints. Within this time, the total energy and the RMSD reached a plateau, and the systems were considered equilibrated. For structural analyses, snapshots of the different systems were created with VMD<sup>73</sup> or Maestro<sup>74</sup> or Chimera.<sup>75</sup> Trajectories were analyzed with Maestro, Gromacs,<sup>76,77</sup> and VMD. Measurements were carried out with Gromacs tools. For the calculation of hydrogen bonds, a cut-off angle of  $30^\circ$  deviation from  $180^\circ$  between the donor-hydrogen-acceptor atoms and a cut-off distance of  $3.5 \text{ \AA}$  between the donor and acceptor atoms were applied.

**Molecular Dynamics Analysis:** We analyzed snapshots at 5 ps intervals of the 100 ns trajectory. Snapshots were aligned to the M2 crystal structure via CA atoms of residues 26-42.

### *Autocorrelation*

Autocorrelation functions of **Figs. S5** and **S7** were calculated by:

$$C(t) = ( \langle A(0)A(t) \rangle - \langle A \rangle^2 ) / ( \langle A^2 \rangle - \langle A \rangle^2 )$$

where A is the variable of interest, and were fit to a mono- or bi-exponential decay function. For angular data, we fit the autocorrelation of the cosine of the angle.

### Intrinsic Spin

Intrinsic spin was calculated by the following procedure: An internal reference frame of the drug was rotated about the X and Y axes of the bundle. The intrinsic spin is the final rotation about the Z axis (long axis of the bundle) to align the drug internal reference frame with the reference frame of the bundle. For intrinsic spin of the amine, the internal reference frame was taken as the following (normalized) vectors:

Amine of amantadine:

origin = center of mass of amine hydrogens

z-axis = C1 – origin

x-axis = H1A – origin

y-axis =  $z \otimes x$

Amine of spiro-adamantyl amine:

origin = center of mass of amine hydrogens

z-axis = C10 – origin

x-axis = HN1 – origin

y-axis =  $z \otimes x$

Adamantane of amantadine:

origin = center of mass of C7, C8, C9

z-axis = N1 – origin

x-axis = C8 – origin

y-axis = z  $\otimes$  x

Adamantane of Spiro-adamantyl amine:

origin = center of mass of C8, C10, C14, C15

z-axis = C4 – origin

x-axis = C8 – origin

y-axis = z  $\otimes$  x

#### *Clustering of MD snapshots by amine position*

After superposition of the snapshots onto the crystal structure as described above, we used a greedy clustering method (see Daura et al.<sup>78</sup>) to cluster the MD snapshots by position of the amine, including hydrogens. No further manipulation of the amine coordinates was taken. Atoms used in the RMSD calculation were C10, N1, HN1, HN1A, and HN1B for amantadine and C1, N1, H1A, H1B, and H1C for spiro-adamantyl amine. The amines were clustered with a 0.6 Å RMSD. At this cutoff, greater than 50% of the MD snapshots were placed into the top 2 (amantadine) or 3 (spiro-adamantyl amine) clusters. All permutations of the hydrogens were considered in the clustering. The positions of the waters from these top clusters are shown in the water density figures.

### 4.8.3 Appendix D References

- 1 Liebschner, D. *et al.* Polder maps: improving OMIT maps by excluding bulk solvent. *Acta Crystallographica. Section D, Structural Biology* **73**, 148-157, doi:10.1107/S2059798316018210 (2017).
- 2 Stouffer, A. L. *et al.* Structural basis for the function and inhibition of an influenza virus proton channel. *Nature* **451**, 596-U513, doi:10.1038/nature06528 (2008).
- 3 Evans, P. Scaling and assessment of data quality. *Acta Crystallographica Section D* **62**, 72-82, doi:10.1107/S0907444905036693 (2006).
- 4 Lebedev, A. A. & Isupov, M. N. Space-group and origin ambiguity in macromolecular structures with pseudo-symmetry and its treatment with the program Zanuda. *Acta Crystallographica Section D* **70**, 2430-2443, doi:10.1107/S1399004714014795 (2014).
- 5 Adams, P. D. *et al.* PHENIX: a comprehensive Python-based system for macromolecular structure solution. *Acta Crystallographica Section D-Biological Crystallography* **66**, 213-221, doi:10.1107/s0907444909052925 (2010).
- 6 Emsley, P., Lohkamp, B., Scott, W. G. & Cowtan, K. Features and development of Coot. *Acta Crystallographica Section D-Biological Crystallography* **66**, 486-501, doi:10.1107/s0907444910007493 (2010).
- 7 Schrodinger, LLC. *The PyMOL Molecular Graphics System, Version 1.3r1* (2010).
- 8 Thomaston, J. L. *et al.* High-resolution structures of the M2 channel from influenza A virus reveal dynamic pathways for proton stabilization and transduction. *Proceedings of the National Academy of Sciences* **112**, 14260-14265, doi:10.1073/pnas.1518493112 (2015).
- 9 Thomaston, J. L. & DeGrado, W. F. Crystal structure of the drug-resistant S31N influenza M2 proton channel. *Protein Science* **25**, 1551-1554, doi:10.1002/pro.2937 (2016).
- 10 Caffrey, M. & Cherezov, V. Crystallizing membrane proteins using lipidic mesophases. *Nature Protocols* **4**, 706-731, doi:10.1038/nprot.2009.31 (2009).
- 11 Wang, J. *et al.* Molecular dynamics simulation directed rational design of inhibitors targeting drug-resistant mutants of influenza A virus M2. *Journal of the American Chemical Society* **133**, 12834-12841, doi:Doi 10.1021/Ja204969m (2011).
- 12 Chae, P. S. *et al.* Maltose-neopentyl glycol (MNG) amphiphiles for solubilization, stabilization and crystallization of membrane proteins. *Nature Methods* **7**, 1003-1008, doi:10.1038/nmeth.1526 (2010).

- 13 Cho, K. H. *et al.* Maltose Neopentyl Glycol-3 (MNG-3) Analogues for Membrane Protein Study. *The Analyst* **140**, 3157-3163, doi:10.1039/c5an00240k (2015).
- 14 Battye, T. G. G., Kontogiannis, L., Johnson, O., Powell, H. R. & Leslie, A. G. W. iMOSFLM: a new graphical interface for diffraction-image processing with MOSFLM. *Acta Crystallographica Section D-Biological Crystallography* **67**, 271-281, doi:10.1107/s0907444910048675 (2011).
- 15 Cowtan, K., Emsley, P. & Wilson, K. S. From crystal to structure with CCP4. *Acta Crystallographica Section D* **67**, 233-234, doi:10.1107/S0907444911007578 (2011).
- 16 Winn, M. D. *et al.* Overview of the CCP4 suite and current developments. *Acta Crystallographica Section D: Biological Crystallography* **67**, 235-242, doi:10.1107/S0907444910045749 (2011).
- 17 McCoy, A. J. *et al.* Phaser crystallographic software. *Journal of Applied Crystallography* **40**, 658-674, doi:10.1107/s0021889807021206 (2007).
- 18 Acharya, R. *et al.* Structure and mechanism of proton transport through the transmembrane tetrameric M2 protein bundle of the influenza A virus. *Proceedings of the National Academy of Sciences* **107**, 15075-15080, doi:10.1073/pnas.1007071107 (2010).
- 19 Jorgensen, W. L., Maxwell, D. S. & Tirado-Rives, J. Development and Testing of the OPLS All-Atom Force Field on Conformational Energetics and Properties of Organic Liquids. *Journal of the American Chemical Society* **118**, 11225-11236, doi:10.1021/ja9621760 (1996).
- 20 Kaminski, G. A., Friesner, R. A., Tirado-Rives, J. & Jorgensen, W. L. Evaluation and Reparametrization of the OPLS-AA Force Field for Proteins via Comparison with Accurate Quantum Chemical Calculations on Peptides. *The Journal of Physical Chemistry B* **105**, 6474-6487, doi:10.1021/jp003919d (2001).
- 21 Rizzo, R. C. & Jorgensen, W. L. OPLS All-Atom Model for Amines: Resolution of the Amine Hydration Problem. *Journal of the American Chemical Society* **121**, 4827-4836, doi:10.1021/ja984106u (1999).
- 22 Jorgensen, W. L., Chandrasekhar, J., Madura, J. D., Impey, R. W. & Klein, M. L. Comparison of simple potential functions for simulating liquid water. *The Journal of Chemical Physics* **79**, 926-935, doi:10.1063/1.445869 (1983).
- 23 Darden, T., York, D. & Pedersen, L. Particle mesh Ewald: An N·log(N) method for Ewald sums in large systems. *The Journal of Chemical Physics* **98**, 10089-10092, doi:10.1063/1.464397 (1993).
- 24 Essmann, U. *et al.* A smooth particle mesh Ewald method. *The Journal of Chemical Physics* **103**, 8577-8593, doi:10.1063/1.470117 (1995).

- 25 Martyna, G. J., Tobias, D. J. & Klein, M. L. Constant pressure molecular dynamics algorithms. *The Journal of Chemical Physics* **101**, 4177-4189, doi:10.1063/1.467468 (1994).
- 26 Humphrey, W., Dalke, A. & Schulten, K. VMD: Visual molecular dynamics. *Journal of Molecular Graphics* **14**, 33-38, doi:[https://doi.org/10.1016/0263-7855\(96\)00018-5](https://doi.org/10.1016/0263-7855(96)00018-5) (1996).
- 27 Schrodinger, L. Maestro, version 8.5. (2008).
- 28 Pettersen, E. F. *et al.* UCSF Chimera—A visualization system for exploratory research and analysis. *Journal of Computational Chemistry* **25**, 1605-1612, doi:10.1002/jcc.20084 (2004).
- 29 Berendsen, H. J. C., van der Spoel, D. & van Drunen, R. GROMACS: A message-passing parallel molecular dynamics implementation. *Computer Physics Communications* **91**, 43-56, doi:[https://doi.org/10.1016/0010-4655\(95\)00042-E](https://doi.org/10.1016/0010-4655(95)00042-E) (1995).
- 30 Hess, B., Kutzner, C., van der Spoel, D. & Lindahl, E. GROMACS 4: Algorithms for Highly Efficient, Load-Balanced, and Scalable Molecular Simulation. *Journal of Chemical Theory and Computation* **4**, 435-447, doi:10.1021/ct700301q (2008).
- 31 Xavier, D. *et al.* Peptide folding: when simulation meets experiment. *Angewandte Chemie International Edition* **38**, 236-240, doi:doi:10.1002/(SICI)1521-3773(19990115)38:1/2<236::AID-ANIE236>3.0.CO;2-M (1999).



## Chapter 5

### Crystal structure of the drug-resistant S31N influenza M2 proton channel in the Inward<sub>open</sub> conformation

#### 5.1 Abstract

The M2 protein is a small proton channel found in the influenza A virus that is necessary for viral replication. The M2 channel is the target of a class of drugs called the adamantanes, which block the channel pore and prevent the virus from replicating. In recent decades mutations have arisen in M2 that prevent the adamantanes from binding to the channel pore, with the most prevalent of these mutations being S31N. Here we report the first crystal structure of the S31N mutant crystallized using lipid cubic phase crystallization techniques and solved to 1.59 Å resolution. The Asn31 residues point directly into the center of the channel pore and form a hydrogen-bonded network that disrupts the drug-binding site. Ordered waters in the channel pore form a continuous hydrogen bonding network from Gly34 to His37.

#### 5.2 Introduction

The influenza A matrix 2 (M2) protein consists of a 97-residue monomer that forms a homotetrameric channel. M2 is an amazingly small multifunctional protein, with different functions localized sequentially along the amino acid chain. The N-terminal 22 residues, which project out of the virus, contribute to budding in influenza A, but are deleted in influenza B virus. The transmembrane helix spanning residues 22-46 forms a tetramer that retains channel-forming function, selectivity and sensitivity to drug.<sup>1</sup> A region C-terminal to the TM helix forms a peripheral membrane-binding helix that stabilizes envelope excision during membrane budding

by stabilizing negative Gaussian curvature,<sup>2,3</sup> and the C-terminal region also interacts with the M1 matrix protein.<sup>4</sup> The M2 protein is a drug target of two FDA approved anti-flu drugs, amantadine and rimantadine, which bind in the pore of the M2 channel.<sup>5,6</sup>

The M2 protein mediates the equilibration of the pH between endosomal compartment and the viral interior at a critical point of the viral reproduction cycle. In some strains of influenza A virus, M2 also serves to delay acidification of the interior of the Golgi apparatus to prevent HA from prematurely undergoing an acid-mediated conformational change.<sup>7,8</sup> Amantadine and rimantadine exert their antiviral effect by binding to the pore of the M2 tetramer and blocking proton conduction.<sup>5,6</sup> In recent years amantadine resistance from the S31N mutant has become so widespread that it has curtailed the use of this class of drugs.<sup>9</sup>

Despite the importance of the S31N mutation, almost all structural work has focused on variants of M2 with Ser at position 31. Chou and coworkers have built homology models for the S31N variant of M2 based on NMR restraints.<sup>10</sup> Although dynamics prevented determination of the location of Asn31, they hypothesized that its sidechain projects out towards the lipid tails. More recently, we used small molecule drugs that bind to the S31N mutant to lock it into a conformation that was more amenable to solution NMR structure determination, allowing the determination of the structure at moderate resolution.<sup>11</sup> Unfortunately, although the overall structure was well defined, conformational exchange of the Asn31 sidechain made it difficult to determine its orientation; we attributed this conformational exchange to the fact that the drug is intrinsically asymmetric while the protein is 4-fold symmetric. Here, we present the first crystal structure of the S31N mutant of influenza M2.

### 5.3 Results and Discussion

The crystal structure of the S31N mutant was obtained using lipid cubic phase (LCP) techniques, giving crystals (**Fig. 5.1**) at pH 8.0 that diffract to a resolution of 1.59 Å in the same space group as the "wild-type" Ser31 channel.<sup>12</sup> A single monomer forms the asymmetric unit (**Fig. 5.2**), which is repeated along a crystallographic four-fold symmetry axis to create the pore. Monoolein molecules interact with the hydrophobic membrane-exposed face of each monomer. There are very few contacts between protein molecules in the crystal lattice; the membrane-exposed face of each M2 monomer interacts with monoolein molecules at its N-terminus and, to a lesser extent, with other M2 monomers near the C-terminus (**Fig. 5.3b**).

*5.3.1 Solvent network and partially occupied waters.* As in other NMR and crystal structures of the M2 channel,<sup>6,12</sup> a continuous pore runs through the membrane-spanning region of the structure, interrupted only at Val27. In the S31N mutant, the polar Asn sidechain points towards the center of the channel; each carboxamide nitrogen of the Asn residue forms a hydrogen bond with the carbonyl of a neighboring Asn31 sidechain. A water molecule was observed at the center of the Asn31 tetrad, bridging the cyclic hydrogen-bonding arrangement (**Fig. 5.3c**). This water might serve a special role in transmitting protons into the channel, although dynamic motions would be required to diffuse past Val27, as described previously.<sup>13 14 15</sup> Four Å below this water is a cluster of waters that form a continuous water wire leading to the proton-shuttling residue His37 (**Fig. 5.3a**). Most of these waters exist at half occupancy. The presence of two partial-occupancy water networks in the channel could result from averaging of the water densities across the four-fold symmetry axis at the center of the channel. A strong spherical density was observed along the 4-fold axis among the water clusters. Of the ions in the buffer,

only chloride fit well into this density. A single chloride at a similar position along the symmetry axis has also been proposed to play a role in stabilizing the M2 tetramer.<sup>16</sup>

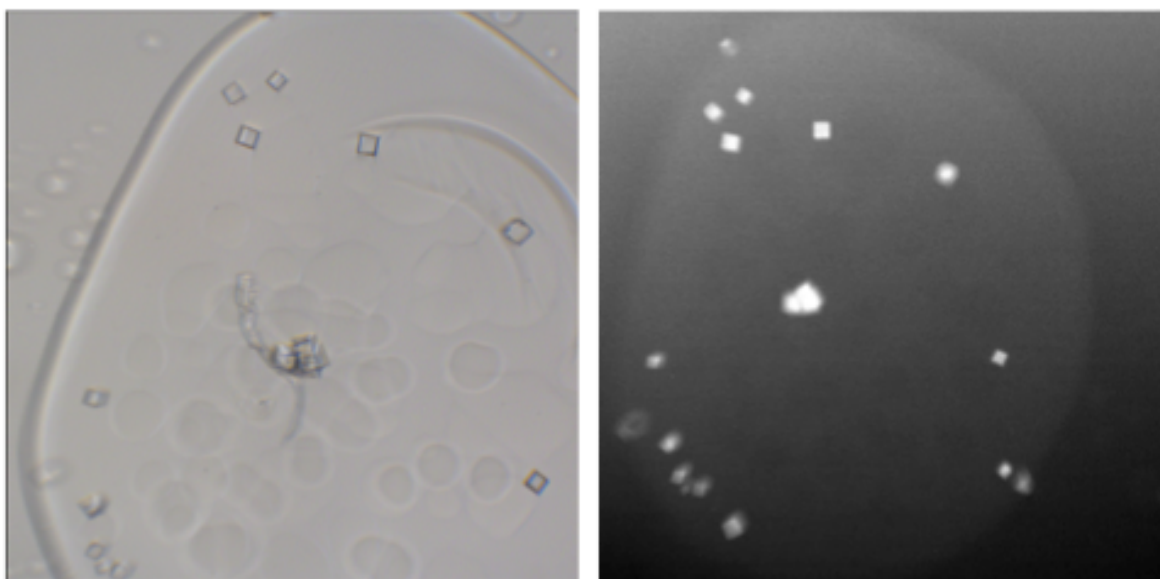


**Figure 5.1. Crystals of M2TM S31N mutant.** Square-shaped S31N(22-46) crystals formed in 0.2 M CaCl<sub>2</sub>, 0.1 M Tris HCl pH 8.0, 44% v/v PEG 400 at 10°C. Visible image to the left, UV image to the right.

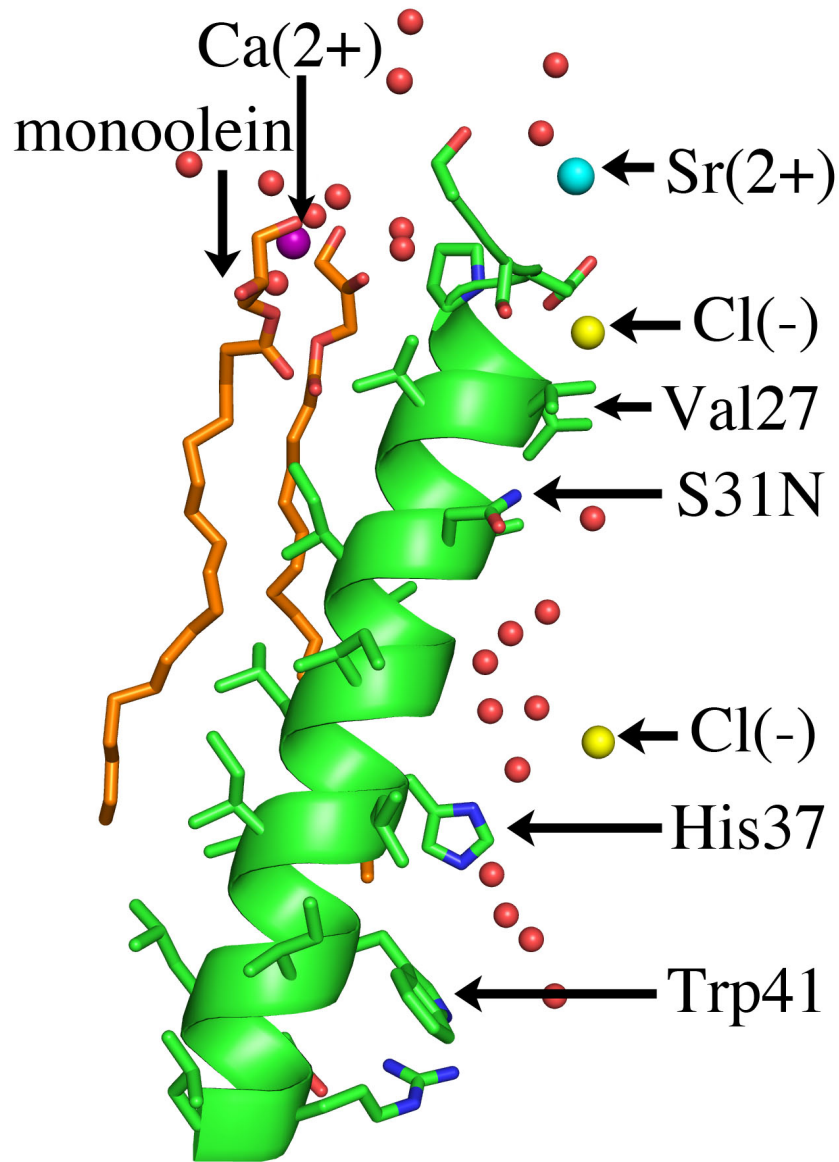


**Figure 5.2. Contents of asymmetric unit of M2 S31N structure.** Contents of the asymmetric unit, which contains one monomer of AM2(22-46) (green), waters (red spheres), ions (blue, yellow and purple spheres), and monoolein (orange).

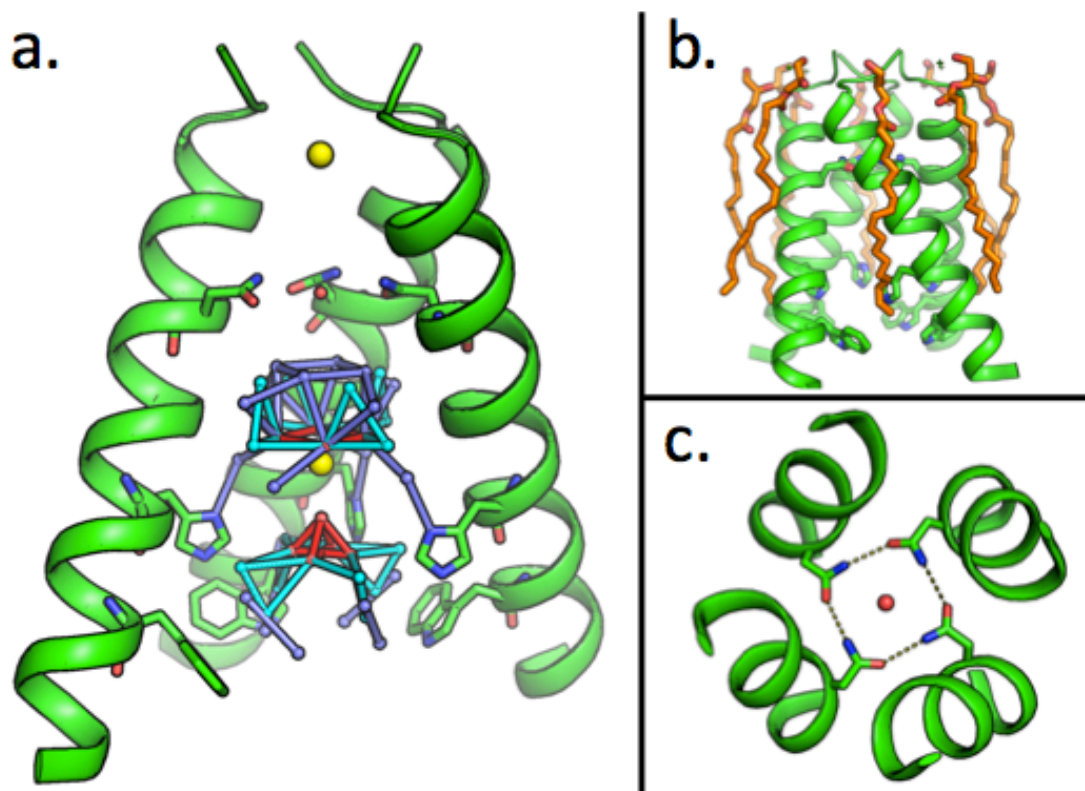


**Figure 5.3. Crystal structure of the S31N mutant of M2 in the Inward<sub>open</sub> conformation.** a. The M2 pore; the M2 tetramer is shown with the front monomer removed. Full occupancy waters are shown as red spheres, partial occupancy waters are shown in cyan and dark blue, and chloride ions are shown in yellow. Hydrogen bonds between pore waters are shown as colored sticks (red, cyan, and dark blue). Asn31, His37 and Trp41 are shown as sticks. b. The M2 tetramer (green) is surrounded by monoolein molecules (orange) within the crystal lattice. c. Top-down view of the channel pore; Asn31 residues form a network of hydrogen bonds (dashed lines). A single water (red sphere) is located in the middle of these residues.

*5.3.2 Resistance to adamantane drugs and inhibitor binding.* The mechanism by which the S31N mutation confers resistance to amantadine can be seen upon overlaying the newly solved LCP structure with the previously solved crystal structure of wild-type M2 in the presence of amantadine (**Fig. 5.4a**). Hydrogen bonding between symmetrically repeated Asn31 residues within the homotetrameric channel narrows the portion of the channel to which the adamantine

drugs bind, providing steric hindrance that reduces the drugs' affinity to that site. Substitution of Ser31 with Asn also adds an extra hydrophilic atom to a site that interacts with the hydrophobic adamantane cage.

**Figures 5.4b** and **5.4c** compare the recently solved structure to the previously solved inhibitor-bound solution NMR structure of S31N.<sup>11</sup> Though the conformations of the asparagine residues in the NMR structure could not be resolved, the position of the inhibitor within the channel is well defined by NOEs. The location of the single water at the center of the S31N crystal structure approximately maps to the position of the nitrogen in the bound inhibitor molecule. This supports the suggestion that the ammonium group of M2 inhibitors occupy the same positions in the channel as ordered waters in the apo structure. The availability of a high-resolution structure of the S31N should also be quite helpful for design of drugs that target drug-resistant mutants bearing this mutation.

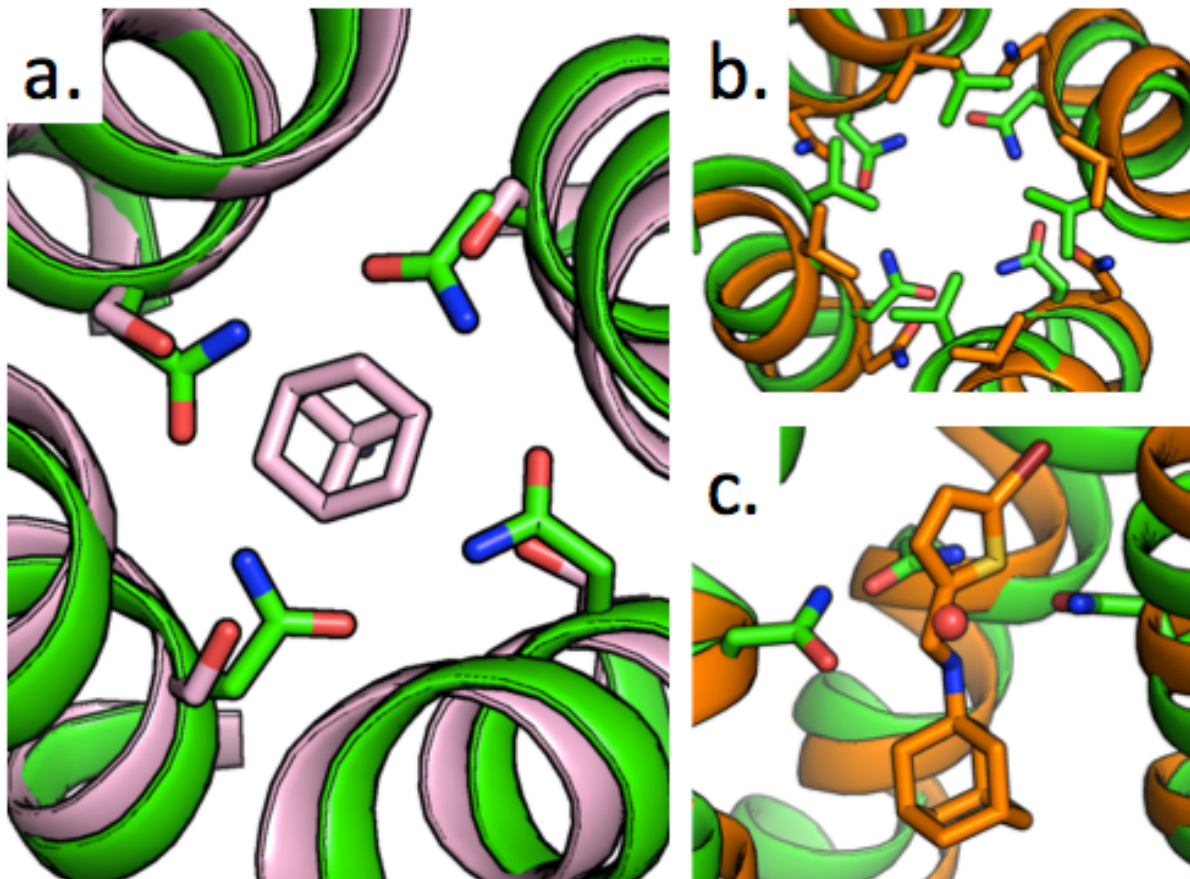


**Figure 5.4. Drug resistance in the M2 S31N mutant.** a. Overlay of S31N mutant structure 5C02 (green) onto the drug-bound structure 3C9J (pink) with Asn31, Ser31, and amantadine shown as sticks. b. Top-down view of 5C02 aligned to M2WJ332-bound solution NMR S31N structure 2MUV (orange), Val27 and Asn31 shown as sticks. c. Side view of inhibitor from 2MUV in channel pore, with water from 5C02 shown as a red sphere.



## 5.4 Methods

*5.4.1 Synthesis, purification, and crystallization of S31N.* The M2TM S31N peptide (Ac-SSDPLVVAANIIGILHLILWILDRL-NH<sub>3</sub>) was synthesized on Rink Amide resin using a Quest 210 peptide synthesizer (Argonaut Technologies) at a temperature of 75°C. Each residue was deprotected in a solution of 5% w/w piperazine and 0.1 M HOBt. The resin was thoroughly rinsed with DMF then a coupling reaction was initiated by addition of 5 molar equivalents of amino acid that had been pre-activated with 5 equivalents of HCTU and 10 equivalents of DIEA. After all of the amino acids were added to the resin, the reaction was cooled to 25°C and the N-terminus of the peptide was acylated by the addition of 20 equivalents of acetic anhydride and 40 equivalents of DIEA. The resin was washed with DCM and hexane then the peptide was cleaved from the resin in a mixture of 94% v/v TFA, 5% TES, and 1% H<sub>2</sub>O. LC-MS confirmed that the mass of the peptide was that of the desired product.

The peptide was purified using reverse-phase HPLC on a Varian ProStar machine using a PROTO300 C4 10 μm column (Higgins Analytical Inc.). A gradient combining buffers A (99.9% water and 0.1% TFA) and B' (60% isopropanol, 30% acetonitrile, 10% water, 0.1% TFA) was used to separate and elute the peptide. The eluted fractions were lyophilized and the purified peptide was stored in ethanol at -80°C.

The lipid cubic phase (LCP) was prepared with some modifications to the protocol described by Caffrey and Cherezov.<sup>17</sup> Peptide stock containing 4.0x10<sup>-7</sup> moles of peptide in ethanol was added to 60mg of monoolein, mixed, then excess ethanol was removed by lyophilized overnight. The resulting peptide/monoolein mixture was warmed to 40°C in a water bath and transferred to a gas-tight Hamilton 200 μL syringe. 50 mM octyl glucopyranoside (OG) in water was added into the syringe at a ratio of 20 μL for every 30 mg of transferred

sample. The sample was then re-heated to 40°C and connected to a second gas-tight Hamilton syringe using a metal syringe coupler. The sample was pushed back and forth through the syringe coupler to form a homogenous mixture. The sample became transparent after 2-3 minutes of transfer between the two syringes via the syringe coupler.

Crystallization conditions were screened in 96-well plastic plates (Molecular Dimensions) that were set up using a LCP crystallization robot (TTP Labtech) using a protocol that combined 100 nL of LCP sample with 1000 nL of screening solution. Square-shaped crystals belonging to space group  $I_4$  formed in a solution of 0.2 M  $\text{CaCl}_2$ , 0.1 M Tris pH 8.0, and 44% v/v PEG 400 after 2-4 weeks of incubation at 10°C. These conditions were optimized to grow 10-40  $\mu\text{m}$  large crystals using the Hampton Additive screen; the conditions that yielded structure 5C02 were: 0.18 M  $\text{CaCl}_2$ , 0.09 M Tris HCl pH 8.0, 36% (v/v) PEG 400, 0.01 M  $\text{SrCl}_2 \cdot 6\text{H}_2\text{O}$ , at 10°C. Crystals were observed and harvested in a 4°C cold room. Because of the high percentage of PEG 400 in the solution, no additional cryoprotectant was added before the crystals were frozen and stored in liquid nitrogen.

*5.4.2 Data collection and processing.* Data were collected at the Advanced Photon Source in Argonne, IL at the 24ID-E beamline using a ADSC Q315 CCD Detector. A total of 60 frames were used for data processing, with an incident beam energy of 12.66 keV, an exposure time of 1s, 1° oscillation, a detector distance of 200 mm, and a data collection temperature of 100 K.

Data processing was done in iMosflm.<sup>18</sup> Phasing was done by molecular replacement in the Phenix suite using Phaser MR<sup>19</sup> with chain A from PDB entry 3C9J<sup>20</sup> as a search model, then refinement was carried out in Phenix Refine.<sup>21</sup> Protein model manipulation and addition of

water and ions were done in Coot,<sup>22</sup> and monoolein molecules were manually fit into Fo-Fc density using both Coot and PyMol.<sup>23</sup>

*5.4.3 Ions and lipid molecules in the S31N crystal structure.* As observed in previously solved structures of AM2 wild type,<sup>20</sup> ions from the crystallization solution interact closely with N-terminal residues. A strontium ion at the N-terminus of the channel is coordinated by the main chain carbonyl groups of four symmetrically repeated Ser22 residues and also by four waters. Below this site, a chloride ion interacts with the side chain hydroxyl groups of four Ser23 residues. A second chloride ion can be seen between residues Gly34 and His37 lying on the axis of fourfold symmetry and coordinating to four water molecules. Calcium ions were observed to interact with hydrophilic monoolein headgroups, and surrounding waters.

Because the M2(22-46) S31N peptide was crystallized in monoolein using lipid cubic phase techniques, the presence of monoolein molecules in the resulting crystal lattice is not surprising. Density corresponding to portions of the two modeled monoolein molecules is visible at a 2Fo-Fc map contour of  $1\sigma$ . The degree to which the modeled monoolein molecules fit into the 2Fo-Fc density is reflected by the B-factor of each atom. Comparing the average B-factors from the peptide chain (21.90) and the monoolein molecules (32.60), the monoolein molecules likely undergo a higher degree of thermal motion within the lattice than the peptide does.

*5.4.4 Accession numbers.* The Protein Data Bank accession number for the 1.59 Å structure of AM2(22-46) S31N is 5C02.

## **5.5 Acknowledgements**

We thank Magdalena Korczynska and Nathan Joh for helpful discussions concerning data collection and structure determination. Experimental work was funded by NIH grant R01-GM056423. Use of the LCP Mosquito robot at UCSF was made possible by Grant 1S10RR027234-01 from the National Center For Research Resources. This work is based upon research conducted at the Advanced Photon Source on the Northeastern Collaborative Access Team beamlines, which are supported by grants from the National Center for Research Resources (5P41RR015301-10) and the NIH (8 P41 GM103403-10). Use of the Advanced Photon Source, operated for the U.S. Department of Energy (DOE) Office of Science by Argonne National Laboratory, was supported under Contract No. DE-AC02-06CH11357.

## 5.6 Supplemental Figures and Tables

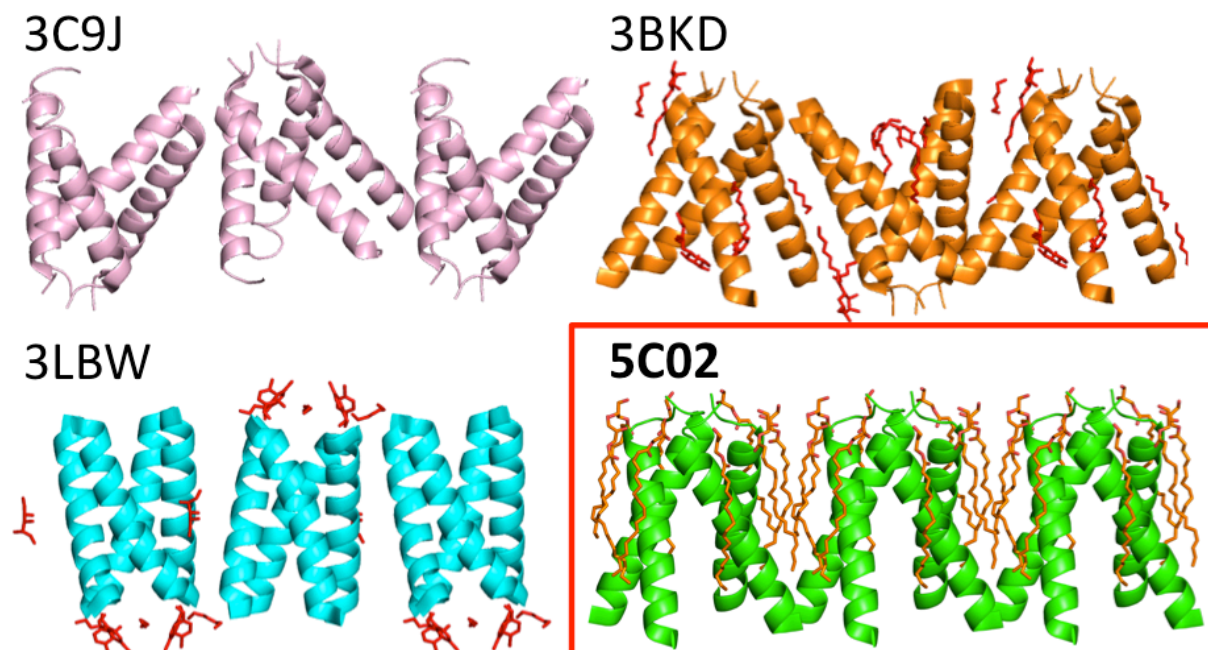
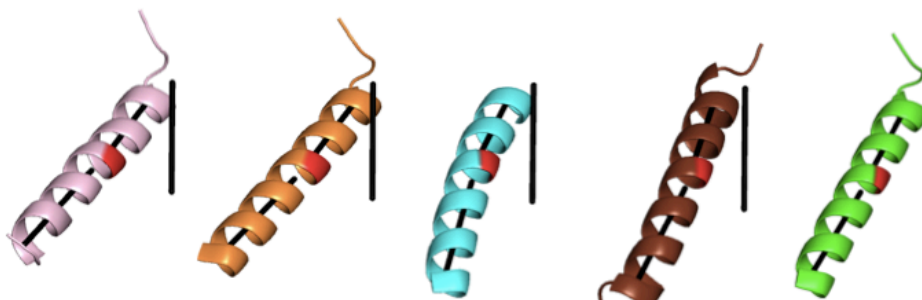


**Figure 5.5. Arrangement of M2 tetramers within the crystal lattice.** Side-view of the arrangement of M2 tetramers in crystal lattices from previously solved structures 3C9J, 3BKD, 3LBW and the recently solved S31N mutant 5C02. In the previously solved structures the orientations of the N and C termini alternate from one tetramer to the next; in 5C02 all of the N- and C- termini are aligned within the crystal lattice.



| Structure  | 3C9J                   | 3BKD             | 3LBW             | 2L0J          | 5C02             |
|------------|------------------------|------------------|------------------|---------------|------------------|
| conditions | xtal, OG, pH 5.3 +drug | xtal, OG, pH 7.3 | xtal, OG, pH 6.5 | ssNMR, pH 7.5 | xtal,LCP, pH 8.0 |
| N-term     | 33.6                   | 33.6             | 32.9             | 32.5          | 28.7             |
| C-term     | 35.4                   | 36.5             | 18.9             | 25.1          | 29.1             |

**Figure 5.6. Tilt of M2 monomers relative to the channel's central axis.** Helical tilts in units of degrees for the N-terminus (residues 25-34) and C-terminus (34-46) of M2 from various structural models. The S31N mutant structure 5C02 is in the Inward<sub>open</sub> conformation, as are structures 3C9J and 3BKD. Structure 3LBW adopts the Inward<sub>closed</sub> conformation, while structure 2L0J has an intermediate degree of helical tilt relative to the Inward<sub>open</sub> and Inward<sub>closed</sub> conformations.

**Table 5.1. Data processing and refinement statistics.**

|   |                    |
|---|--------------------|
| <b>5C02</b>                                 |                    |
| <b>Space group</b>                          | $I_4$              |
| <b>Cell dimensions</b>                      |                    |
| <b>a=b, c (Å)</b>                           | 28.65, 68.38       |
| <b><math>\alpha=\beta=\gamma</math> (°)</b> | 90                 |
| <b>Data collection</b>                      |                    |
| <b>Wavelength (Å)</b>                       | 0.979338           |
| <b>Resolution (Å)</b>                       | 1.59 (1.64 - 1.59) |
| <b>No. reflections</b>                      | 11589 (613)        |
| <b>Redundancy</b>                           | 3.2 (2.2)          |
| <b>I/<math>\sigma</math>I</b>               | 17.2 (3.3)         |
| <b>Completeness (%)</b>                     | 98.9 (94.3)        |
| <b>R<sub>merge</sub></b>                    | 0.041 (0.243)      |
| <b>Refinement</b>                           |                    |
| <b>Resolution (Å)</b>                       | 1.59               |
| <b>R<sub>work</sub></b>                     | 0.1571             |
| <b>R<sub>free</sub></b>                     | 0.1949             |
| <b>Number of non-hydrogen atoms</b>         | 276                |
| <b>Protein</b>                              | 194                |
| <b>Ligands</b>                              | 58                 |
| <b>Water</b>                                | 21                 |
| <b>B factors</b>                            |                    |
| <b>Protein</b>                              | 21.90              |
| <b>Ligands</b>                              | 32.60              |
| <b>Solvent</b>                              | 36.30              |
| <b>RMS deviations</b>                       |                    |
| <b>Bond Lengths (Å)</b>                     | 0.010              |
| <b>Bond Angles (°)</b>                      | 1.71               |

## 5.7 References

- 1 Ma, C. L. *et al.* Identification of the functional core of the influenza A virus A/M2 proton-selective ion channel. *Proc. Natl. Acad. Sci. U. S. A.* **106**, 12283-12288, doi:10.1073/pnas.0905726106 (2009).
- 2 Rossman, J. S. *et al.* Influenza Virus M2 Ion Channel Protein Is Necessary for Filamentous Virion Formation. *J. Virol.* **84**, 5078-5088, doi:10.1128/jvi.00119-10 (2010).
- 3 Schmidt, N. W., Mishra, A., Wang, J., DeGrado, W. F. & Wong, G. C. L. Influenza Virus A M2 Protein Generates Negative Gaussian Membrane Curvature Necessary for Budding and Scission. *J. Am. Chem. Soc.* **135**, 13710-13719, doi:10.1021/ja400146z (2013).
- 4 Chen, B. J., Leser, G. P., Jackson, D. & Lamb, R. A. The Influenza Virus M2 Protein Cytoplasmic Tail Interacts with the M1 Protein and Influences Virus Assembly at the Site of Virus Budding. *J. Virol.* **82**, 10059-10070, doi:10.1128/jvi.01184-08 (2008).
- 5 Cady, S. D. *et al.* Structure of the amantadine binding site of influenza M2 proton channels in lipid bilayers. *Nature* **463**, 689-692, doi:nature0872210.1038/nature08722 (2010).
- 6 Stouffer, A. L. *et al.* Structural basis for the function and inhibition of an influenza virus proton channel. *Nature* **451**, 596-599, doi:nature06528 10.1038/nature06528 (2008).
- 7 Ciampor, F. *et al.* Evidence that the amantadine-induced, M2-mediated conversion of influenza-A virus hemagglutinin to the low pH conformation occurs in an acidic transgolgi compartment. *Virology* **188**, 14-24, doi:10.1016/0042-6822(92)90730-d (1992).
- 8 Grambas, S. & Hay, A. J. Maturation of influenza-A virus hemagglutinin - estimates of the pH encountered during transport and its regulation by the M2 protein. *Virology* **190**, 11-18, doi:10.1016/0042-6822(92)91187-y (1992).
- 9 Dong, G. *et al.* Adamantane-Resistant Influenza A Viruses in the World (1902,Äì2013): Frequency and Distribution of M2 Gene Mutations. *PLoS One* **10**, e0119115, doi:10.1371/journal.pone.0119115 (2015).
- 10 Pielak, R. M., Schnell, J. R. & Chou, J. J. Mechanism of drug inhibition and drug resistance of influenza A M2 channel. *Proc. Natl. Acad. Sci. U. S. A.* **106**, 7379-7384, doi:10.1073/pnas.0902548106 (2009).
- 11 Wang, J. *et al.* Structure and inhibition of the drug-resistant S31N mutant of the M2 ion channel of influenza A virus. *Proc Natl Acad Sci U S A* **110**, 1315-1320, doi:10.1073/pnas.1216526110 (2013).



- 12 Thomaston, J. L. *et al.* High-resolution structures of the M2 channel from influenza A virus reveal dynamic pathways for proton stabilization and transduction. *Proceedings of the National Academy of Sciences* **112**, 14260-14265, doi:10.1073/pnas.1518493112 (2015).
- 13 Khurana, E. *et al.* Molecular dynamics calculations suggest a conduction mechanism for the M2 proton channel from influenza A virus. *Proceedings of the National Academy of Sciences* **106**, 1069-1074, doi:10.1073/pnas.0811720106 (2009).
- 14 Yi, M., Cross, T. A. & Zhou, H. X. A secondary gate as a mechanism for inhibition of the M2 proton channel by amantadine. *J Phys Chem B* **112**, 7977-7979, doi:10.1021/jp800171m (2008).
- 15 Liang, R., Li, H., Swanson, J. M. & Voth, G. A. Multiscale simulation reveals a multifaceted mechanism of proton permeation through the influenza A M2 proton channel. *Proc Natl Acad Sci U S A* **111**, 9396-9401, doi:10.1073/pnas.1401997111 (2014).
- 16 Wei, C. & Pohorille, A. Activation and proton transport mechanism in influenza A M2 channel. *Biophys J* **105**, 2036-2045, doi:10.1016/j.bpj.2013.08.030 (2013).
- 17 Caffrey, M. & Cherezov, V. Crystallizing membrane proteins using lipidic mesophases. *Nat. Protoc.* **4**, 706-731, doi:10.1038/nprot.2009.31 (2009).
- 18 Battye, T. G. G., Kontogiannis, L., Johnson, O., Powell, H. R. & Leslie, A. G. W. iMOSFLM: a new graphical interface for diffraction-image processing with MOSFLM. *Acta Crystallogr. Sect. D-Biol. Crystallogr.* **67**, 271-281, doi:10.1107/s0907444910048675 (2011).
- 19 McCoy, A. J. *et al.* Phaser crystallographic software. *J. Appl. Crystallogr.* **40**, 658-674, doi:10.1107/s0021889807021206 (2007).
- 20 Stouffer, A. L. *et al.* Structural basis for the function and inhibition of an influenza virus proton channel. *Nature* **451**, 596-U513, doi:10.1038/nature06528 (2008).
- 21 Adams, P. D. *et al.* PHENIX: a comprehensive Python-based system for macromolecular structure solution. *Acta Crystallogr. Sect. D-Biol. Crystallogr.* **66**, 213-221, doi:10.1107/s0907444909052925 (2010).
- 22 Emsley, P., Lohkamp, B., Scott, W. G. & Cowtan, K. Features and development of Coot. *Acta Crystallogr. Sect. D-Biol. Crystallogr.* **66**, 486-501, doi:10.1107/s0907444910007493 (2010).
- 23 Schrodinger, LLC. *The PyMOL Molecular Graphics System, Version 1.3r1* (2010).

## Chapter 6

### **X-ray crystal structure of the S31N mutant of the influenza M2 proton channel in two conformational states: an open and shut case**

#### **6.1 Introduction**

Resistance to influenza antivirals is an ongoing concern. Most currently circulating strains of influenza are resistant to the adamantane drugs,<sup>1,2</sup> which target the influenza M2 proton channel.<sup>3,4</sup> Some strains are resistant to both NA inhibitors and M2 channel blockers.<sup>5</sup> The most prevalent drug-resistant mutant in currently circulating influenza viruses is S31N,<sup>6-9</sup> which is found in over 98% of adamantane-resistant strains of influenza.<sup>1</sup>

Only a small number of M2 mutants result in fit viruses. The TM domain of the influenza M2 proton channel is well-conserved relative to the rest of the protein.<sup>10</sup> Mutating one residue of the M2 monomer introduces four perturbations into the homotetrameric channel, so pore-lining mutations can have a large effect on channel conductance. The rate of proton conductance in the M2 channel is finely tuned; protons must be conducted at a rate that is fast enough to allow for the acidification of the viral interior and uncoating of viral RNA before HA-mediated membrane fusion occurs,<sup>11,12</sup> yet proton conductance cannot occur at a rate that is fast enough to cause toxicity within the host cell. As a result, only a few pore-lining drug resistant mutations are observed in transmissible viruses, with the most notable being S31N, V27A, and L26F.<sup>2,13,14</sup> These mutations have proton conductance rates and pH activation curves that resemble the wild type channel.<sup>15</sup> Because the S31N mutation is prevalent among currently circulating adamantane-resistant viruses, it is an important target for structural characterization.

## 6.2 Results and discussion

Here we present a new X-ray crystal structure of the drug-resistant M2 S31N mutant. The asymmetric unit of these crystals contains two M2 tetramers in two distinct conformational states: one tetramer adopts the Inward<sub>open</sub> conformation, and the second tetramer adopts the Inward<sub>closed</sub> conformation (**Fig. 6.1**). The Inward<sub>open</sub> conformation seen here is very similar to the previously solved structure of the S31N mutant in this state,<sup>16</sup> with RMSD = 0.509 Å (**Fig. 6.2**). The structure of the S31N mutant in the Inward<sub>closed</sub> conformation is characterized here for the first time at atomic resolution.

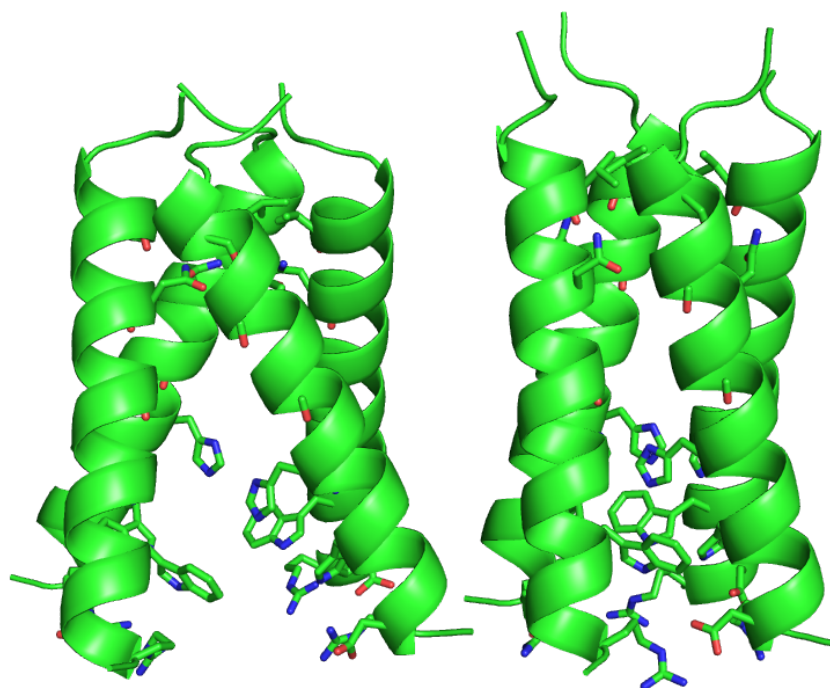


**Figure 6.1. Two conformations of the M2 S31N mutant are observed in the asymmetric unit of a new crystal form.** The Inward<sub>open</sub> conformation of the S31N mutant seen here resembles the previously solved structure 5C02. The Inward<sub>closed</sub> conformation of this mutant is characterized here for the first time.

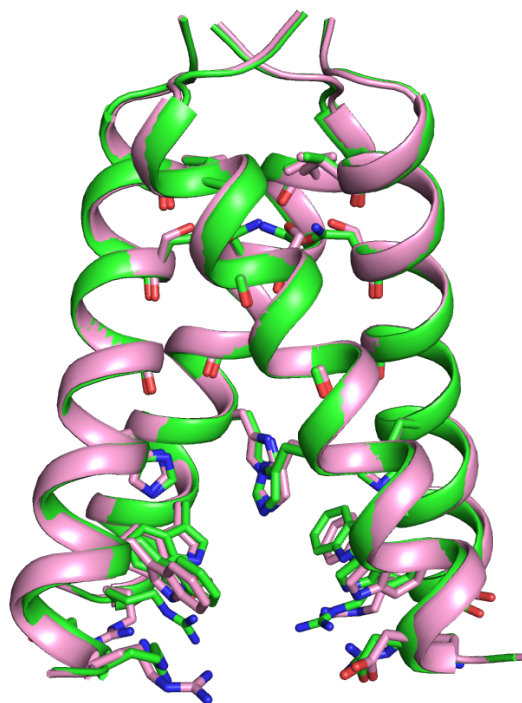


**Figure 6.2. Alignment of S31N Inward<sub>open</sub> conformation crystal structures.** The S31N Inward<sub>open</sub> conformation observed here (green) is nearly identical to the conformation previously observed in structure 5C02 (pink).

*6.2.1. Conformation of the mutant Asn31 side chain.* In the previously solved structure of the S31N mutant in the Inward<sub>open</sub> conformational state, the Asn31 side chains face toward the aqueous channel pore and form hydrogen bonds with symmetrically repeated Asn31 residues from neighboring monomer units. The same side chain configuration is observed in this new structure of the Inward<sub>open</sub> conformation. However, in the Inward<sub>closed</sub> conformation, these Asn31 side chains face away from the channel pore and instead form hydrogen bonds with carbonyls at the tetramer's monomer-monomer interface (**Fig. 6.3**). The nitrogen of the Asn31 carboxamide forms one intra-helix H-bond with the carbonyl from Val27 and a second H-bond with Leu26 from a neighboring monomer unit (**Fig 6.4**).

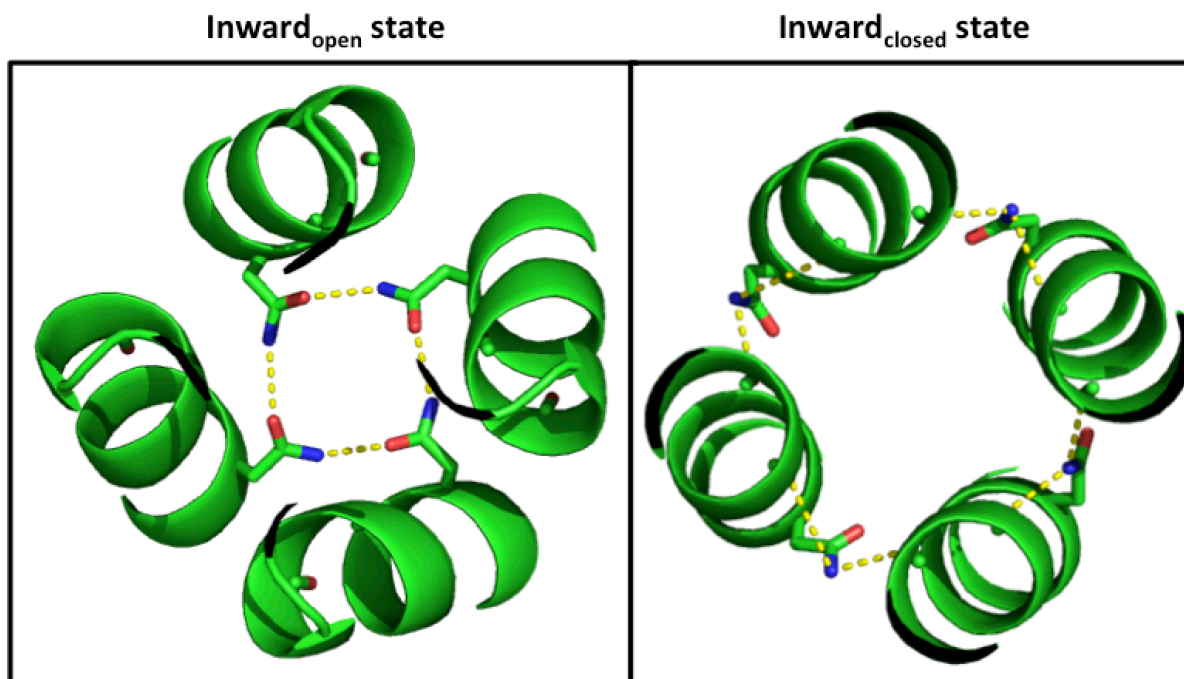


**Figure 6.3. Top-down view of the M2 S31N crystal structure.** The  $\text{Inward}_{\text{open}}$  conformation is at left, and the  $\text{Inward}_{\text{closed}}$  conformation is at right. As previously observed in structure 5C02, Asn31 faces the center of the pore and forms H-bonds with Asn31 side chains from neighboring monomers in the  $\text{Inward}_{\text{open}}$  conformation. In the  $\text{Inward}_{\text{closed}}$  conformation, Asn31 faces away from the pore and forms H-bonds with carbonyls at the monomer-monomer interface.

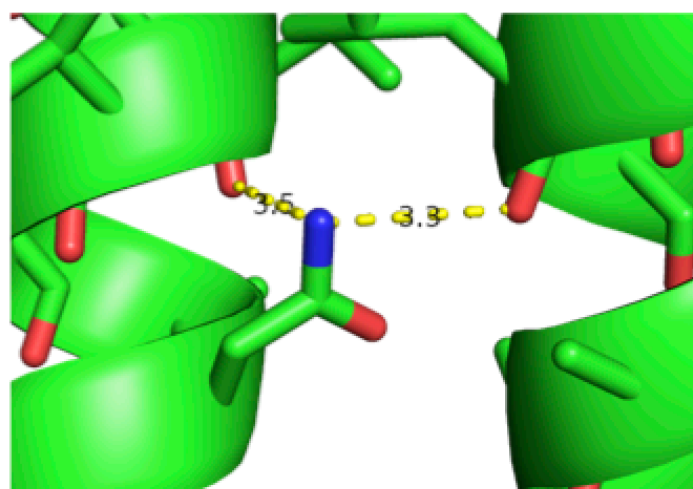


**Figure 6.4. Side view of Asn31 from the  $\text{Inward}_{\text{closed}}$  conformation.** The mutant Asn faces the monomer-monomer interface and forms two hydrogen bonds.

The conformation of this Asn31 side chain holds the key to adamantane resistance in the M2 channel. In the wild type channel, the Ser31 hydroxyl engages in just one intra-helix Val27 hydrogen bond, and the Ser31 side chain faces toward the center of the channel pore. The hydrogen bond between the mutant Asn31 side chain and the Leu26 carbonyl at the monomer-monomer interface twists the monomer helices at the N-terminus. This causes the Asn31 carboxamide to face away from the pore, while the Ala30 side chain that interacts with the monomer-monomer interface in the WT channel rotates toward the center of the pore in the S31N mutant channel. This results in a constriction of the pore at the adamantane binding site, as well as an elongation of the channel pore at the N-terminus below the Val27 gate (**Fig. 6.5**).

Based on the previously solved structure of S31N in the Inward<sub>open</sub> conformation,<sup>16</sup> the hypothesized mechanism of drug resistance in the S31N mutant channel was assumed to be a steric block of the binding site as a result of replacing the Ser31 hydroxyl with the larger and more hydrophilic Asn31 carboxamide. However, in this newly solved structure of the Inward<sub>closed</sub> conformation of the S31N mutant, Asn31 is observed to face away from the center of the pore. Hydrogen bonds between the Asn31 carboxamide nitrogens and the carbonyls of Leu26 exert a torsional force on the monomer helices, causing the pore in this N-terminal region to constrict.

The shape of the channel pore in both conformational states could play a role in inhibition of the M2 channel. Both of the adamantane drugs, amantadine and rimantadine, have been observed to form stable complexes with both conformational states of the M2 wild type channel in X-ray crystal structures.<sup>17,18</sup> This is consistent with inhibition of proton conduction upon addition of adamantanes at both high and low pH ranges;<sup>4,19</sup> though the channel exists in conformational equilibrium at low pH,<sup>20-22</sup> the adamantanes can bind to both states. The

structures presented here will aid the design of new inhibitors to target both conformational states of the adamantane-resistant S31N mutant M2 channel.

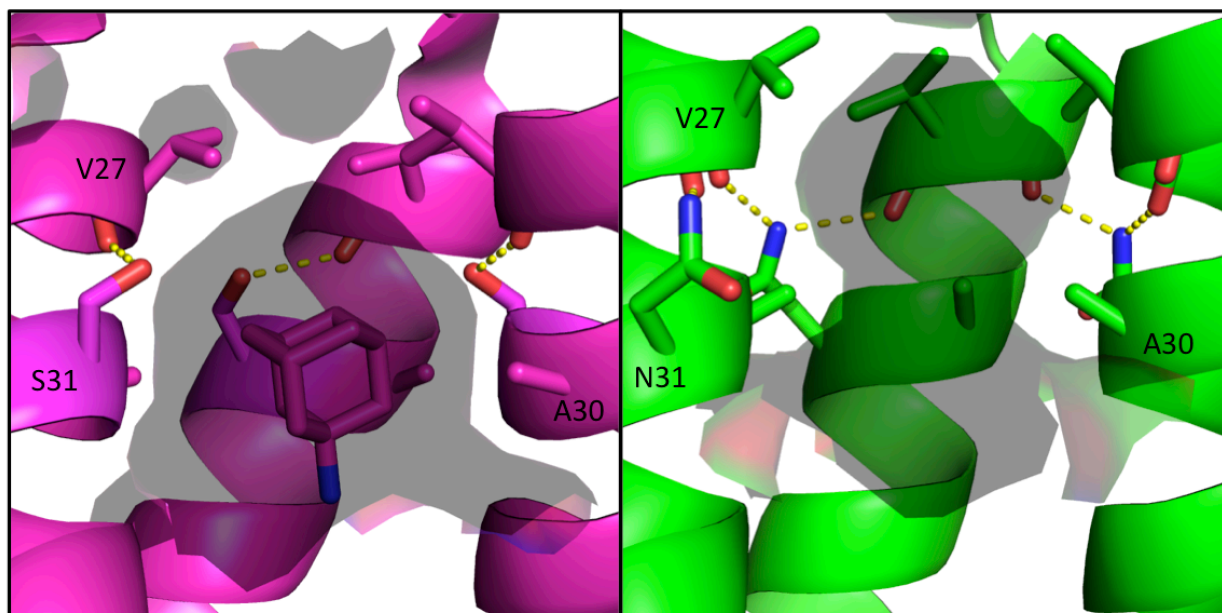


**Figure 6.5. Solvent-accessible surface area inside the M2 pore at the adamantane binding site.** Amantadine-bound WT structure in the Inward<sub>closed</sub> conformation (left, magenta) vs. S31N Inward<sub>closed</sub> conformation (green, right); solvent-accessible surface area (calculated using a 1.4 Å probe) is shown as a transparent surface. In the WT channel, Ser31 forms an intra-helix hydrogen bond and partially faces the pore. In the S31N mutant, Asn31 faces the monomer-monomer interface, twisting the monomer helices such that Ala30 faces the center of the pore. This constricts and elongates the pore at the amantadine binding site for the S31N mutant M2 channel.

### 6.3 Methods

Synthesis and purification of M2TM S31N was carried out as previously described.<sup>16,23</sup>

The sequence of this construct is as follows:



This peptide was reconstituted into the lipid cubic phase (LCP) with some modifications to the protocol described by Caffrey and Cherezov.<sup>24</sup> M2 peptide dissolved in ethanol was added to dry monoolein (Sigma) and vortexed to mix. The excess ethanol was blown off with N<sub>2</sub> gas, then the mixture was placed under vacuum (< 100 mTorr) overnight to dry. This dried mixture was melted at 40 °C then transferred into a glass syringe. Aqueous solution was added at a ratio of 20  $\mu$ L per 30 mg lipid/peptide sample. In this experiment, DMNG<sup>25,26</sup> detergent was used to stabilize the Inward<sub>closed</sub> conformation of M2, as DMNG was shown to stabilize this conformational state in solution NMR experiments. The melted lipid/peptide mix and the aqueous detergent solution were heated to 40 °C and mixed using a metal syringe coupler for approximately 3 minutes to produce the optically transparent lipid cubic phase. High-throughput screening of crystallization conditions was carried out in plastic LCP sandwich trays (Laminex) using an LCP Mosquito crystallization robot (TTP Labtech); 100 nL LCP was dispensed into each well, then 1  $\mu$ L precipitant solution was dispensed.

Crystals grew as thin, square plates up to 100  $\mu$ m in size along the longest edge. Single crystals were harvested from the cubic phase using MiTeGen litholoops and frozen in liquid nitrogen for transport and data collection. Crystals diffracted to 2.06 Å resolution and belonged to the P2<sub>1</sub> space group, with unit cell dimensions a, b, c (Å) = 36.29, 36.15, 76.45;  $\alpha$ ,  $\beta$ ,  $\gamma$  (°) = 90, 103.6, 90. Data was collected at Advanced Light Source beam 8.3.1 using the following data collection protocol: 360 frames of data; detector distance = 250 mm; oscillation = 1°; exposure time = 0.75 s; E = 11.111 keV.

Data processing was carried out in Mosflm.<sup>27</sup> Space group determination was complicated by the presence of a high degree of noncrystallographic symmetry, as well as



streaking of spots along one axis. Scaling and merging were carried out in Aimless.<sup>28</sup> Phasing was carried out using Phaser-MR<sup>29</sup> in the Phenix suite using PDB code 3LBW<sup>30</sup> as the starting model for the Inward<sub>closed</sub> conformation and 5JOO<sup>31</sup> as the starting model for the Inward<sub>open</sub> conformation. Refinement was done in Phenix,<sup>32</sup> with adjustment of the model to fit the electron density in Coot<sup>33</sup> and PyMOL.<sup>34</sup>

**Table 6.1. Data processing and refinement statistics.**

| <b>Crystal</b>                                | <b>S31N_TwoConf</b>         |
|---|-----------------------------|
| <b>Space group</b>                            | P 1 21 1                    |
| <b>Cell dimensions</b>                        |                             |
| <b>a, b, c (Å)</b>                            | 36.29 36.15 76.45           |
| <b><math>\alpha, \beta, \gamma</math> (°)</b> | 90 103.6 90                 |
| <b>Data collection</b>                        |                             |
| <b>Wavelength (Å)</b>                         | 1.1159                      |
| <b>Resolution (Å)</b>                         | 37.15 - 2.06 (2.12 - 2.06)  |
| <b>No. reflections</b>                        | 11019 (780)                 |
| <b>Redundancy</b>                             | 5.7 (5.0)                   |
| <b>I/<math>\sigma</math>I</b>                 | 8.0 (2.1)                   |
| <b>Completeness (%)</b>                       | 92.36 (89.72)               |
| <b>R<sub>pim</sub></b>                        | 0.062 (0.476)               |
| <b>Refinement</b>                             |                             |
| <b>Resolution (Å)</b>                         | 35.24 - 2.06 (2.134 - 2.06) |
| <b>R<sub>work</sub></b>                       | 0.2037 (0.2254)             |
| <b>R<sub>free</sub></b>                       | 0.2411 (0.2855)             |
| <b>Number of non-hydrogen atoms</b>           | 1641                        |
| <b>Protein</b>                                | 1546                        |
| <b>Ligands</b>                                | 28                          |
| <b>Water</b>                                  | 67                          |
| <b>B factors</b>                              | 27.65                       |
| <b>Protein</b>                                | 27.28                       |
| <b>Ligands</b>                                | 35.82                       |
| <b>Solvent</b>                                | 32.73                       |
| <b>RMS deviations</b>                         |                             |
| <b>Bond Lengths (Å)</b>                       | 0.010                       |
| <b>Bond Angles (°)</b>                        | 1.19                        |

## **6.4 Acknowledgements**

The authors would like to thank Pil Seok Chae (Hanyang University, Seoul, South Korea) for providing DMNG detergent for crystallization trials. J.L.T. and W.F.D. were supported by NIH grant R01-GM056423. Use of the LCP crystallization robot was made possible by National Center for Research Resources Grant 1S10RR027234-01. Data collection was carried out at ALS 8.3.1. Beamline 8.3.1 at the Advanced Light Source is operated by the University of California Office of the President, Multicampus Research Programs and Initiatives grant MR-15-328599 and NIGMS grants P30 GM124169 and R01 GM124149. The authors thank George Meigs and James Holton at ALS 8.3.1 for support during data collection.

## 6.5 References

- 1 Bright, R. A. *et al.* Incidence of adamantane resistance among influenza A (H3N2) viruses isolated worldwide from 1994 to 2005: a cause for concern. *Lancet* **366**, 1175-1181, doi:10.1016/s0140-6736(05)67338-2 (2005).
- 2 Furuse, Y., Suzuki, A. & Oshitani, H. Large-Scale Sequence Analysis of M Gene of Influenza A Viruses from Different Species: Mechanisms for Emergence and Spread of Amantadine Resistance. *Antimicrobial Agents and Chemotherapy* **53**, 4457-4463, doi:10.1128/AAC.00650-09 (2009).
- 3 Hay, A. J., Wolstenholme, A. J., Skehel, J. J. & Smith, M. H. The molecular basis of the specific anti-influenza action of amantadine. *The EMBO Journal* **4**, 3021-3024 (1985).
- 4 Wang, C., Takeuchi, K., Pinto, L. H. & Lamb, R. A. Ion-channel activity of influenza-A virus M(2) protein - characterization of the amantadine block. *Journal of Virology* **67**, 5585-5594 (1993).
- 5 Sheu, T. G. *et al.* Dual Resistance to Adamantanes and Oseltamivir Among Seasonal Influenza A(H1N1) Viruses: 2008–2010. *The Journal of Infectious Diseases* **203**, 13-17, doi:10.1093/infdis/jiq005 (2011).
- 6 Deyde, V. *et al.* Genomic events underlying the changes in adamantane resistance among influenza A(H3N2) viruses during 2006–2008. *Influenza and Other Respiratory Viruses* **3**, 297-314, doi:10.1111/j.1750-2659.2009.00103.x (2009).
- 7 Deyde, V. M. *et al.* Surveillance of Resistance to Adamantanes among Influenza A(H3N2) and A(H1N1) Viruses Isolated Worldwide. *The Journal of Infectious Diseases* **196**, 249-257, doi:10.1086/518936 (2007).
- 8 Krumbholz, A. *et al.* High prevalence of amantadine resistance among circulating European porcine influenza A viruses. *Journal of General Virology* **90**, 900-908, doi:doi:10.1099/vir.2008.007260-0 (2009).
- 9 Simonsen, L. *et al.* The Genesis and Spread of Reassortment Human Influenza A/H3N2 Viruses Conferring Adamantane Resistance. *Molecular Biology and Evolution* **24**, 1811-1820, doi:10.1093/molbev/msm103 (2007).
- 10 Dong, G. *et al.* Adamantane-resistant influenza A viruses in the world (1902-2013): frequency and distribution of M2 gene mutations. *Plos One* **10**, e0119115, doi:10.1371/journal.pone.0119115 (2015).
- 11 Grambas, S., Bennett, M. S. & Hay, A. J. Influence of amantadine resistance mutations on the pH regulatory function of the M2-protein of influenza-A viruses. *Virology* **191**, 541-549, doi:10.1016/0042-6822(92)90229-i (1992).

- 12 Grambas, S. & Hay, A. J. Maturation of influenza-A virus hemagglutinin - estimates of the pH encountered during transport and its regulation by the M2 protein. *Virology* **190**, 11-18, doi:10.1016/0042-6822(92)91187-y (1992).
- 13 Dong, G. *et al.* Adamantane-Resistant Influenza A Viruses in the World (1902–2013): Frequency and Distribution of M2 Gene Mutations. *PLoS ONE* **10**, e0119115, doi:10.1371/journal.pone.0119115 (2015).
- 14 Furuse, Y., Suzuki, A., Kamigaki, T. & Oshitani, H. Evolution of the M gene of the influenza A virus in different host species: large-scale sequence analysis. *Virology Journal* **6**, 67-67, doi:10.1186/1743-422X-6-67 (2009).
- 15 Balannik, V. *et al.* Functional studies and modeling of pore-lining residue mutants of the influenza A virus M2 ion channel. *Biochemistry* **49**, 696-708, doi:10.1021/bi901799k (2010).
- 16 Thomaston, J. L. & DeGrado, W. F. Crystal structure of the drug-resistant S31N influenza M2 proton channel. *Protein Science* **25**, 1551-1554, doi:10.1002/pro.2937 (2016).
- 17 Stouffer, A. L. *et al.* Structural basis for the function and inhibition of an influenza virus proton channel. *Nature* **451**, 596-U513, doi:10.1038/nature06528 (2008).
- 18 Thomaston, J. L. P., N.F.; Konstantinidi, A.; Wang, J.; Kolocouris, A.; DeGrado, W.F. Inhibitors of the M2 proton channel engage and disrupt transmembrane networks of hydrogen-bonded waters. *in preparation* (2018).
- 19 Martin, K. & Helenius, A. Nuclear transport of influenza virus ribonucleoproteins: The viral matrix protein (M1) promotes export and inhibits import. *Cell* **67**, 117-130, doi:[http://dx.doi.org/10.1016/0092-8674\(91\)90576-K](http://dx.doi.org/10.1016/0092-8674(91)90576-K) (1991).
- 20 Li, C., Qin, H., Gao, F. P. & Cross, T. A. Solid-state NMR characterization of conformational plasticity within the transmembrane domain of the influenza A M2 proton channel. *Biochim Biophys Acta* **1768**, 3162-3170 (2007).
- 21 Schnell, J. R. & Chou, J. J. Structure and mechanism of the M2 proton channel of influenza A virus. *Nature* **451**, 591-U512, doi:10.1038/nature06531 (2008).
- 22 Wang, J. *et al.* Structure and inhibition of the drug-resistant S31N mutant of the M2 ion channel of influenza A virus. *Proc Natl Acad Sci U S A* **110**, 1315-1320, doi:10.1073/pnas.1216526110 (2013).
- 23 Thomaston, J. L. *et al.* High-resolution structures of the M2 channel from influenza A virus reveal dynamic pathways for proton stabilization and transduction. *Proceedings of the National Academy of Sciences* **112**, 14260-14265, doi:10.1073/pnas.1518493112 (2015).

- 24 Caffrey, M. & Cherezov, V. Crystallizing membrane proteins using lipidic mesophases. *Nature Protocols* **4**, 706-731, doi:10.1038/nprot.2009.31 (2009).
- 25 Chae, P. S. *et al.* Maltose-neopentyl glycol (MNG) amphiphiles for solubilization, stabilization and crystallization of membrane proteins. *Nature Methods* **7**, 1003-1008, doi:10.1038/nmeth.1526 (2010).
- 26 Cho, K. H. *et al.* Maltose Neopentyl Glycol-3 (MNG-3) Analogues for Membrane Protein Study. *The Analyst* **140**, 3157-3163, doi:10.1039/c5an00240k (2015).
- 27 Battye, T. G. G., Kontogiannis, L., Johnson, O., Powell, H. R. & Leslie, A. G. W. iMOSFLM: a new graphical interface for diffraction-image processing with MOSFLM. *Acta Crystallographica Section D-Biological Crystallography* **67**, 271-281, doi:10.1107/s0907444910048675 (2011).
- 28 Winn, M. D. *et al.* Overview of the CCP4 suite and current developments. *Acta Crystallographica Section D-Biological Crystallography* **67**, 235-242, doi:10.1107/s0907444910045749 (2011).
- 29 McCoy, A. J. *et al.* Phaser crystallographic software. *Journal of Applied Crystallography* **40**, 658-674, doi:10.1107/s0021889807021206 (2007).
- 30 Acharya, R. *et al.* Structure and mechanism of proton transport through the transmembrane tetrameric M2 protein bundle of the influenza A virus. *Proceedings of the National Academy of Sciences* **107**, 15075-15080, doi:10.1073/pnas.1007071107 (2010).
- 31 Thomaston, J. L. *et al.* XFEL structures of the influenza M2 proton channel: Room temperature water networks and insights into proton conduction. *Proceedings of the National Academy of Sciences* **114**, 13357-13362, doi: <https://doi.org/10.1073/pnas.1705624114> (2017).
- 32 Adams, P. D. *et al.* PHENIX: a comprehensive Python-based system for macromolecular structure solution. *Acta Crystallographica Section D-Biological Crystallography* **66**, 213-221, doi:10.1107/s0907444909052925 (2010).
- 33 Emsley, P., Lohkamp, B., Scott, W. G. & Cowtan, K. Features and development of Coot. *Acta Crystallographica Section D-Biological Crystallography* **66**, 486-501, doi:10.1107/s0907444910007493 (2010).
- 34 Schrodinger, LLC. *The PyMOL Molecular Graphics System, Version 1.3r1* (2010).

## Chapter 7

### Works in progress

#### 7.1 Motivation

Having characterized the binding of drugs and inhibitors to the wild type M2 channel in crystal structures of the transmembrane (TM) domain construct (residues 22-46), our next goals are to examine the binding of new inhibitors to drug-resistant M2 mutants and to characterize the binding of drugs and inhibitors to longer M2 constructs.

#### 7.2 Structure of drug-resistant V27A mutant bound to a spiro-adamantyl amine inhibitor

Here we present an X-ray crystal structure of the drug-resistant V27A M2 channel bound to a spiro-adamantyl amine inhibitor. This compound inhibits conductance of protons in both the V27A mutant and the wild type channel in two electrode voltage clamp (TEVC) assays using *Xenopus* oocytes<sup>1</sup> (**Fig. 7.1**). When Val27 is mutated to Ala, the diameter of the channel pore at the drug binding site increases, and hydrophobic interactions that stabilize the binding of adamantanes to the wild type channel are removed. As a result of this widening of the pore at the channel's N-terminus, the spiro-adamantyl amine compound binds with its adamantyl group higher in the channel than previously observed in structures of the adamantane drugs bound to the wild type M2 channel. The inhibitor binds with its ammonium group pointed down the channel pore, in the direction of the gating His37 residues. An alignment of the amantadine-bound structure of wild type M2 to this new structure of the inhibitor-bound V27A channel shows that the ammonium groups of amantadine and spiro-adamantyl amine localize to approximately the same position (0.5 Å distance between the two ammonium nitrogens) (**Fig.**

7.2). As previously observed in the amantadine- and rimantadine- bound structures of M2WT, here we see two layers of carbonyl-associated waters in the channel pore below the bound inhibitor. These waters form a hydrogen bonding network that leads down to the gating His37 residues and could play a role in proton transport.

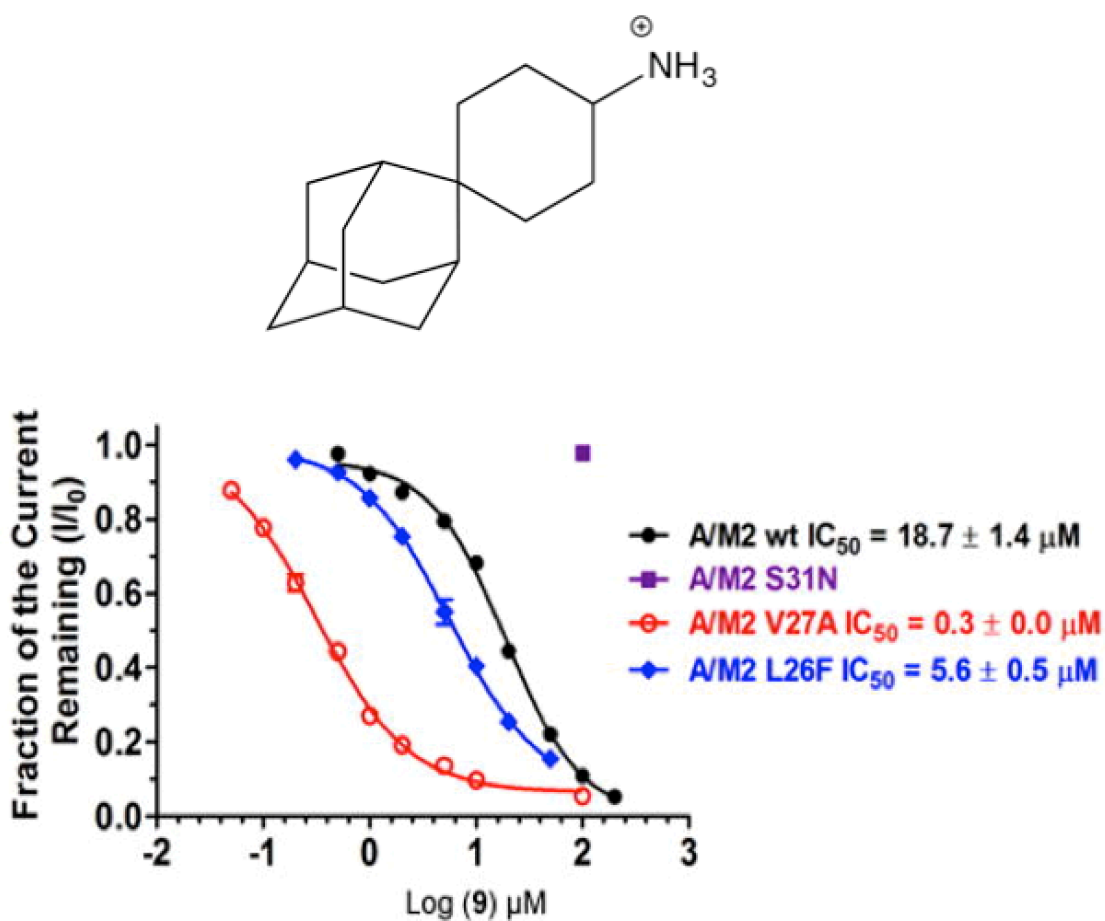
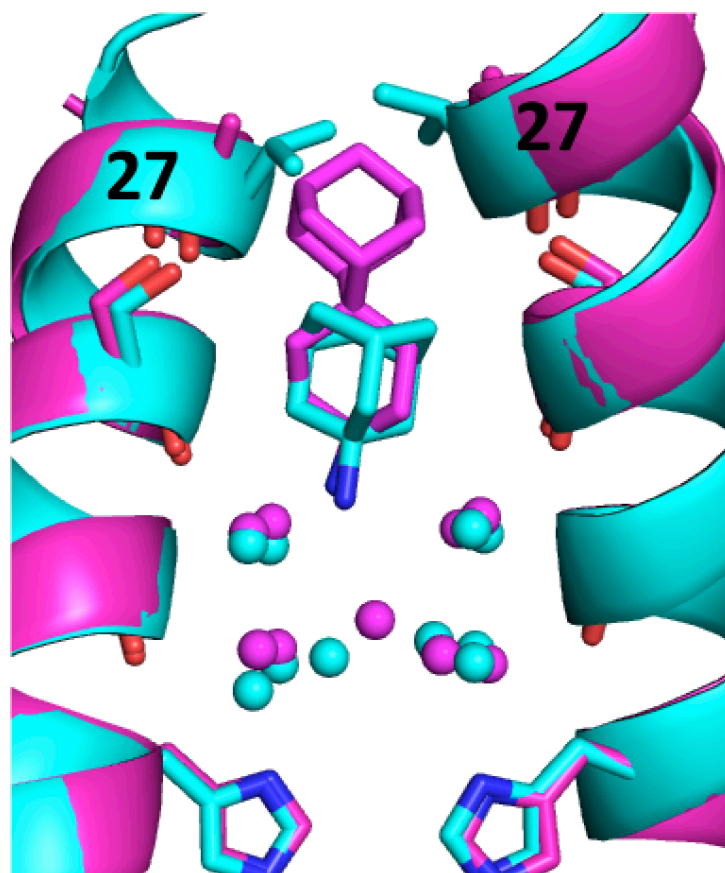


Figure 7.1. A spiro-adamantyl amine compound inhibits proton conduction in wild type, V27A, and L26F M2. Figure adapted from Wang et al. JACS 2011.<sup>1</sup>



**Figure 7.2. Alignment of inhibitor-bound V27A M2 structure to amantadine-bound WT M2 structure.** V27A structure is shown in magenta with waters as magenta spheres, wild type structure is shown in cyan with waters as cyan spheres. The drug/inhibitor ammonium group localizes to approximately the same position in both structures. The adamantyl group localizes higher in the channel in the V27A structure, and occupies the extra room at the top of the channel created by the Val27 to Ala mutation. In both structures we observe two layers of carbonyl-associated waters.

Previously, we solved a structure of this spiro-adamantyl amine inhibitor bound to the wild type M2 channel. The four symmetrically repeated Val27 residues form a valve that completely occludes the N-terminus of the channel in the  $\text{Inward}_{\text{closed}}$  conformation; breathing motions of this secondary Val27 gate are predicted to allow water, ions, and drugs/inhibitors to enter the N-terminus of the channel.<sup>2,3</sup> In the WT M2 structure, the adamantyl group of the bound spiro-adamantyl amine inhibitor localizes to approximately the same position as the adamantyl



groups of the amantadine- and rimantadine-bound WT M2 structures. The ammonium group, however, binds deeper in the channel pore than that of the adamantane drugs, and the hydrophobic scaffold of the inhibitor displaces the layer of waters associated with the four pore-facing Ala30 carbonyls.

These X-ray crystal structures reveal that this spiro-adamantyl amine compound inhibits both the wild type and the V27A mutant M2 channel by shifting its binding position depending on which residue is present at position 27 (**Fig. 7.3**). When binding to the V27A mutant channel, the inhibitor ammonium forms hydrogen bonds with the layer of waters associated with the Ala30 carbonyls, similar to previously observed structures of amantadine binding to wild type M2. When binding to the wild type channel, the ammonium group forms hydrogen bonds to the water layer associated with the Gly34 carbonyls. This is consistent with molecular dynamics simulations in which positive charges within the M2 pore are predicted to be stabilized at multiple positions within the channel.<sup>1</sup>

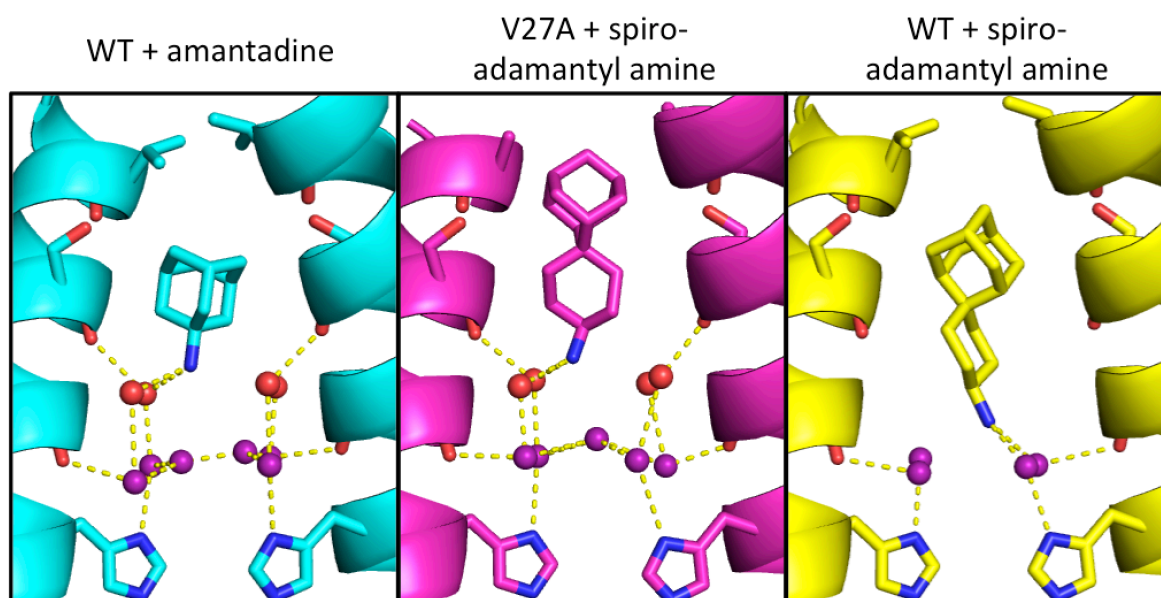


**Figure 7.3. Binding of spiro-adamantyl amine inhibitor to adamantane-resistant V27A mutant.** Structure of wild type channel bound to amantadine (6BKK) is shown in cyan, V27A bound to spiro-adamantyl amine is shown in magenta, WT bound to spiro-adamantyl amine (6BMZ) is shown in yellow. The waters forming hydrogen bonds to pore-facing Ala30 carbonyls are shown as red spheres; the waters forming hydrogen bonds to Gly34 carbonyls are purple spheres. In the structure of V27A with bound inhibitor, the ammonium group of the inhibitor localizes to the same position as the ammonium of amantadine in the wild type structure. The adamantyl group is positioned higher in the channel pore, occupying the extra space created by the Val27 to Ala mutation. In the previously solved structure of spiro-adamantyl amine inhibitor bound to the wild type channel, the adamantyl group of the inhibitor binds lower in the channel pore, and the four waters in the Ala30 solvent layer are displaced.

### 7.3 Structures of longer M2 constructs

Additionally, we are currently investigating the binding of drugs and inhibitors to longer constructs of M2. The TM domain of M2 is the minimum construct needed for selective proton transport,<sup>4,5</sup> however, truncation of the C-terminus and cytosolic helix (residues 46-60) results in a lower rate of proton transport relative to the full length construct.<sup>5,6</sup> The cyto helix also has functional importance for budding and membrane scission.<sup>7-9</sup> There is ongoing debate within the M2 community about the possible effect of this truncation on the conformation of the channel at

its C-terminus, thus highlighting the importance of atomic-resolution structures of constructs that include this domain.

We have collected datasets of the M2 transmembrane domain plus cytosolic helix (M2TMC construct, residues 22-60) to examine the binding of the spiro-adamantyl amine inhibitor to the drug-resistant M2TMC V27A mutant. The cytosolic helix appears to increase the mobility of the protein and impede crystallization trials. However, after much optimization, we were able to grow crystals diffracting to 3.16 Å resolution (**Fig. 7.4**). As is the case for other M2 datasets, large degrees of noncrystallographic symmetry have complicated space group determination and structure solution.

A preliminary molecular replacement solution ( $R_{\text{free}} = 0.3129$ ) has been obtained, in which we observe electron density corresponding to residues 47-52. The addition of the cyto helix results in slightly tighter packing of the tetrameric bundle at the C-terminus relative to structures of the TM construct (**Fig. 7.5**). All four Asp44 and Arg45 residues face the aqueous pore, associating with electron density that seems to correspond with a water or ion at the channel's center. These residues could contribute to the stabilization of a hydronium ion as a proton travels down the C-terminal portion of the channel after passing through the His37 gate. In some structures of the TM construct, Asp44 is observed to form hydrogen bonds at the monomer-monomer interface with Arg45 from a neighboring monomer unit (6BKK, 6BKL). This could potentially be an artifact resulting from truncation of the cyto helix. Further refinement is needed to resolve the structural features of this V27A TMC construct.

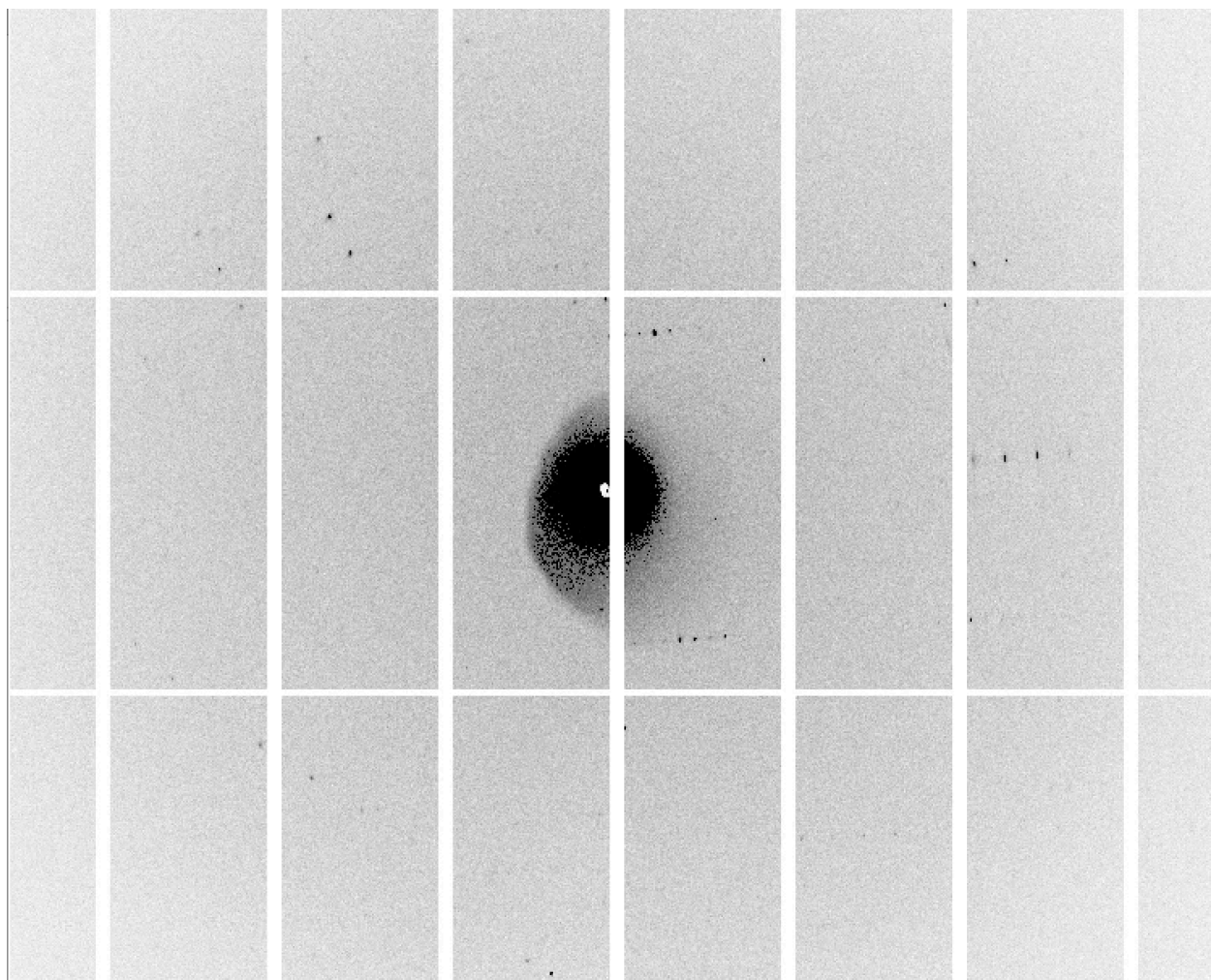


**Figure 7.4. Diffraction of V27A M2TMC plus spiro-adamantyl amine inhibitor to 3 Å resolution.**

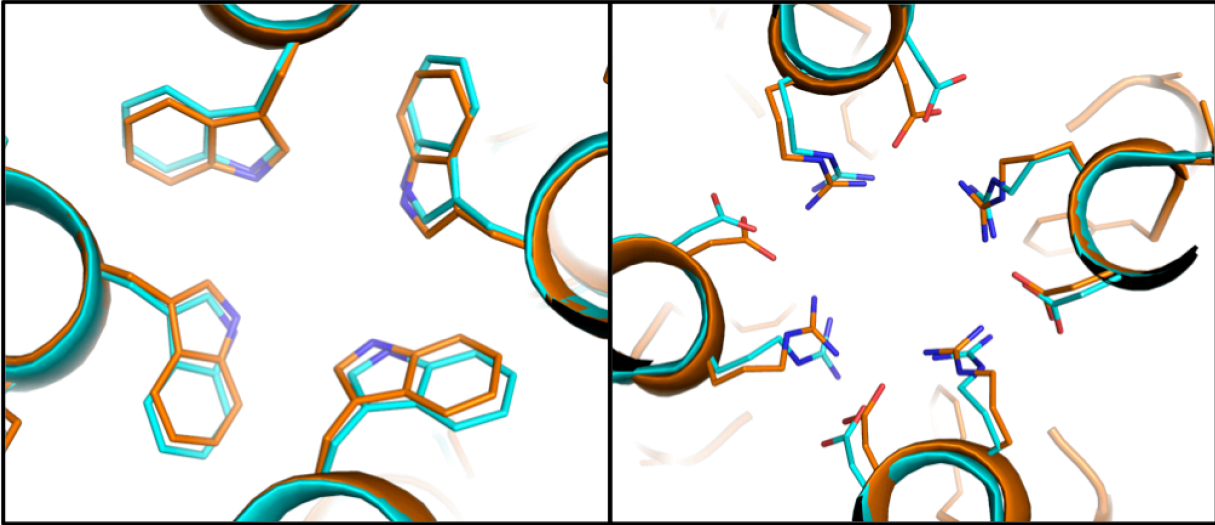


**Figure 7.5.** The M2 channel's C-terminus is slightly more constricted with inclusion of the cyto helix. Alignment of V27A TMC structure (orange) and wild type TM structure (3LBW, cyan). Trp41 is shown in the left panel, Asp44 and Arg45 are at right. The channel is slightly more constricted with inclusion of the cyto helix, though the overall conformation remains similar.

#### 7.4 Attempts to solve structure of S31N bound to inhibitors

Much effort has been made to crystallize the S31N mutant bound to inhibiting compounds. However, the structures resulting from these trials do not contain density corresponding to bound inhibitors within the M2 pore. This is possibly a result of the large degree of hydrophobicity of these inhibiting compounds; these hydrophobic inhibitors could be partitioning into the bilayer of the lipid cubic phase during crystallization trials. Co-crystallization trials are currently being attempted with more soluble S31N inhibiting compounds. Preliminary diffraction has been achieved using these compounds in co-crystallization trials with the M2TMC S31N construct (**Fig. 7.6**). However, additional trials are needed to obtain crystals that diffract to a usable resolution range.

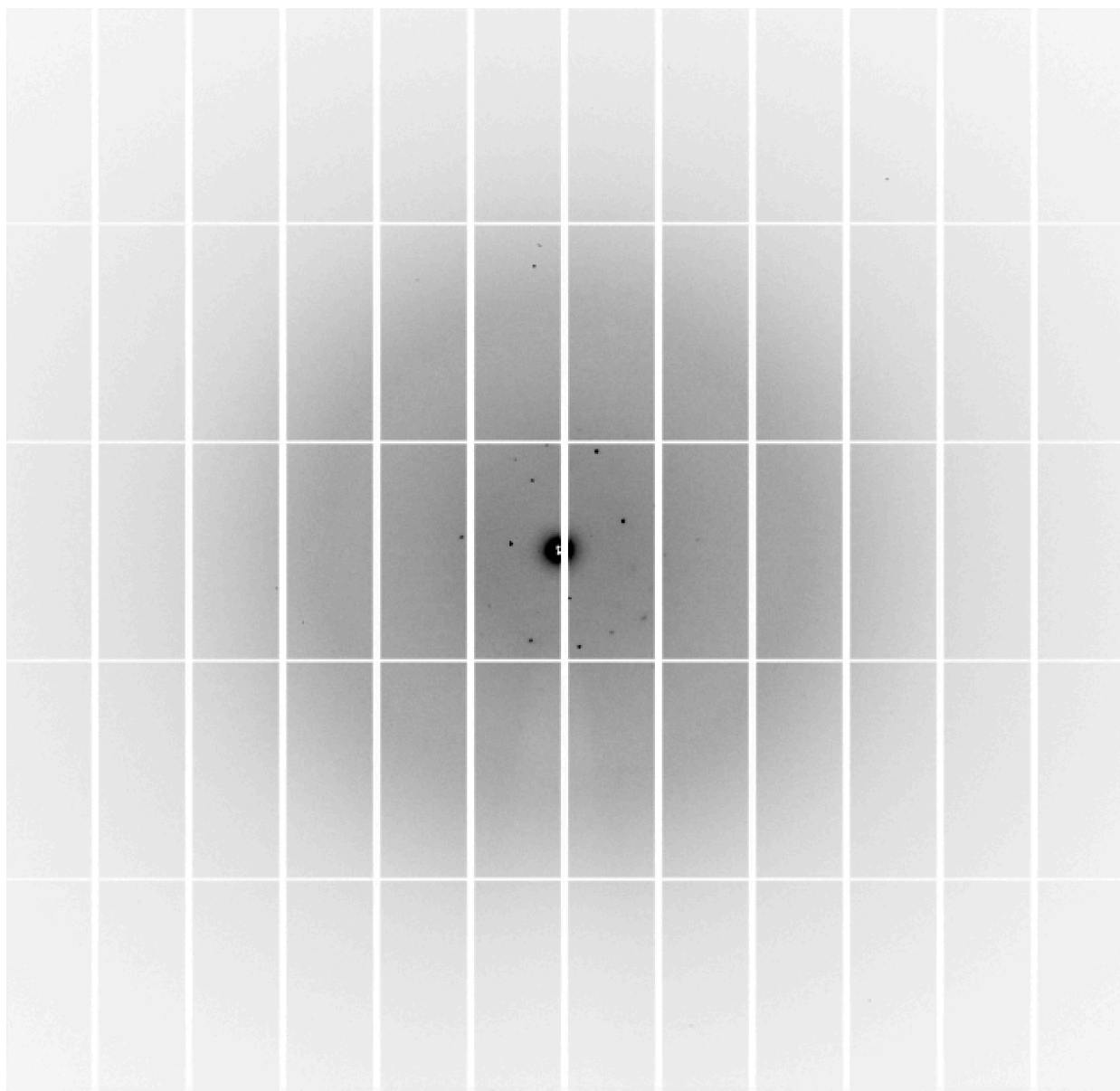


**Figure 7.6. Preliminary  $\sim 6$  Å diffraction from crystals containing S31N TMC plus WJ352 inhibitor.**

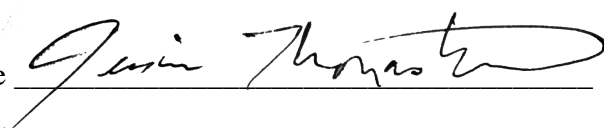
## 7.5 References

- 1 Wang, J. *et al.* Molecular dynamics simulation directed rational design of inhibitors targeting drug-resistant mutants of influenza A virus M2. *Journal of the American Chemical Society* **133**, 12834-12841, doi:Doi 10.1021/Ja204969m (2011).
- 2 Khurana, E. *et al.* Molecular dynamics calculations suggest a conduction mechanism for the M2 proton channel from influenza A virus. *Proc Natl Acad Sci U S A* **106**, 1069-1074, doi:10.1073/pnas.0811720106 (2009).
- 3 Yi, M., Cross, T. A. & Zhou, H. X. A secondary gate as a mechanism for inhibition of the M2 proton channel by amantadine. *J Phys Chem B* **112**, 7977-7979, doi:10.1021/jp800171m (2008).
- 4 Duff, K. C. & Ashley, R. H. The transmembrane domain of influenza A M2 protein forms amantadine-sensitive proton channels in planar lipid bilayers. *Virology* **190**, 485-489, doi:[http://dx.doi.org/10.1016/0042-6822\(92\)91239-Q](http://dx.doi.org/10.1016/0042-6822(92)91239-Q) (1992).
- 5 Ma, C. L. *et al.* Identification of the functional core of the influenza A virus A/M2 proton-selective ion channel. *Proceedings of the National Academy of Sciences* **106**, 12283-12288, doi:10.1073/pnas.0905726106 (2009).
- 6 Tobler, K., Kelly, M. L., Pinto, L. H. & Lamb, R. A. Effect of cytoplasmic tail truncations on the activity of the M(2) ion channel of influenza A virus. *Journal of Virology* **73**, 9695-9701 (1999).
- 7 Roberts, K. L., Leser, G. P., Ma, C. & Lamb, R. A. The amphipathic helix of influenza A virus M2 protein is required for filamentous bud formation and scission of filamentous and spherical particles. *Journal of Virology* **87**, 9973-9982, doi:10.1128/JVI.01363-13 (2013).
- 8 Rossman, J. S., Jing, X., Leser, G. P. & Lamb, R. A. Influenza virus M2 protein mediates ESCRT-independent membrane scission. *Cell* **142**, 902-913, doi:10.1016/j.cell.2010.08.029 (2010).
- 9 Schmidt, N. W., Mishra, A., Wang, J., DeGrado, W. F. & Wong, G. C. L. Influenza virus A M2 protein generates negative gaussian membrane curvature necessary for budding and scission. *Journal of the American Chemical Society* **135**, 13710-13719, doi:10.1021/ja400146z (2013).

## **Publishing Agreement**

It is the policy of the University to encourage the distribution of all theses, dissertations, and manuscripts. Copies of all UCSF theses, dissertations, and manuscripts will be routed to the library via the Graduate Division. The library will make all theses, dissertations, and manuscripts accessible to the public and will preserve these to the best of their abilities, in perpetuity.

I hereby grant permission to the Graduate Division of the University of California, San Francisco to release copies of my thesis, dissertation, or manuscript to the Campus Library to provide access and preservation, in whole or in part, in perpetuity.

Author Signature  Date August 26, 2018